

CERN/LHCC 2000-001
ALICE TDR 7
7 January 2000

ALICE

Technical Design Report

of the

Time Projection Chamber

This edition contains a few minor modifications, essentially corrections of typographical errors, relative
to the first, limited, edition.

Cover design by CERN Desktop Publishing Office

AliRoot Event Display of TPC

Printed at CERN
December 1999

ISBN 92-9083-155-3

ALICE Collaboration

Alessandria, Italy, Facoltà di Scienze dell’Università:
G. Dellacasa, L. Ramello, E. Scalas and M. Sitta.

Aligarh, India, Physics Department, Aligarh Muslim University:
N. Ahmad, S. Ahmad, T. Ahmad, W. Bari, M. Irfan and M. Zafar.

Athens, Greece, Nuclear and Particle Physics Division, University of Athens:
A.L.S. Angelis¹⁾, G. Mavromanolakis and A.D. Panagiotou.

Athens, Greece, Institute of Nuclear Physics, NRC Demokritos:
K. Kalfas.

Bari, Italy, Dipartimento di Fisica dell’Università and Sezione INFN:
R. Caliandro, D. Cozza, G. De Cataldo, D. Di Bari, D. Elia, R.A. Fini, B. Ghidini, V. Lenti, V. Manzari,
E. Nappi¹⁾, F. Navach and F. Posa.

Bari, Italy, Politecnico and Sezione INFN:
F. Corsi, D. De Venuto, R. Dinapoli, A. Grimaldi, G. Lisco, C. Marzocca and E. Monno.

Beijing, China, China Institute of Atomic Energy:
X. Li, S. Lu, Z. Lu, B. Sa, J. Yuan, J. Zhou, S. Zhou and X. Zhu.

Bergen, Norway, Department of Physics, University of Bergen:
K. Fanebust, H. Helstrup, A. Klovning, J.A. Lien, O.A. Mæland, O.H. Odland, D. Röhrich, R. Rongved,
K. Ullaland and A.S. Vestbø.

Bhubaneswar, India, Institute of Physics:
S.N. Behera, A.K. Dubey, D.P. Mahapatra, B. Mohanty and S.C. Phatak.

Birmingham, United Kingdom, School of Physics and Space Research, University of Birmingham:
I.J. Bloodworth, D. Evans, G.T. Jones, P. Jovanović, J.B. Kinson, A. Kirk, O. Villalobos Baillie and
M.F. Votruba.

Bologna, Italy, University/INFN:
F. Anselmo, P. Antonioli, G. Bari, M. Basile, L. Bellagamba, D. Boscherini, A. Bruni, G. Bruni,
G. Cara Romeo, E. Cerron-Zeballos, F. Cindolo, N. Coppola, M. Corradi, S. De Pasquale, D. Falchieri,
A. Gabrielli, E. Gandolfi, P. Giusti, D. Hatzifotiadou, N.Y. Kim, G. Laurenti, M.L. Luvisetto,
A. Margotti, M. Masetti, R. Nania, F. Palmonari, A. Pesci, F. Pierella, A. Polini, G. Sartorelli,
A. Semak, G. Valenti, M.C.S. Williams and A. Zichichi.

Bratislava, Slovakia, Faculty of Mathematics and Physics, Comenius University:
J. Braciník, V. Černý, J. Ftáčnik, V. Hlinka, R. Janík, R. Lietava, M. Pikna, J. Pišút, N. Pišútová,
P. Rosinsky, B. Sitar, P. Strmeň, I. Szarka and M. Zagiba.

Bucharest, Romania, National Institute for Physics and Nuclear Engineering:
A. Andronic, V. Catanescu, M. Ciobanu, M. Duma, C.I. Legrand, D. Moisa, M. Petrovici, V. Simion
and G. Stoicea.

Budapest, Hungary, KFKI Research Institute for Particle and Nuclear Physics, Hungarian Academy of Sciences:

E. Denes, B. Eged, Z. Fodor, G. Harangozo, Z. Meggyesi, G. Palla, G. Rubin¹⁾, J. Sulyan, J. Sziklai, B.N. Vissy and J. Zimanyi.

Cagliari, Italy, Dipartimento di Fisica dell'Università and Sezione INFN:

C. Cicalo, A. De Falco, M.P. Macciotta-Serpi, A. Masoni, A. Pataki, G. Puddu, P. Randaccio, S. Serci, E. Siddi and G. Usai.

Calcutta, India, Saha Institute of Nuclear Physics:

P. Bhattacharya, S. Bose, Sukalyan Chattopadhyay, N. Majumdar, S. Mukhopadhyay, A. Sanyal, S. Sarkar, P. Sen, S.K. Sen, B.C. Sinha and T. Sinha.

Calcutta, India, Variable Energy Cyclotron Centre:

Subhasis Chattopadhyay, M.R. Dutta Majumdar, M.S. Ganti, T.K. Nayak, S. Pal, R.N. Singaraju, Bikash Sinha, M.D. Trivedi and Y.P. Viyogi.

Catania, Italy, Dipartimento di Fisica dell'Università and Sezione INFN:

A. Badalà, R. Barbera, M. Gulino, S. Ingrassia, A. Insolia, L. Lo Nigro, D. Lo Presti, A. Palmeri, G.S. Pappalardo, L. Pappalardo, C. Petta, N. Randazzo, S. Reito, F. Riggi, G.V. Russo and S. Vanadia.

CERN, Switzerland, European Laboratory for Particle Physics:

Y. Andres, J. Bächler, J.A. Belikov²⁾, V. Berejnoi³⁾, J.-C. Berset, R. Brun, M. Burns, M. Campbell, W. Carena, F. Carminati, S. Chapeland, P. Chochula⁴⁾, V. Colin de Verdière, J. Cruz de Sousa Barbosa, M. Davenport, J. de Groot, A. Di Mauro, R. Divià, C. Eisenberg, C. Engster, J. Espírito Santo, R. Esteve Bosch, M. Flammier, F. Formenti, D. Fraissard, E. Futo⁵⁾, B. Goret, T. Grassi⁶⁾, C. Gregory, M. Hoch, P.G. Innocenti, W. Klempt, A. Kluge, X. Lagrue, G. Lecoeur, J.C. Legrand, L. Leistam, B. Lenkeit, P. Lenoir, Y. Lesenechal, C. Lourenço, P. Martinengo, M. Mast, T. Meyer, R. Monnin, A. Morsch, M. Mota, L. Musa, B. Perrin, F. Piuz, J. Raynaud, A. Rivetti, K. Šafařík, J.-C. Santiard, K. Schossmaier, J. Schukraft, E. Schyns, W. Snoeys, P. Sonderegger, M. Spegel, D. Swoboda, P. Szymanski, J. Van Beelen, P. Vande Vyvre, A. Vascotto, S. Wenig, P. Wertelaers and J. Zalipska.

Chandigarh, India, Physics Department, Panjab University:

M.M. Aggarwal, A.K. Bhatia, V.S. Bhatia and G. Sood.

Clermont-Ferrand, France, Laboratoire de Physique Corpusculaire (LPC), IN2P3-CNRS and Université Blaise Pascal:

IN2P3: A. Baldit, V. Barret, N. Bastid, G. Blanchard, J. Castor, T. Chambon, P. Crochet, F. Daudon, A. Devaux, P. Dupieux, B. Espagnon, P. Force, F. Jouve, L. Lamoine, J. Lecoq, L. Royer, P. Saturnini and G. Savinel.

A. Genoux-Lubain⁷⁾, F. Manso⁷⁾ and P. Rosnet⁷⁾.

Coimbra, Portugal, Departamento de Física, Faculdade de Ciências e Tecnologia:

R. Ferreira Marques, P. Fonte, J. Pinhao and A. Policarpo.

Columbus, U.S.A., Department of Physics, Ohio State University:

H.L. Caines, H.M. Dyke, T.J. Humanic, M. Lisa, B.S. Nilsen, G. Paic¹⁾ and E. Sugarbaker.

Copenhagen, Denmark, Niels Bohr Institute:

I. Bearden, H. Bøggild, P. Christiansen, J.J. Gaardhøje, O. Hansen, A. Holm, B.S. Nielsen and D. Ouerdane.

Cracow, Poland, Henryk Niewodniczanski Institute of Nuclear Physics, High Energy Physics Department:
 J. Bartke, E. Gładysz-Dziaduś, E. Górnicki, M. Kowalski, A. Rybicki, P. Stefański and Z. Włodarczyk⁸⁾.

Darmstadt, Germany, Gesellschaft für Schwerionenforschung (GSI):
 R. Averbeck, E. Badura, C. Blume, P. Braun-Munzinger, H.W. Daues, A. Deusser, A. Devismes,
 C. Finck, P. Foka, U. Frankenfeld, C. Garabatos, G. Hering, M. Ivanov⁴⁾, J. Lühning, P. Malzacher,
 C. Markert, A. Mischke, D. Miśkowiec, W.F.J. Müller, F. Rademakers, H. Sako, A. Sandoval, H. Sann,
 H.R. Schmidt, S. Sedykh, H. Stelzer, R. Veenhof and D. Vranic.

Darmstadt, Germany, Institut für Kernphysik, Technische Universität:
 A. Förster, H. Oeschler and F. Uhlig.

Frankfurt, Germany, Institut für Kernphysik, Johann Wolfgang Goethe-Universität:
 C. Adler, W. Amend, J. Berger, J. Berschin, A. Billmeier, P. Buncic, D. Flierl, M. Gaździcki, J. Hehner,
 S. Lange, R. Renfordt, H. Rheinfels-Immans, C. Roland, G. Roland, R. Stock, H. Ströbele and
 C. Struck.

Gatchina, Russia, St. Petersburg Nuclear Physics Institute:
 K. Egorov, B. Komkov, V. Kozlov, N. Miftakhov, V. Nikouline, V. Samsonov, O. Tarasenkova,
 V. Vishnevskii, S. Volkov and A. Vorobiev.

Heidelberg, Germany, Kirchhoff Institute for Physics:
 R. Achenbach, O. Braun, M. Keller, F.O. Lesser, V. Lindenstruth, R. Schneider, M. Schulz, T. Steinbeck
 and L. Voerg.

Heidelberg, Germany, Physikalisches Institut, Ruprecht-Karls Universität:
 H. Appelhäuser, S. Damjanovic, T. Dietel, S.I. Esumi, K. Filimonov, P. Glässel, N. Herrmann,
 A. Marin, V. Petráček, J. Rak, A. Reischl, M.J. Richter, E. Schäfer, W. Schmitz, W. Seipp, J. Slivova,
 H.K. Soltveit, H.J. Specht, J. Stachel, H. Tilsner, J.P. Wessels, T. Wienold, B. Windelband and
 S. Yurevich.

Ioannina, Greece, University of Ioannina, Department of Physics:
 X. Aslanoglou and N.G. Nicolis.

Jaipur, India, Physics Department, University of Rajasthan:
 A. Bharti, S.K. Gupta, R. Raniwala and S. Raniwala.

Jammu, India, Physics Department, Jammu University:
 S.K. Badyal, A. Bhasin, A. Gupta, V.K. Gupta, S. Mahajan, L.K. Mangotra, B.V.K.S. Potukuchi,
 N.K. Rao and S.S. Sambyal.

JINR, Russia, Joint Institute for Nuclear Research:
 P.G. Akichine, V.A. Arefiev, V.I. Astakhov, A.A. Baldine, A.M. Baldine, V.D. Bartenev, B.V. Batiounia,
 I.V. Boguslavsky, Z.V. Borissovskaia, P. Bylinkine, A.V. Chabounov, G.S. Chabratova, I.A. Chichov,
 V. Danilov, V.I. Datskov, V.K. Dodokhov, L.G. Efimov, A.G. Fedounov, O.A. Golubitsky,
 B.N. Guouskov, O.I. Iouldachev, V.G. Kadychevsky, I.E. Karpunina, E.K. Koshurnikov,
 A.D. Kovalenko, A. Lioubimtsev, V.L. Lioubochits, V.I. Lobanov, G.I. Lykasov, E.A. Matiouchevski,
 K.V. Mikhailov, I. Minaev, P.V. Nomokonov, I.V. Pouzynin, I. Roufanov, I.A. Shelaev, A.V. Sidorov,
 M.K. Suleimanov, G.P. Tsvineva and A.S. Vodopianov.

V. Kuznetsov⁹⁾ and V. Shestakov⁹⁾.

Ts. Baatar¹⁰⁾, B. Khurelbaatar¹⁰⁾ and R. Togoo¹⁰⁾.

K.G. Akhobadze¹¹⁾, A.K. Djavrishvili¹¹⁾, T. Grigalashvili¹¹⁾, E.S. Ioramashvili¹¹⁾, A.V. Kharadze¹¹⁾, L. Khizanishvili¹¹⁾, T.V. Khuskivadze¹¹⁾, L.V. Shalamberidze¹¹⁾ and N. Shubitidze¹¹⁾.

N. Grigalashvili¹²⁾, M. Nioradze¹²⁾, M. Tabidze¹²⁾ and Y. Tevzadze¹²⁾.

D. Felea¹³⁾, A. Gheata¹³⁾, M. Gheata¹³⁾, M. Haiduc¹³⁾, D. Hasegan¹³⁾, R. Marginean¹³⁾, R.I. Nanciu¹³⁾ and S.I. Zgura¹³⁾.

Jyväskylä, Finland, Department of Physics, University of Jyväskylä and Helsinki Institute of Physics:
J. Aystö, M. Bondila, M. Komogorov, V. Lyapin, V. Ruuskanen and W. Trzaska.

Kangnung, South Korea, Kangnung National University:

H. Chae, C. Choi, Y. Jung, K.S. Kang, D.W. Kim, D. Kim, J. Kim, K. Lee and S. Lee.

Kharkov, Ukraine, National Scientific Centre ‘Kharkov Institute of Physics and Technology’: G.L. Bochek, V.F. Boldyshev, A.N. Dovbnya, V.I. Kulibaba, N.I. Maslov, S.V. Naumov, S.M. Potin, I.M. Prokhorets and A.F. Starodubtsev.

Kharkov, Ukraine, Scientific and Technological Research Institute of Instrument Engineering: V.N. Borshchov, S.K. Kiprich, O.M. Listratenko, G. Protsay, A.N. Reznik, A.N. Ryabukhin and V.E. Starkov.

Kiev, Ukraine, Department of High Energy Density Physics, Bogolyubov Institute for Theoretical Physics, National Academy of Sciences of Ukraine:
T. Hryna, D.E. Kharzeev, O.P. Pavlenko, A. Velytsky and G. Zinovjev.

Košice, Slovakia, Institute of Experimental Physics, Slovak Academy of Sciences and Faculty of Science P.J. Šafárik University:

J. Bán, J. Fedorišin, M. Hnatič, A. Jusko, I. Králik, A. Kravčáková, F. Kriváň, M. Krivda, M. Lupták, G. Martinská, B. Pastirčák¹⁾, L. Šándor, J. Urbán, S. Vokál and J. Vrláková.

Lausanne, Switzerland, Integrated System Laboratory (ISL), Ecole Polytechnique Fédérale de Lausanne (EPFL):

A. Aizza, F.A. Cherigui, M. Mattavelli and D. Mlynek.

Legnaro, Italy, Laboratori Nazionali di Legnaro:

A. Bologna, M. Lombardi, R.A. Ricci and L. Vannucci.

Lisbon, Portugal, Departamento de Física, Instituto Superior Técnico:

P. Branco, R. Carvalho, J. Seixas and R. Vilela Mendes.

Lund, Sweden, Division of Cosmic and Subatomic Physics, University of Lund:

L. Carlen, S.I.A. Garpmann, H.-A. Gustafsson, P. Nilsson, A. Oskarsson, L. Osterman, I. Otterlund, D. Silvermyr and E.A. Stenlund.

Lyon, France, Institut de Physique Nucléaire de Lyon (IPNL), IN2P3-CNRS and Université Claude Bernard Lyon-I:

M.Y. Chartoire, M. Chevallier, B. Cheynis, L. Ducroux, E. Gangler, M. Goyot, J.Y. Grossiord, R. Guernane, A. Guichard, D. Guinet, G. Jacquet, P. Lautesse and S. Tissot.

Marburg, Germany, Fachbereich Physik, Philipps Universität:
V. Friese, C. Höhne and F. Pühlhofer.

Mexico City, Mexico, Centro de Investigación y de Estudios Avanzados:
R. Hernández Montoya, G. Herrera Corral and L.M. Montaño.

Moscow, Russia, Institute for Nuclear Research, Academy of Science:
K.A. Chileev, M.B. Goloubeva, F.F. Gouber, T.L. Karavitcheva, A.B. Kourepin, A.I. Maevskaia,
V.I. Razine, A.I. Rechetine and N.S. Topilskaia.

Moscow, Russia, Institute for Theoretical and Experimental Physics:
A.N. Akindinov, V. Golovine, A.B. Kaidalov, M.M. Kats, I.T. Kiselev, S.M. Kisseelev, E. Lioublev,
M. Martemianov, A.N. Martemyanov, P.A. Polozov, V.S. Serov, A.V. Smirnitski, M.M. Tchoumakov,
I.A. Veltlitski, K.G. Volochine, L.S. Vorobiev and B.V. Zagreev.

Moscow, Russia, Russian Research Center ‘Kurchatov Institute’:
V. Antonenko, S. Beliaev, I. Doubovik, S. Fokine, M. Ippolitov, K. Karadjev, A.L. Lebedev, V. Lebedev,
V.I. Manko, T. Moukhanova, A. Nianine, S. Nikolaev, S. Nikouline, O. Patarakine, D. Peressounko,
I. Sibiriak, A. Vasiliev, A. Vinogradov and M. Volkov.

Moscow, Russia, Moscow Engineering Physics Institute:
V.A. Grigoriev, V.A. Kapline and V.A. Loguinov.

Münster, Germany, Institut für Kernphysik, Westfälische Wilhelms Universität:
D. Bucher, R. Glasow, N. Heine, T. Peitzmann, K. Reygers, R. Santo, H. Schlagheck, W. Verhoeven,
M. Wahn and A. Walte.

Nantes, France, Laboratoire de Physique Subatomique et des Technologies Associées (SUBATECH),
Ecole des Mines de Nantes, IN2P3-CNRS and Université de Nantes:
L. Aphecetche, A. Boucham, S. Bouvier, J. Castillo, L. Conin, J.P. Cussonneau, H. Delagrange,
D. D'Enterria, M. Dialinas, C. Drancourt, B. Erazmus, G. Guilloux, H.H. Gutbrod, M.S. Labalme,
P. Lautridou, F. Lefèvre, M. Le Guay, L. Luquin, L. Martin, G. Martinez, V. Métivier, M.J. Mora,
W. Pinganaud, G. Puil, O. Ravel, F. Retiere, C.S. Roy, D. Roy, Y. Schutz and A. Tournaire.

NIKHEF, The Netherlands, National Institute for Nuclear and High Energy Physics:
M. Botje¹⁴⁾, A. Buijs¹⁵⁾, J.J.F. Buskop¹⁴⁾, A.P. De Haas¹⁵⁾, P.K.A. De Witt Huberts^{14,15)},
R. Kamermans^{14,15)}, P.G. Kuijer^{14,15)}, D. Muigg¹⁵⁾, G. Nooren¹⁴⁾, C.J. Oskamp¹⁵⁾, A. Van Den Brink¹⁵⁾
and N. Van Eijndhoven¹⁵⁾.

Novosibirsk, Russia, Budker Institute for Nuclear Physics:
A.R. Frolov and I.N. Pestov.

Oak Ridge, U.S.A., Instrumentation and Controls Division, Oak Ridge National Laboratory:
T. Awes, C.L. Britton, W.L. Bryan and A.L. Wintenberg.

Orsay, France, Institut de Physique Nucléaire (IPNO), IN2P3-CNRS and Université de Paris-Sud:
L. Bimbot, P.F. Courtat, R. Douet, P. Edelbruck, D. Jouan, Y. Le Bornec, M. Mac Cormick, J. Peyré,
J. Pouthas and N. Willis.

Oslo, Norway, Department of Physics, University of Oslo:
A.K. Holme, G. Løvhøiden, B. Skaali, T.S. Tveter and D. Wormald.

Padua, Italy, Dipartimento di Fisica dell’Università and Sezione INFN:
 F. Antinori¹⁾, N. Carrer, M. Morando, A. Pepato, E. Quercigh, F. Scarlassara, G. Segato, F. Soramel and
 R. Turrisi.

Pohang, South Korea, Pohang Accelerator Laboratory:
 J. Choi, M.G. Kim, T.Y. Lee and E.S. Park.

Prague, Czech Republic, Institute of Physics, Academy of Science:
 A. Bejtlerova, J. Mareš, E. Mihoková, M. Nikl, K. Píška, K. Polák and P. Závada.

Protvino, Russia, Institute for High Energy Physics:
 A.M. Blik, M. Bogolyubsky, G. Britvitch, S. Erine, G.V. Khaoustov, I.V. Kharlov, V. Lichine,
 M. Lobanov, N. Minaev, S.A. Sadovski, V.D. Samoilenko, P.A. Semenov, V.I. Suzdalev and
 V. Tikhonov.

Řež u Prahy, Czech Republic, Academy of Sciences of Czech Republic, Nuclear Physics Institute:
 V. Hanzal, J. Hošek, I. Hřivnáčová¹⁾, S. Kouchpil, V. Kouchpil, A. Kugler, M. Šumbera, P. Tlustý,
 V. Wagner and D. Zákoucký.

Rome, Italy, Dipartimento di Fisica, Università di Roma ‘La Sapienza’ and Sezione INFN:
 S. Di Liberto, M.A. Mazzoni, F. Meddi¹⁾, D. Prosperi and G. Rosa.

Saclay, France, Centre d’Etudes Nucléaires, DAPNIA:
 P. Ageron, A. Baldisseri, H. Borel, D. Cacaut, I. Chevrot, P. De Girolamo, J. Gosset, L. Gosset,
 P. Hardy, D. Jourde, J.C. Lugol and F.M. Staley.

Salerno, Italy, Dipartimento di Scienze Fisiche ‘E.R.Caianiello’ dell’Università and INFN:
 L. Cifarelli, G. Grella, M. Guida, J. Quartieri, G. Romano, A. Seganti, D. Vicinanza and T. Virgili.

Sarov, Russia, Russian Federal Nuclear Center (VNIIEF):
 V. Basmanov, D. Budnikov, V. Ianowski, R. Ilkaev, L. Ilkaeva, A. Ivanov, A. Khlebnikov,
 E. Kolokolnikov, S. Nazarenko, V. Punin, S. Poutevskoi, I. Selin, I. Vinogradov, S. Zhelezov and
 A. Zhitnik.

Shanghai, China, Shanghai Institute of Ceramics (SICCAS):
 Q. Deng, P. Li, J. Liao and D. Yan.

St. Petersburg, Russia, Institute for Physics of St. Petersburg State University, Mendeleev Institute
 for Metrology and Meson Scientific Association:
 L.Y. Abramova, V.S. Alexandrov, P. Bolokhov, A.A. Bolonine, M.A. Braun, V.M. Dobulevitch,
 G.A. Feofilov, S. Guerassimov, S.N. Igolkine, M.I. Ioudkine, A.A. Kolojvari, V. Kondratiev,
 I.A. Novikov, S.V. Potapov, O.I. Stolyarov, A.M. Switchev, T.A. Toulina, F.A. Tsimbal, F.F. Valiev,
 V.V. Vetchernine and L.I. Vinogradov.

Strasbourg, France, Institut de Recherches Subatomiques (IRIS), IN2P3-CNRS and Université Louis
 Pasteur:
 L. Arnold, J. Baudot, D. Bonnet, J.P. Coffin, M. Germain, C. Gojak, B. Hippolyte, C. Kuhn, J. Lutz and
 A. Tarchini.

Trieste, Italy, Dipartimento di Fisica dell’Università and Sezione INFN:
 V. Bonvicini, L. Bosisio, P. Camerini, E. Fragiacomo, N. Grion, G. Margagliotti, C. Piemonte,
 A. Rachevski, R. Rui and A. Vacchi.

Turin, Italy, Dipartimenti di Fisica dell’Università and INFN:

G. Alberici, B. Alessandro, R. Arnaldi, P. Barberis, S. Beolé, E. Botta, P.G. Cerello, E. Chiavassa,
 P. Cortese, E. Crescio, F. Daudo, N. De Marco, A. Ferretti, L. Gaido, M. Gallio, G. Giraudo,
 P. Giubellino, A. Marzari-Chiesa, M. Masera, G. Mazza, P. Mereu, B. Minetti, M. Monteno, O. Morra,
 A. Musso, D. Nouais, C. Oppedisano, A. Piccotti, G. Piragino, L. Riccati, E. Scomparin, F. Tosello,
 E. Vercellin, A. Werbrouck and R. Wheadon.

Warsaw, Poland, Soltan Institute for Nuclear Studies:

D. Czerwinski, A. Deloff, K. Karpio, S. Kozak, M. Kozlowski, L. Lukaszek, H. Malinowski,
 T. Siemiarczuk, G. Stefanek, L. Tykarski and G. Wilk.

Warsaw, Poland, University of Technology, Institute of Physics:

J. Grabski, P. Leszczynski, T.J. Pawlak, W.S. Peryt, J. Pluta and M. Przewlocki.

Wuhan, China, Institute of Particle Physics, Huazhong Normal University:

X. Cai, S.Q. Feng, Y. Hu, W. Li, F. Liu, F.M. Liu, H. Liu, L.S. Liu, Y. Liu, W.Y. Qian, X.R. Wang,
 S.Q. Wu, T. Wu, C.C. Xu, C.B. Yang, Z.B. Yin, D.C. Zhou and D.M. Zhou.

Yerevan, Armenia, Yerevan Physics Institute:

M. Atayan, V. Danielyan, A. Grigorian, S. Grigoryan, H. Gulkanyan, V. Kakoyan, Yu. Margaryan,
 S. Mehrabyan, L. Parlakyan, R. Shahoyan and H. Vardanyan.

Zagreb, Croatia, Ruder Bošković Institute:

T. Anticic, K. Kadija and T. Susa.

¹⁾ Also at CERN, Geneva, Switzerland.

²⁾ On leave from JINR, Dubna, Russia.

³⁾ On leave from IHEP, Protvino, Russia.

⁴⁾ On leave from Comenius University, Bratislava, Slovakia.

⁵⁾ On leave from Budapest University, Hungary.

⁶⁾ On leave from Dipartimento di Fisica dell’Università and Sezione INFN, Padua, Italy.

⁷⁾ Institut Universitaire de Technologie de Monluçon, Allier, France.

⁸⁾ Institute of Physics, Pedagogical University, Kielce, Poland.

⁹⁾ Research Centre for Applied Nuclear Physics (RCANP), Dubna, Russia.

¹⁰⁾ Institute of Physics and Technology, Mongolian Academy of Sciences, Ulaanbaatar, Mongolia.

¹¹⁾ Institute of Physics, Georgian Academy of Sciences, Tbilisi, Georgia.

¹²⁾ High Energy Physics Institute, Tbilisi State University, Tbilisi, Georgia.

¹³⁾ Institute of Space Sciences, Bucharest, Romania.

¹⁴⁾ Foundation of Fundamental Research of Matter in The Netherlands.

¹⁵⁾ Utrecht University, Utrecht, The Netherlands.

Acknowledgements

The Collaboration wishes to thank all the technical and administrative staff involved during the preparation of the TDR, in particular: S. Barras, D. Birker, P. Bonneau, M. Bosteels, B. Cantin, R. Cook, A. Ferrand, F. Hahn, S. Haider, L. Levrat, F. Marcastel, S. Maridor, P. Mato, F. Morel, J. Navarria, G. Peón, A. Przybyla, D. Sanchez, S. Stappers, M. Wensveen, and M. Wilhelmsson. We would also like to acknowledge the contributions made by the late R. Brockmann and by H.G. Fischer in the R&D stage of the TPC project, in particular to the RCC prototype and slow simulator. The help provided by the NA49 and CERES collaborations throughout the years is greatly appreciated.

Summary

This Technical Design Report describes the ALICE Time Projection Chamber (TPC), which is the main detector for tracking in the central barrel. In the following we summarize the main design considerations and specifications for the TPC and outline the proposed technical solutions.

In Chapter 1 we describe briefly the main physics goals for ALICE and the resulting design specifications for the TPC. A ‘traditional’ focus of physics with the TPC will be hadronic physics, where in addition to efficient track reconstruction in the expected high-multiplicity background the emphasis will be on energy-loss resolution and two-track separation. A new development is that a major part of the physics program with the TPC will be, in conjunction with the Transition Radiation Detector (TRD) and Inner Tracking System (ITS), the measurement of high- p_t electrons. This implies excellent rate capability (we plan to inspect 200 central Pb–Pb collisions per second) and very good energy-loss and momentum resolution for large momenta.

In Chapter 2 the resulting requirements on precision and tolerances of the mechanical structures of the TPC are discussed. Here, our approach is to combine the best reasonably achievable precision for the gas gain, electric drift field, temperature and gas composition with frequent and precise calibrations using laser beams and radioactive krypton, and with constant monitoring of the temperature and composition of the drift gas.

The TPC field cage, described in Chapter 3, is to provide a highly uniform electrostatic field in a cylindrical high-purity gas volume to transport primary charges over long distances (2.5 m) towards the readout end-plates. Two such field configurations are chosen, back-to-back in a common gas volume, with a common high-voltage (up to 100 kV) electrode located at the axial centre of the cylinder. The mechanical structure of the TPC field cage is composed of six major components: the ‘outer and inner field-cage vessels’ to form the sensitive detector volume, the ‘outer and inner containment vessels’ to provide protective detector containment, and the two ‘end-plates’ where the readout chambers are mounted. The requirements on structural accuracy and gas tightness combined with small multiple scattering imply that composite materials have to be used throughout. An approximately half-sized prototype was built and thoroughly tested. The results demonstrate that the required performance can indeed be achieved. As drift gas we will use the mixture 90% Ne, 10% CO₂, as is currently used in the NA49 experiment.

In Chapter 4 we present our choice for the readout chambers. The ALICE TPC readout chambers will be conventional multiwire proportional chambers with cathode pad readout as used in many TPCs before. This choice was made after looking in some detail, as described in Chapter 8, into various different technologies such as Ring-Cathode Chambers (RCC) or Gas Electron Multipliers (GEM). The azimuthal segmentation of the readout plane follows that of the subsequent ALICE detectors, leading to 18 trapezoidal sectors, each covering 20 degrees in azimuth. The radial decrease of the track density leads to changing the requirements for the readout chamber design as a function of radius. Consequently, there will be two different types of readout chambers, the *inner* and *outer* chambers. Each outer chamber is further subdivided into two sections with different pad sizes, leading to a triple radial segmentation of the readout plane, with 570 000 readout pads in all. The electrostatics of the chambers has been simulated in detail and the design of the pad and wire planes was adjusted accordingly. The chambers have to run at a relatively large gas gain (about 2×10^4), but simulations and tests with existing chambers indicate that this should pose no problems.

The front-end electronics and readout of the TPC are discussed in Chapter 5. The readout chambers deliver on their pads a current signal with a fast rise time (less than 1 ns), and a long tail due to the motion of the positive ions. The signal amplitude has a typical value of 7 μ A. The design for the readout electronics is based on an approach in which part of the required tail cancellation is done in a digital chip, thus simplifying the analog chip considerably. Each readout channel hence comprises three basic units: a charge sensitive preamplifier/shaper with a gain of 12 mV/fC, a shaping time of 200 ns and

an equivalent noise charge below 1000 electrons; a 10-bit 10 MHz low-power ADC; an ASIC which contains a shortening digital filter for tail cancellation, baseline subtraction and zero-suppression circuits, and a multiple-event buffer. The preamplifier/shaper will be implemented in submicron technology.

The readout of the TPC, as discussed in Chapter 5, was adapted to the new role of the TPC as a relatively high rate detector for dielectron measurements. In this scenario the TPC data are sent directly into the host processors of a Level-3 Trigger/DAQ processor farm. The system is scalable in terms of processing power and bandwidth in order to meet the computing requirements of the various physics programmes. In a first stage, zero-suppressed raw data are recorded without any further processing. The intelligent readout system (Level-3) guarantees the readout of unprocessed full TPC events at a rate of 10 Hz. Having understood the TPC response to central Pb–Pb collisions, the Level-3 system will take over more functionalities. Almost lossless data compression and selective readout can be implemented relatively easily, since these techniques do not need large computing power. Finally, by adding more computing power, online track finding in the whole TPC and, therefore, effective data-compression methods and TPC-based selective readout schemes become feasible. If there should be a need for a higher rate of unprocessed full TPC events, the bandwidth of the system can be further increased.

In Chapter 6 we summarize the material budget for the TPC. Because of the consistent efforts to use extremely small amounts of and only low-Z materials the total thickness of the TPC structure and gas does not exceed about 3% of a radiation length.

An evaluation of the performance of the proposed TPC in the LHC Pb–Pb collision environment is presented in Chapter 7. With a microscopic simulator containing all relevant processes for signal creation in the TPC a detailed study was performed to determine the radial dependence of the TPC occupancy for central Pb–Pb collisions at the maximum expected particle density. The thus-determined maximum occupancy reaches about 40% in the innermost sections of the readout chambers and decreases to about 15% near the outer radius. These studies also provide detailed information on the role of field- and space-charge distortions, on the expected backgrounds and detector load, and were used to validate the design choices for the readout chambers and front-end electronics made on the basis of somewhat simplified simulations and analytic calculations reported in Chapter 4. Furthermore, the microscopic simulations provide the input for the cluster finder and track-reconstruction program. Track finding in the ALICE TPC is based on the Kalman-filtering approach which provides simultaneous track recognition and fitting and the possibility to reject incorrect space points ‘on the fly’, during the only tracking pass over a track. The tracking simulations are still under development, but the results reported in Chapter 7 are encouraging: better than 90% track-reconstruction efficiency even for the highest multiplicity densities and a resolution in energy loss below 10%, as required by the hadron and electron programs. The momentum resolution for a 4 GeV/c electron is about 8.5% for the highest conceivable multiplicities at a magnetic field of 0.2 T. Taking into account the additional improvements from using the ITS and TRD in the track fit (estimated to be more than a factor of two), the required 2.5% resolution for separation of the Υ states should be attainable for runs with magnetic field of about 0.4 T. First estimates also show excellent matching of the TPC tracks with the ITS and TRD.

Installation, slow control and safety are discussed in Chapter 9. As demonstrated there, the installation of the TPC is not easy but manageable. An elaborate slow control system is planned to monitor many parameters of the TPC such as currents and voltages for the high-voltage system of the readout chambers and for the low-voltage system of the front-end electronics, as well as temperature and gas purity. A detailed investigation revealed no serious safety issues for the TPC.

Organizational aspects, budgets and schedules are presented in Chapter 10. The TPC group now comprises 13 institutes with considerable experience and manpower. The budget of approximately 17 MCHF is in line with expectation and previous estimates and all time lines imply that construction of the TPC should be finished by the autumn of 2003, in line with the overall ALICE planning.

Contents

Summary	xi
1 Physics objectives and design considerations	1
1.1 The ALICE experiment	1
1.2 Physics requirements	1
1.2.1 Hadronic observables	2
1.2.2 Leptonic observables	3
1.3 TPC design considerations	3
2 Design objectives and mechanical structure	5
2.1 Precision and tolerance	5
2.2 Stability of the mechanical structure	7
3 Field cage and gas system	9
3.1 Field cage	9
3.1.1 General layout and choice of material	9
3.1.2 Assembly and testing	16
3.1.3 Voltage divider	22
3.1.4 Temperature stabilization and thermal screen	27
3.1.5 Tests and prototypes	29
3.2 Gas system	32
3.2.1 Specific operational requirements	32
3.2.2 Gas choices	33
3.2.3 Design choices and layout	33
4 Readout chambers and calibration	41
4.1 Readout chambers	41
4.1.1 Mechanical structure and support	41
4.1.2 Wire planes and readout pads	44
4.1.3 Electrostatic calculations	58
4.1.4 Electronics mounting and cooling	69
4.1.5 Link between field cage and readout chambers	74
4.1.6 Tests and prototyping	78
4.2 Gating system	80
4.2.1 Design considerations	80
4.2.2 Gating circuit design	81
4.2.3 Performance	81
4.2.4 Implementation	82
4.3 Calibration	82
4.3.1 Laser system	82
4.3.2 Electronics calibration	86
4.3.3 Krypton calibration	88
5 Front-end electronics and readout	91
5.1 Front-end electronics	91
5.1.1 Introduction and overview	91

5.1.2	Interconnection to the readout pad plane	94
5.1.3	Front-end basic components	96
5.1.4	Front-End Card	110
5.1.5	Readout bus	111
5.1.6	Readout control and services	116
5.1.7	Front-end electronic readout efficiency	118
5.1.8	Low-voltage power supplies and distribution	120
5.1.9	System implementation	121
5.2	Readout	122
5.2.1	Physics requirements	122
5.2.2	Data rate reduction	124
5.2.3	Architecture	131
5.2.4	Interfaces	136
5.2.5	Data acquisition and Level-3 software	140
6	Material budget	143
6.1	Estimate of radiation length in η space	143
6.2	Estimate of radiation length in ϕ space	145
7	Detector performance	147
7.1	Requirements and detector parameters	147
7.2	Simulation of TPC response	147
7.2.1	Microscopic simulator	147
7.2.2	Background and detector load	154
7.3	Track reconstruction	155
7.3.1	Tracking environment	155
7.3.2	Cluster finding	162
7.3.3	Track finding	163
7.4	Tracking performance	165
7.4.1	Tracking efficiency	166
7.4.2	Two-track efficiency	167
7.4.3	Momentum resolution	168
7.4.4	dE/dx resolution	168
7.5	Track matching	169
7.5.1	Connection to ITS	169
7.5.2	Connection to TRD	170
8	R&D for alternative readout chambers	173
8.1	Ring-Cathode Chamber	173
8.1.1	Preamplifier/Shaper	174
8.1.2	TAB bonding	174
8.1.3	Pad response function	176
8.1.4	Gating	177
8.1.5	Isochrony	178
8.1.6	Lead-beam tests	179
8.1.7	Conclusions on RCC	180
8.2	GEM-based readout chambers	180
8.2.1	Principle of operation of GEMs	180
8.2.2	Basic properties of GEMs relevant for TPC readout chambers	181
8.2.3	Conclusions on GEMs	186

9 Installation, slow control and safety	187
9.1 Implementation and infrastructure	187
9.1.1 ALICE experimental area	187
9.1.2 Implementation of the TPC detector	188
9.1.3 Access, maintenance and services	190
9.1.4 Assembly and installation schedule	192
9.2 Slow control	194
9.2.1 Hardware	195
9.2.2 Communication	195
9.2.3 Software	195
9.3 Safety and quality management	198
9.3.1 Mechanical	198
9.3.2 Gas	198
9.3.3 Radiation protection	198
9.3.4 RF shielding	199
9.3.5 Electrical system protection	199
9.3.6 Laser	200
9.3.7 Safety aspects	200
10 Organization	201
References	205

1 Physics objectives and design considerations

1.1 The ALICE experiment

ALICE (A Large Ion Collider Experiment) [1] is an experiment at the Large Hadron Collider (LHC) optimized for the study of heavy-ion collisions, at a centre-of-mass energy ~ 5.5 TeV. The prime aim of the experiment is to probe, in detail, nonperturbative aspects of QCD such as deconfinement and chiral-symmetry restoration. Furthermore, of interest to the experiment are the newly emerging physics topics related to the study of QCD at very high field strengths as detailed in Ref. [2].

The strategy of the ALICE experiment to study the behaviour of matter at high densities and temperatures at near zero baryochemical potential is to combine a nearly exclusive measurement of particle production in the central region with spectroscopy of quarkonia states at central and intermediate rapidities and characterization of the event centrality. It therefore combines three major components:

- The central barrel, contained in the large L3 magnet and composed of detectors devoted mainly to the study of hadronic signals [1] and dielectrons [3]. It covers the pseudorapidity range $-0.9 < \eta < 0.9$ over the full azimuth.
- The forward muon spectrometer, dedicated to the study of muon pairs [4] from the decay of quarkonia in the interval $2.5 < \eta < 4.0$.
- The forward detectors, $\eta > 4$, for a determination of the photon multiplicity and a measurement of the charged particle multiplicity, also to be used as a fast trigger on the centrality of the collision.

The set-up of the ALICE experiment, with emphasis on the central barrel, is shown in Colour Fig. I. The Time Projection Chamber (TPC) surrounds the Inner Tracking System (ITS) which is optimized for the determination of the primary and secondary vertices and precision tracking of low-momentum particles. On the outside the Transition Radiation Detector (TRD) is designed for electron identification. The outermost Time-Of-Flight (TOF) array provides pion, kaon and proton identification. In addition, there are two single-arm detectors: the Photon Spectrometer (PHOS) and an array of RICH counters optimized for High-Momentum Particle IDentification (HMPID).

1.2 Physics requirements

The physics objectives of the ALICE central barrel have been detailed in Ref. [1]. However, the recent addition of the TRD has expanded the physics objectives of the experiment as demonstrated in Ref. [3]. As a consequence, the performance and corresponding design criteria had to be reassessed and optimised, taking also into account the requirements for dielectron studies.

The ALICE TPC is the main tracking detector of the central barrel and together with the ITS, TRD, and TOF has to provide charged particle momentum measurement, particle identification and vertex determination with sufficient momentum resolution, two track separation and dE/dx resolution for studies of hadronic and leptonic signals in the region $p_t < 10$ GeV/c and pseudorapidities $|\eta| < 0.9$. In addition we plan, with the central barrel detectors, to select low cross section signals and rare processes and, therefore, to generate a fast online ‘Level-3’ trigger.

All these requirements need to be fulfilled at the design luminosity for Pb–Pb collisions at LHC which corresponds to an interaction rate of 8 kHz of which ~ 1 kHz are central collisions with impact parameter $b < 5$ fm. The produced particle multiplicities are difficult to predict and for central Pb–Pb

collisions are expected to be in the range of 2000–8000 charged particles per rapidity unit at midrapidity. For the design of the detector the maximal expected multiplicity of $dN_{\text{ch}}/dy = 8000$ was used which results in 20 000 charged primary and secondary tracks in the TPC. At the design presented here this particle multiplicity results in occupancies (defined as the ratio of the number of readout pads and time bins above threshold to all bins in pad and time space) of the order of 40% at the innermost radius and 15% at the outermost radius.

The challenge to the TPC design group was to ensure that the physics dictated requirements can be realized in this environment.

1.2.1 Hadronic observables

The TPC is the main tool to investigate hadronic observables in Pb–Pb collisions. Hadronic measurements give information on the flavour composition of the fireball via the spectroscopy of strange and multi-strange hadrons, on the space–time extent of the fireball at freeze-out via the investigation of single-particle and two-particle spectra and correlations, and on event-by-event fluctuations of the fireball.

Hadronic correlation observables place the highest demand on relative momentum and two-track resolution. In two-pion Bose–Einstein correlation analysis ('Hanbury-Brown–Twiss' analysis, HBT) one considers correlation functions in all components of the 4-momentum difference, with special emphasis on the domains $\delta q \rightarrow 0$. The momentum widths of these correlation functions are sensitive to the geometrical space–time source extent of the expanding hadronic fireball. Extrapolating from typical sizes of about 8 fm observed in HBT analysis of SPS Pb–Pb collisions, we expect the effective source sizes to increase in proportion to the cube root of the rapidity density dN_{ch}/dy which grows from 400 charged particles at the SPS to about 6000–8000 at the LHC. Thus, measurements have to be sensitive to sizes of up to 25 fm or $\delta q \leq 8 \text{ MeV}/c$. Note that this relative momentum accuracy is needed mostly for transverse momenta below the average value of p_t , i.e. approximately 500 MeV/c for pions. For the correlation functions in the so-called sideward and longitudinal directions (δq_{side} and δq_{long}) these requirements are fulfilled, as is demonstrated in Section 7.4. More critical is the 'outward' correlation in δq_{out} where source sizes of 25 fm will probably only be measurable by running with a higher-than-standard magnetic field.

Another important requirement on the TPC is sufficient acceptance in rapidity and p_t for the study of space–time fluctuations of the decomposing fireball at the level of individual events. For a detailed analysis of kaon spectra and the kaon/pion ratio on an event-by-event basis, one typically needs 250 analysed kaons, again supporting the need for large acceptance and good particle identification.

Specific requirements on the TPC from hadron physics are the following.

- **Two-track resolution:** The two-track resolution has to be such that HBT measurements with a resolution in relative momentum of a few (< 5) MeV/c can be performed. This may require running at higher magnetic fields.
- **Resolution in dE/dx :** For hadron identification a dE/dx resolution of 8% is desirable, following the experience of NA49. Depending on the final particle multiplicity this can just be reached with the current design.
- **Track matching capability to ITS and TOF:** For the measurement of D-mesons via hadronic decay channels, of multi-strange baryons, and of HBT correlations, efficient matching with the ITS is very important. Depending on the p_t range considered, the matching efficiency should be 85%–95%.

1.2.2 Leptonic observables

The Transition Radiation Detector (TRD) [3] will provide, in conjunction with data from the TPC and ITS detectors, sufficient electron identification to measure, in the dielectron channel, the production of light and heavy vector-meson resonances for Pb–Pb collisions at the LHC, as well as allow to study the dilepton continuum. In addition, the electron identification provided by the TPC and TRD at relatively large transverse momenta ($p_t > 1 \text{ GeV}/c$) can be used, in conjunction with the impact-parameter determination of electron tracks in the ITS, to determine the overall amount of open charm and open beauty produced in the collision. With a similar technique one can also separate directly produced J/ψ mesons from those resulting from B-decay. The latter could potentially mask the expected J/ψ suppression due to quark-gluon plasma formation and its study is, therefore, of crucial importance for such measurements. Furthermore, since the TRD is a fast tracker, it can be used as an efficient trigger for high transverse momentum electrons. This can be used to considerably enhance yields for Υ detection, for the measurement of the high-mass part of the dilepton continuum, and for J/ψ detection at high transverse momentum.

Specific requirements on the TPC from electron physics are as follows.

- **Tracking efficiency:** Since we are mainly interested in electron pairs the tracking efficiency for tracks with $p_t > 1 \text{ GeV}/c$ should be larger than 90%.
- **Momentum resolution:** The momentum resolution for electrons with momenta of about $4 \text{ GeV}/c$ should be better than 2.5%. This is necessary to keep the mass resolution for Υ mesons below 100 MeV, so that the members of the Υ family can be resolved. As discussed in Section 7.4 this resolution can be achieved, but only in conjunction with the ITS and when running at magnetic fields around 0.4 T.
- **Resolution in dE/dx :** For electron identification the TPC has to provide a dE/dx resolution of better than 10% in the high-multiplicity environment of a Pb–Pb collision. This will, in conjunction with electron identification from the TRD, lead to a pion rejection of $> 10^3$ at 90% electron efficiency for electron momenta larger than $1 \text{ GeV}/c$. From the simulations made for the TRD TP [3] this is sufficient for all dielectron physics planned with the ALICE detector. Current simulations, reported in Section 7.4, imply that such resolutions can be obtained with the present design.
- **Rate capability:** For the inspection and tracking of electron candidates identified in the TRD the TPC should be operated at central collision rates of up to 200 Hz. While there is not much experience with the operation of large TPCs at these rates, the current load on the readout chambers is not excessive as discussed in Section 7.2.2.

Detailed simulations for the electron physics potential of the ITS–TPC–TRD combination were presented in Ref. [3] and will not be repeated here.

1.3 TPC design considerations

The general considerations listed above have led to a design of the TPC which is ‘conventional’ in the overall structure, but with many innovative aspects in detail. Central aspects of the design are listed below.

- **Acceptance:** The overall acceptance of $|\eta| < 0.9$ matches that of the ITS, TRD, and TOF detectors. This acceptance is important for event-by-event studies of fluctuations in hadronic observables such as the K/π ratio, from which one can determine the strangeness content of the fireball. For electron physics the full acceptance is absolutely crucial to collect significant statistics for high-mass and/or high- p_t electron pairs [3]. To cover this acceptance the TPC is of cylindrical design with an inner radius of about 80 cm, an outer radius of about 250 cm, and an overall length in the beam direction of 500 cm.

- **Material budget:** The material budget of the TPC has to be kept as low as possible to ensure minimal multiple scattering and low secondary-particle production. This requires special attention to materials used in the construction of the field cage and enforces the use of a light counting gas, 90% Ne, 10% CO₂. The overall thickness of the TPC was kept to less than 3% of a radiation length. Details and summaries are given in Chapter 6.
- **Field cage:** For very general requirements of minimal material near 90° relative to the beam direction, the field cage is based on a design with a central electrode at high voltage. Because of the gas mixture used in the TPC and the needed high rate capability the field cage for the TPC has to run at voltage gradients of 400 V/cm, implying voltages in excess of 100 kV at the central electrode. This has led to extensive prototyping. The resulting design is discussed in Section 3.1.
- **Readout chambers:** The readout chambers cover the two end-caps of the TPC cylinder. The overall area to be instrumented is 32.5 m². The chambers will be conventional multiwire proportional chambers with cathode pad readout. To keep the occupancy as low as possible and to ensure the necessary dE/dx and position resolution, there will be about 570 000 readout pads with three different sizes varying from 0.3 cm² near the inner radius to 0.9 cm² near the outer radius. Details of the design strategy are discussed in Section 4.1.
- **Electronics:** At about 570 000 channels the front-end electronics for the TPC has to be highly integrated. It will consist of three basic units for each channel: a low-impedance charge-sensitive preamplifier/shaper, a commercial 10-bit ADC with up to 10 MHz frequency range, and an ASIC with a digital filter for tail cancellation, with base-line subtraction and zero-suppression circuitry, and a multiple event buffer, all to be implemented in CMOS technology. Design considerations and expected capabilities are discussed in Section 5.1.
- **Intelligent TPC readout:** After zero-suppression and data encoding the event size of data from the TPC for a typical central Pb–Pb collision will be about 60 MBytes. Considering that one needs about 40 Hz data-taking capability from the TPC for dielectron physics (in fact, 200 Hz are currently considered, see Chapter 5) this makes it mandatory to investigate possibilities for an ‘intelligent’ readout. We are planning to build, to this extent, a Level-3 processor farm, which will operate on the raw data shipped via optical links to the ALICE counting house. This will allow almost no-loss data compression, selective readout for electron candidates identified by the TRD, as well as online track finding and eventually tracking of the whole TPC. The farm will be built as much as possible from commercially available components. Details of the intelligent readout including strategies for its implementation are discussed in Section 5.2.

2 Design objectives and mechanical structure

2.1 Precision and tolerance

Experimental conditions at the LHC set stringent design and performance criteria for the TPC in order to address the full range of physics accessible at the LHC and plausibly achieve our objectives for momentum and dE/dx resolution, as well as for pattern recognition in a highly congested environment. To fulfil these goals, the TPC, being a large but conceptually simple detector, must be built with very high precision, if the individual track information is to be retained over long drift distances or times. Nonlinear systematic effects lead to unrecoverable track distortions and errors in the energy-loss measurements, and must therefore be reduced to a minimum at the outset of the detector construction. Thus, the ultimately achievable precision in track reconstruction and energy-loss measurement depends on the ability to provide high stability and uniformity within the sensitive volume of the TPC for:

- the gas gain or wire amplification,
- the drift field,
- the temperature,
- the drift gas purity.

The TPC is designed to minimize effects from misalignment and mechanical deformation of all parts that define the drift field, i.e. the central electrode, the potential degrader network and the end-plates. Careful choice of materials will furthermore reduce environmental influences on gas temperature and purity. To give clear design directions as to the precision to which the TPC must be built, we must first assess the maximum tolerances that can be allowed for the above four parameters.

Tolerances on gas gain.

For a fixed wire geometry (and drift gas mixture) the gas gain is entirely determined by the voltage applied to the anode wires. As shown in Section 4.1.3.4, to achieve a gas gain of 2×10^4 an anode voltage of 1.7 kV is required. This voltage is sufficiently high to cause electrostatic deflection of the anode wires towards the readout plane, resulting in a wire sagitta of 5 μm for the shortest (300 mm) and 75 μm for the longest (900 mm) wires. This leads to variations in gas gain along the anode wire of 3% and 5%, respectively. The effect can be alleviated by calibrating the signal response with the injection of radioactive ^{83}Kr into the drift gas (see also Section 4.3.3). This method was successfully applied, amongst other detectors, to the NA49 TPCs [1] and allowed overall gain variations in electronics and wire amplification of the order of 10% to be corrected for with a precision of 0.5%. Thus, the maximum variations of 5% in gas gain expected from the wire sag in the TPC are easily mapped out with the above calibration method.

Tolerances on drift field uniformity

Radial field components in the drift field change the trajectory of electrons from an ideally straight path (in z) towards the readout plane of the TPC and thus have an effect on the space-point resolution. These field nonuniformities should be well below the intrinsically achievable resolution of the TPC. Under ideal conditions the space-point resolution, depending on the drift length and track orientation, varies between 300 and 2000 μm in $r\phi$, and 600 and 2000 μm in z . It has been shown that radial field components of order 10^{-4} compared to the field component in z lead to deviations of the electron trajectory, however,

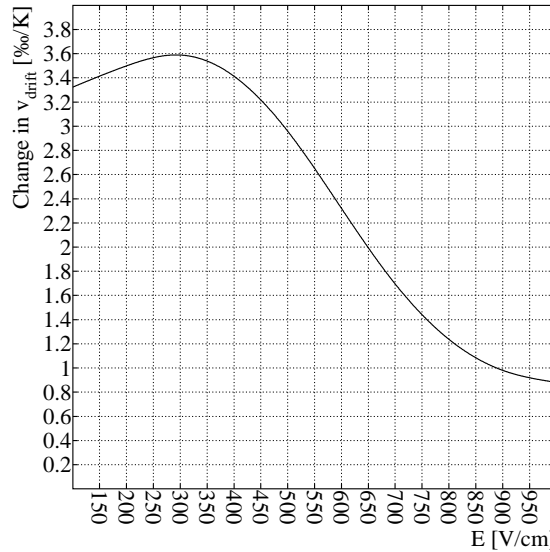


Figure 2.1: Relative change of the electron drift velocity for a temperature gradient of 1 °C for 90% Ne, 10% CO₂, as a function of the drift field.

not exceeding 200 μm in r and 150 μm in $r\phi$, respectively. Hence, the mechanical structure and field defining network of the TPC are designed to keep radial field nonuniformities to $\leq 10^{-4}$.

Temperature effects

If the drift velocity of electrons in the TPC is not saturated, i.e. depends on the drift field, the gas pressure and gas temperature, external influences on the drift gas must be reduced to a minimum. In particular, temperature variations cause local fluctuations in density, and thus directly affect the velocity of drifting electrons. For reasons outlined later, we have chosen a 90% Ne, 10% CO₂ mixture and an electric field of 400 V/cm for optimum operation of the ALICE TPC. These operating parameters, however, lead to a nonsaturated drift velocity. Our studies and experience with the NA49 [1] experiment show that the long drift path of electrons imposes a tight control on temperature gradients to stay below 0.1 °C within the sensitive drift volume of the TPC, in particular, between its inner and outer radius. As the TPC is exposed to potentially large heat sources in its immediate neighborhood, it is very challenging to guarantee temperature gradients below 0.5 °C, although technical solutions on thermal isolation of the TPC look promising. While it is possible to correct, with the laser calibration system, for long-term distortions arising from time related temperature effects, local temperature differences in the drift volume cannot be mapped and hence lead to unrecoverable errors in the track measurement. Therefore, we aim at a temperature stability of 0.1 °C, because even under these conditions the relative change in drift velocity with temperature is 0.34% per degree in 90% Ne, 10% CO₂ (see Fig. 2.1), and distortions of the particle trajectory can be as high as 850 μm for the full drift distance. Although this value is comparable to the space-point resolution in z , this type of distortion causes a systematic error in dip angle.

Limits on gas impurities

Since the total electron yield in the chosen 90% Ne, 10% CO₂ mixture is rather low, electron capture by gas impurities is a matter of prime concern. Past experience with this drift gas in the NA49 experiment has proven that the electron attachment coefficient is equal to 1% per metre of drift per ppm of oxygen [1]. We conclude that 5 ppm of oxygen and 10 ppm of water contamination are acceptable in terms of signal loss at the readout front-end.

2.2 Stability of the mechanical structure

The TPC is designed to be the major particle tracking system for ALICE, placed between the inner tracking system (ITS) [2] and the transition radiation detector (TRD) [3]. Jointly with the ITS and TRD, the TPC must play the role of a high-precision tracking system of its own and yet be compatible with the physics objectives of its neighbours.

Hence, the TPC must be of very low mass to minimize interference with its partner detector systems, and of high stability to satisfy the precision and reliability requirements for a stand-alone tracking system. Constructing the detector from modular cylindrical elements, using composite material throughout, provides an optimum in terms of low mass, high rigidity and safety. The system is designed to provide structural integrity and to compensate for effects arising from different coefficients of expansion. In particular, the outer cylindrical vessels, together with the end-plates constitute the main structural element of the whole detector, guaranteeing its high stability in z and $r\phi$. The inner structure of the TPC, together with the outer one, provides the required parallelism of the end plates with the central electrode mounted inside the TPC. The inner vessel is designed to position and hold in place both the ITS and the multiplicity counters with high precision.

The readout chambers of the TPC are mounted on three points, i.e. kinematically independent of each other and of the end-plate support structure. Knowing their centre of gravity, they are positioned within the end-plate frame such that no bending moments are exerted on the end-plate structure, preserving its planarity. Thus, by not overconstraining the readout assembly with respect to the support structure, the end-plates can be built light and the individual detectors will not be subject to internal deformations. The detectors can also be optimally aligned in this fashion to build an overall co-planar detection system.

The central electrode will be constructed from composite material as well. This is to maintain its flatness despite the forces due to ground inclination (1.39% or $\sim 0.8^\circ$) of the experimental area and a unidirectional gas flow within the field cage volume.

After transport to the space frame the entire detector will be placed on four adjustable support points (Fig. 2.2) that are mounted on the end-plates where the bulk of the detector mass is concentrated. Hydraulic jacks on these support points allow isostatic, i.e. kinematically independent, adjustment of the TPC to align it with the particle beam. Damping elements can be placed between the support points and the space frame rails in order to isolate the detector from external structural vibrations should they exist.

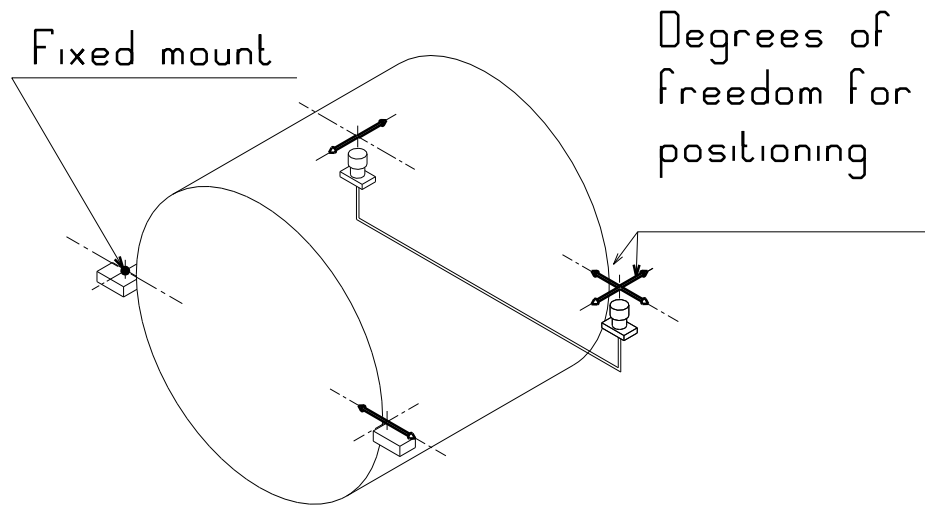


Figure 2.2: Isostatic placement of the TPC within the space frame.

3 Field cage and gas system

3.1 Field cage

3.1.1 General layout and choice of material

The basic design philosophy of the TPC field cage is to provide a highly uniform electrostatic field in a cylindrical high-purity gas volume to transport primary charges over long distances (2.5 m) towards the readout end-plates. For reasons of symmetry in colliding beam arrangements, two such field configurations are chosen, back-to-back in a common gas volume, with a common high-voltage (HV) electrode located at the axial centre of the cylinder (see Fig. 3.1). The central HV electrode and two opposite axial

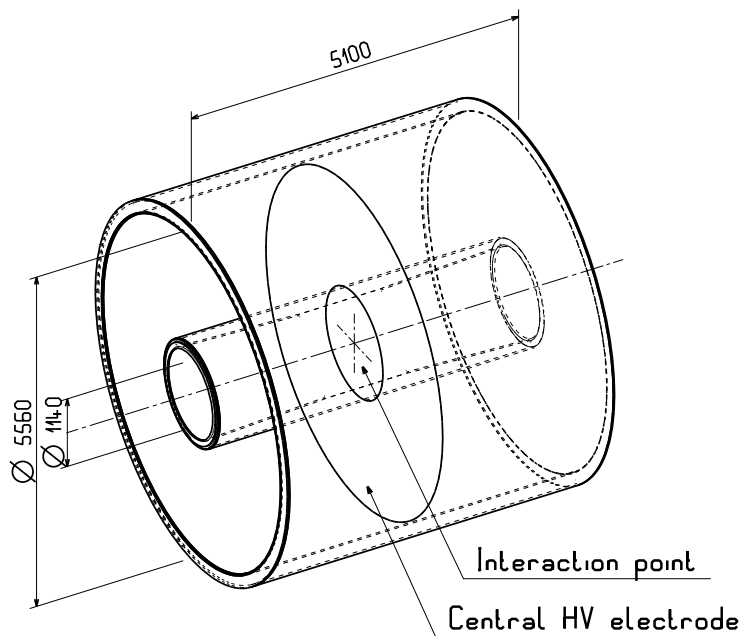


Figure 3.1: Conceptual view of the TPC field cage.

potential degraders provide uniform drift fields of up to 400 V/cm. The drift field is chosen in line with the intrinsic properties of the drift gas affecting the drift velocity and the diffusion of primary ionization electrons in that gas. Thus, given the maximum drift path of 2.5 m, the HV at the central electrode will be as large as 100 kV. The maximum over-pressure allowed for the field cage will be 5 mbar.

The actual field cage volume is surrounded by an insulating gas envelope (containment) as shown in Fig. 3.2. Containment of the drift volume is essential for personnel and operational safety and also for minimizing the amount of material traversed by particles. Its functions are described in detail in Section 3.1.1.1 and Section 3.1.1.2.

The beam tube and the Inner Tracking System (ITS) require that both the field cage and the containment volume are constructed from two concentric cylinders each and sealed by an annular disc, called the end-plate, on either side of the cylindrical structure. Thus, the mechanical structure of the TPC field cage is composed of six major components (see Colour Fig. II): the ‘outer and inner field cage vessels’ to form the sensitive detector volume, the ‘outer and inner containment vessels’ to provide protective detector containment, and the two ‘end-plates’ where readout chambers are mounted to amplify and register

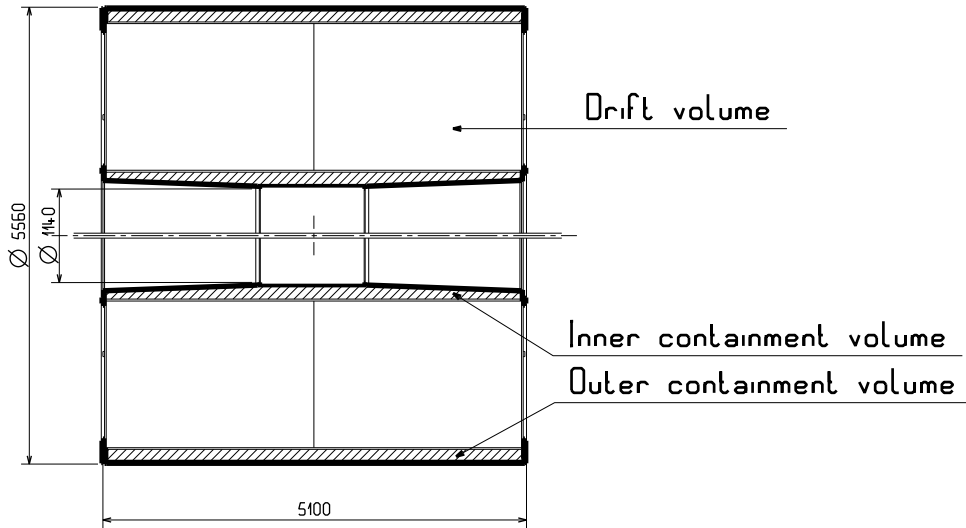


Figure 3.2: Lateral view of the TPC showing the sensitive detector and insulation volumes.

the primary charge of particle tracks. This modular structure allows each component to be optimized individually in terms of cost and performance. The construction of the field cage and consequently the choice of material are driven by the following constraints:

- high structural integrity against gravitational and thermal loads;
- very low permeability to atmospheric gas components considered harmful to the drift gas (O_2 , N_2 and H_2O);
- negligible vapour pressure of contaminants emanating from material exposed to the drift volume;
- adequate surface smoothness to protect against HV discharges;
- low-density and low-Z material to reduce multiple scattering and conversion processes.

This has led to the choice of composite materials for all four cylinders. Composite sandwich structures today provide the highest stability/mass ratio and are commonly used in the aerospace industry providing the competence and tooling also for the manufacture of the TPC cylinders. The cylinder skins are mainly composed of (see also Fig. 3.3):

- an inner honeycomb-like structure of Aramide fibre (Nomex), rectangular in shape, and with a cell size of 4.8 mm, covered on either side by:
- two layers of Kevlar prepreg, i.e. woven Aramide fibers embedded in an epoxy resin, and
- gas-tight foils of Tedlar, type TWH 20 BS3.

In order to obtain uniform and homogeneous quality of the detector, the curing of resins used for the different components must be carried out in an autoclave. The basic properties of the TPC field cage material components are listed in Table 3.1.

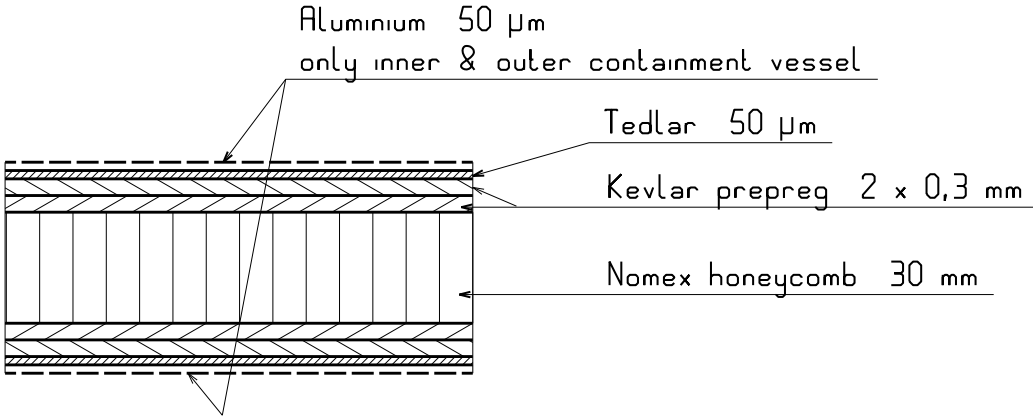


Figure 3.3: Cross-section of the composite material used for the TPC field cage.

Table 3.1: List of materials used in the TPC field cage and their mechanical and electrical properties.

Material	Density [g/cm ³]	Modulus/ tensile strength [GPa]	Surface resistivity [Ω/□]	Gas permeability [cm ³ /(100 in ²)(d)(atm)(mil)]
Kevlar 49	1.45	120	n.a.	n.a.
Glass-fibre	2.54	69	n.a.	n.a.
Tedlar	1.71	0.062	6×10^{15}	0.25 (N ₂), 3.2 (O ₂), 11.1 (CO ₂)
Mylar	1.39	4.5	$> 5 \times 10^{14}$	n.a.
Nomex (3.62% filling)	0.03	0.055 (compression)	n.a.	n.a.
Glue	1.25	n.a.	n.a.	n.a.
Macrolon	1.2 – 1.44	n.a.	$10^{14} – 10^{15}$	n.a.
Aluminium	2.7	n.a.	n.a.	n.a.

3.1.1.1 Outer containment vessel

The outer containment vessel (Fig. 3.4) is the outermost and largest of the four TPC cylinders that comprise the entire field cage assembly. It is 5.1 m long and has a diameter of 5.56 m. It has five functions:

1. provide mechanical stability and precision for the entire assembly;
2. provide containment of the very high voltages applied to the field-cage network;
3. provide additional protection of the drift gas against leakage of atmospheric gases and vapours into the gas volume;
4. serve as an exterior heat shield against temperature variations/gradients in the drift volume;
5. reduce radiofrequency interference with the sensitive front-end readout system.

The two flanges are made of a compact structure of prepreg with the following composition: solid laminate epoxy resin (125 °C) with a glass-fibre fabric of minimum 50% fibre content by volume. It is envisaged to cover the surfaces in contact with the O-rings with 50 μm of Tedlar to improve gas tightness

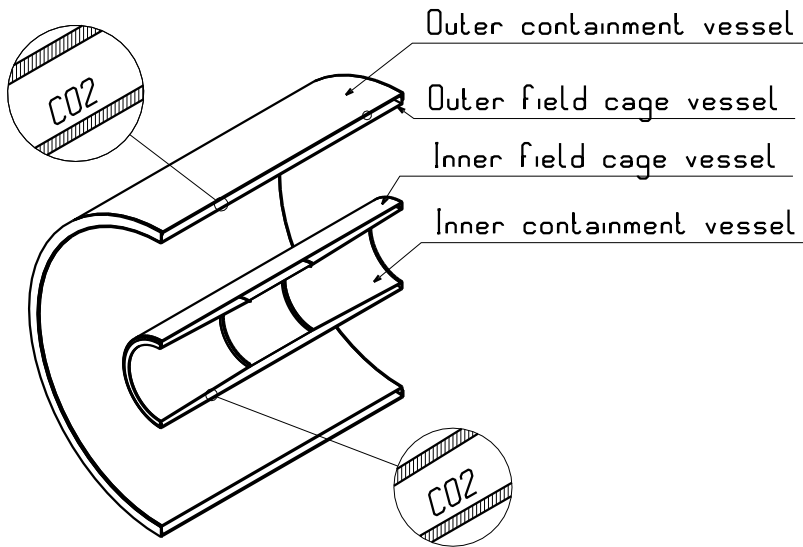


Figure 3.4: Lateral view of the entire field-cage assembly.

of these seals. Sealing is achieved with O-rings made of fluorine based elastomers, such as Viton, with a high shore value (for example, 70 shore).

For the cylindrical walls of the outer containment vessel the following composition is foreseen:

- 1 layer of aluminium foil, 50 μm thick;
- 1 layer of Tedlar, type TWH 20 BS3, 50 μm thick;
- 2 layers of prepreg (weaving layout 77–81, 60% fibre and 40% resin by volume, epoxy resin at 125 °C), 0.3 mm thick each;
- 1 honeycomb-like structure Nomex (height = 30 mm, 29 kg/m³);
- 2 layers of prepreg (as above);
- 1 layer of Tedlar (as above);
- 1 layer of aluminium foil (as above).

The aluminium foils need to be glued *longitudinally* onto the surfaces, i.e. along the cylinder axis. This is to ensure continuous electrical conductivity along the entire length of the cylindrical shell. Thereafter, the finished layers will be electrically connected together at both ends of the cylinder. This provides protection against electrical shock and also acts as electrostatic shielding against spurious radiofrequency noise. Furthermore, during operation of the detector the inner conductive surface of this vessel is exposed to the potential of the central HV electrode (100 kV), mounted inside the field cage vessel, across a 150 mm thick, CO₂ filled, gap. This surface must therefore be smooth to minimize the risk of HV breakdowns. The outer vessel weighs approximately 420 kg.

3.1.1.2 Inner containment vessel

The inner containment vessel is the innermost and hence smallest of the four TPC cylinders (Fig. 3.4). Its functions are otherwise identical to those of the outer containment vessel. Though considerably smaller than its counterpart it consists of three parts:

- two conical end-pieces, called the left and right conical drum, which integrate the conical front-end absorber of the muon arm. They are identical and of the same composition as the outer vessel;
- an ultra-light cylindrical central drum at small radius within the acceptance region of the TPC ($|\eta| < 0.9$), in order to put material as close as possible to the vertex, which minimizes the influence of multiple scattering on momentum resolution. The inner diameter of the ‘central drum’ is such that it allows the installation and mounting of the ITS.

Each of these three drums will be produced in an autoclave. In addition to its outside flange, each conical drum will also have a light positioning flange, to hold and position the central drum and the ITS. The attachment of the two conical drums to the central one is to be carried out at a later stage through bonding at room temperature. The exact composition of the three drums is as follows:

- Conical drums:
 - 1 layer of aluminium foil, 50 μm thick;
 - 1 layer of Tedlar, type TWH 20 BS3, 50 μm thick;
 - 2 layers of prepreg (weaving layout 77–81, 60% fibre and 40% resin by volume, epoxy resin curing at 125 °C), 0.3 mm thick each;
 - 1 honeycomb-like structure Nomex (height = 20 mm, 29 kg/m³);
 - 2 layers of prepreg (as above);
 - 1 layer of Tedlar (as above);
 - 1 layer of aluminium (as above);
 - positioning flanges of prepreg (solid laminate epoxy resin at 125 °C, glass fibre fabric of minimum 50% fibre by volume).
- Central drum:
 - 1 layer of aluminium, 50 μm thick;
 - 1 layer of Tedlar, type TWH 20 BS3, 50 μm thick;
 - 2 layers of prepreg (weaving layout 120, 50% fibre and 50% resin by volume, epoxy resin at 125 °C); 0.1 mm thick each;
 - 1 honeycomb-like structure Nomex (height = 5 mm, 29 kg/m³);
 - 2 layers of prepreg (as above);
 - 1 layer of Tedlar (as above);
 - 1 layer of aluminium (as above).

Similar to the outer containment vessel, the inner and outer aluminium layers of each of the three cylinders will be electrically connected together at the ends of each cylinder. Insulation against HV breakdowns in the central drum is assured by smooth surfaces opposite the field cage wall and a CO₂ gap of 150 mm, tapering in the conical sections. The handling and transporting of the delicate inner vessel will be secured with a support tube as shown in Fig. 3.5. The inner containment vessel weighs approximately 85 kg.

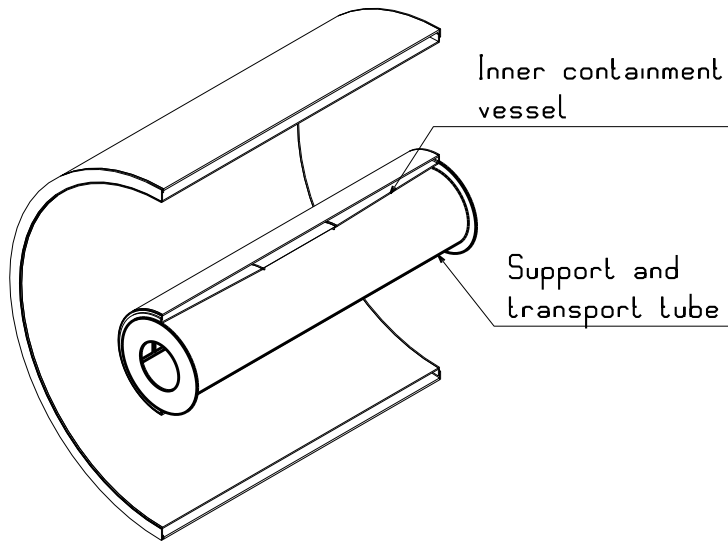


Figure 3.5: The inner containment vessel with its transport tube.

3.1.1.3 Inner and outer field cage vessels

The inner field cage vessel, together with the outer one, comprises the drift or sensitive volume of the TPC (Fig. 3.4 on page 12). Thus, the composition and fabrication of these vessels underlie stringent quality and selection criteria to ensure that:

- residual oxygen and water levels are maintained at < 5 and < 10 ppm, respectively;
- a minimum of pollutants is released into the gas;
- the insulating wall material is of high dielectric strength;
- high parallelism (< 100 μm) between the central electrode and the readout chambers can be achieved;
- multiple scattering and e/ γ conversion are reduced to a minimum.

These criteria are again best met with composite structures fabricated in autoclaving cycles. The two flanges of each vessel will be made of prepreg with the following composition: Solid laminate epoxy resin (125 °C) with a glass-fibre fabric of minimum 50% fibre content by volume.

For the cylindrical parts the following composition was chosen:

- 1 layer of Tedlar, type TWH 20 BS3, 50 μm thick;
- 2 layers of prepreg (weaving layout 120, 50% fibre and 50% resin by volume, epoxy resin at 125 °C); 0.1 mm thick per layer;
- 1 honeycomb-like structure Nomex (height = 20 mm, 29 kg/m³);
- 2 layers of prepreg (as above);
- 1 layer of Tedlar (as above).

As we will demonstrate in Section 3.1.3, we have adopted a scheme [1] in which the voltage-dividing network of the field cage is physically decoupled from the field-cage walls (Fig. 3.6). Thus, the prime

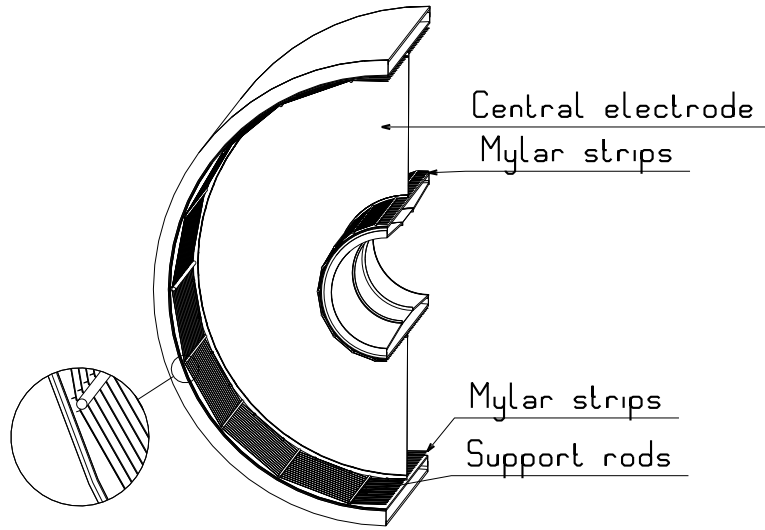


Figure 3.6: View of the field cage vessels with the potential degrader separated from the cylinder walls.

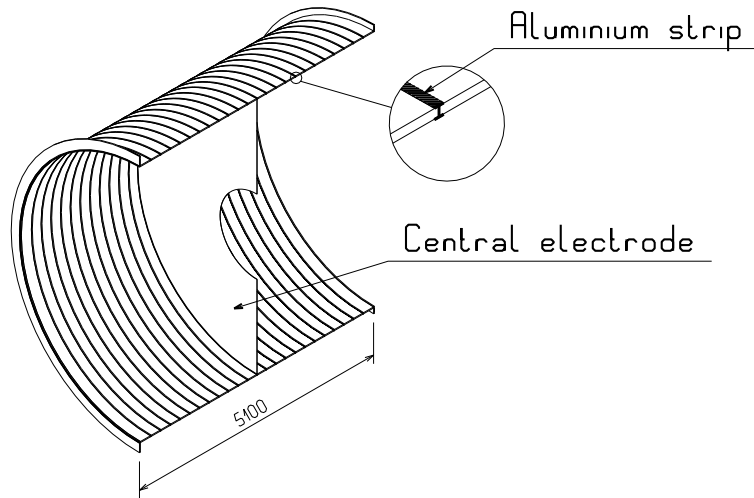


Figure 3.7: Scheme of the potential follow-up strips on the field cage vessel.

function of the field-cage vessels is to contain and maintain a pure gas volume, and arrange the electric field separately.

Nonetheless, to avoid the accumulation of static surface charges, the highly insulating walls of the field-cage vessels must be equipped with a few potential strips which are, contrary to the potential divider, directly glued to the inner *and* outer surfaces of the vessels. These are narrow aluminium strips (0.05 mm thick and 13 ± 0.2 mm wide) applied equidistantly (270 mm) along the vessel walls. They are glued to the surface with epoxy resins that release no significant vapours to the gas [2]. Thus, every 270 mm, concentric aluminium rings, connected to each other across the field cage walls, gradually ‘follow’ the potential of the actual voltage divider as shown in Fig. 3.7. This ensures a gradual potential decrease across the insulation gap with the containment vessels towards the end-plates held at ground. The outer and inner field-cage vessels weigh approximately 370 and 80 kg, respectively.

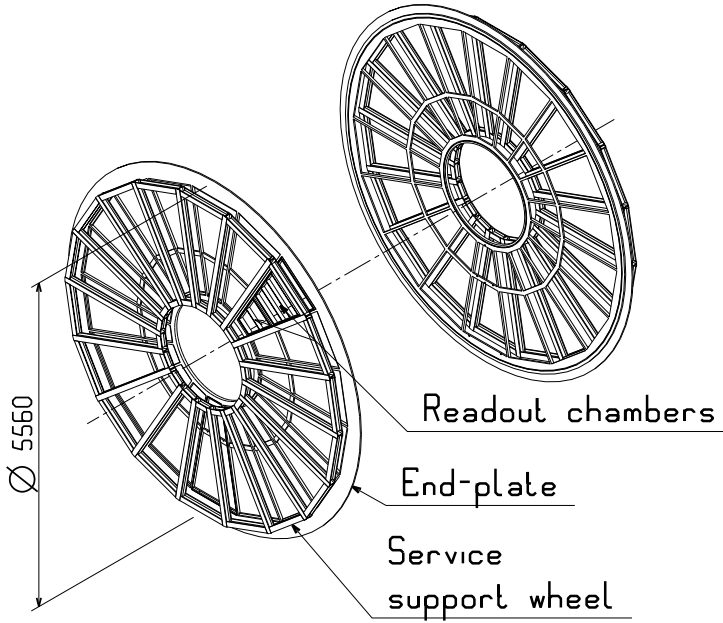


Figure 3.8: Design of the end-plate and the service support wheel.

3.1.1.4 End-plates

The end-plates will be made of an aluminium alloy (Fig. 3.8). They are a welded structure, machined after welding, in order to obtain the required mechanical precision of order $100 \mu\text{m}$. For optimum sealing with the cylinder flanges and also with the readout chambers, the end-plate structure must be of high rigidity and surface quality.

In view of the considerable weight to be supported on both ends of the TPC field cage we have chosen to mount the readout chambers without the front-end electronics on the end-plates and to distribute the bulk load given by the electronics and the associated cabling and services on special support wheels adjacent to the end-plates (Fig. 3.8).

This scheme of separating loads considerably reduces stress and thus deformations of the precisely machined end-plates that need to be well aligned with respect to the central electrode as shown in Section 4.1.5.4. It also eases the mounting and positioning of the readout chambers in the end-plate frame.

3.1.2 Assembly and testing

The modular, low-mass structure of the TPC requires that the individual cylinders and the end-plates are assembled in a vertical position. In order to reduce the risk of damaging the very delicate vessels, special tooling and handling structures must be used throughout the assembly procedure. It is thus foreseen to reuse the movable assembly frame of the DELPHI Barrel RICH detector, allowing the necessary movements and rotation of the bulky components of the TPC with high precision. In particular, the assembly of the electrical components inside the field cage requires a clean area of at least 250 m^2 . In the following sections we describe the exact assembly sequence of the TPC until its installation in the space frame. Prior to the assembly of the system, every individual part of the TPC field cage will be thoroughly tested and certified. Also, in the course of the mounting procedure, it is useful to test partially assembled units before proceeding with final assembly. This is part of our quality-control measures to assure reliability of the system at the outset of the construction and assembly.

3.1.2.1 Assembly of the inner and outer containment volumes

The first phase of assembling the TPC is to build the two containment volumes separately from their individual parts. These parts are

- the inner containment vessel together with the inner field-cage vessel, and
- the outer containment vessel together with the outer field-cage vessel.

For the inner containment volume, first the inner containment cylinder is placed vertically on a precision mounting table (Fig. 3.9). The slightly larger inner field-cage cylinder is then concentrically slid over the

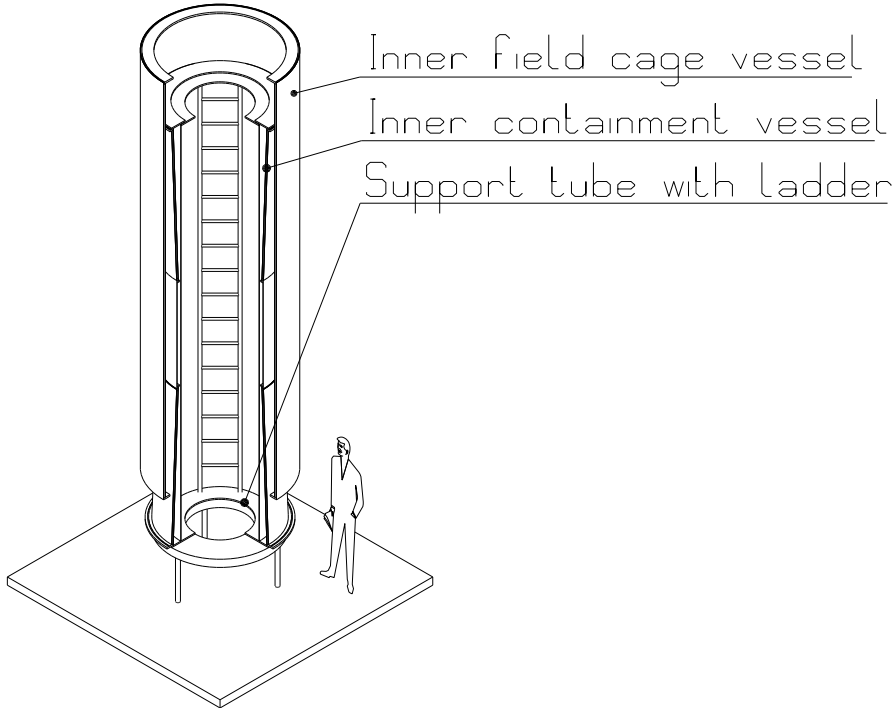


Figure 3.9: Mounting of the inner containment volume.

other vessel and bolted to it. This completes the assembly of the inner containment volume which will subsequently undergo leak and HV testing prior to further assembly.

The procedure for mounting the outer vessels is slightly different in that first the outer field-cage cylinder is precisely positioned before the outer containment cylinder is placed around it (Fig. 3.10). Also the outer containment volume will be tested before continuing the general assembly of the TPC.

3.1.2.2 Mounting of the support brackets for the potential degrader rods

Before the two containment volumes are combined to form the actual drift volume, provisions must be made for mounting the potential degrader rods which support the Mylar strips. The support rods themselves will be installed at a later stage. To do this, both containment volumes are moved into horizontal position and held on a rotating mandrel for ease of manipulation (Fig. 3.11). A high-precision ruler marks and positions the mounting brackets of the rods before they are glued on the outer surface of the inner containment volume or the inner surface of the outer containment volume. This fixes the position of the degrader rods that are to be mounted in a later step.

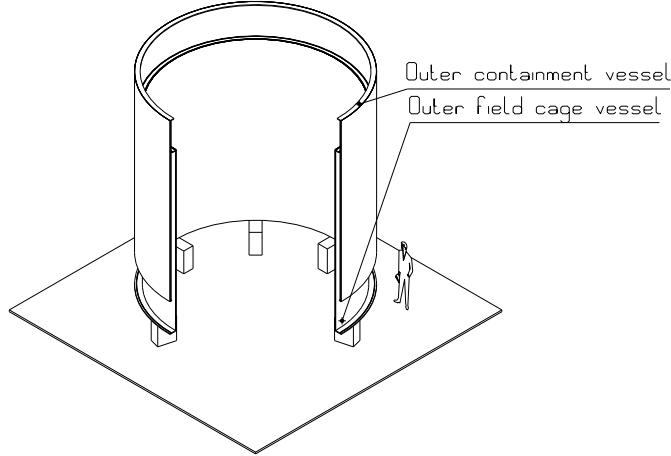


Figure 3.10: Mounting of the outer containment volume.

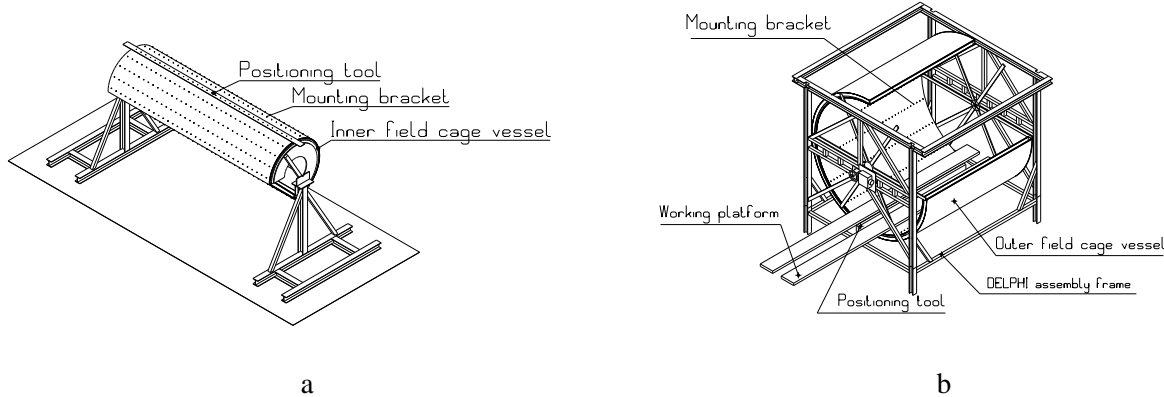


Figure 3.11: Preparation of inner (a) and outer (b) potential degrader.

3.1.2.3 Assembly of the drift volume

To assemble the drift volume, the two containment volumes need to be fixed vertically on one end-plate that is placed flat on a precision mounting table (Fig. 3.12a). The second end-plate will only be mounted after one half of the electrical network of the potential degrader has been installed inside the drift volume as described in the next section.

3.1.2.4 Mounting of the potential degrader and the central electrode

With one end-plate mounted to the cylinders of the drift volume, the installation of the potential degrader can commence. A detailed description of the potential defining network is given in Section 3.1.3. The assembly is kept in a vertical position. Entering the drift volume from below the end-plate, the inner and outer support rods are now mounted on their brackets, although for only half the full length of the cylinder. Thereafter, the Mylar strips are stretched around the rods and fixed into position with high precision tooling ($\leq 50 \mu\text{m}$) (Fig. 3.12b).

A simple voltage test of the resistor chain checks for shorts between strips at regular intervals during the winding process.

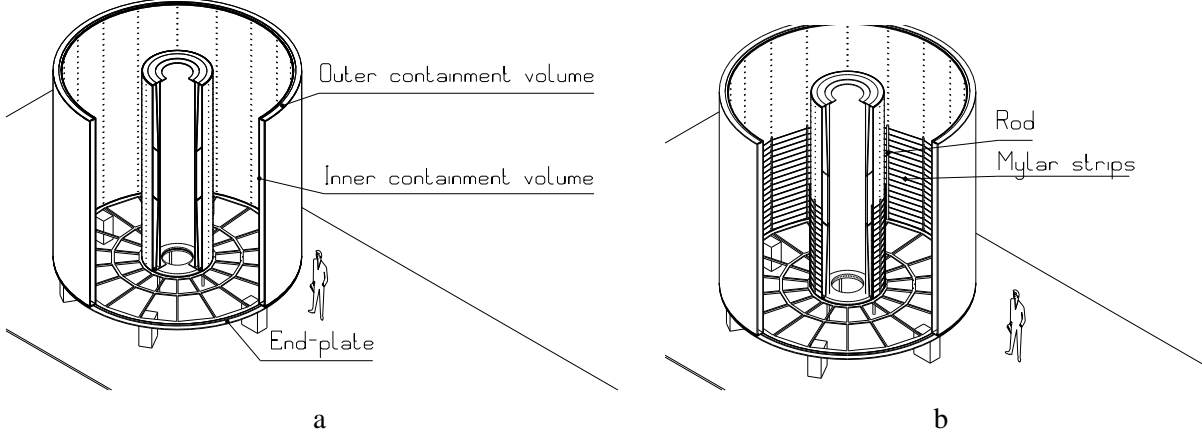


Figure 3.12: (a) Mounting of the two containment volumes on one end-plate and (b) the lower section of the potential degrader network.

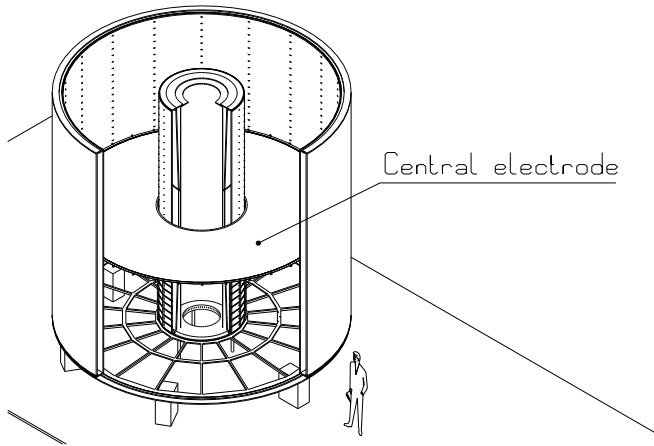


Figure 3.13: Mounting of the central electrode.

Having mounted the potential degrading network in the lower part of the TPC drift volume, the central HV electrode can be lowered through the top opening of the assembly and fixed into its final position (Fig. 3.13). The precision of its position is determined by the end-points of the rods, which are also machined with high precision.

Once the central HV electrode is in place, a first HV test of the system can be performed in air. If no electrical problems are encountered, the entire assembly will be turned around by 180 degrees, after the other end-plate has been mounted on top of the field cage volume. In the new position the other half of the potential degrader network will be installed and tested similarly to the first half. Upon completion, the TPC field cage will be moved into horizontal position to prepare the mounting of the readout chambers.

3.1.2.5 Mounting of the readout chambers into the end-plates

Before the readout chambers are fixed to the end-plate structure, a detailed survey of the end-plate and the mounting provisions for the chambers must be made. Photogrammetry has been chosen to measure, in particular, the position of the three mounting points. According to the outcome of this survey, the mounting brackets will be adjusted prior to the installation of the readout chambers. This is described in more detail in Section 4.1.5.6.

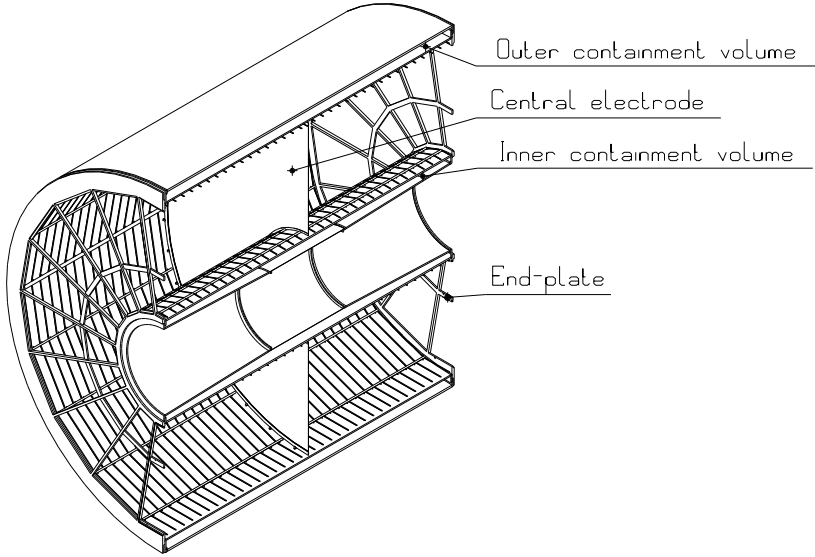


Figure 3.14: The fully assembled field cage without readout chambers.

The fully assembled field cage without the readout chambers is shown in Fig. 3.14.

3.1.2.6 Dedicated leak tests

Gas tightness of all vessels of the TPC is of prime importance for the proper functioning of the detector when in operation. The maximum permissible leak rates for atmospheric oxygen are given in Ref. [3]. Thus, as a measure of quality assurance, four different leak tests must be carried out to determine the residual oxygen and water level in a test gas (for example argon) due to leaks and outgassing in the vessels. These tests must be carried out prior to delivery at CERN. The leak rates in the different compartments of the TPC field-cage system, i.e. in the outer containment (CO_2), the inner containment (CO_2) and the drift gas volume, are experimentally determined by flushing the recipient with a test gas of defined oxygen content. In an equilibrium state, the residual oxygen content of the test gas, measured at the outlet of the recipient, determines the total leak rate in the recipient including its sealing. As test gas we envisage using argon with a maximum of 1–4 ppm of oxygen. The level of oxygen will be measured with a high-precision oxygen meter (precision of ± 0.1 ppm in the range of 50 ppm). The gas flow into the vessel under test determines the oxygen level, after an equilibrium state has been reached for a given leak rate. Furthermore, both the flow rate and the gas volume define the time constant in the exponential function that describes the change of oxygen content with time. It should be emphasized that the tolerable oxygen level in the outer and inner CO_2 volumes during operation of the TPC could be significantly higher than that of the actual drift gas. The assumptions on flows made in these calculations are such that an equilibrium state of 10 ppm residual oxygen is to be reached with a test gas containing no oxygen itself.

Inner and outer containment volumes

It is assumed that the recipient under test is exposed to atmosphere. The maximum over-pressure of the test gas, with respect to atmospheric pressure, will be 5 mbar. Furthermore, we assume that the front faces of the cylindrical volume are perfectly leak tight. In case the cylinders, forming the containment volumes, are built from several segments glued together, the glue joints between segments are assumed to be as gas tight as the segment surfaces themselves.

Given the specific leak rates of the sealing material, i.e. the Tedlar foils and Viton O-rings [3], and the size of the surfaces in contact with the containment volume, one can expect a total leak rate for oxygen of $\sim 6 \text{ cm}^3/\text{h}$ for the inner and $\sim 25 \text{ cm}^3/\text{h}$ for the outer containment volume. Hence, if a residual oxygen content of 10 ppm must be reached in these volumes, a gas flow of $\sim 0.6 \text{ m}^3/\text{h}$ and $\sim 2.5 \text{ m}^3/\text{h}$ must be provided for the inner and outer CO₂ containers, respectively.

End-plates

For the leak rate measurement of the drift volume, as described in the next section, we must first determine the leak rate of the two end-plate seals. A simple method to check the tightness of the end-plate seals is to mount them back-to-back against each other, using the two O-rings as foreseen for the final mounting (Fig. 3.15). To simulate the sealing properties around the readout chambers, which are them-

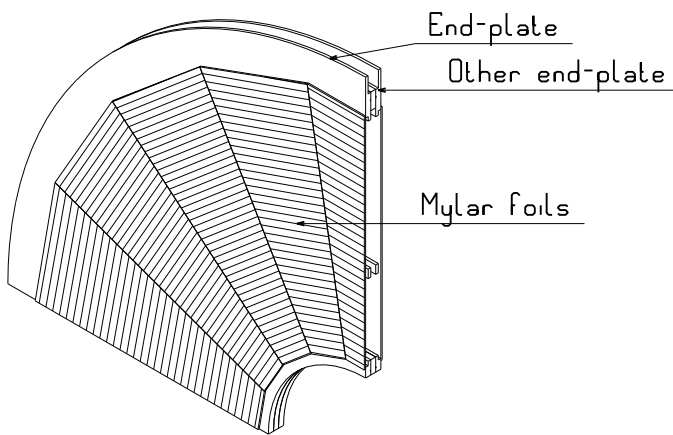


Figure 3.15: Arrangement of the two end-plates (back-to-back) with Mylar seals to replace the readout chambers.

selves not subject to this testing, we cover the end-plate openings with aluminized Tedlar or Mylar foils mounted via O-rings on the end-plate frame structure (Fig. 3.15). To correctly estimate the leak rate of the end-plate ensemble, one needs to compute the total surface covered with foils (32.5 m^2) and the length of all O-ring seals ($\sim 370 \text{ m}$). From this we derive a total leak rate for oxygen of $22 \text{ cm}^3/\text{h}$. Hence, for 10 ppm of residual oxygen in this volume, a flow rate of $2.2 \text{ m}^3/\text{h}$ is necessary.

Drift volume without readout chambers

This leak test will be performed by closing the drift volume on either side with the end-plates carrying foils that replace the readout chambers as described in the previous section (Fig. 3.16). The leak tightness of the end-flange is then determined by the leak rate of the foil surface, the sealing of the foils with the end-plate and the sealing of the end-plate with the field-cage flange. There are two O-rings on each side. It is assumed that, in this test, both the outer and inner containment volumes are flushed with CO₂ so that the diffusion of oxygen through the surface of the inner and outer field-cage cylinders can be neglected. Thus, the total leak rate for oxygen is estimated to be $20 \text{ cm}^3/\text{h}$, requiring a flow of $2 \text{ m}^3/\text{h}$ for 10 ppm of residual oxygen.

Drift volume with readout chambers

In this leak test the end-plates are fully equipped with readout chambers instead of the foils used, before and described in the previous paragraph. Since the leak rate of the chambers is lower by a factor of ~ 3 than that of the foils, the total leak rate to be expected for oxygen in this test is only $18 \text{ cm}^3/\text{h}$, which

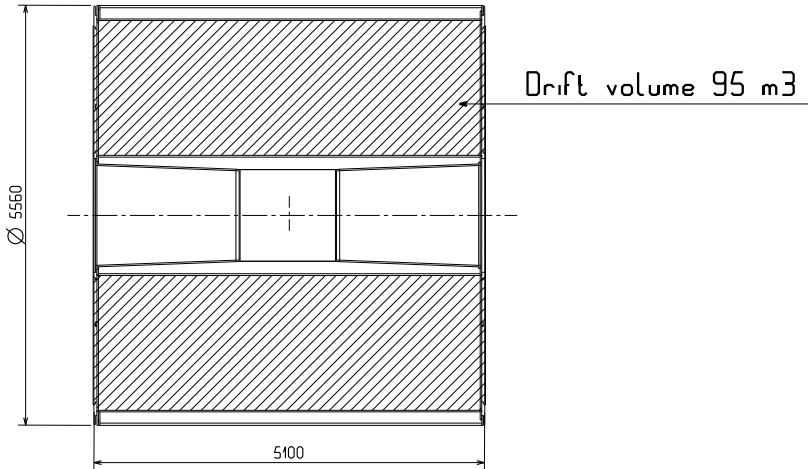


Figure 3.16: Test of the drift volume without readout chambers (replaced by Mylar/Tedlar foils).

translates into a gas flow of $1.8 \text{ m}^3/\text{h}$ for 10 ppm oxygen residual gas. For this test the final ALICE TPC gas system could be used which provides gas flows of $> 15 \text{ m}^3/\text{h}$.

Special potential degrader support rods

Some of the strip supporting rods of the potential degrading network are made hollow to use them for special functions described in Section 3.1.3.2. Among them, the four resistor rods with their internally mounted voltage dividing resistor chain need to be flushed with a liquid coolant to remove the waste heat produced by the resistors (60 W). For the other rods, in particular the HV supply rod feeding the HV of 100 kV to the central electrode, CO₂ gas will be used as an additional safety measure against HV breakdowns and oxygen intrusion into the drift volume. These special rods are extensively leak tested prior to their installation in the field cage. Thus, we do not expect any significant leaks in these rods.

3.1.3 Voltage divider

3.1.3.1 Design considerations

An important design element of the TPC is to physically separate the potential defining circuitry of the field cage from the walls of the field-cage cylinders. This scheme is not obvious a priori as it compromises physical acceptance for improving field uniformity in drift space. It was successfully applied in the NA49 TPCs [1] and showed that the improvement in field quality warrants the trade-off in space deliberately given up for this purpose. The surfaces of the TPC field-cage walls are made of a highly insulating material (Tedlar) and are thus prone to charge accumulation. These static charges would interfere with the precise field defining network of the field cage if the annular potential strips were in physical contact with the field-cage walls. This leads to far-reaching distortions of the drift field and hence significantly reduces the acceptance of the detector in radial space. Therefore, following the NA49 example, the entire potential defining network of the TPC is arranged on 18 support rods mounted equidistantly over 360 degrees, 31 mm away from the cylinder walls. This is shown in Fig. 3.6 on page 15 and done for both the inner and outer field-cage cylinders on either side of the TPC central plane. The following sections will demonstrate how our requirements on field uniformity, as outlined in Chapter 2, are satisfied with the chosen arrangement of the ALICE TPC voltage divider network.

A central electrode at high voltage and the readout end-plates define the drift field, foreseen to be 400 V/cm. This requires the central electrode to be at 100 kV, the drift length being 2.5 m on either side. To ensure the uniformity of the drift field in the sensitive volume the central HV electrode and the readout plane must be parallel to within $\leq 100 \mu\text{m}$. The required precision is achieved by adjusting the individual mounting provisions for the readout chambers with respect to the central electrode (Section 4.1.5.6). A schematic of the potential degrader system is shown in Fig. 3.17. The rather high voltage of 100 kV on

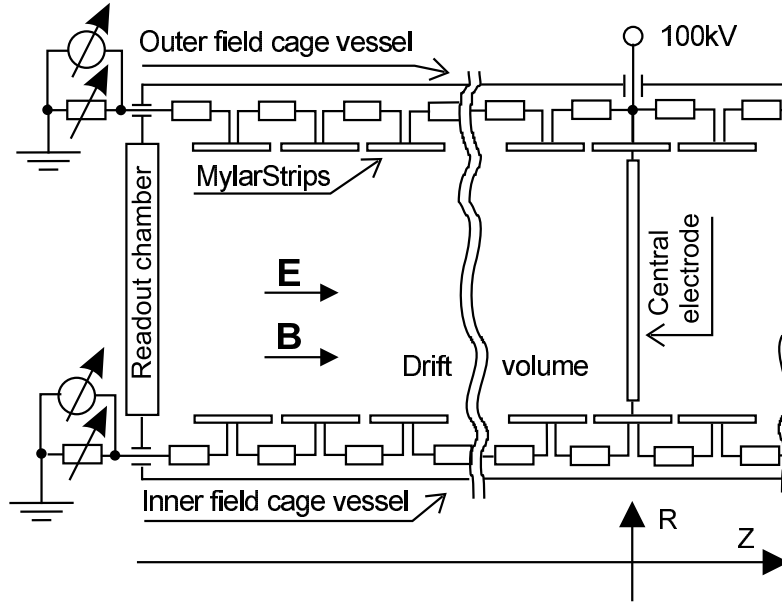


Figure 3.17: Schematic of the TPC potential degrader system.

the central electrode is screened from the ground potential by a CO₂-filled gap (150 mm) between the field and containment vessels. Therefore, in the design of the system, two aspects have been given special attention: the distance of the high voltage from the grounded containment cylinder, and the distortion of the sensitive field inside the TPC. Both of these have been thoroughly tested with simulations as well as with experiment (see also Section 3.1.5.1). The matching of the readout plane to the drift field of the TPC is also crucial to the design and detailed analysis of this problem has been performed accordingly. In the following we describe the design and optimization of each component of the TPC potential degrader.

3.1.3.2 System components

Central electrode

In line with the overall TPC design, the central electrode should be as light as possible and yet, at the centre of the TPC field cage, define a ‘solid’ reference for the two adjacent drift fields. Low-mass designs for a membrane of nearly 20 m² surface require the use of composite material, if one wants to support the actual electrode material parallel to the readout plane and preserve its alignment to within $< 250 \mu\text{m}$ when installed. The design currently being investigated for the central electrode is one which employs a Nomex honeycomb sheet, 6 mm thick and covered with thin layers of carbon fibre and aluminized Mylar (Fig. 3.18). This results in a self-supporting low-mass electrode necessitating no further reinforcement or additional support. The central electrode will be inserted into the field cage, in vertical position, via a piston-like insertion tool (shown in detail in Section 3.1.2).

Furthermore, the incorrect matching of the end-plate potential with the field cage cylinder can be caused by misalignment of components or by wrong potential. This can also lead to distortions of the

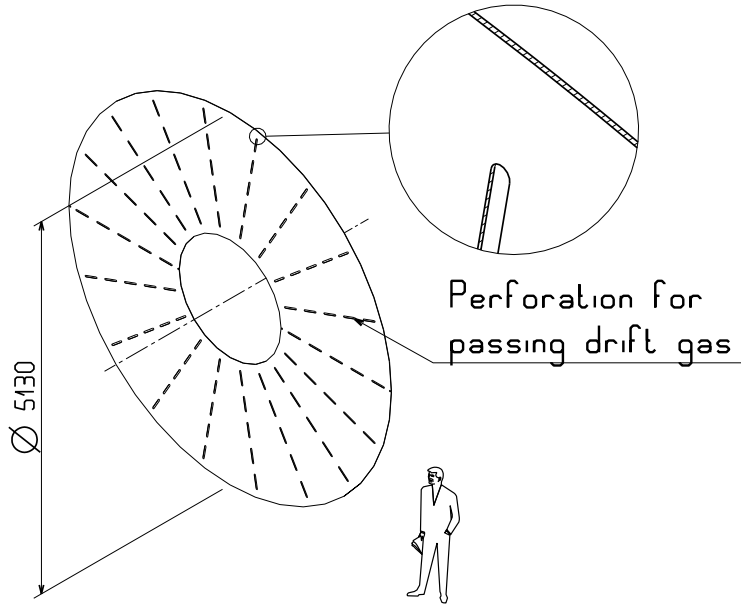


Figure 3.18: The central electrode of the TPC field cage.

order of $250 \mu\text{m}$ if the end-plate is not parallel to the equipotentials to within 10^{-4} . This issue will be addressed in more detail in Section 4.1.3 where also the effect of end-plate deformation will be investigated.

Potential degrader network

Following conceptually the NA49 scheme the potential degrading circuitry is suspended on 18 rods in an 18-fold polygonal symmetry around the inner and outer field-cage walls as shown in Fig. 3.19a. A close-up view of one of these rods is shown in Fig. 3.19b. This segmentation matches the modular structure of the readout chambers and the Transition Radiation Detector (TRD) in our efforts to jointly optimize the acceptance of both detection systems in azimuthal space.

There are 166 potential steps along one z -direction, made by strips, over a distance of 2.5 m. Thus,

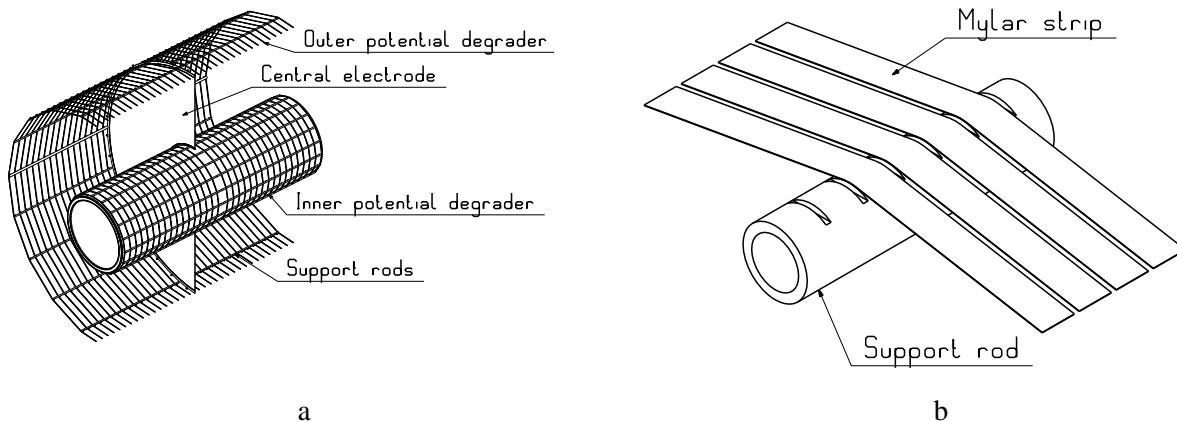


Figure 3.19: (a) Arrangement of the Mylar strips on rods inside the TPC field cage and (b) a close-up view of a support rod for the TPC potential degrader strips.

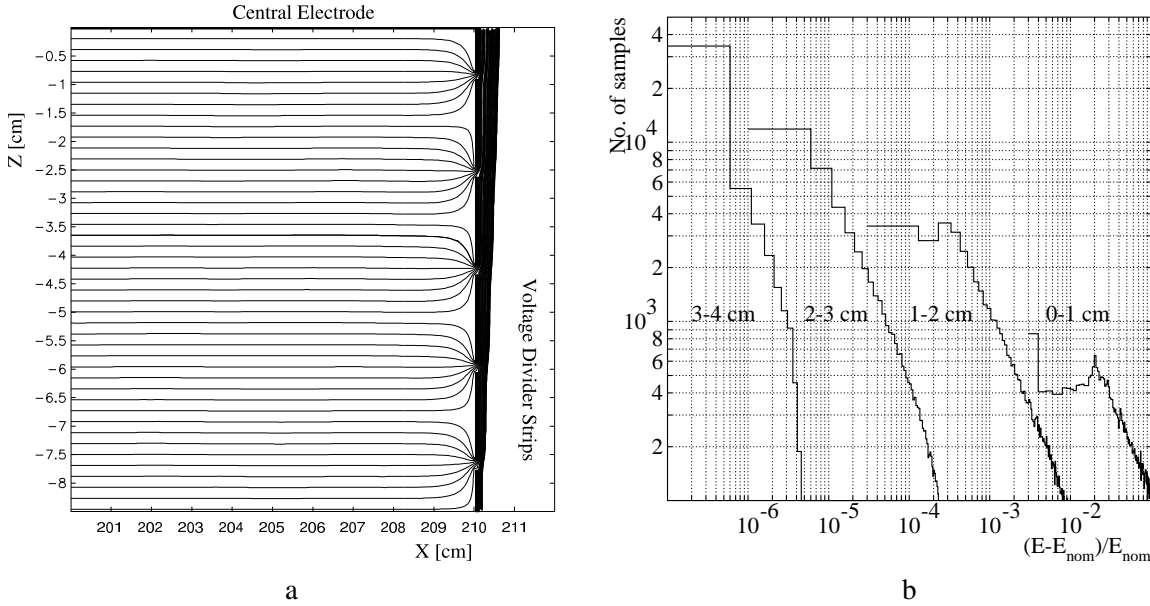


Figure 3.20: (a) Equipotential lines in the vicinity of the strips and (b) histograms of the relative deviations of the electric field from the nominal drift field in slices of 1 cm thickness parallel to the plane of the strips. The four contour lines indicate the zones in drift space in which residual field inhomogeneities are to be expected. From 2 cm inwards the drift space these inhomogeneities have dropped to $\leq 10^{-4}$.

the pitch of these strips, i.e. their width plus the gap between strips, is 15 mm. This value has been optimized with analytic calculations [4] and through finite element analysis. Each strip is placed with a voltage corresponding to its centre position in z from the central electrode since the distortions are minimum at the centres of the strip and the gap, as seen in Fig. 3.20a. This results in a drift-field nonuniformity of 10^{-4} , i.e. with a radial-field component $E_r < 10^{-4}$ relative to the longitudinal field E_z inside the sensitive volume. The strips are of 25 μm thick aluminized Mylar.

Precise positioning of the strips also plays an important role, since a displacement will result in field distortions. This is ensured by a positioning tool which puts the Mylar strips into place to within $< \pm 50 \mu\text{m}$.

Taking a close-up look at the equipotentials in a corner of the intersection between the central electrode and the field cage strips, we compute the drift field along a radial line at different distances from the central electrode at several z (Fig. 3.20b). We show here the worst possible region of distortions in the whole TPC sensitive volume. The average distortions in the slice nearest to the strips are of the order of 20%. Between 1 cm and 2 cm the distortions are already down to 0.3%, and between 2 cm and 3 cm the average deviations are 4×10^{-5} . The figure shows the field distortions in the drift volume resulting from the finite strip width and gap as well as the presence of the ground plane in the outer containment vessel. The appropriate voltage to the Mylar strips is supplied by a voltage divider resistor chain. The value of the resistors of $1 \text{ M}\Omega$ between strips was chosen such that the total chain current ($\sim 600 \mu\text{A}$) will not be changed by any reverse currents provoked by positive ions in the drift volume. Current changes in the resistor chain will alter the voltage settings on the Mylar strips and thus lead to changes of the drift field. However, the maximum positive ion density in the drift volume is only $2 \times 10^{-18} \text{ C}/\text{cm}^3$. The resistors are mounted in a sequence of parallel pairs of $2 \text{ M}\Omega$ each inside four of the 72 rods (the resistor rods) on which the Mylar strips are held. A sketch of the resistor chain and the resistor rod is shown in Fig. 3.21. Mounting the resistors inside the rod has several advantages. First, it protects the resistors and their junctions to the strips from mechanical damage during installation. Second, part of the heat

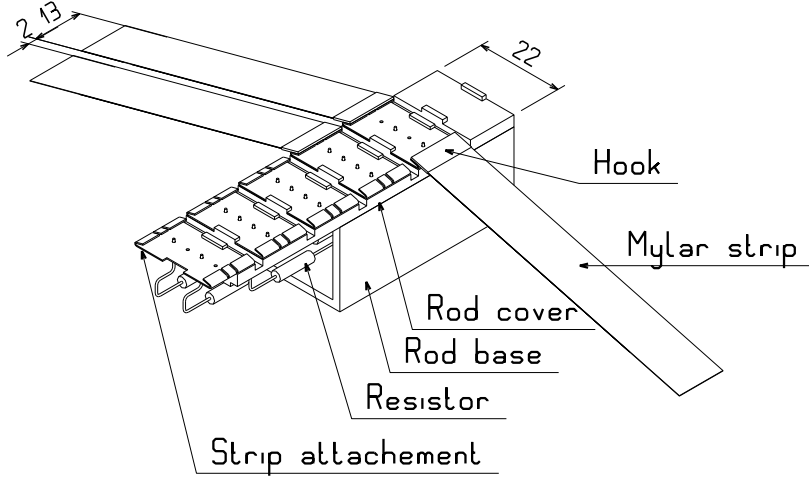


Figure 3.21: View of the resistor rod with the voltage divider mounted inside.

dissipated at maximum voltage setting along the rod (60 W) can be carried away to prevent local heating of the drift gas surrounding these rods. Thus, the constant flow of an insulating liquid through this rod, which is to provide additional electrical protection to the resistor chain, will also serve to transport the bulk of this heat away by forced convection (see Section 3.2.3.5).

The resistors need to be of good tolerance. Metal-oxide resistors are in general more insensitive to temperature changes than carbon resistors. If resistors fail or break, resulting in short circuits or open connections, field distortions will occur that may well reach into the sensitive volume. Figure 3.22 shows plots of equipotential contours for the case when two strips are connected by a shorted resistor. The risk of having an open circuit between two strips is substantially reduced by the fact that two resistors are mounted in parallel for each voltage step.

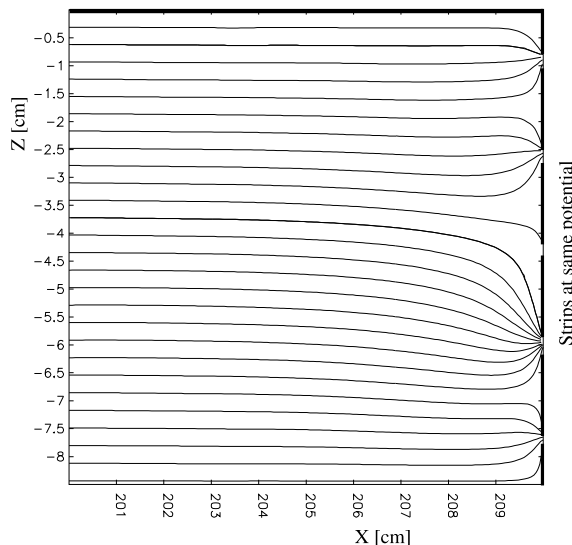


Figure 3.22: Effect of a resistor short between two neighbouring strips on the equipotential.

HV supply system

The voltage of 100 kV will be supplied by a commercial rack-mounted power supply and delivered to the field cage via a coaxial cable rated at 125 kV maximum. The far end of this cable is inserted into a special hollow HV supply rod. This rod, being one of the strip supporting rods on the outer field cage volume, makes electrical contact with the central electrode and is flushed with CO₂ for additional electrical protection. To avoid voltage mismatches within the electrical field-cage system, only this cable feeds, via the central electrode, both the inner and outer potential degrader chains on either side of the TPC (Fig. 3.23). A second reserve power system including the feed cable will also be installed next to the TPC to replace the main system in case of failure. This intervention, however, requires access to the TPC.

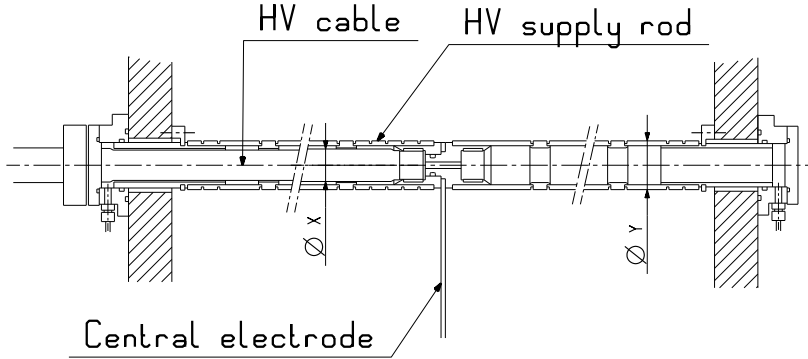


Figure 3.23: Layout of the HV feed system in the TPC field cage.

3.1.4 Temperature stabilization and thermal screen

3.1.4.1 Operating temperature of the TPC and thermal insulation

The gases to be used in the TPC are a consequence of carefully chosen overall design and operation parameters that shall guarantee optimum performance of the TPC at a minimum risk of failure. However, even at electric drift fields as high as 400 V/cm, electron drift velocities in these gases are not saturated and are thus subject to variations in temperature. As stipulated in Section 2.1, temperature variations of a fraction of a degree are already detrimental to the precise track measurements. Thus, one of the principal design objectives for the field cage is to protect the TPC drift volume from the influence of any heat sources that could cause local and time-related temperature changes of the drift gas by more than 0.1 °C.

If one assumes that all detectors inside the L3 magnet are internally cooled to maintain a constant global temperature environment of say 20 °C no net heat flow is exerted on the TPC, and only local or time-related temperature variations have an influence. Spurious local heating can be produced by exposed power-transmitting components, such as cables, the field-cage resistor chain and nearby electronics, while time-related temperature excursions occur when neighbouring detectors are subject to power and/or cooling failures which gradually change their bulk temperature until normal operation and thermal equilibrium are restored. For the outer TPC surface, for example, one can assume the event of an unforeseen heat transfer of the order of 30 W/m² between the TRD and the TPC across an air gap of 160 mm. Furthermore, heat sources that are in direct contact with the TPC cannot be entirely shielded from the TPC drift gas. These are for example the TPC front-end electronics and the voltage divider resistor chains where every effort needs to be made to remove waste heat, and cool them to the same temperature as the TPC drift gas.

3.1.4.2 System options and choices

For those heat sources that are not in direct contact with the TPC, active thermal screens offer best insulation and regulation properties at a minimum of physical space and material taken. Contrary to purely passive insulation schemes, thermal panels allow selected local heating and cooling, thus enabling a flat temperature ‘profile’ to be maintained on and around the skin of the detector. The possibility of controlled global cooling will also avoid the risk of thermal run-away of the system. In order to keep the amount of passive material near the inner radius of the TPC at a minimum, no thermal screening between the ITS and the central inner containment vessel of the TPC is as yet foreseen. However, the conical sections of the inner containment vessel, which are exposed to power and service cables of the ITS, should be protected by a screen. At present, we estimate that thermal panels enveloping the outer surface of the TPC and the conical sections of the inner containment vessel can provide a temperature stabilization of < 0.5 °C. Further smoothing of residual temperature gradients is given by the CO₂ containment volume and the 20 mm and 30 mm thick honeycomb skins of the TPC vessels. The temperature profile of the drift volume will be computed from data provided by temperature probes located outside and inside the detector. The latter shall be placed inside the support rods of the field cage (Section 3.1.3.2), near the end-plates.

3.1.4.3 Heat/cooling panels

First studies indicate that, in terms of particle interference, the lightest panels are made of aluminium. They offer better mechanical and heat-transfer properties than comparable screens made of intrinsically lighter materials such as polycarbonates. Two 200 μm thick aluminium foils, suitably profiled, are sandwiched to provide 1–1.5 mm thick flow channels such that internal temperature gradients within the panel itself are nearly eliminated. A schematic of such a panel is shown in Fig. 3.24. For the amount of heat to be removed and consequently the mass of coolant to be transferred, these flow channels need to be adequately designed in order to avoid buckling of the material. For example, in a panel of $1.25 \times 1 \text{ m}^2$ size, designed for a water flow of 60 l/h, these flow channels are at least 15 mm wide. As far as the outer surface of the TPC is concerned, the thermal screen is best placed on the space-frame structure inside the TPC–TRD air gap. A suitable and economic solution would be to construct the panels such that they match the 18-fold sector geometry of the TPC and TRD in φ with four additional segmentations per sector along the TPC z -axis. For the inner screen, the same segmentation around each conical drum, though with no subdivision in z , would be sufficient. In this case, the panels would be mounted on the TPC containment vessel.

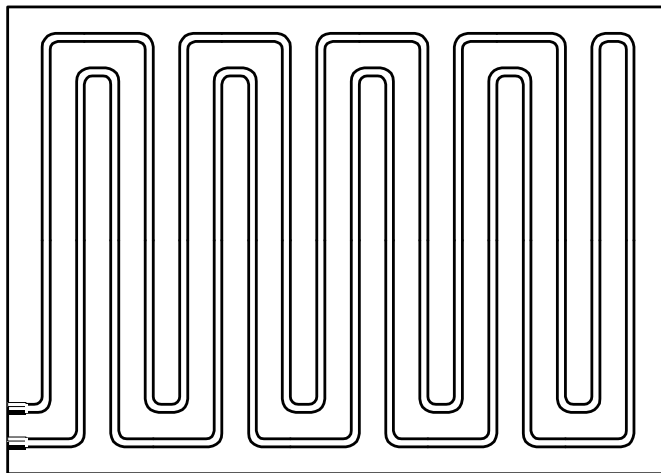


Figure 3.24: A thermal screen panel with parallel zigzag channels.

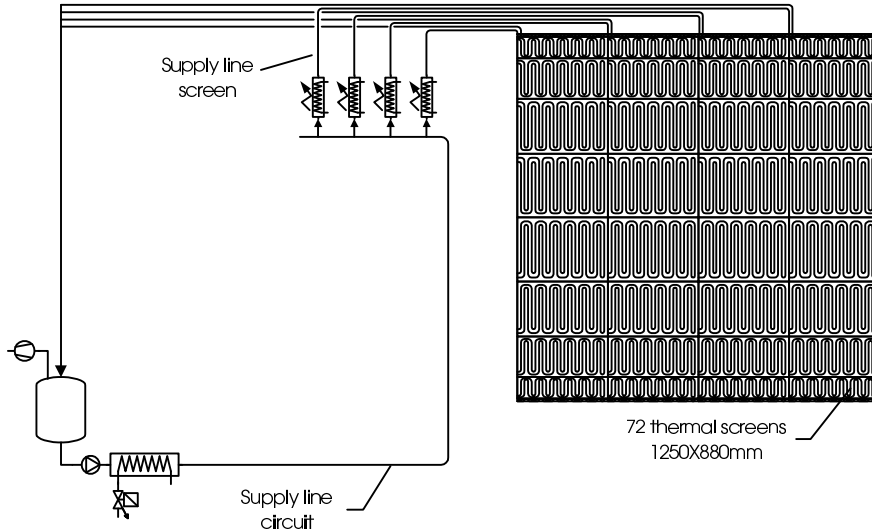


Figure 3.25: Schematics of the water circulation system for the outer TPC thermal screen.

3.1.4.4 Closed-circuit water cooling system

The proposed granularity of the thermal screen increases the complexity and mass of the system and, in particular, bears the danger of fluid leakage. The amount of distribution manifolds and pipe routing that are necessary for the entire system raise the question of using an under-pressure (called leakless) cooling circuit to avoid damage of the detectors from loss of fluid. Figure 3.25 shows such a cooling system consisting of a pump, located in the experimental cavern, and individual flow regulators and heaters for each separate panel. Thus, the temperature equilibrium of the system is controlled by separate temperature measurements on each panel and, in case of differences, the fluid to each individual section is selectively heated until a common temperature profile is achieved.

3.1.5 Tests and prototypes

To put the proposed ideas on composite materials to a thorough test, a 2.7 m long and 1.1 m diameter prototype vessel was manufactured by industry. It was built from a 20 mm thick honeycomb sandwich (Nomex) structure covered with layers of glass fibre and Tedlar prepregs. The prototype TPC field cage is shown in Fig. 3.26. It was constructed from two cylinders, each 1.35 m long, and each made from

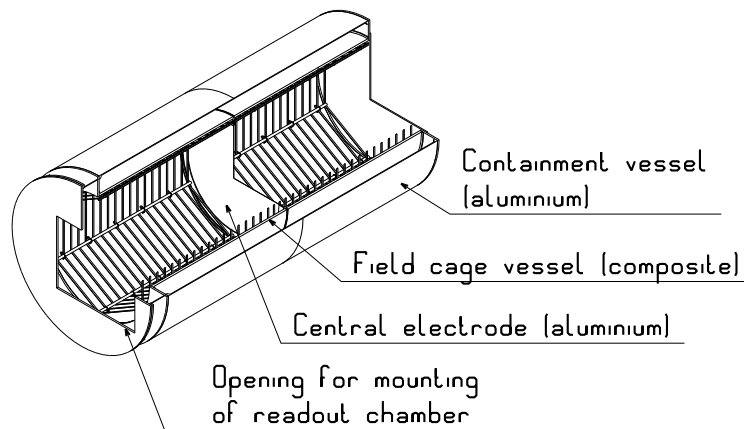


Figure 3.26: The prototype TPC field cage.

two axial half-shells of the same length, glued together after the autoclaving process. This glue joint was sealed with an additional Tedlar foil to avoid leakage. It should be noted that assembly of the large TPC cylinders from prefabricated segments is to be expected, as many manufacturers do not operate large autoclaves to cure these cylinders in one piece.

Following its delivery in early 1999, this field-cage cylinder has undergone various mechanical inspections and tests, including gas tightness. After inspection and certification, the prototype field cage was installed in a slightly larger aluminium vessel (Fig. 3.26) providing safe containment of the electrical network and avoiding leakage of oxygen into the drift volume. Similar to the field-cage arrangement for the ALICE TPC, a CO₂ insulation gap of 150 mm between cylinder walls assured HV operation of ≥ 100 kV. The prototype vessel was successfully installed with no detectable leaks.

To verify the electrostatic performance of the field cage, the prototype vessel was equipped with a similar field-defining network to that foreseen for the final TPC. The test programme consisted of two phases:

- verification of the purely electrostatic behaviour of the device including safety margins of 20% beyond nominal values; and
- performance of the device as a real prototype TPC with a pad readout chamber mounted on one of its end-plates.

Therefore, in the field cage prototype, a thin aluminium plate was mounted halfway along its axis to form the central HV electrode (see Fig. 3.26). Five concentric aluminium rings per half-side were taped equidistantly on the inner and outer surfaces of the honeycomb structure and interconnected via gas-tight feedthroughs (see Fig. 3.7 on page 15). These rings were also connected to the voltage divider chain, directly opposite the nearest resistor of the chain. This avoids the accumulation of charges on the highly resistive surface of the field cage and also the build-up of high potentials near the end-plates typically held at ground.

In all, 91 strips configuring the actual drift field along the axis of the cylinder were made of aluminized Mylar, 12.7 mm wide, and placed at 15 mm pitch, i.e. with a gap of 2.3 mm between adjacent strips. They are suspended by six insulating support rods of Macrolon attached to the inner field-cage shell and mounted on thin Stesalite stand-offs. One of these rods has a larger diameter to accommodate the voltage-dividing resistor chain on its outside surface, and the HV supply cable inside of it. The far end of this rod was tied to the central electrode and the second HV distribution rod in the opposite drift volume. The nominal drift field of 400 V/cm implies a maximum potential of 55 kV for a drift length of ~ 1.30 m.

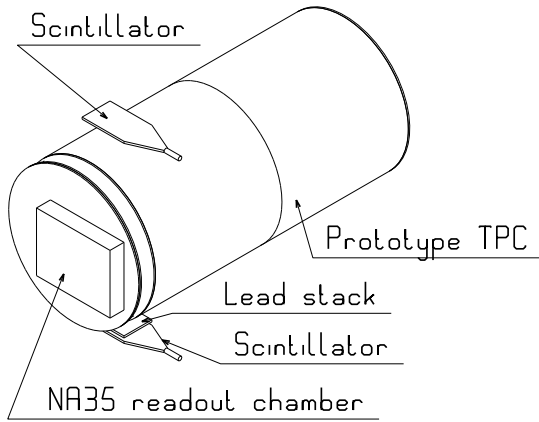
3.1.5.1 Electrostatic tests

After testing all individual components of the HV distribution network, the entire field cage, fully equipped with 91 potential-defining Mylar strips in each half-volume, was tested with argon and neon gas mixtures. To monitor the current in the resistor chain and detect HV breakdowns, a 1.8 k Ω external resistor was mounted between the last potential strip and ground. Variations of the voltage drop across this resistor indicate HV instabilities within the voltage-dividing network, thus giving the possibility of manual intervention before damage can occur.

The results are summarized in Table 3.2. They demonstrate the envisaged stability of the field cage and its suspended field-defining network up to fields of 600 V/cm. The last row of this table shows results of a special HV test made in a separate set-up designed to investigate the limiting potential between neighbouring Mylar strips. With an improved geometry of the hooks and the attachment of the strips we could reach voltages of 8 kV between neighbouring strips, i.e. approximately 10 times the nominal value for a field of 400 V/cm.

Table 3.2: List of electrostatic tests performed with the TPC field-cage prototype.

System on test	Voltage applied [kV]	Equivalent field [kV/cm]	Tested in	Outcome
Bare sandwich shell	70	n.a.	Ambient air	OK, no measured current
HV supply rods	80	n.a.	Dry air	OK, stable current through resistor chain
FC + containment (150 mm gap)	120	8	CO ₂	OK, no measured current for 1 hour
FC + voltage divider	82.5	0.6	Ar-CO ₂ [80–20]	OK, stable current for 1 day
FC + voltage divider	82.5	0.6	Ar-CO ₂ [90–10]	OK, after stabilization for few hours
FC + voltage divider	82.5	0.6	Ne-CO ₂ [80–20]	OK, stable current for 1 day
FC + voltage divider	55	0.4	Ne-CO ₂ [90–10]	OK, stable current
FC + voltage divider	82.5	0.6	Ne-CO ₂ [90–10]	~ 2 μA dark current
Mylar strips and new hooks	8	5.3	Ar-CO ₂ [80–20]	stable, no breakdowns

**Figure 3.27:** Arrangement of the readout chamber with the prototype field cage.

3.1.5.2 Cosmic-ray tests

A conclusive bench test of the chosen TPC field-cage concept is to measure particle tracks over nearly the entire acceptance range of the field cage. Straight tracks produced by cosmic rays are suitable tools to search for nonlinear effects indicating electrostatic defects in the field configuration. In particular, edge effects near the field-cage boundaries are of prime interest, but also those near the readout chamber interface with the field cage. The transition from the field region to the amplification and readout region becomes particularly difficult for the envisaged high drift fields of 400 V/cm. Thus, matching of the drift field with the field of the readout chambers at a minimum loss of efficiency and precision was the aim of these tests. The chamber chosen for readout was a wire chamber of the NA35 TPC [5] (Fig. 3.27).

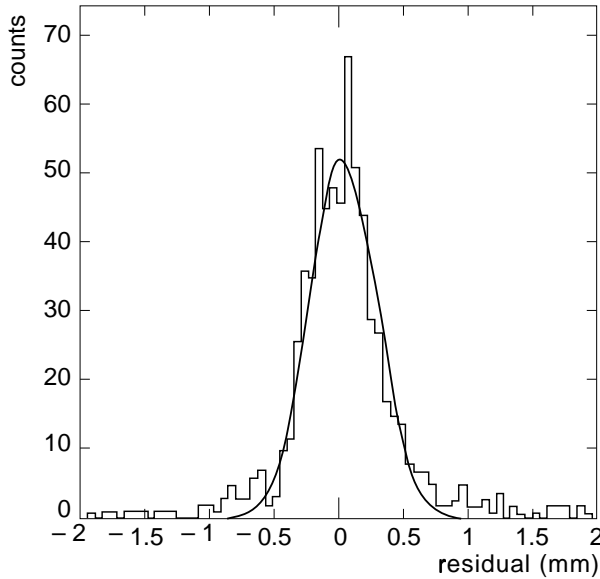


Figure 3.28: Distribution of the residuals from a straight-line fit on cosmic-ray tracks measured in the prototype TPC.

Its active wire-pad area was large enough to accept tracks from the central region of the TPC to and beyond the edges of the field cage. Thus, a systematic study of the field quality over the entire field-cage acceptance could be made.

Initially, high-energy cosmic rays were selected with a simple scintillator array interleaved with 10 cm of lead (also shown in Fig. 3.27). The NA35 module and its associated electronics allowed us to read 448 pads per cosmic trigger and record the events for data analysis. A track-fitting algorithm, applied to selected data samples, reconstructed cosmic tracks to better than $260 \mu\text{m}$ deviation from a straight line (Fig. 3.28). These preliminary results indicate that the chosen principle of configuring the electric field inside the TPC is viable with regard to the physics performance stipulated in Section 2.1.

3.2 Gas system

3.2.1 Specific operational requirements

The long (2.5 m) drift distance of the ALICE TPC and the use of CO₂ in the operating gas mixture make it mandatory to limit the concentration of oxygen and water vapour in the drift volume to a minimum. This is one of the main requirements for the gas system and the detector itself. The accuracy and stability of the gas mixture, along with its pressure regulation, is also important, as well as the correct design of the containment vessels.

Oxygen molecules in CO₂ are very prone to electron attachment. In the case of Ne–CO₂ mixtures, the electron attachment is 1% per ppm oxygen and metre of drift. Oxygen contamination comes mainly from sealing joints, which roughly scales with the total surface of the detector. The large volume-to-surface ratio of our TPC and the purity achieved in other TPC gas volumes (see Table 3.3) makes it feasible to limit the oxygen content to near 1 ppm, provided the sealing concept, the purification of the gas, and its flow are designed accordingly. Physics requirements set the absolute maximum to 5 ppm.

A CO₂ gas volume envelops the drift volume for reasons of HV insulation, thus providing extra sealing against potential leaks along the inner and outer cylinder walls. In addition, several hollow rods, located inside the drift volume, will also be flushed with CO₂ for cooling reasons. These insulation and service volumes are flushed with a single-pass gas system.

Table 3.3: Oxygen levels attained in existing TPCs. The maximum limit for the case of the ALICE TPC is quoted.

	Volume/surface [m]	O ₂ [ppm]	Ref.
DELPHI	0.34	1–2	[6]
ALEPH	0.55	20	[7]
NA49 VTPC	0.26	3–4	[1]
NA49 MTPC	0.47	1–2	[1]
CERES	0.28	5–7	[8]
ALICE	0.70	< 5	

3.2.2 Gas choices

The well-known 90% Ne, 10% CO₂ [9] is the baseline gas mixture chosen for operating the detector at a reasonable drift field and still ensuring attractive charge transport properties with a nonflammable gas. For reasons of primary yield and stability of the readout chambers at relatively high gains, the addition of an extra, warm quencher such as CF₄ is being studied. An extra 10% CF₄ in the gas mixture would increase the primary electron yield by 10% with no increase in diffusion or electric field. It would also increase the maximum attainable gain of the detector since there would be more quencher available to absorb photons produced in the avalanches. The possible electron attachment of the fluorocarbon and the chemical compatibility of this substance with the materials of the TPC remain to be determined. The addition of argon would contribute to the primary yield as well, at the expense of an increase in multiple scattering and, more importantly, in space charge in the drift volume due to the slower positive ions. This effect would also increase the corresponding field distortions by a factor of 5 compared to neon.

The gas used for insulating the high voltage against the exterior is CO₂, for practical reasons: it is a low-cost gas, it has good dielectric strength, and it is also one of the components of the TPC operating gas mixture.

3.2.3 Design choices and layout

The large detector volume and the use of a high-cost gas mixture make a closed-loop circulation system compulsory. The system proposed will consist of functional modules that are designed and built as standard units for all LHC gas systems. Table 3.4 indicates the location of these modules. The mixing and purification units, as well as an optional gas recovery plant, are located in the gas building on the surface (SGX2). The circulation rack will be located on the shielding plug in the pit PX24. However,

Table 3.4: Functional modules of the TPC gas system and their locations.

Functional modules	Location
Primary gas supplies	SGX2 Building
Mixer	SGX2 Building
Inside circulation loop	
Distribution	Pit PX24
Purifier	SGX2 Building
Pump and pressure regulation	Pit PX24
Ne recovery (optional)	SGX2 Building

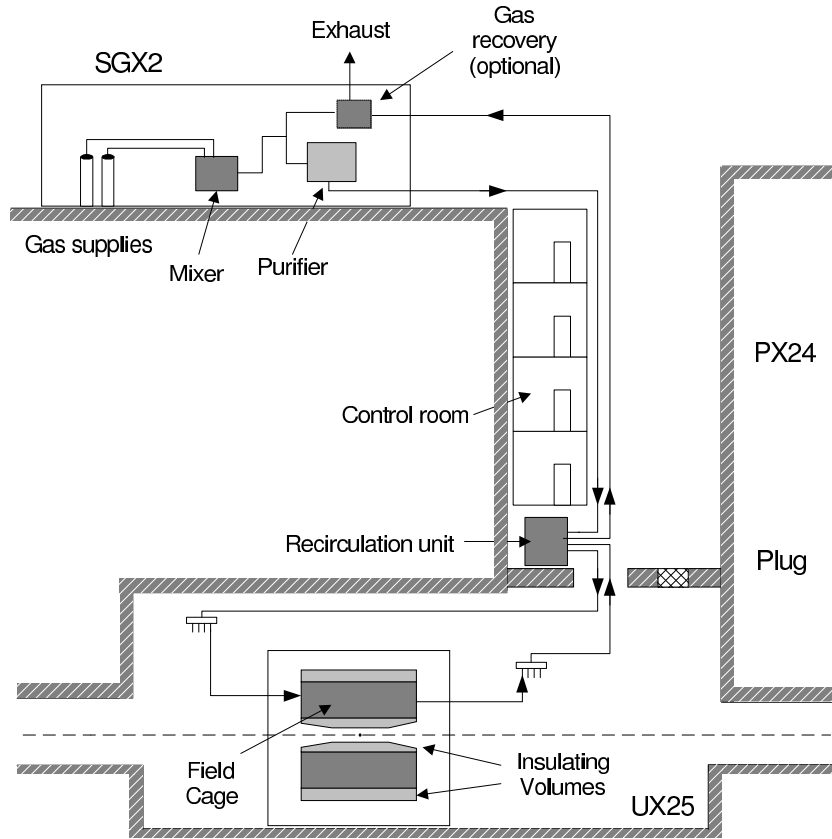


Figure 3.29: Overview of the gas distribution system

the component sizes and ranges are adapted to meet the specific requirements of the TPC system. An overview of the gas distribution system can be seen in Fig. 3.29. The basic function of the gas system is to mix the components in the appropriate proportions and circulate the gas through the TPC drift volume at a pressure of 1 mbar above atmospheric pressure. Some basic parameters of the TPC gas system are given in Table 3.5.

Table 3.5: Basic parameters of the TPC gas system.

	Drift	Outer insulation	Inner insulation
Volume	95 m ³	12.62 m ³	2.77 m ³
gas mixture	Ne CO ₂	CO ₂	CO ₂
Working overpressure	1 mbar	≤ 1 mbar	≤ 1 mbar
Filling rate	4 m ³ /h		
Circulation flow rate	19.4 m ³ /h	2.5 m ³ /h	0.64 m ³ /h
Fresh gas injection (Vol)	1 %	100 %	100 %
Operational period	8 months	12 months	12 months

3.2.3.1 Mixing unit

An LHC gas mixing unit, schematically shown in Fig. 3.30, will be used to mix the components in the appropriate proportions. The flows of component gases are metered by mass-flow controllers, which have an absolute stability of 0.3% over one year, and a medium term stability of 0.1% in steady-state

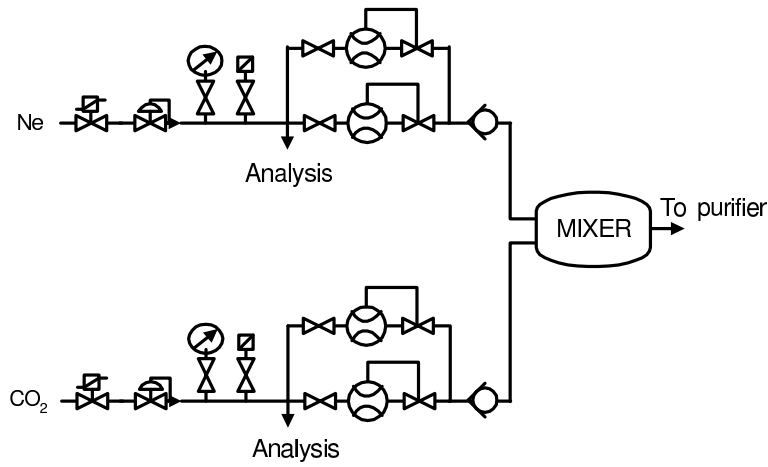


Figure 3.30: Gas mixer unit located in the surface gas building

conditions. Flows are monitored by a process-control computer, which continually calculates the mixture percentages supplied to the system. At a regeneration rate of 99% the expected fresh-gas flow at operating conditions is of the order of 200 l/h. Filling of the detector will be done without recirculation with 20 times higher inlet flows using a second set of mass-flow controllers. This device change will allow a full TPC volume exchange with fresh gas in one day. The 6–8 volume changes needed for achieving the gas operating condition leads to a start-up period of one week.

3.2.3.2 Gas circulation system

A flow diagram of the circulation system can be seen in Fig. 3.31. The gas mixture is circulated in a closed loop with an anticipated regeneration rate of 99%. This will allow high gas flows in the detector, as shown in Table 3.5, with a moderate fresh-gas injection. Return gas from the drift volume must be compressed to approximately 100 mbar above atmospheric pressure to pump it back to the surface gas building where it will be recycled through the purifier. The gas pressure inside the field cage is regulated to 1 mbar above atmospheric pressure by a control valve mounted in parallel to the compressor. The HV central electrode of the field cage has a gas passage transparency of 15%, resulting in a negligible impedance to the flow. The gas input pressure is reduced to a few mbar downstream of the flow regulator in the inlet pipe on the plug. This regulator allows manual flow adjustments from the accessible zone, combined with remote monitoring of the total gas flow. Effective over- or under-pressure protection for the delicate field-cage structure is achieved in two steps:

- Three pressure transducers, independent of the regulation, measure the pressures on the inlet after the flow controller, at the field cage and at the input of the compressor; thus, the control system can permanently check these values and stop the gas flow if necessary.
- For ultimate protection, a safety bubbler is installed in the rack situated in the cavern very near the detector.

During operation, changes in atmospheric pressure are automatically compensated for by the pressure regulation system. If the gas flow is stopped, a back-up system is available at the outlet of the TPC. This will either add gas from a pre-mixed bottle or relieve gas to atmosphere through a bubbler adjusted to 1 mbar. In this manner, rapid changes of atmospheric pressure in the event of a power failure can be followed without modifying the gas mixture inside the TPC.

Filling and purging of the operating gas is done in single-pass mode by switching the three-way valve situated in the SGX2 building to direct the gas to an exhaust or to a recovery plant if required. Gas

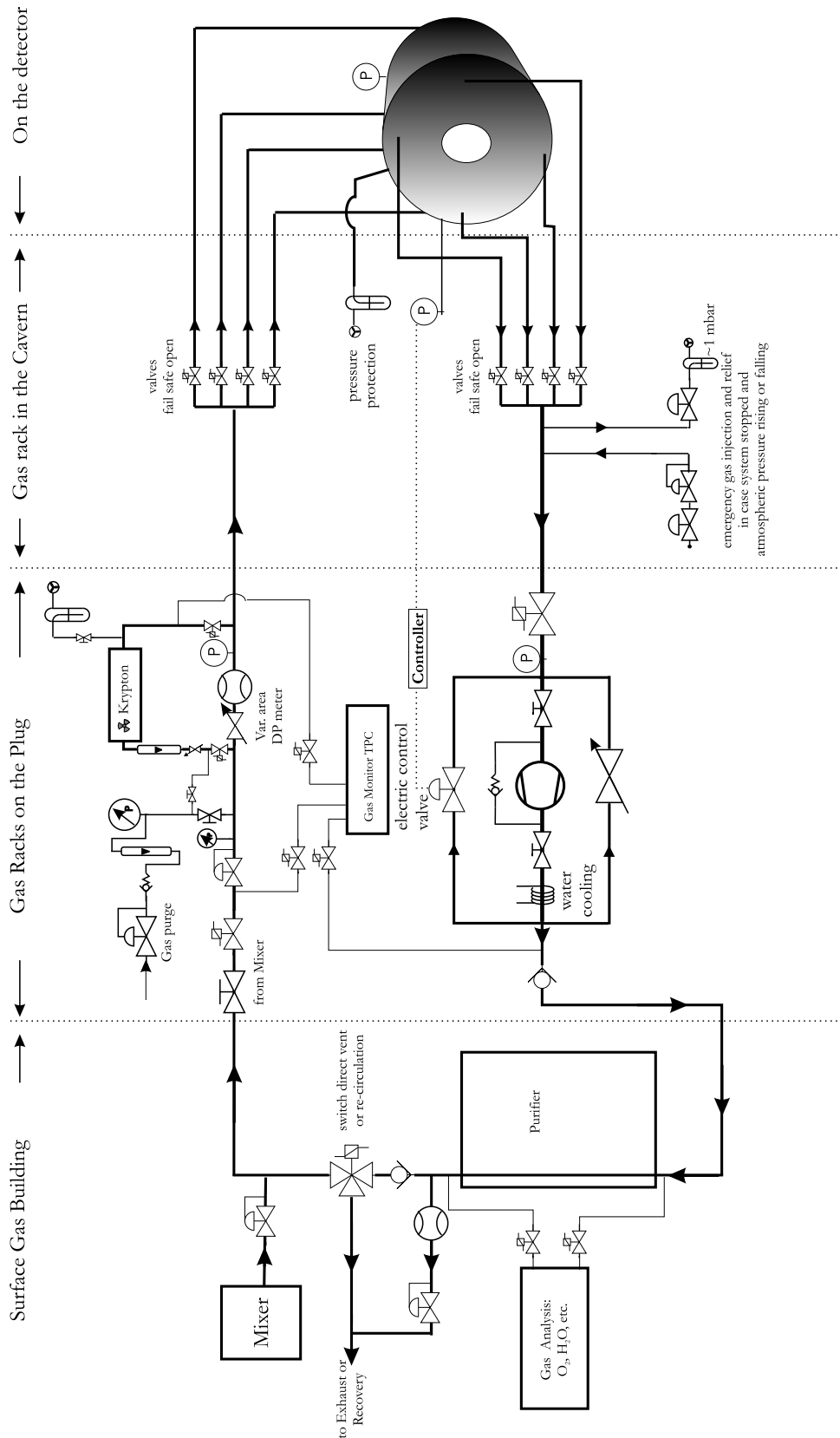


Figure 3.31: Basic component layout of the TPC gas circulation loop. The pressure in the field cage is regulated to +1 mbar relative to atmospheric pressure by the control valve in parallel to the compressor. The input pressure signal for the controller is taken directly from the TPC. The total circulation flow is adjusted by the manual flow regulator in the input line.

replacement for filling can be optimized by injecting the lighter Ne CO₂ mixture (density 0.99 kg/m³) at the upper side of the TPC while extracting the CO₂ (density 1.94 kg/m³) from the lower side. During shutdown periods, the detector will be flushed with CO₂ in one of the two following ways:

- Closed-loop circulation as during operation. This requires, however, electricity for running and controlling the gas system, as well as minimal operator surveillance.
- Manual purge mode where CO₂ is supplied from the plug, flushed through the detector and exhausted through a bubbler. The control system can monitor flows and pressures, but this is not mandatory.

In case of a longer shutdown period, the field cage can be filled with CO₂, and the back-up injection and relief system can just maintain 1 mbar over-pressure in the detector by injecting or venting a minimal amount of gas.

3.2.3.3 Purification system

Closed-loop gas circulation systems require gas purification in the return line from the detectors in order to achieve high recycling rates (of the order of 99%) and low fresh-gas input. The main impurities of concern which accumulate in the system are oxygen and water vapour, entering via the joints of the vessel walls [3]. TPC detectors are very sensitive to these components, which must remain below 5 and 10 ppm, respectively. The purifier system removes these contaminants from the gas mixture. A schematic layout of the purifier unit can be seen in Fig. 3.32.

Purification will be done with cartridges filled with two cleaning agents: a molecular sieve (3A) to remove water vapour, and activated copper as a reducing agent for oxygen. A configuration in parallel allows one to run the gas through one purification cylinder whilst the other one is being regenerated.

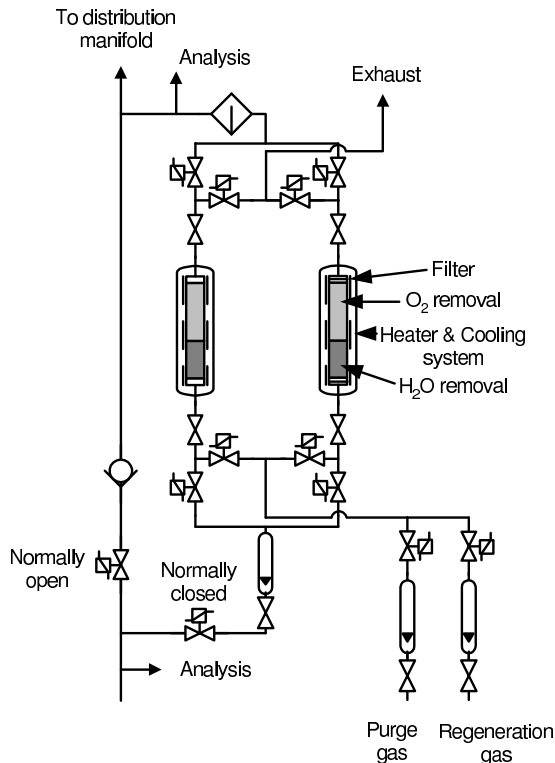


Figure 3.32: Schematic layout of the purifier unit.

Both agents in the same cylinder can be regenerated at the same time by heating the columns to 220 °C in an 93% Ar, 7% H₂ mixture.

Nitrogen cannot be removed by the purification system, and as a consequence the amount of N₂ penetrating into the circuit will limit the achievable regeneration rate. This in turn determines whether or not a gas recovery plant is needed. Purging rates below 1% could be affordable in terms of gas cost. Studies of the amount of nitrogen as a function of purge flow will be carried out in a prototype facility.

3.2.3.4 Calibration and monitoring

As discussed in Section 4.3.3, X-rays from decays of ⁸³Kr will be used for calibrating the gain of all readout channels of the TPC. A bypass vessel containing the radioactive source will be foreseen in the gas system, after the mixing unit. Continuous monitoring of the gas gain and the drift velocity, which are sensitive to pressure, temperature, gas-composition, and water-vapour fluctuations, is also necessary. A set of small drift and proportional detectors will be implemented into the slow control system for this purpose. The detectors will monitor the gas properties at various locations in the gas circuit. Direct monitoring of oxygen and water vapour will also take place before and after the purifier unit. Detected levels above set values will generate alarm signals, which may stop the gas circulation if necessary. Other parameters relevant to the operation of the gas system, such as gas flows, pressures at different locations, and CO₂ content, will also be monitored through the slow control system.

3.2.3.5 Ancillary gas volumes

The inner and outer containment volumes which protect the field cage will be filled with CO₂, in order to provide sufficient electrical insulation to maintain the 100 kV high tension between the two surfaces. In addition, it is foreseen to flush certain hollow support rods with CO₂. These rods have special functions such as feeding the HV to the central electrode and provide temperature measurements. A flow -diagram of the system can be seen in Fig. 3.33. It will be a single-pass system using mechanical pressure and flow regulation devices, and will maintain a constant pressure in the volumes of 1 mbar. Outlet gas from these volumes will be exhausted directly to atmosphere via bubblers.

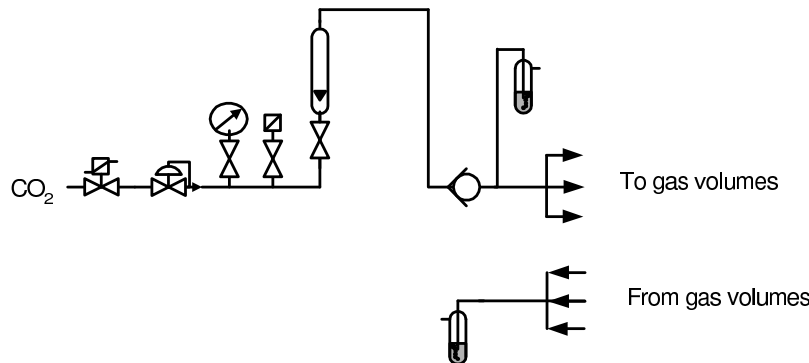


Figure 3.33: Schematics of the CO₂ purge system.

3.2.3.6 Distribution pipework

All tubes and fittings within the drift-gas system will be made of stainless steel. The tubes will be butt-welded together to reduce the possibility of contamination and leaks to a minimum. Existing gas pipes at the pit will be reused as far as possible. Table 3.6 shows an overall view of the main piping parameters. At the shielding-plug end, the tubes will be modified to link up with the new position of the distribution rack. In the experimental cavern (UX25) they will be extended into the L3 solenoid magnet and up to the

Table 3.6: Main piping parameters.

	Number of pipes	Pipe inner diameter [mm]	Pipe length [m]	Normal flow [m ³ /h]	Gas velocity [m/s]	Reynolds number	Pressure drop [mbar]
Drift volume							
SGX-plug	2	73	90	20	2.58	16 000	2.1
Plug-manifold	2	73	100	20	2.58	16 000	2.3
Manifold-TPC	8	33	20	5	3.15	8 800	1.8
CO ₂ volume							
Outer	2	20	120	2.5	1.62	6 600	0.5
Inner	2	20	120	2.5	0.39	1 600	0.04

TPC. Input pipes to the TPC will be thermally insulated, thus adding 15 mm to the diameters quoted in Table 3.6. Inlet and outlet pipes to the drift and containment volumes will be appropriately manifolded near the detector. When the detector is in the extracted position, it will be linked to the gas system by supplementary manifolds located outside of the L3 magnet to maintain the gas circulation. Unless the TPC needs to be opened, no air should enter the drift volume during any kind of manoeuvre.

4 Readout chambers and calibration

4.1 Readout chambers

It is the task of the ALICE TPC to provide, for the central detector, the main charged particle tracking capability and momentum determination, combined with particle identification via the measurement of the specific energy loss dE/dx . Large-scale TPCs have been employed and proven to work in collider experiments before [1–3], but none of them had to cope with the particle densities and fluxes anticipated for the ALICE experiment. For the design of the readout chambers, this leads to requirements that go beyond an optimization in terms of momentum and dE/dx resolution. In particular, the questions of rate capability and two-track separation in a high track density environment have to be considered.

The ALICE TPC readout chambers will be conventional multiwire proportional chambers with cathode pad readout as used in many TPCs before. Different technologies such as Ring Cathode Chambers (RCCs) or Gas Electron Multipliers (GEMs) [4] have been considered and tested in various R&D projects (see Chapter 8 for an overview), but none of them have been proven to meet the ALICE TPC requirements.

In the following, we describe the concept for the readout chambers and demonstrate how the technical solution is adapted to the requirements.

4.1.1 Mechanical structure and support

4.1.1.1 Size and segmentation of the readout plane

The overall design of the readout plane is chosen to optimize, in the high multiplicity environment of a central Pb–Pb collision, the momentum and dE/dx resolution, providing full azimuthal coverage. This leads to the requirement to maximize the total active area, leaving a minimal dead area in radial and azimuthal direction. However, for practical reasons there has to be a subdivision of the readout planes into individual modular readout chambers. The readout chambers will be mounted into the sector cutouts of the end-plates (Fig. 4.1).

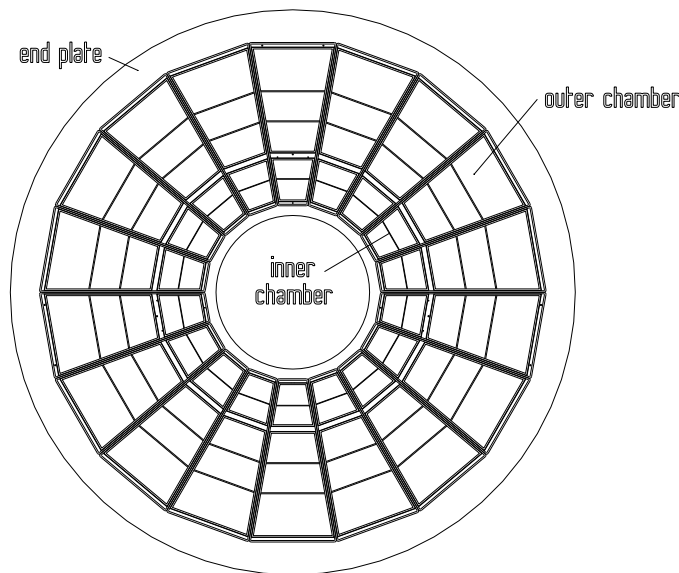


Figure 4.1: Segmentation of the readout plane.

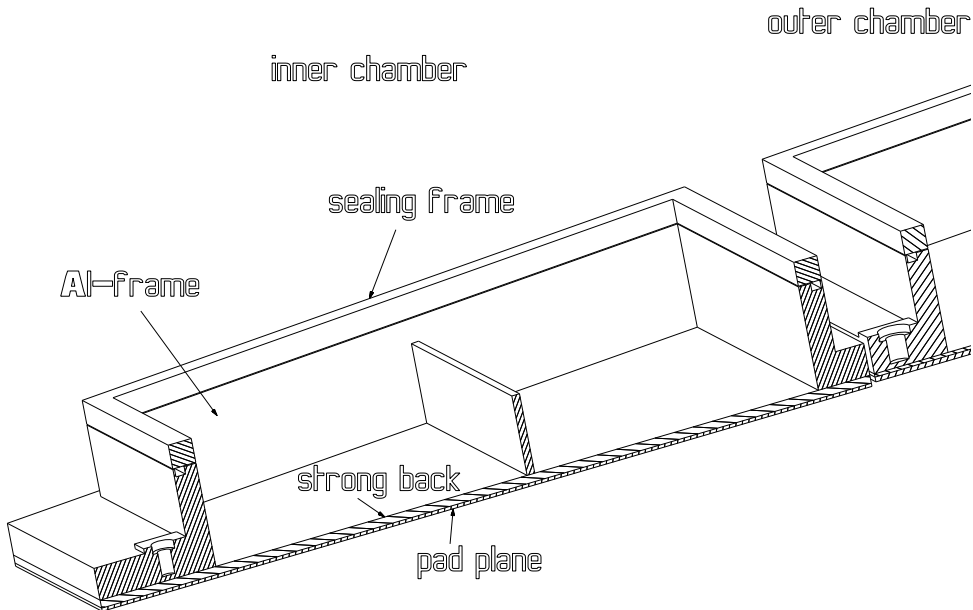


Figure 4.2: Cross-section through an inner readout chamber. Shown are the aluminium frame with the stiffening ribs, the O-ring groove and threads for the three-point suspension, the pad plane PCB, and the auxiliary strong back plate.

The azimuthal segmentation of the readout plane follows that of subsequent ALICE detectors [5], leading to 18 trapezoidal sectors, each covering 20° in azimuth.

The radial dependence of the track density leads to changing the requirements for the readout chamber design as a function of radius. Consequently, there will be two different types of readout chambers, henceforth called the *inner* and *outer* chambers, leading to a radial segmentation of the readout plane. This decision is supported by the ease of assembling, handling and integrating two smaller types of readout chambers compared to one large one, covering the full radial extension of the TPC.

The dead space between neighbouring readout chambers can be minimized by a special mounting technique (described in Section 4.1.5) by which the readout chambers are attached to the end-plate from inside the drift volume.

The inner and outer readout chambers are radially aligned, again matching the acceptance of the following detectors. The active radial length varies from 84.1 cm to 132.1 cm (134.6 cm to 246.6 cm) for the inner (outer) readout chambers. The dead space between two adjacent chambers in the azimuthal direction is 27 mm. This includes the width of the wire frames of 12 mm on each chamber (see below) and a gap of 3 mm between two chambers. The total active area of the ALICE TPC is 32.5 m².

4.1.1.2 Mechanical structure of the readout chambers

Fig. 4.2 shows a cross-section of a TPC readout chamber. A readout chamber consists of three main components: the pad plane made of a multilayer printed circuit board (PCB), an additional *strong back* plate made of fibreglass-epoxy, and a trapezoidal aluminium frame. To minimize mechanical stress to the readout chambers and the end-plate, a three-point mounting and a stressfree seal to the end-plate was chosen, as described in Section 4.1.5.

The aluminium frame provides the overall mechanical stability of the readout chambers. It is reinforced by stiffening ribs to prevent deformation from gravitational forces and wire tension. The result of a finite element calculation of the outer chambers is shown in Fig. 4.3. Deformations are largest in *z*-direction, but not exceeding 25 μm. They are hence smaller than the expected wire sag caused by electrostatic forces (see Section 4.1.3).

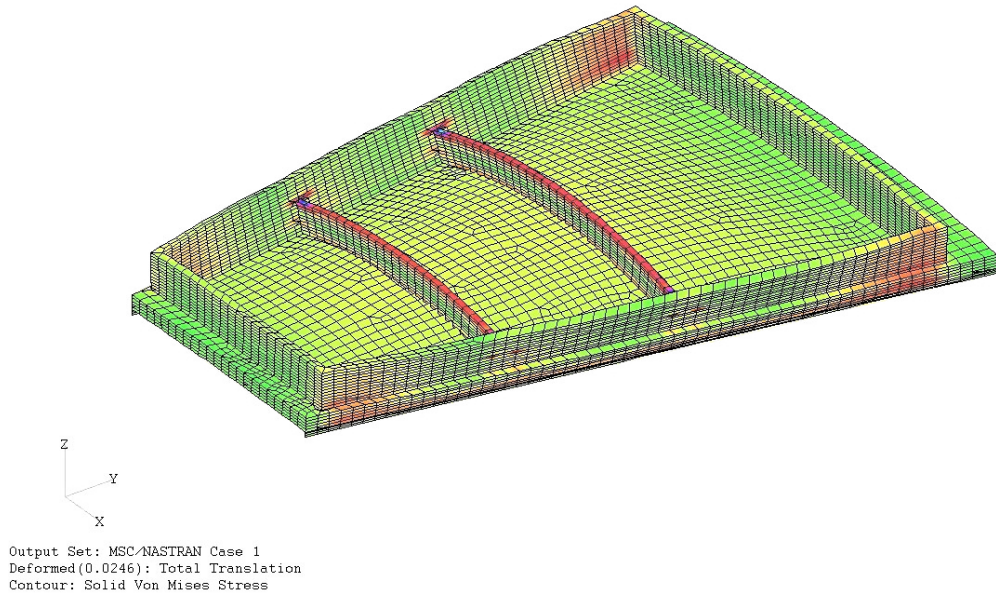


Figure 4.3: Finite element calculation of the deformation of the outer chamber caused by the wire tension. The maximum deformation is $25 \mu\text{m}$.

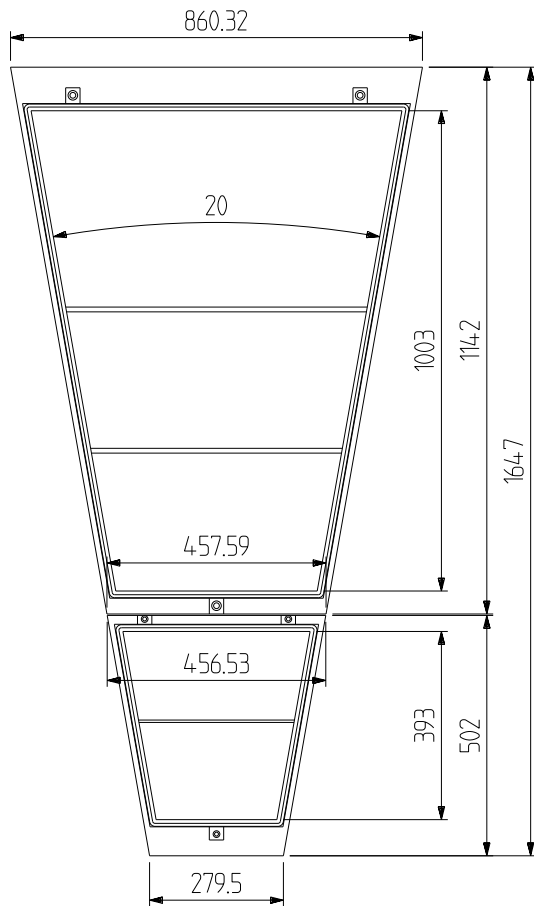


Figure 4.4: Overall dimensions of the ALICE TPC readout chambers (in mm).

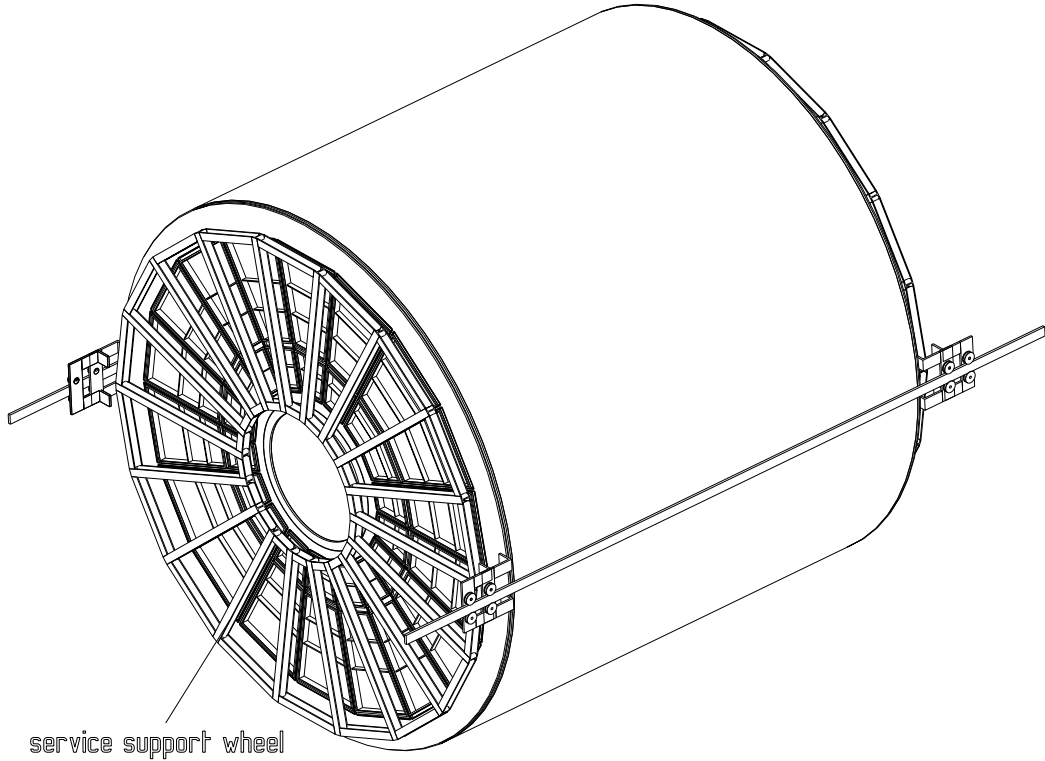


Figure 4.5: Service support wheel in front of the TPC.

The pad plane consists of a multilayer PCB, with the readout pad pattern exposed to the drift volume. The signals induced on the pads are read out on the rear side of the pad plane (see Section 4.1.4). The thickness of the pad plane PCB is 2 mm. The geometrical accuracy of the pad structure is $50 \mu\text{m}$, which can be achieved using glass masks for the PCB etching process [6]. The multilayering technique for the pad plane PCB allows the through-plated holes to be displaced in the different layers to avoid leaks. The *strong back plate* (3 mm thickness) is glued on top of the pad plane PCBs, for added mechanical stiffness of the sandwich structure. This also improves gas tightness, since the strong back covers all the through-plated holes, leaving only cut-outs for the transfer points to the front-end electronics (see Section 4.1.4).

The assembly and mechanical tolerances of the ALICE TPC readout chambers, staying well below $50 \mu\text{m}$, are in line with similar designs used in other TPCs [1, 2, 6, 7]. The weight of one inner (outer) readout chamber is 12 kg (32 kg). The overall dimensions of the readout chambers are shown in Fig. 4.4.

4.1.1.3 Service support wheel

To relieve the readout chambers and the end-plate from the stress of gravitational forces caused by the readout electronics and services, a so-called service support wheel is mounted in front of each of the TPC end-plates (see Fig. 4.5 and Section 4.1.4). It is made of aluminium I-beams, designed to withstand a stress of 200 kg/m^2 . The service support wheel has a mass of 300 kg and is suspended on the same rail system that also supports the TPC. A ‘soft’ connection is made between the end-plate and the service support wheel to avoid any additional mechanical stress on the end-plate. The design of the service support wheel allows individual readout chambers to be exchanged *in situ*.

4.1.2 Wire planes and readout pads

Charged particles traversing the TPC volume ionize the gas along their path, liberating electrons. These electrons drift towards the end-plates of the TPC. The primary electrons by themselves do not induce a

sufficiently large signal in the cathode segments (*readout pads*). The necessary signal amplification is provided by avalanche creation in the vicinity of the anode wires. The two-dimensional segmentation of the cathode plane provides the measurement of many individual space points per particle track in the $r\text{-}\phi$ -plane. The additional measurement of the drift time of each of the pad signals allows a three-dimensional reconstruction of the particle track [8].

4.1.2.1 Wire planes

The ALICE TPC readout chambers employ a scheme of wire planes commonly used in a TPC, i.e. a grid of anode wires above the pad plane, a cathode wire grid, and a gating grid. All wires run in the azimuthal direction. Since the design constraints are different for the inner and outer chambers (see below), their wire geometry is different, as shown in Fig. 4.6. The gap between the anode wire grid and the pad plane is 3 mm for the outer chambers, and only 2 mm for the inner chambers. The same is true for the distance between the anode wire grid and the cathode wire grid. The gating grid is located 3 mm above the cathode wire grid in both types of chambers. The anode wires and gating grid wires are staggered with respect to the cathode wires. Henceforth we abbreviate the wire geometry of the inner chamber by (2-2), and that of the outer chamber by (3-3).

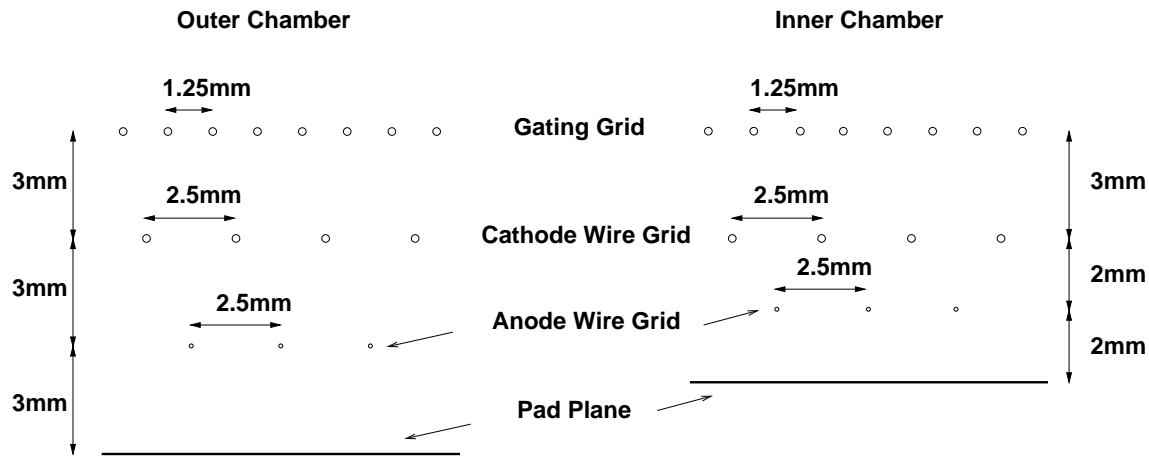


Figure 4.6: Wire geometry of the ALICE TPC outer (left) and inner (right) readout chambers.

Anode wire grid

Because of the high particle multiplicity and the relatively large gas gains required for the readout chambers (see below) a small anode wire pitch was chosen for the ALICE TPC to minimize the accumulated charge per unit length of the anode wire and hence the risk of rate-induced gas gain variations. This led to the choice of a 2.5 mm pitch for the anode wires (see also Section 4.1.3). Since the anode wires are not read out, there are no field wires in between them to prevent crosstalk between adjacent anode wires. Furthermore, field wires would reduce the signal coupling to the pads, as they pick up a significant fraction of the signal [9]. The absence of field wires also considerably reduces the mechanical forces on the wire frames. However, a chamber without field wires requires a somewhat higher voltage to achieve the required gas gain, as shown in Section 4.1.3.

Cathode wire grid

The cathode wire grid separates the drift volume from the amplification region. A large amount of the ions produced in the amplification avalanche are collected at the cathode wires without causing a noticeable reduction in electron transmission. The cathode wire pitch is 2.5 mm.

Gating grid

The gating grid is located above the cathode wire grid, with alternate wires connected together electrically. In the open gate mode, all the gating grid wires are held at the same potential V_G , admitting electrons from the drift volume to enter the amplification region. In the absence of a valid trigger, the gating grid is biased with a dipolar field $V_G \pm \Delta V$, which prevents electrons from the drift volume from entering the amplification region. This considerably reduces the integral charge deposit on the anode wires.

In addition, the closed gate stops ions created in the avalanche processes of previous events from drifting back into the drift volume. This is important because escaping ions accumulate in the drift volume and can cause severe distortions of the drift field (see Section 7.3.1.2). The goal is therefore not to increase the ion charge density above that created by primary ionization. The resulting requirement is that the ion leakage from the amplification region has to be less than 10^{-4} . To achieve an electron transparency close to 100% in the open mode while trapping ions and electrons in the closed mode, the offset and bias potentials of the gating grid have to be carefully adjusted (see Section 4.1.3). On the other hand, any ionization produced by particles traversing the gap between the gating grid and pad plane will unavoidably be amplified at the anode wires and thus contribute to the integral charge accumulation¹. To minimize this effect, the gap between the gating and cathode wire grid is only 3 mm, sufficient to trap the ions within a typical gate opening time of 100 μs (Section 4.1.3). To keep the alternating bias voltages low, the pitch between the gating grid wires is 1.25 mm.

Table 4.1: Wire parameters.

	Anode wires	Cathode wires	Gating grid wires
Material	Au plated W	Cu/Be	Cu/Be
Diameter	20 μm	75 μm	75 μm
Stretching force	0.45 N	1.2 N	1.2 N
Length (inner)	27 – 44 cm	27 – 44 cm	27 – 44 cm
Length (outer)	45 – 84 cm	45 – 84 cm	45 – 84 cm
Total number (inner)	200	201	400
Total number (outer)	456	457	912

Wire diameter, length, material and stretching force

The wire length is given by the overall detector layout and varies from 27 cm to 44 cm in the inner chambers, and from 45 cm to 84 cm in the outer chambers.

Owing to their superior strength, gold-plated tungsten wires are preferable to copper-beryllium wires (an alloy of 98% Cu and 2% Be). However, tungsten has a 4.1 times shorter radiation length and a 2.6 times larger Z than copper. Tungsten is, therefore, used only for the thin anode wires, whilst the thicker cathode and gating grid wires will be made of copper-beryllium.

¹The contribution of direct radiation to the integral charge accumulation is of the order of 10%, see Section 7.2.2.

At constant potential, the gas gain increases with decreasing anode wire diameter. Thus, a small anode wire diameter is preferred. However, electrostatic and gravitational forces cause the anode wires to sag, leading to gas gain variations along the wire. The electrostatic sag is approximately proportional to the square of the length of the wire, and inversely proportional to the stretching force, whilst the gravitational sag depends on the density of the wire material. Therefore, the wires need to be mechanically strong enough to withstand the required stretching forces. We have chosen for the anode wires a diameter of $20\ \mu\text{m}$ and a stretching force of $0.45\ \text{N}$. The cathode and gating grid wires have a diameter of $75\ \mu\text{m}$ and a stretching force of $1.2\ \text{N}$. The wire parameters are summarized in Table 4.1. For a computation of the resulting wire sag and gain variations see Section 4.1.3.

Wire frames

The space taken by the attachment of the wires along the edges of the readout chambers inevitably leads to insensitive regions. Therefore, the wire frames should be built as compact as possible. On the other hand, they must provide sufficient room for proper gluing and reliable electrical contact of the wires. Finally, the wire frames themselves and their attachment to the aluminium frame of the readout chamber have to be mechanically strong enough to not deform under wire tension. Several different solutions have been proven to work for TPC readout chambers in the past.

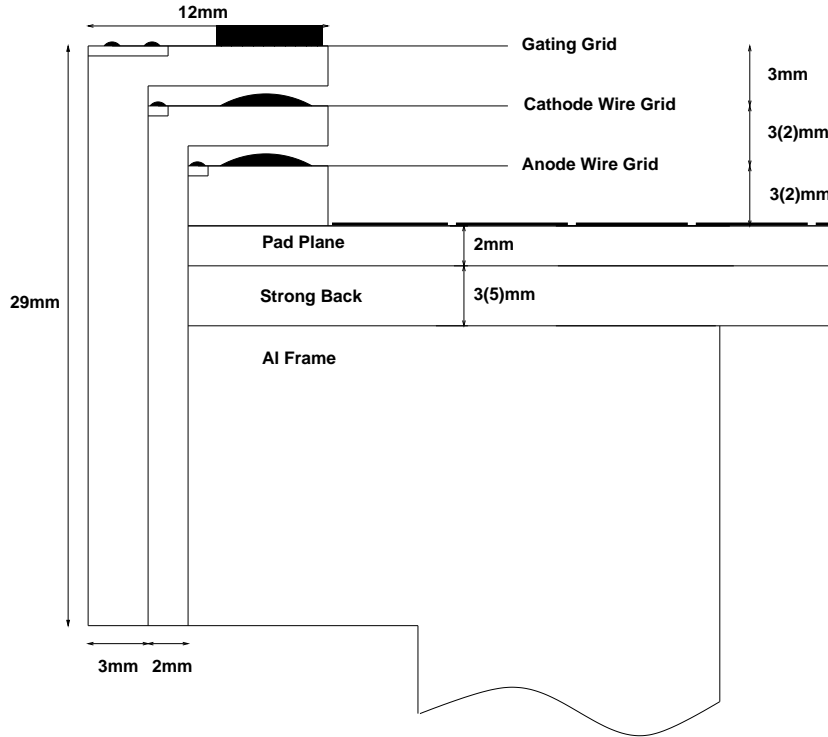


Figure 4.7: Wire fixation in the outer readout chamber (dimensions for the inner readout chamber are in parentheses). The frames are made of fibreglass-epoxy.

The wire frames for the ALICE TPC readout chambers are shown in Fig. 4.7. The positions of the anode wire grid and the cathode wire grid will be adjusted with respect to the pad plane surface to minimize gas gain variations. Displacements of the gating grid give rise to distortions of the drift field.

It will therefore be aligned with respect to the aluminium frame of the readout chamber via an external reference (granite table). This way, the position of the gating grid can be surveyed after integration of the readout chambers into the end-plate (see Section 4.1.5). Based on experience with existing TPC experiments employing similar readout designs [1, 2, 6, 7], a precision of $20 \mu\text{m}$ can be achieved for positioning the wires.

4.1.2.2 Optimization of the pad layout

Moving from the anode wire towards the surrounding electrodes, positive ions, created in an avalanche process, induce a positive signal on the pad plane. A very precise measurement of the location of the avalanche can be obtained if the induced signal is distributed over several adjacent readout pads (charge sharing), using an appropriate centre-of-gravity algorithm. The position of the particle track in the drift direction can be determined by sampling the time distribution of each pad signal. The resulting two-dimensional pulse height distribution in pad-time space is called a *cluster*.

In the following, we present the optimization of the readout pad design. The emphasis was put on the question of occupancy, the minimization of which was the major aspect during the optimization procedure. Momentum and dE/dx resolution, as will be shown below, turn out to be widely independent of the actual pad shape, as long as the total number of readout channels and the full coverage of the readout plane are preserved.

Pad response function

The pulse height on a given pad represents the (time-dependent) integral of the induced charge distribution over the pad area (see Section 7.2). The relative pulse height distribution of signals on adjacent pads, induced by a point-like avalanche, is called the pad response function (PRF). Whilst the shape of the induced charge density distribution depends only on the wire geometry and not on the shape and size of the readout pads, the PRF depends on both, because the pad geometry defines the limits of the integration of the induced charge distribution in two dimensions. In the following, the pad length l is the extension of a single pad in the radial direction, and the pad width w its extension in azimuth (Fig. 4.8).

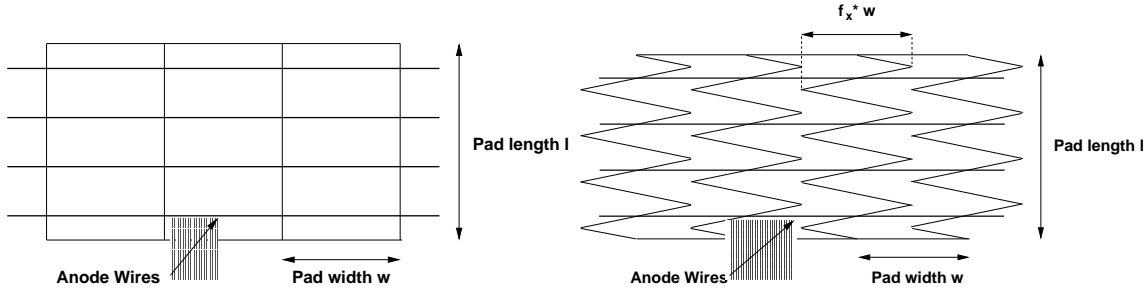


Figure 4.8: Definition of pad width w and pad length l for rectangular pads (left panel) and displaced chevron pads with an overlapping factor $f_x = 1$ (right panel). Also shown is the position of the anode wires.

The PRF can be calculated in the following way (see also Section 7.2):

$$\text{PRF}(x, y) = \int_S Q(x', y') dS, \quad (4.1)$$

where S is the pad area and $Q(x', y')$ is the induced charge distribution, which is determined by the wire geometry [10]. The integral in (4.1), however, depends on the size and the shape of the pads. In addition

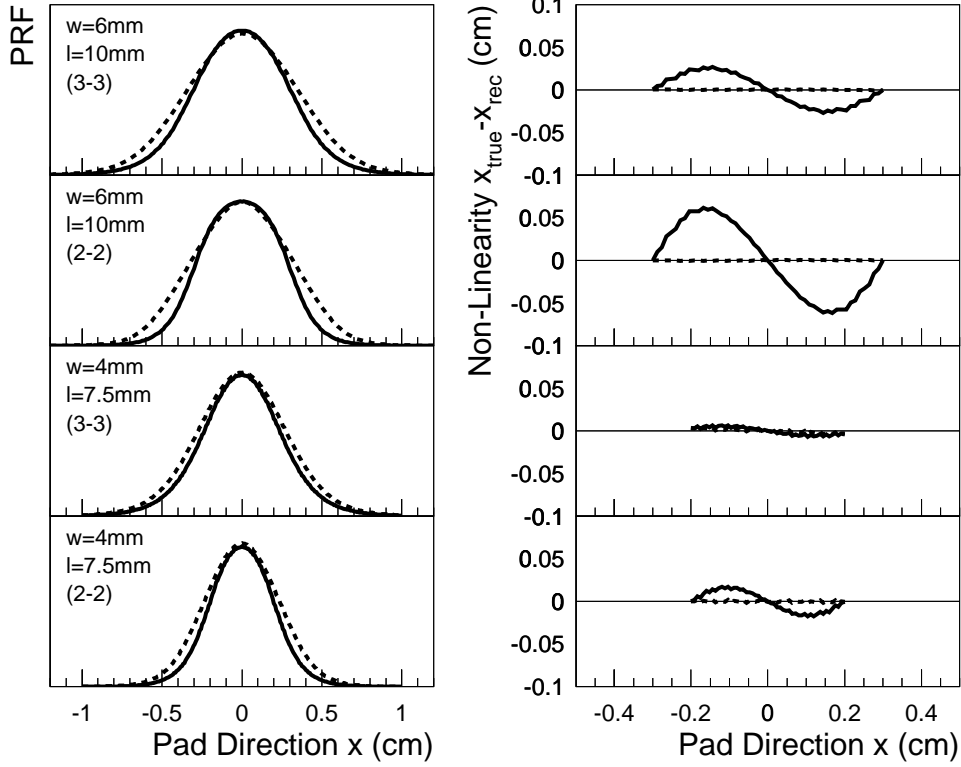


Figure 4.9: Left panel: PRF for $6 \times 10 \text{ mm}^2$ and $4 \times 7.5 \text{ mm}^2$ pads and for the (2-2) and (3-3) wire geometry. Right panel: Non-linearity $x_{\text{true}} - x_{\text{rec}}$ as a function of the avalanche position x along the wire. Solid lines: rectangular pads; dashed lines: displaced chevron pads with $f_x = 1$.

to rectangular pads, alternative pad shapes, such as chevrons [11], have also been used in TPC readout chambers [7]. The considerations for the proper choice of the PRF are the following:

- The signal should be spread over two or three adjacent pads to allow the centre of the distribution to be determined with a high resolution. If more than four pads receive a signal, the resolution generally suffers from a low signal-to-noise ratio.
- The pad response should be linear. Non-linearity is defined as the difference between the true position and the reconstructed position of the avalanche $x_{\text{true}} - x_{\text{rec}}$.

The PRF has been calculated for different pad and wire geometries by evaluating Eq. (4.1), using the parametrization from Ref. [10] for the induced charge distribution $Q(x', y')$. The results are shown in Fig. 4.9 for $6 \times 10 \text{ mm}^2$ and $4 \times 7.5 \text{ mm}^2$ pads and for the (2-2) and (3-3) wire geometry. The calculations are made for rectangular pads (solid lines) and for displaced chevron pads [11] with an overlapping factor $f_x = 1$ (dashed lines). The two aforementioned conditions are met if the pad width w is two times larger than the gap between the anode wires and pad plane [12]. The non-linearity is smaller for chevron pads, but still negligible for rectangular pads. On the other hand, chevron pads give rise to a wider PRF, which is unwanted for reasons of occupancy (see below). We have therefore chosen rectangular pads for the ALICE TPC readout chambers; with a gaussian fit to the calculated PRFs we obtain $\sigma_{\text{PRF}} = 2 \text{ mm}$ for the 4 mm wide pads in the inner chamber (2-2) and $\sigma_{\text{PRF}} = 3 \text{ mm}$ for the 6 mm wide pads in the outer chamber (3-3).

Cluster size

As pointed out in Section 7.2.1, the relative pad pulse height distribution is not entirely determined by the PRF, because the distribution of primary electrons arriving at the anode wires cannot be considered as point-like. Therefore, the size and shape of a cluster also depends on the diffusion in the gas, the track inclination, and $\mathbf{E} \times \mathbf{B}$ -effects in the vicinity of the anode wire [8]. The latter effect is small in the case of the ALICE TPC, because the magnetic field is relatively weak and the 90% Ne, 10% CO₂ gas mixture leads to a small $\omega\tau$ (see Section 7.1). Whilst the diffusion contribution is given by the drift length and the diffusion constant of the drift gas, the influence of the track inclination depends on the pad geometry. Since the azimuthal width of the charge distribution from an inclined track represents a projection of the track segment over the pad length, the cluster size can in principle be minimized by choosing short pads.

Similar arguments hold for the drift direction. The width of a pad signal generated by a single electron avalanche is given by the shaping constant of the front-end electronics (190 ns FWHM, see Section 5.1.1). Again, the electron distribution from an ionizing particle is broadened by diffusion and track inclination, the latter depending on the pad length.

Because of the high particle density anticipated in the ALICE TPC, the number of closely spaced tracks which tend to produce overlapping clusters in pad-time space is likely to be significant. The track density F in a given pad-time region is expressed in terms of occupancy, defined as the number of pad-time bins above a certain threshold divided by the total number of pad-time bins. Equivalently, the occupancy O is given by (see also Section 7.3.1.1):

$$O = 1 - \exp(-F \cdot s_{\text{eff}}). \quad (4.2)$$

The single-track cluster area s_{eff} is the extent of an isolated cluster in pad-time space. It can be calculated by counting the number of pad-time bins above threshold and multiplying it by the pad width and the length of one time bin (0.566 cm at a drift velocity of 2.83 cm/ μ s and a sampling frequency of 5 MHz). Note that for low track densities the occupancy depends linearly on s_{eff} , whilst the occupancy starts to saturate if the number of overlaps becomes significant (see Section 7.3.1.1).

For a given overall detector size, the track density depends on the details of the particle production cross-sections. However, the single-track cluster area s_{eff} depends on the properties of the detector. Since the unfolding of overlapping clusters usually comes at the expense of a loss in momentum and dE/dx resolution, and in the limit of very high occupancies fails completely, an optimization of the pad layout in terms of occupancy becomes necessary. The goal is to find a pad configuration for which the resulting average single-track cluster area is minimal.

To reduce the contribution from diffusion a ‘cool’ drift gas with small diffusion constants D_T and D_L in the transverse and longitudinal direction was chosen (90% Ne, 10% CO₂: $D_T = D_L = 220 \mu\text{m}/\sqrt{\text{cm}}$). This issue is discussed in Section 7.1.

For budgetary reasons, the pad size cannot be chosen arbitrarily small. As a consequence, the average pad area should not be smaller than 60 mm², leaving sufficient freedom in the choice of its aspect ratio. Therefore, a variety of different pad shapes was investigated in terms of their impact on the resulting average cluster size.

In a first optimization step, pads of approximately constant area (60–70 mm²) have been investigated. The results of a microscopic simulation (see Section 7.2.1) are shown in Fig. 4.10. The one-dimensional cluster size can be expressed in terms of the number of pads or time bins per cluster above a certain threshold. This is relevant because a minimum number of pads and time bins (typically 2–3 in each direction) is needed to provide a proper centre-of-gravity determination. This requirement is fulfilled by all pad shapes under consideration. On the other hand, if the number of pads above threshold exceeds four, as is the case for pad lengths $l > 10$ mm, the signal-to-noise ratio deteriorates². However, in view of occupancy, the cluster size in physical dimensions is relevant, and therefore the number of pads (time bins) has to be multiplied by the pad width (spatial length of a time bin). On the left panel in Fig. 4.10

²The latter argument does not hold in time direction since the signal is not integrated over the length of a time bin.

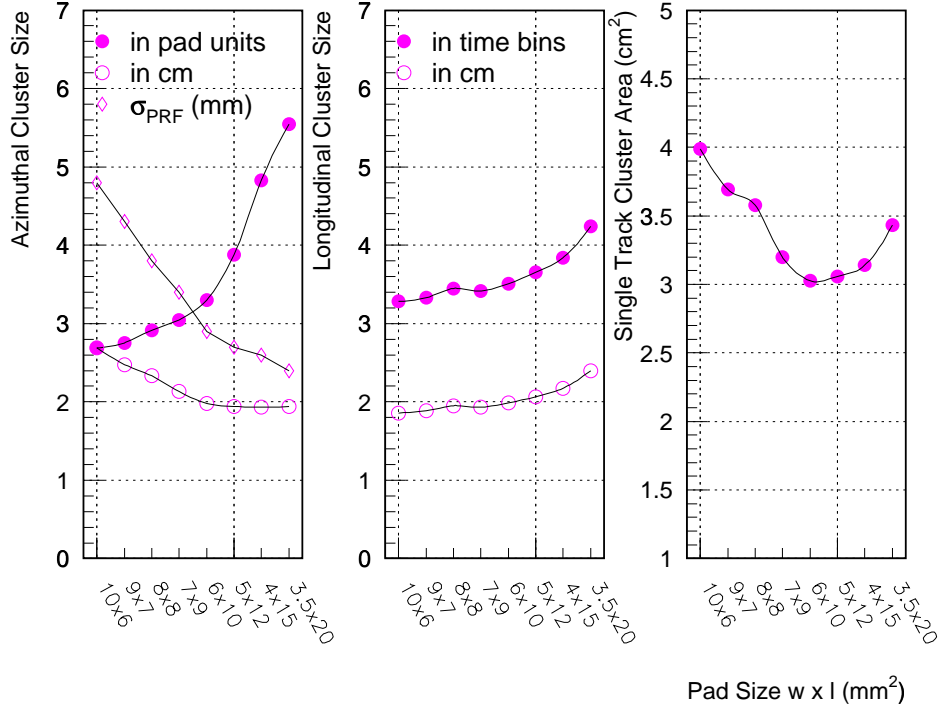


Figure 4.10: Azimuthal and longitudinal cluster size and average single-track cluster area s_{eff} for pads of approximately equal area ($60\text{--}70\text{ mm}^2$), but different aspect ratios.

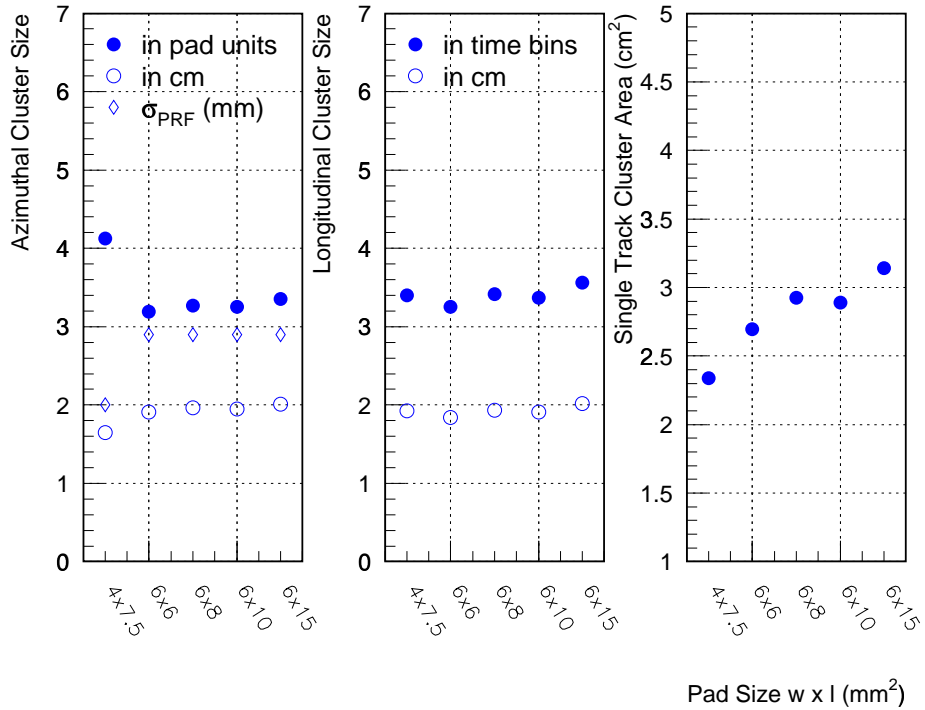


Figure 4.11: Cluster size for pads of different area and aspect ratios. The points for $4 \times 7.5\text{ mm}^2$, $6 \times 6\text{ mm}^2$, and $6 \times 8\text{ mm}^2$ are calculated for $r < 130\text{ cm}$; $6 \times 10\text{ mm}^2$ is for $130\text{ cm} < r < 200\text{ cm}$; and $6 \times 15\text{ mm}^2$ is for $r > 200\text{ cm}$.

the cluster size in the pad direction is shown. Also shown is the width of the PRF used in the calculation for the different pad shapes. The number of pads per cluster that have at least one time bin above threshold increases when the pad width decreases. However, if the number of pads is multiplied by the actual pad width, the cluster size in the pad direction increases when the pad width is increased. This is because a widening of the pads has to be accounted for by the choice of a wider PRF, which consequently leads to larger clusters. In the middle panel the same is shown for the time direction. In this case the transformation from time bins to spatial extent is trivial, because each time bin corresponds to 0.566 cm. It can be seen that the cluster size in the time direction decreases when the pads become shorter, as the projection length for inclined tracks is reduced. It should be mentioned that the projection effect in the pad direction is generally smaller than that in the time direction, because the average bending of the tracks in the magnetic field is small compared to the average polar angle.

The average single-track cluster area s_{eff} is shown in Fig. 4.10 (right panel) for different pad geometries, demonstrating a clear minimum for a pad size of $6 \times 10 \text{ mm}^2$.

The next optimization step took into account the fact that the track density is not constant throughout the TPC, but is highest at small radii. In order to improve the above results further, smaller pad sizes at small radii have been considered. In addition, a narrower PRF leads to an even smaller single-track cluster area. A PRF width of 2 mm can be obtained by choosing an anode wire to pad plane distance of 2 mm in conjunction with a pad width of 4 mm (see Fig. 4.9).

The average single-track cluster area s_{eff} in the region $r < 130 \text{ cm}$ is shown in Fig. 4.11 for a set of smaller pads. From this, the most significant improvement can be achieved with a pad size of $4 \times 7.5 \text{ mm}^2$ and an anode wire to pad plane distance of 2 mm, resulting in $\sigma_{\text{PRF}} = 2 \text{ mm}$.

On the other hand, the requirements on pad size are less stringent at the outer radii of the TPC as the overall track density decreases by $1/r^2$.³ Therefore, a pad size of $6 \times 15 \text{ mm}^2$ was chosen for radii $r > 200 \text{ cm}$.

The overall pad layout of the inner and outer chambers is shown in Fig. 4.12 and summarized in Table 4.2. The inner chambers have a pad size of $4 \times 7.5 \text{ mm}^2$. The total number of pads in the inner chamber is 5732, distributed over 64 pad rows running parallel to the wires. To minimize angular effects contributing to the cluster area and the position resolution, the pads are radially oriented according to the average local track angle. This results in a slight tilt with respect to the wire normal being a maximum of $\pm 10^\circ$ at the edges of the chamber.

The number of pads in the outer chamber is 10110, with a pad size of $6 \times 10 \text{ mm}^2$ for $r < 198.6 \text{ cm}$ (64 rows) and $6 \times 15 \text{ mm}^2$ for $r > 198.6 \text{ cm}$ (32 rows). In this chamber the pads are also oriented radially. Note that there are two different pad sizes in the outer chambers, whereas the wire geometry is the same. This is due to the fact that all pads have the same pad width and therefore the same PRF for a fixed wire geometry, whilst all pad lengths are a multiple of the anode wire pitch of 2.5 mm.

The total number of pads in the ALICE TPC is 570 312 (see Table 4.2).

Table 4.2: Readout pads.

	Pad size [mm^2]	Number of rows	Number of pads
Inner chamber ($84.1 < r < 132.1 \text{ cm}$)	4×7.5	64	5 732
Outer chamber ($134.6 < r < 198.6 \text{ cm}$)	6×10	64	6 038
Outer chamber ($198.6 < r < 246.6 \text{ cm}$)	6×15	32	4 072
TPC total		160	570 312

³Because of saturation effects the decrease in occupancy is only $\sim 1/r$ at small radii and large occupancies (see Section 7.3.1.1).

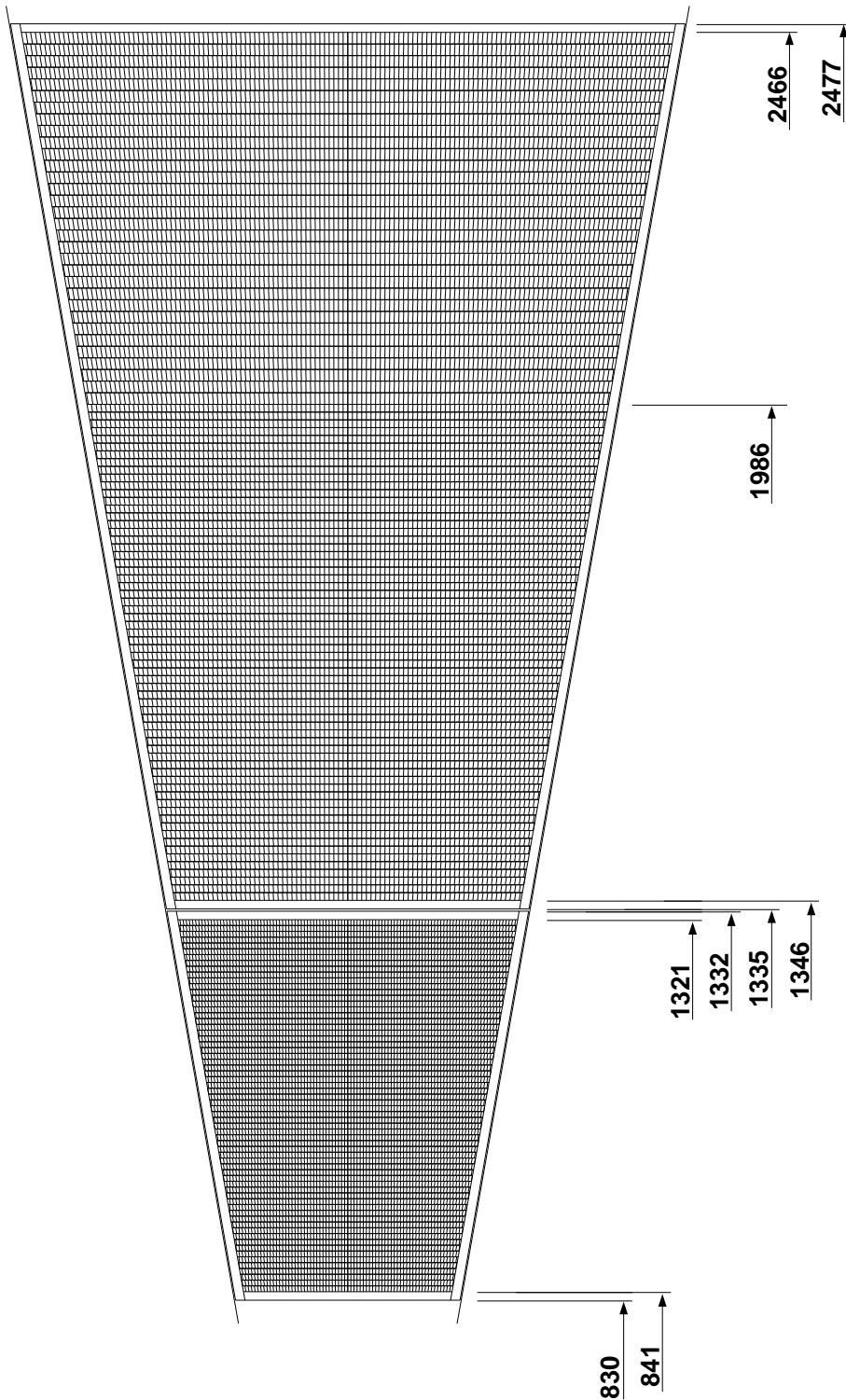


Figure 4.12: Pad layout of the ALICE TPC readout chambers. Distances from the beam axis are in mm.

4.1.2.3 Resolution and gas gain

This section addresses the impact of the chosen readout pad geometry on the performance of the TPC in terms of momentum and dE/dx resolution, with special attention to the question of gas gain.

Position and momentum resolution

At a given magnetic field B , a charged particle with transverse momentum p_t is bent along a track segment with curvature ρ , according to:

$$p_t = 0.3 \cdot \frac{B}{\rho} . \quad (4.3)$$

The nominal value of the magnetic field is $B = 0.2$ T. However, a higher field of $B \geq 0.4$ T will be used in specific physics runs to optimize the mass resolution of Υ states. The radius $R = 1/\rho$ of a track segment is determined by fitting the individual space points along the trajectory. The azimuthal position resolution of a single space point $r\delta\phi$ leads to a transverse momentum error according to Ref. [13]:⁴

$$\Delta p_t / p_t^2 = \frac{r\delta\phi}{0.3 \cdot B \cdot L^2} \sqrt{\frac{720}{N+4}} . \quad (4.4)$$

L is the total visible track length, N is the number of space points on the trajectory. Whereas B and L are given by the overall design of the ALICE TPC, the resolution $r\delta\phi$ and N are design parameters of the readout chambers. Note that Eq. (4.4) assumes that the momentum is determined in the TPC alone and that the contributions from multiple scattering and energy loss are not included here [14].

In the following we list the effects that influence the azimuthal position resolution $r\delta\phi$ [8]:

- the amount of ionization contributing to the individual space point measurements, in terms of the number of electrons n_e .
- the diffusion broadening of the electron cloud during drift, which is determined by the transverse diffusion constant D_T .
- exponential fluctuations in the gas amplification of single electrons, which effectively enhance the delocalization caused by diffusion by a factor $\sqrt{2}$.
- the nature of secondary electron production (Landau fluctuations). This contribution enters only when the track is inclined with respect to the pad orientation.
- the signal-to-noise ratio.
- effects of digitization and threshold.

Some of these contributions are related to the pad geometry. The pad length determines the total number of electrons n_e , limiting the statistical significance of the centre-of-gravity of the electron cloud. On the other hand, angular contributions are enhanced when the pad length is increased. Instead of an analytic evaluation of the resulting position resolution, a detailed microscopic simulation has been performed.

⁴The angular resolution is determined by the longitudinal position resolution δz and enters the total momentum resolution as well. However, this contribution is small and will not be discussed here.

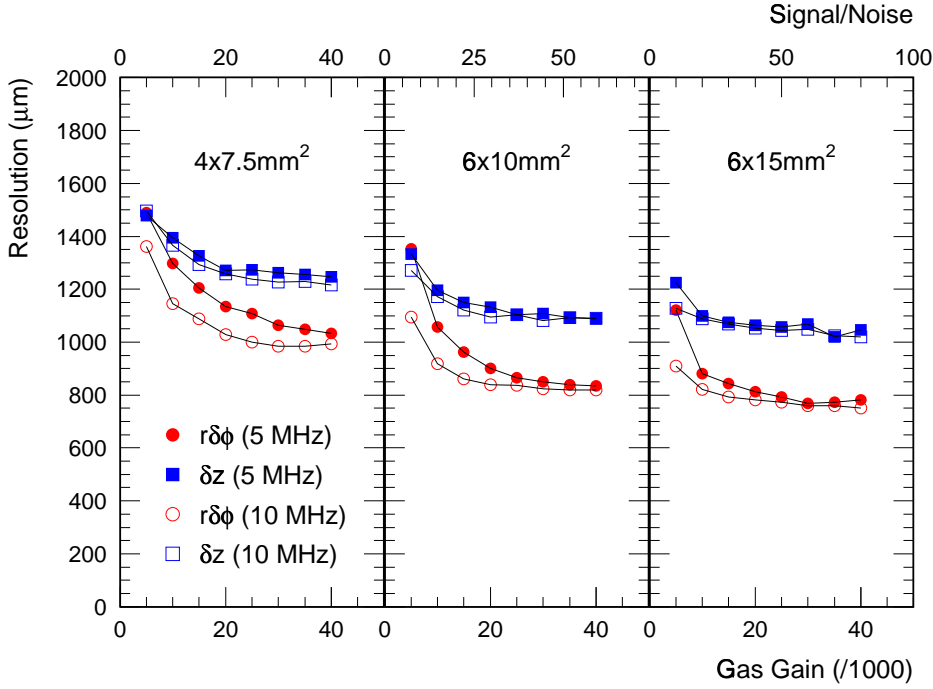


Figure 4.13: Position resolution as a function of the gas gain for the different pad sizes. The closed symbols are for a sampling frequency of 5 MHz, the open symbols are for 10 MHz.

For a given front-end noise level (here, we assume a noise level of $1000 e^-$), the overall signal-to-noise ratio⁵ depends entirely on the gas gain. In general one wishes to keep the gas gain as low as possible and it is therefore important to investigate when the position resolution no longer improves. Results from simulations with minimum ionizing particles (MIPs) are shown in Fig. 4.13 for the three different pad sizes used in the ALICE TPC. Whilst the improvement in δz , the resolution in drift direction, already saturates at relatively low gas gains, the azimuthal resolution $r\delta\phi$ still benefits from gas gains as high as 2.5×10^4 to 3×10^4 in the inner chamber, and 1.5×10^4 to 2×10^4 in the outer chamber, both corresponding to a signal-to-noise ratio of about 30. The azimuthal resolution $r\delta\phi$ is then $1100 \mu\text{m}$ in the inner chambers and $800\text{-}850 \mu\text{m}$ in the outer chambers. However, reducing the gas gain in the inner chambers from 3×10^4 to 1.5×10^4 results in a deterioration of $r\delta\phi$ of only 10%. In the drift direction, the resolution δz is $1250 \mu\text{m}$ in the inner chambers and $1100 \mu\text{m}$ in the outer chambers.

For reasons of operational safety, these gas gains are still rather high. It is, therefore, worthwhile searching for means to decrease the wire amplification without a loss in performance. For example:

- an increased sampling frequency enhances the probability for a given pad to have more time bins above threshold, and thus contribute to the centre-of-gravity calculation. This allows the gas gain to be reduced significantly, as shown in Fig. 4.13, albeit at the expense of an increased data volume.
- the signal that is induced on the pad plane corresponds only to a fraction of the total charge produced in the avalanche, the rest being induced on the surrounding wire planes. In addition, the finite shaping time of the preamp causes a loss in efficiency. Based on the experience with existing experiments, we assume that the combination of both effects reduces the signal by a factor of 5 (compare Section 7). In addition to improving the readout electronics, the pad coupling can be increased by further optimization of the wire geometry. In particular, asymmetric wire geometries offer a larger signal coupling to the pads, as discussed in Section 4.1.3.

⁵The signal-to-noise ratio for a given cluster is defined as the pulse height in the maximum pad-time bin divided by the noise level.

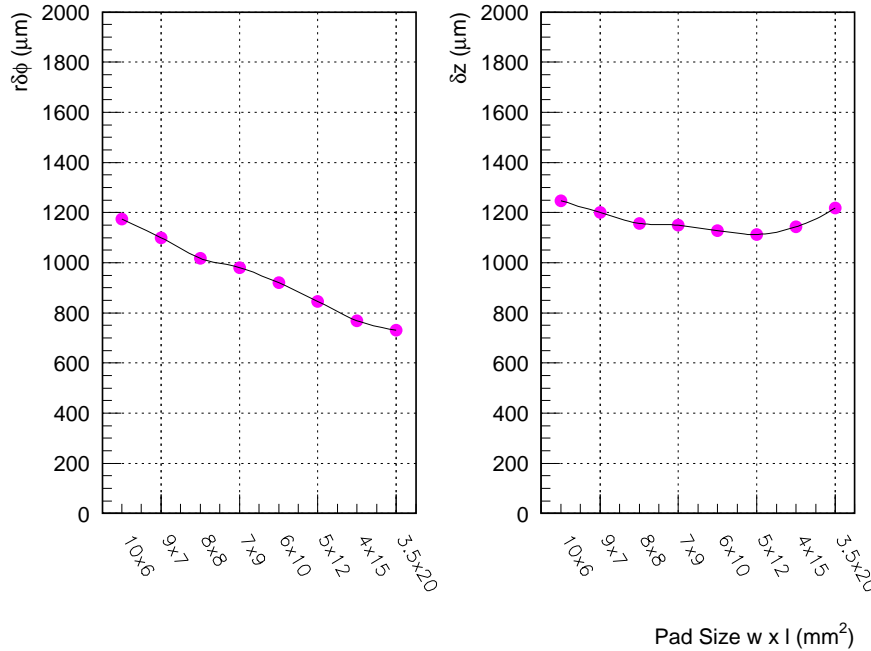


Figure 4.14: Average position resolution in azimuthal (left panel) and longitudinal (right panel) direction for different pad shapes.

Figure 4.14 shows the average position resolution for various pad shapes, calculated for a signal-to-noise ratio of 30. In the azimuthal direction, the resolution visibly improves when the pad length is increased. This is a consequence of the increasing amount of ionization contributing to the measurement. In the drift direction the situation is different: the resolution δz levels off at around $1100 \mu\text{m}$, and even deteriorates when using the longest pads. This is because the gain in ionization from longer pads is offset by a stronger influence of angular effects. Again, this behaviour reflects that angular contributions are much more pronounced in the drift direction than in the azimuthal direction.

Even though the azimuthal position resolution is best for the longest pads, this is not necessarily true for the transverse momentum resolution, because shorter pads allow more single point measurements along the track (compare Eq. (4.4)). This is demonstrated in Fig. 4.15, where the transverse momentum resolution $\Delta p_t/p_t^2$ is plotted as a function of p_t for different pad sizes ($B = 0.2 \text{ T}$). In fact, for very small p_t the resolution is worst for the longest pads, because low p_t tracks have the largest deflection and hence are more sensitive to angular effects. However, multiple scattering dominates the momentum resolution for low p_t tracks. At $p_t \geq 0.5 \text{ GeV}/c$ the contribution of the single point resolution saturates at $\Delta p_t/p_t^2 \approx 1\% (\text{GeV}/c)^{-1}$ for all pad sizes under consideration, whilst at $p_t = 1.0 \text{ GeV}/c$, the contributions of the position resolution and multiple scattering are approximately comparable.

dE/dx resolution

Similar to momentum resolution, dE/dx resolution is also not expected to depend drastically on the pad length (sampling thickness), as long as the total length of the measured track, i.e. the product of the pad length l and the number of points N per track, is constant. Lehraus [15] proposed an empirical relationship between dE/dx resolution and N and l :

$$\frac{\Delta dE/dx}{dE/dx} = \frac{13.5}{2.35} (N \cdot l)^{-0.37}. \quad (4.5)$$

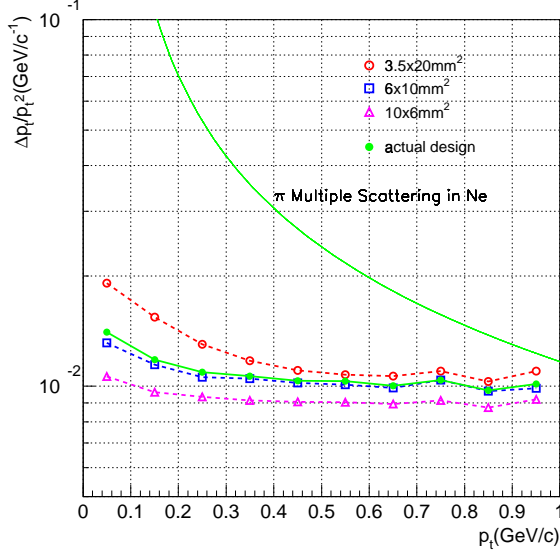


Figure 4.15: Transverse momentum resolution for different pad shapes ($B = 0.2$ T).

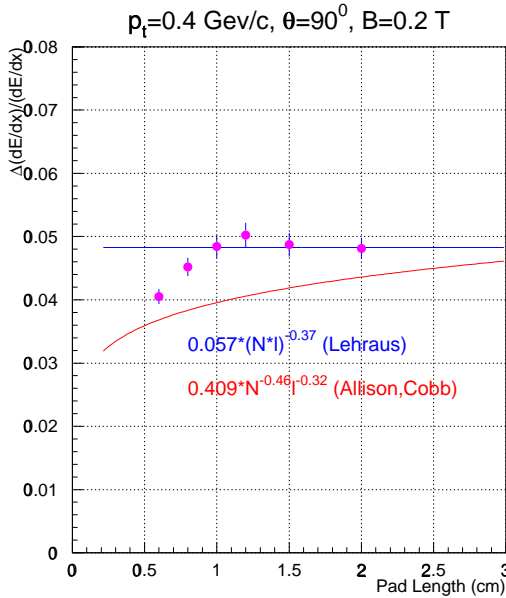


Figure 4.16: dE/dx resolution for isolated tracks in the ALICE TPC as a function of the pad length (sample thickness).

Allison and Cobb [16] found a different parametrization, which slightly favours shorter pads and hence more individual measurements for a given track length at atmospheric pressure:

$$\frac{\Delta dE/dx}{dE/dx} = \frac{0.96}{2.35} N^{-0.46} l^{-0.32}. \quad (4.6)$$

Our results from microscopic simulations are in good agreement with these parametrizations, as demonstrated in Fig. 4.16. The dE/dx resolution for a 0.4 GeV/c MIP, emitted at a polar angle of 90° , is shown for different pad sizes. Assuming that all points on a track are found and a truncation of the upper 30% is applied, a dE/dx resolution of 5% for isolated tracks can be achieved in the ALICE TPC.

4.1.3 Electrostatic calculations

In this section, a detailed evaluation of the electrostatic properties of the ALICE TPC readout chambers is presented. It addresses the question of optimization of TPC readout chambers in more general terms, however, showing that the baseline design presented in Section 4.1.2 is well suited to meet the requirements of the ALICE TPC. All electrostatic simulations have been performed in the framework of the GARFIELD package [9].

4.1.3.1 Layout

Various kinds of readout chambers have been considered for the ALICE TPC, all of which feature readout of a cathode plane with a two-dimensional segmentation into individual readout pads (see Chapter 8 for more information). In the following we will assume flat pads. Other shapes such as ring cathodes have been considered but are not part of the current baseline design.

We have, as a baseline solution, opted for amplification on anode wires. It is customary to sandwich the anode wires between the pad plane and a cathode wire plane which is held at the same potential as the pads. Such a cathode wire plane enhances the gain, absorbs some of the ions produced in the avalanches, and decouples the adjustment of the field in the amplification region from the field in the drift volume. It does not cause a loss in electron efficiency.

All TPC readout schemes contain a gate which prevents electrons from entering the amplification region outside a gating time window. The gating grid has, due to the presence of the cathode wires, little influence on the optimization of the readout part proper. However, a careful adjustment of the gating grid potentials is mandatory to obtain a smooth transition between drift volume and amplification region, and to meet the requirements in terms of electron and ion transparency.

We will, throughout, express potentials relative to the pad potential (i.e. ground).

4.1.3.2 Parameter space

Assuming amplification is achieved on anode wires, the following parameters determine the layout of a TPC readout chamber:

- The gas used in the chamber and the drift field.
- Pad shape and size.
- Wire diameter, wire length, wire material, and tension.
- Anode wire pitch, distance to pads, and voltage.
- Cathode wire pitch, distance to pads, and voltage.
- Gating grid wire pitch, distance to pads, and voltage.
- Presence or absence of field wires between individual anode wires.

The baseline design to which we refer below is described in Section 4.1.2. All the calculations were made assuming 20 μm diameter W anode wires stretched with 0.45 N, and 75 μm diameter Cu/Be cathode and gating grid wires stretched with 1.2 N.

The drift lines of ionization electrons to the inner and outer readout chamber are shown in Fig. 4.17.

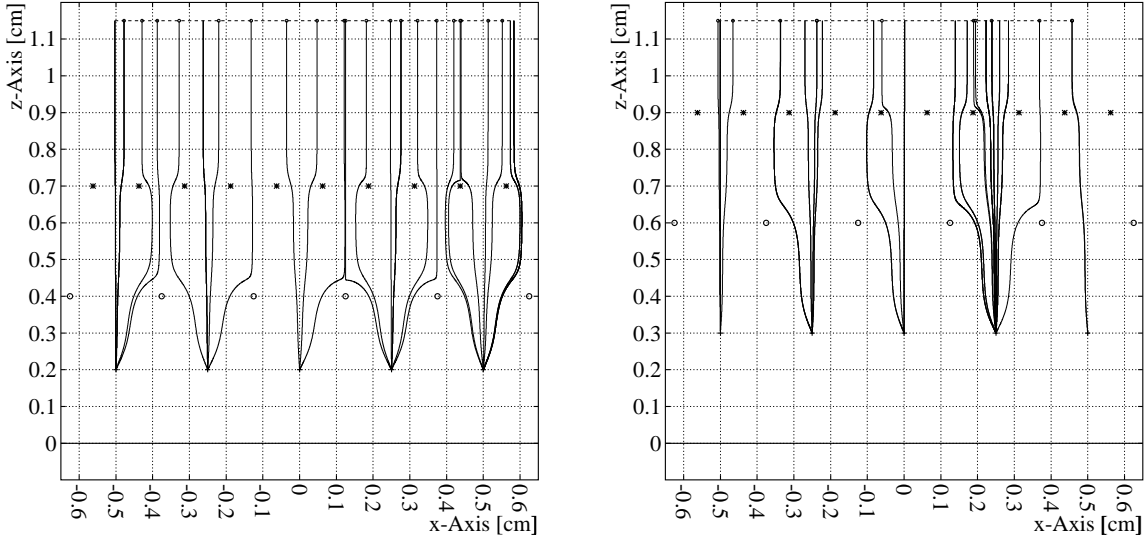


Figure 4.17: Drift lines of electrons from a track in the inner (left panel) and outer (right panel) readout chamber.

4.1.3.3 Optimization goals

- **Amplification:** To ensure a signal-to-noise ratio of about 20–30, the amplification should be of the order of 1.5×10^4 to 2×10^4 . (see Section 4.1.2.3).
- **Isochrony:** The electron collection isochrony should be smaller than the arrival time spread caused by the diffusion and track inclination.
- **Signal collection:** In order to have a high signal-to-noise ratio with the given amplification, which is desirable in order to reduce the risk of wire ageing and rate-induced gain variations, as large a part as possible of the induced charge over a typical preamplifier/shaper integration time of 200 ns should flow into the readout pads.
- **Signal shape:** The signal should not display secondary peaks caused by the arrival of ions on electrodes.
- **Gas gain homogeneity:** Wire displacements towards and away from the pad plane, mainly caused by the electrostatic force, result in gain inhomogeneities. Such deflections should be limited so that the gain is homogeneous at a level $\leq 5\%$.
- **Gate transparency:** Ionization electrons produced in the drift region should be able to enter the readout chambers when the gate is open, but should be stopped when the gate is closed. The gate should not let more than one ion per avalanche enter the drift region.

4.1.3.4 Choice of parameters

Gas and drift field

The gas choice is made primarily on the basis of ionization properties and diffusion in the drift volume. The ALICE TPC drift gas is a mixture of 90% Ne and 10% CO₂. This gas has, for drift fields in the range of 200–400 V/cm, a drift velocity of 1.35–2.83 cm/ μ s, and an approximately equal transverse and longitudinal diffusion constant of 210–220 μ m/ $\sqrt{\text{cm}}$. The presence of a 0.4 T magnetic field parallel

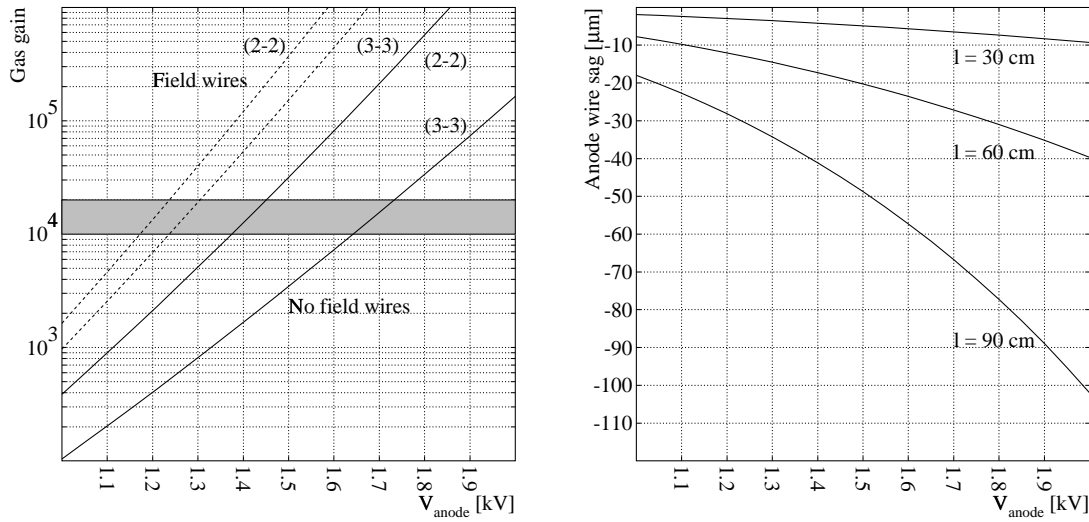


Figure 4.18: Left: Gas gain vs. anode wire voltage in the ALICE TPC readout chambers. The grey band indicates the desired amplification. The accuracy of the gain calculations is of the order of 20%, resulting in a potential uncertainty of ± 30 V. Right: Sag of the anode wires as a function of V_{anode} , for different wire lengths.

to the electric field, reduces the transverse diffusion by only 4%. Ne^+ ions have a mobility of 3.9–4.1 cm²/Vs in this gas mixture for drift fields ranging from 200 to 400 V/cm [17, 18].

The use of a gas mixture with higher primary ionization appears attractive, because this would potentially lead to a better spatial resolution at lower gas gains. Replacing neon by argon makes the gas 20% faster at 400 V/cm, increases the diffusion by 10%, and more than doubles the number of ionization electrons per cm. However, the ion mobility in an argon-based mixture is less than 40% of that in a neon-based mixture, which would considerably aggravate the charge accumulation in the drift volume. Neon is also preferable because of its longer radiation length: 3.5×10^4 cm compared to 1.2×10^4 cm for argon, the use of argon would therefore lead to a deterioration of the momentum resolution due to multiple scattering.

The gas mixture does not contain organic components, which should make the chamber less prone to ageing than mixtures that contain, for example, methane or ethane as a quencher [8].

The drift field is chosen to be 400 V/cm, in order not to exceed a drift time of 90 μs for electrons starting from the central electrode. This is well matched with the gate opening time of 100 μs . Diffusion spreads the electrons laterally over 3.4 mm and causes an arrival time spread of 120 ns. Ions need up to 160 ms to reach the central electrode.

Pad shape and size

The pad shape is chosen to minimize the occupancy and to maximize the momentum and dE/dx resolution within a reasonable budget (Section 4.1.2). ALICE has chosen for the pads a size of 4×7.5 mm² in the inner chambers, and 6×10 mm² and 6×15 mm² in the outer chambers. The pad shape, however, has a negligible impact on the electrostatic properties of the readout chamber.

Anode wire voltage

A given gas gain can be achieved by the choice of the proper anode wire voltage. Apart from the anode wire voltage and diameter, the gain also depends on the gas, the presence or absence of field wires, and on

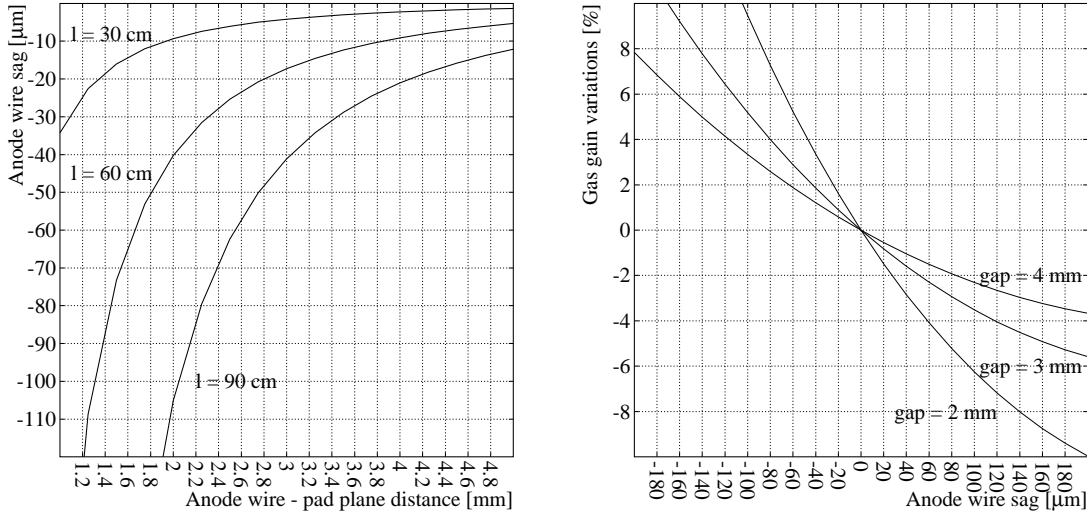


Figure 4.19: Left: Anode wire sag as a function of anode wire to pad plane distance for an anode wire voltage of 1450 V. Right: Sensitivity of the gain to electrostatic sag, computed for three different anode wire to cathode distances, called gap in the figure. Negative sags are towards the pad plane. The anode wire voltage is adjusted to a gas gain of 2×10^4 .

the distances between the anode wires and the neighbouring electrodes. However, the applicable anode wire voltage reaches a limit when electrostatic displacements of the anode wires exceed the tolerances.

The highest potentials required to achieve a given gain are needed in chambers without field wires, with a maximal distance between anode wires and pads, and with minimal anode wire pitch. The ALICE TPC readout chambers (Section 4.1.2), which do not have field wires, are expected to reach a gas gain of 2×10^4 at a voltage of 1450 V for the inner chambers (2-2), and 1720 V for the outer chambers (3-3) (see Fig. 4.18, left panel). The increase of the anode wire sag as a function of the anode wire voltage and for different wire lengths is shown in Fig. 4.18 (right panel) for the (3-3) geometry of the outer chamber (see also next paragraph).

Anode wire to pad plane distance

The distance between the anode wires and the pad plane is constrained by the desired pad response function (see Section 4.1.2). The distance should also be sufficiently small to achieve the required gain, yet large enough to ensure that the gain variations due to electrostatic sag remain within tolerance. We will, in this paragraph, assume that the distance between the anode wires and the pad plane is the same as the distance between the anode wires and the cathode wires. The implications of an asymmetric layout are discussed in the next paragraph.

The anode wire sag as a function of the distance between the pad plane and anode wires is shown in Fig. 4.19 (left panel) for different wire lengths and the operational voltage of the inner chamber (1450 V). Thus, the expected anode wire sag in the inner chamber varies between $10\text{ }\mu\text{m}$ and $35\text{ }\mu\text{m}$. In the outer chamber, the anode wire sag varies between $25\text{ }\mu\text{m}$ and $70\text{ }\mu\text{m}$ (Fig. 4.18, right panel). The relative gain variation as a function of the wire sag for different anode wire to pad plane distances is shown in Fig. 4.19 (right panel).

The anode wire voltage is adjusted to a gas gain of 2×10^4 in all cases. The above mentioned anode wire sags for the inner and outer readout chambers result in a relative gain variation $\leq 4\%$, hence staying well within the requirements.

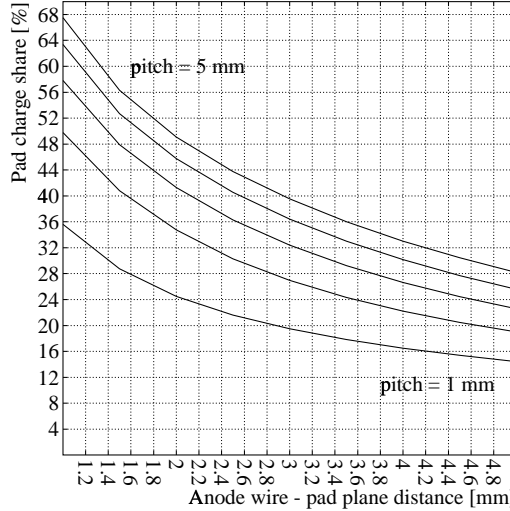


Figure 4.20: The charge which flows to the pads for ions heading for the drift volume (0°), integrated over the first 200 ns. Results for different anode wire pitches are shown.

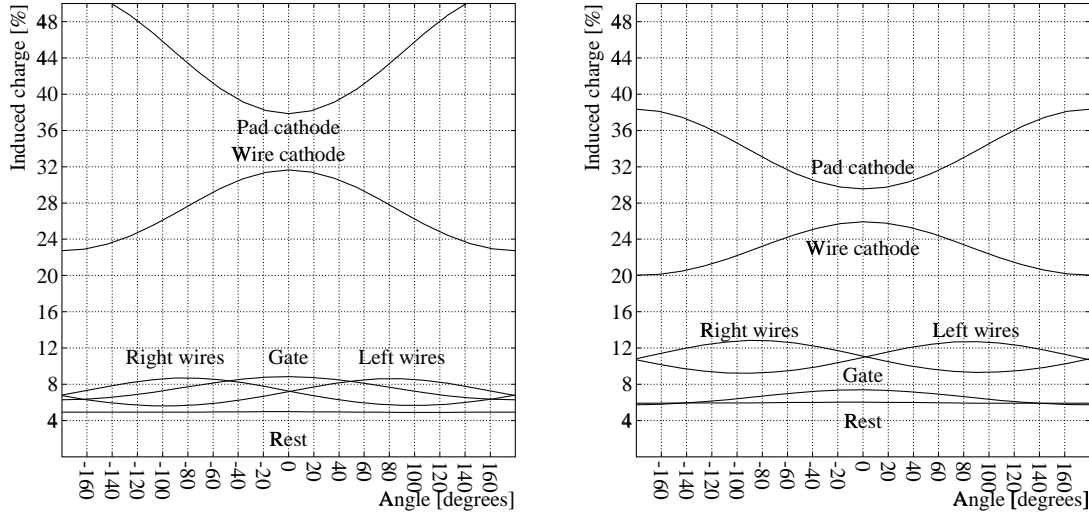


Figure 4.21: Fractions of charge flowing to the various electrodes in the inner (left panel) and outer (right panel) readout chamber as a function of the angle under which the ions leave the anode wire. 0° is towards the drift region.

During the first 200 ns, ions produced in the avalanche induce as much charge in the anode wire where the avalanche takes place as in all the other electrodes combined. Of the latter part, only a certain fraction is seen on the readout pads. This fraction depends on the anode wire to pad plane distance and on the anode wire pitch, as demonstrated in Fig. 4.20. In Fig. 4.21 the fraction of charge flowing to the various electrodes as a function of the angle under which the ions leaves the anode wire is shown. For the inner chamber (Fig. 4.21, left panel), 40% of the signal is seen on the readout pads, while 30% are induced on the cathode wires and 15% on the neighbouring anodes. Owing to the larger anode wire to pad plane distance in the outer chamber, the readout pads see only 32% of the signal, 22% are induced on the cathode wires, and 22% on the neighbouring anodes (Fig. 4.21, right panel).⁶

⁶Note that the angular distribution of ions leaving the anode wire is expected to be isotropic only in the limit of very high gas gains. For the gas gains discussed here, the angular distribution of the incident electrons is preserved (see Fig. 4.17 on page 59), resulting in a peak of the ion distribution around 0° .

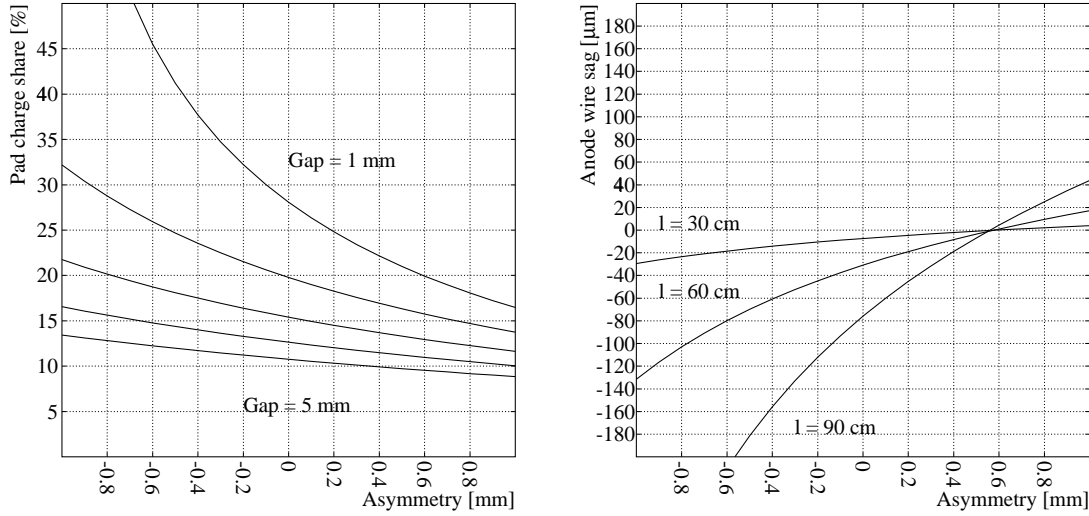


Figure 4.22: Left: In the nominal configuration, the anode wires are half-way between the pad and the cathode wire plane. When they are moved towards the pads (negative asymmetry in the figure), the pads collect more charge. Right: At the same time the sag of the anode wires increases, as shown here for the outer chambers with an anode wire voltage of 1700 V.

Implications of an asymmetric layout

The charge collected by the pads increases when the distance between the pad plane and anode wires decreases with respect to the distance between the cathode wires and anode wires ('asymmetric layout'). This increase is substantial, as demonstrated in Fig. 4.22 (left panel).

Such an asymmetry does however increase the electrostatic anode wire sag. In the outer chambers (Fig. 4.22, right panel), one cannot move the longest wires by more than 100 μm before reaching a sag of 100 μm (corresponding to a gain variation of 5%; compare Fig. 4.19, right panel). This leads to only a 5%–10% increase of the pad signal. Although the wires are shorter and the anode voltage is lower in the inner chamber, leading to smaller sags for a given asymmetry, the situation is similar, because in the inner chamber the gas gain variations are more sensitive to wire sag, as shown in Fig. 4.19 (right panel).

Asymmetric layouts appear attractive, because they would potentially allow the readout chambers to be operated at lower gas gains. However, since the expected gain variations exceed the tolerances, asymmetric layouts are not considered in the baseline design.

Anode wire pitch

For a given distance between the anode wires and pad plane, the fraction of the signal which goes to the pads can be increased when increasing the anode wire pitch (Fig. 4.20). In addition, in chambers without field wires the gain increases with increasing anode wire pitch for a given anode wire voltage (Fig. 4.23, left panel). A large anode wire pitch also reduces the collection isochrony, but this effect is small compared with the diffusion spread (Fig. 4.23, right panel).

On the other hand, a smaller anode wire pitch slightly reduces the wire sag (Fig. 4.24, left panel). Mutual repulsion of the anode wires increases however, and can potentially lead to alternating displacements of the anode wires. However, alternating displacements are, due to the asymmetry of the cathodes, only probable with an anode wire pitch less than 1 mm and an anode wire potential larger than 3000 V. For a pitch larger than 2 mm, the most probable instability is that of an anode wire hitting the pad plane after an external mechanical shock. The zone near the pad plane which is energetically favoured over the

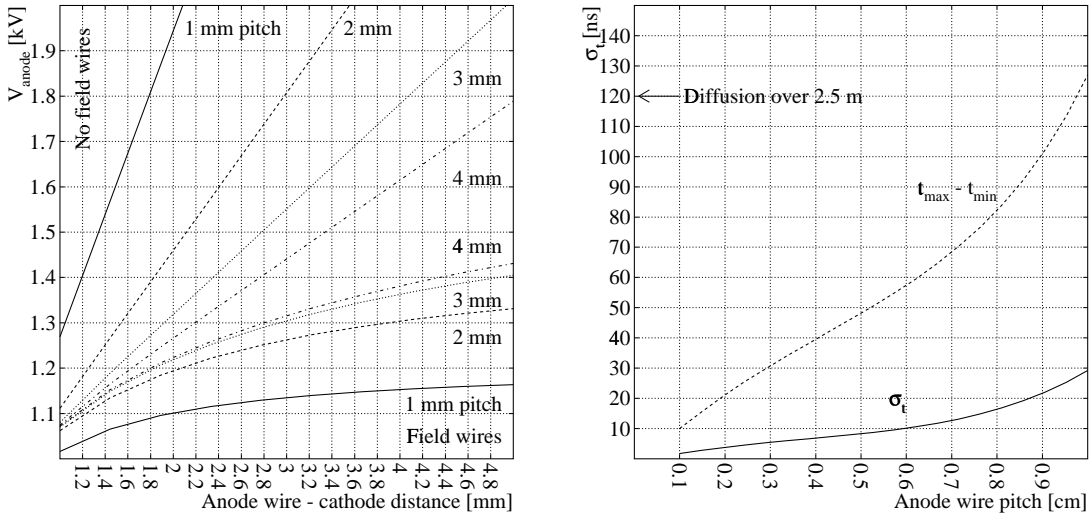


Figure 4.23: Left: Variation of the voltage required to achieve a gain of 2×10^4 with a given anode-cathode distance and anode wire pitch. Right: The collection isochrony deteriorates when the pitch increases, but the RMS is lower than the diffusion spread for all values of the anode wire pitch considered here.

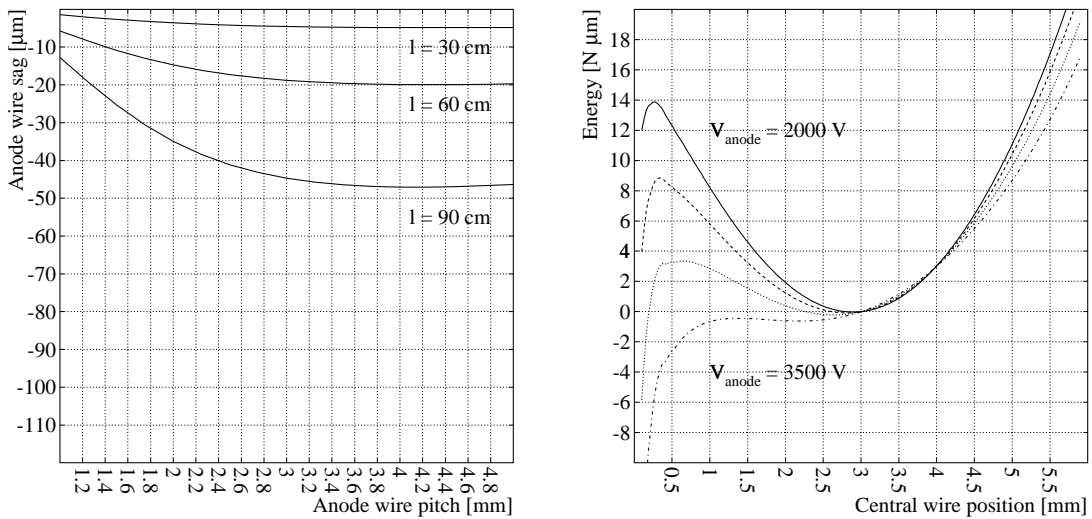


Figure 4.24: Left: The anode wire sag is not a strong function of the anode wire pitch, computed here for a anode wire potential of 1400 V. Right: The energy required to force the anode wire into a parabolic shape with a given position of the middle of the wire (ordinate) has a clear minimum for anode wire potentials up to 3000 V. The anode wire pitch and the distance between anode wires and cathodes are 3 mm in this calculation.

equilibrium position reaches a thickness of 200 μm when the anode wire potential is 3000 V (Fig. 4.24, right panel). The anode wires are therefore intrinsically stable for all anode wire potentials and anode wire pitches which are of practical importance.

On average, about 60 ionization electrons per mm^2 reach the readout chambers in a central Pb–Pb event (see Section 7.2.2). This translates into a rate of $6 \times 10^5 \text{ e mm}^{-2} \text{ s}^{-1}$ during the readout time

of $100 \mu\text{s}$. The estimated gain variations caused by these rates are negligible [8]. Measurements indicate [19] that at these rates gain variations in multiwire proportional chambers are below 3% but reach already 10% at ten times higher rates. Taking the uncertainties into account, a smaller anode wire pitch reduces the risk of rate-induced gain variations, since the total number of avalanches is spread over a larger number of anode wires.

As a compromise between the aforementioned arguments, we have chosen an anode wire pitch of 2.5 mm.

Ageing is not a major issue [8] in the design of the ALICE TPC readout chambers thanks to the use of a gas mixture without organic components and an integrated charge of only 1.1 mC per year and per cm of anode wire for the innermost anode wires in Pb–Pb interactions, assuming a multiplication of 2×10^4 and an anode wire pitch of 2.5 mm.

Field wires

Field wires enhance the field on the anode wires, thus reducing the potential needed to achieve a given gain. They also reduce, for a given anode wire potential, the electrostatic sag of the anode wires. In contrast, they attract, in certain configurations, some of the ions produced in the avalanche. Owing to the substantial fields in the vicinity of the field wires, the arrival of the ions on these wires can give rise to a secondary signal. Furthermore, the signal induced on the readout pad is drastically reduced by the presence of field wires [9]. We have therefore chosen a geometry without field wires.

4.1.3.5 Gate adjustments

In the open state, equal voltages are applied to all gating grid wires, this voltage is called *offset voltage* V_G . To close the gating grid, alternating lower and higher voltages are applied to the gating grid wires. The difference between the offset voltage and the potential of the gating grid wires when the gate is closed is called *bias voltage* ΔV .

Offset voltage

For a proper choice of V_G , the following conditions have to be met:

- In the open state, the gating grid has to be entirely transparent for electrons coming from the drift volume.
- The isochrony of electrons arriving at the anode wires should be better than the arrival time spread caused by diffusion and track inclination, i.e. 120 ns.
- Ions starting from the anode wires should not be able to reach the gating grid in less than the gate opening time, i.e. $100 \mu\text{s}$.

Fig. 4.25 (left panel) demonstrates that the gating grid in the open mode is transparent for electrons over a large range of offset voltages. The isochrony has a broad minimum between $-500 \text{ V} < V_G < 0 \text{ V}$, staying well below the arrival time spread of the electrons (Fig. 4.25, right panel).

The time needed by Ne^+ ions to drift from the anode wires to the gating grid in the inner and outer readout chamber is shown in Fig. 4.26. Apart from V_G , the drift time depends on the anode wire voltage and the chamber geometry (distance between the anode wires and cathode wires). At the operational anode wire voltages, both chamber types require $V_G \geq -100 \text{ V}$ to achieve a Ne^+ drift time of at least $100 \mu\text{s}$.

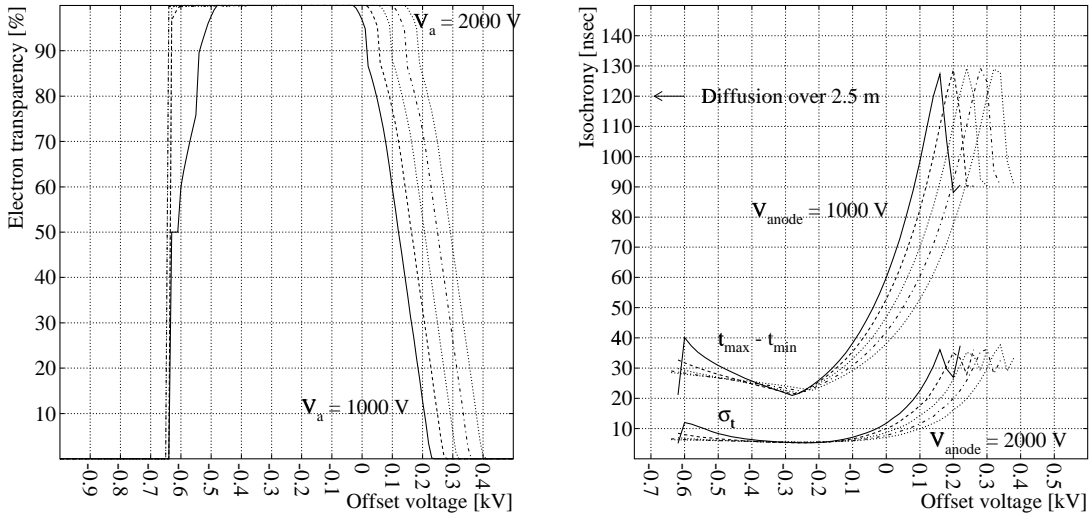


Figure 4.25: Electron transparency (left panel) and isochrony (right panel) as a function of the offset voltage V_G . The calculations are made for the outer chamber and different anode wire voltages. The results for the inner chamber lead to the same conclusions.

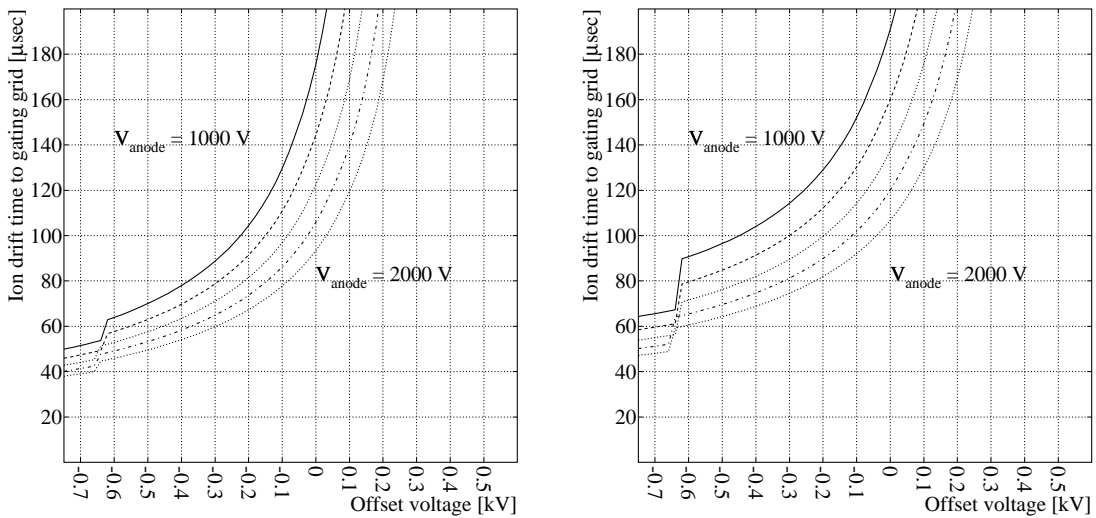


Figure 4.26: Drift time of Ne^+ ions from the anode wires to the gating grid as a function of the offset voltage V_G . The calculations are made for the inner chamber (left panel) and outer chamber (right panel), and for different anode wire voltages in steps of 250 V.

Bias voltage

To prevent electrons and ions from passing the gating grid, alternating potentials $V_G \pm \Delta V$ are applied on the gating grid wires. The bias voltage ΔV depends on the gating grid wire spacing and the magnetic field. Apart from this, it depends strongly on V_G , and weakly on the anode wire voltage (Fig. 4.27). Applying a bias voltage of $\Delta V > 80 \text{ V}$ at $V_G = -100 \text{ V}$, the electron transmission through the closed gate is less than 2%.

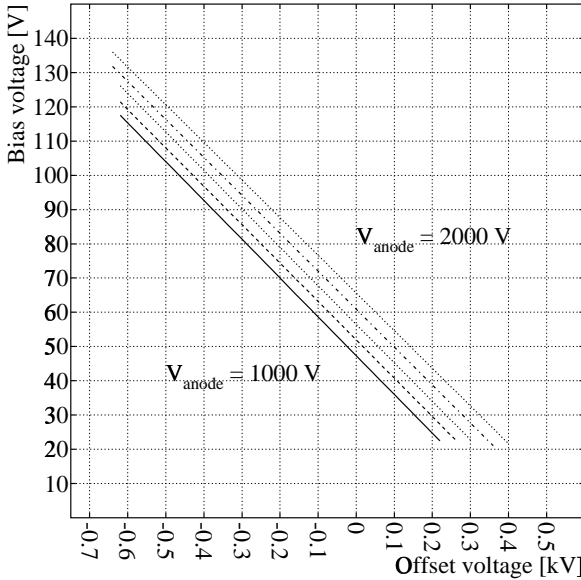


Figure 4.27: Minimum bias voltage ΔV to be applied to achieve an electron transmission smaller than 2% as a function of the offset voltage V_G . The calculations are shown for the outer chamber and different anode wire voltages. The results for the inner chamber look similar.

4.1.3.6 Electrostatic matching of inner and outer chamber

Ideally, the drift field is determined by the potential of the central electrode and terminated by the cathode wires of the readout chambers which are on ground potential. This, however, is not exactly true since part of the amplification field leaks through the cathode wire plane, penetrating into the drift volume, and resulting in a shift of the effective ground plane. If this shift is similar for the inner and outer readout chambers, it can be compensated for by proper adjustment of the last resistor of the voltage divider chain (see Section 4.1.5.1).

In their nominal position, the gating grid wires of the inner and outer readout chambers have the same distance to the central electrode. However, inner and outer readout chambers have different wire geometry and anode wire voltages, and hence the magnitude of field leaking into the drift volume is also different. This can, in principle, be compensated for by slightly shifting the z -positions of the inner and outer readout chambers with respect to each other.

We define here as *virtual ground* the position of the plane where the potential, extrapolated from the region of constant field inside the drift volume into the readout chambers, is equal to zero. As mentioned above, we do not expect this plane to coincide with the cathode wire plane.

The location of the virtual ground plane relative to the cathode wire grid, computed for inner and outer readout chambers and a gating offset voltage $V_G = -100$ V, is shown in Fig. 4.28 as a function of the anode wire voltage.

For both the inner and the outer readout chambers, the virtual ground plane is located between the cathode wires and the gating grid, at a distance of about 0.9 mm from the cathode wires in the inner chamber, and at about 0.7 mm from the cathode wires in the outer chamber. The difference is explained by the more compact structure of the inner chamber, which makes the anode wire field penetrate deeper into the region between the cathode wires and gating grid. Both for the inner and for the outer chamber, the location of the virtual ground plane varies by less than 250 μm for anode wire voltages ranging from 1000 V to 2000 V.

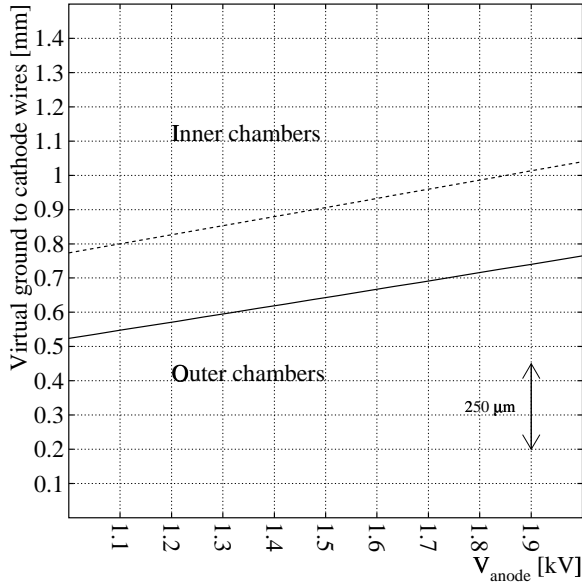


Figure 4.28: Position of the virtual ground plane relative to the cathode wire plane for the inner and outer readout chamber as a function of the anode wire voltage.

From Fig. 4.28 we conclude that the inner and outer readout chambers should be shifted with respect to each other by $180 \mu\text{m}$ in the z -direction to match their virtual ground planes. However, the drift field non-uniformities resulting from the observed mismatch of the virtual ground planes are $\leq 10^{-4}$ and hence within tolerances.

4.1.3.7 Operational parameters

In Table 4.3 we summarize the operational parameters of the ALICE TPC readout chambers, as derived from electrostatic calculations.

Table 4.3: Operational parameters of the ALICE TPC readout chambers.

	Inner chamber	Outer chamber
Anode wire voltage	1450 V	1720 V
Gas gain	2×10^4	2×10^4
Signal-to-noise	20	30,40
Anode wire sag (max)	$35 \mu\text{m}$	$75 \mu\text{m}$
Gas gain variation (max)	4%	4%
Gate offset voltage	-100 V	-100 V
Gate bias voltage	$\pm 80 \text{ V}$	$\pm 80 \text{ V}$
Pad coupling	40%	32%
σ_{PRF}	2 mm	3 mm

4.1.4 Electronics mounting and cooling

4.1.4.1 Distribution of front-end electronics

Each Front-End electronic Card (FEC) contains all the analog and digital components necessary to read out 128 pad signals (for a detailed description of the FEC see Section 5.1.4). The high channel density of up to $0.33 \text{ channels}/\text{cm}^2$ in the inner chamber, and the limited accessibility from the rear side require a very compact arrangement of the FECs, as shown in Fig. 4.29.

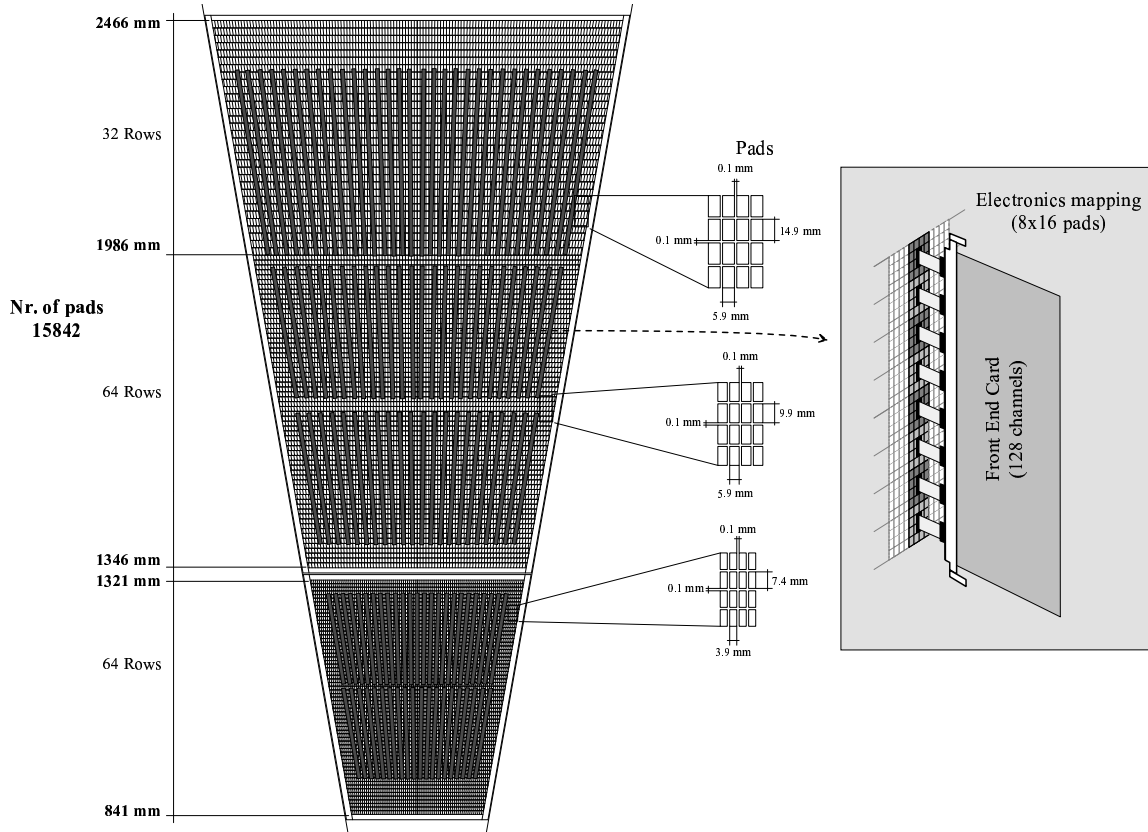


Figure 4.29: Distribution of the FECs on the readout chambers.

Owing to the different pad sizes used in the readout chambers (see Section 4.1.2) three types of FECs are needed. They are identical in functionality but different in size. The 64 pad rows in the inner chamber (pad size $4 \times 7.5 \text{ mm}^2$) will be read out by FECs of dimension $14 \times 19 \text{ cm}^2$. Arranged in two rows, a total of 45 of these FECs are needed for the inner chamber. The first 64 pad rows of the outer chamber (pad size $6 \times 10 \text{ mm}^2$) are read out by a total of 48 FECs of dimensions $14 \times 29 \text{ cm}^2$. The last 32 pad rows of the outer chamber (pad size $6 \times 15 \text{ mm}^2$) are equipped with one row of 32 FECs of size $14 \times 40 \text{ cm}^2$. An arrangement with FECs of identical size would have drastically increased the average trace and cable lengths between the pads and the preamplifier/shapers.

There will be no electronic components bonded on the pad plane PCB. The analog pad signals are

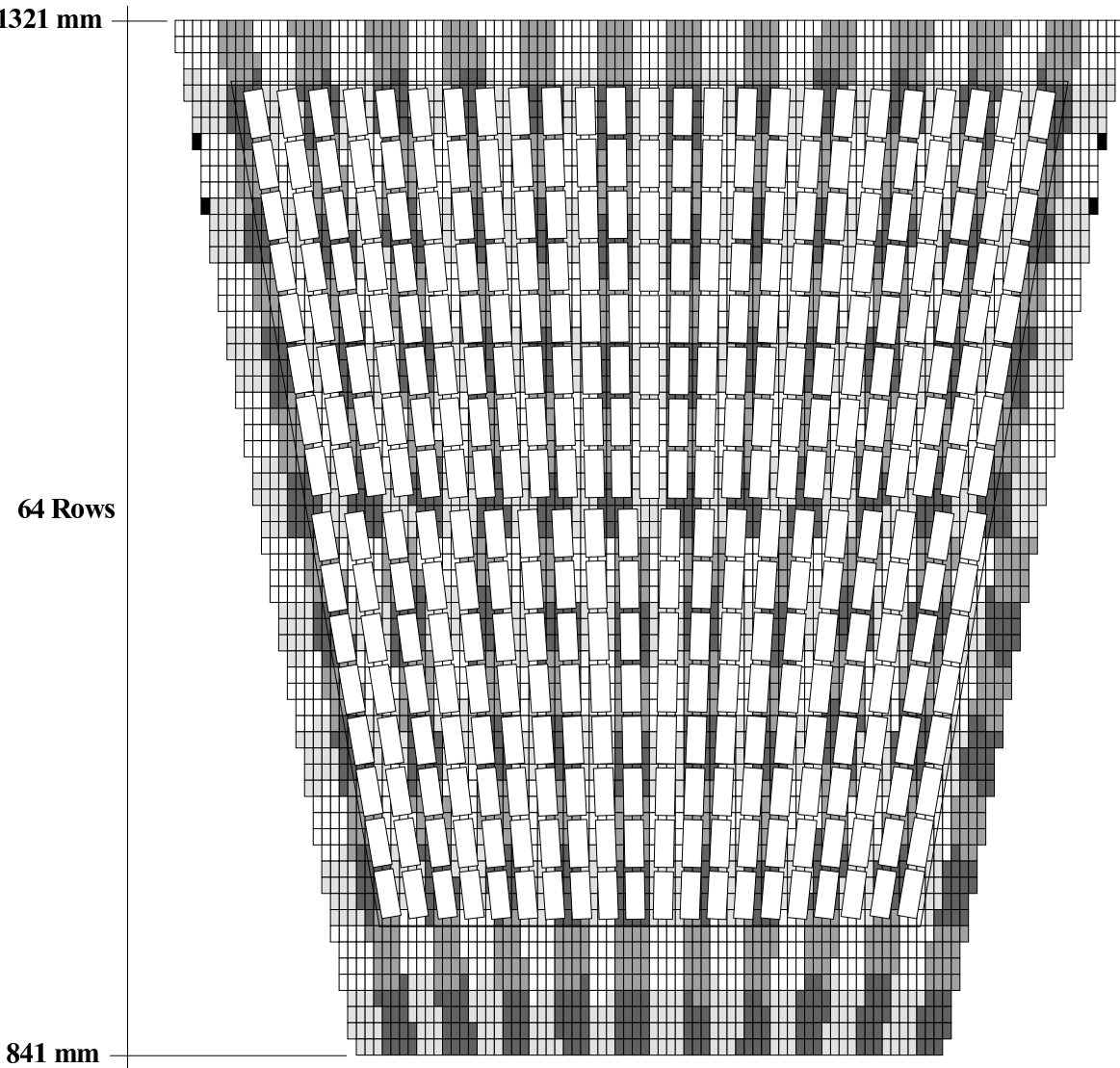


Figure 4.30: Distribution of transfer points on the back side of the pad plane PCB of the inner chamber. Also shown are the inner dimensions of the aluminium frame.

collected on the pad plane PCB to a transfer point in groups of 16. Flexible cables (see Section 5.1.2) are soldered to these transfer points. Multipin-connectors at the other end of the flexible cables are plugged into the FECs. In this way, the signals of 16 neighbouring pads are connected to the same preamplifier/shaper chip. The multilayering technique for the pad plane PCB and the flexible cables provides good shielding from external noise sources and between neighbouring signals, since the pad signals are always surrounded by grounded lines and surfaces. In addition, a constant and continuous impedance seen by the signals can be provided.

The distribution of the transfer points in the inner chamber, which has the highest channel density, is shown in Fig. 4.30. Also shown are the inner dimensions of the aluminium frame, which limit the accessible area. The open squares are the transfer points of size $9 \times 22 \text{ mm}^2$ where the collected pad signals arrive at the surface of the pad plane PCB and to which the flexible cables are soldered. In Fig. 4.30 groups of 16 pads are marked in different gray scales, indicating that their signals are collected on the same transfer point. Fig. 4.31 shows details of the connection between the readout pads and the transfer points on different layers of the pad plane PCB.

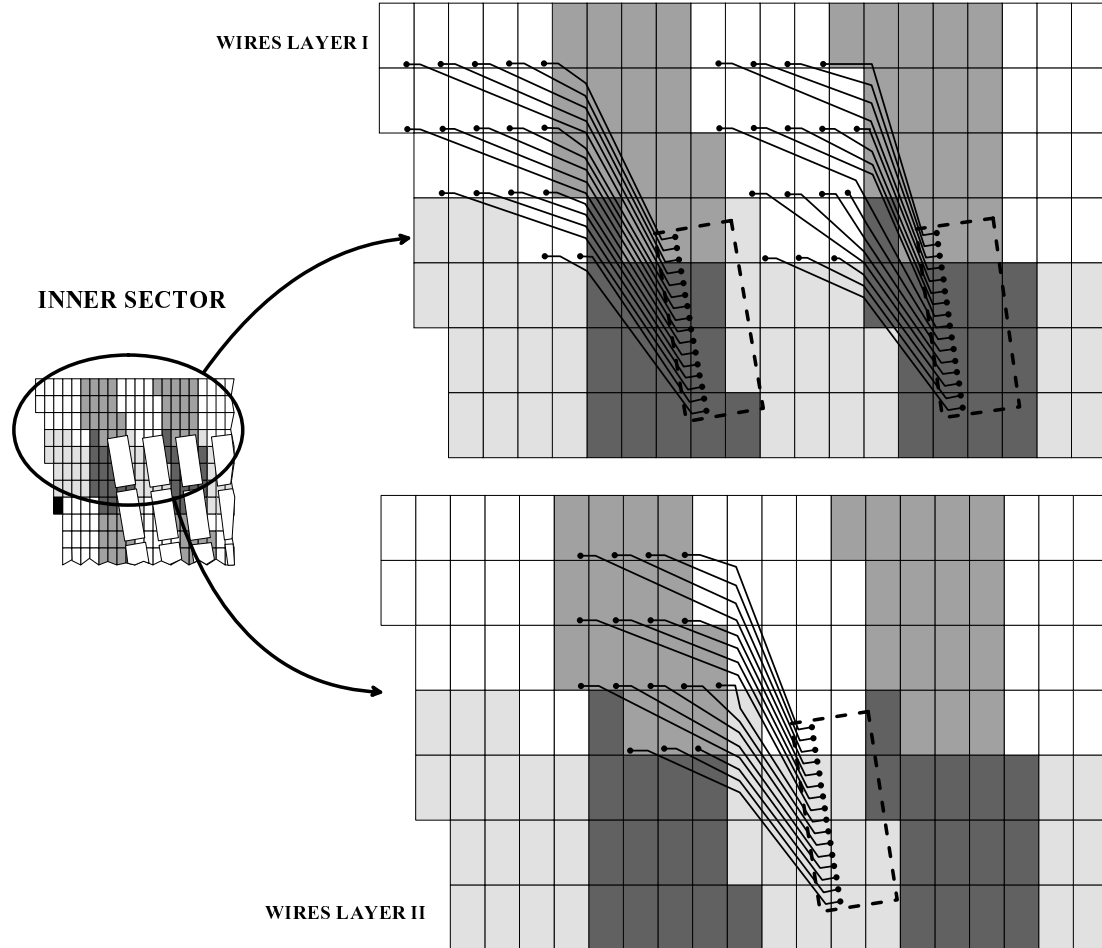


Figure 4.31: Connection scheme between pads and transfer points.

The distance between the pad and the preamplifier/shaper circuit varies because of this connecting scheme. It has a minimum of 60 mm for the majority of the pads, but can reach up to 120 mm in the worst case, for example at the corners of the inner chambers. This variation is dictated by mechanical constraints of the readout chamber design.

A single pad has a capacity of about 4 pF. The present scheme of mounting the electronics and collecting the pad signals adds a capacitive load of 6 to 12 pF to the preamplifier/shaper. These numbers are consistent with a noise level below 1000 electrons.

Details of the mechanical structure for positioning and mounting the FECs at the chamber are sketched in Fig. 4.32. Support bars which are attached to the service support wheel are mounted in the radial direction, between adjacent FEC columns. For the longitudinal fixation of the FECs, two holes are foreseen into which two dowel pins are fed. These dowel pins are attached to a brass angle which is screwed together with the brass cooling pipe to the FEC. This provides a flexible but exact positioning of the FECs to the service support wheel, without introducing any gravitational forces on the readout chambers or the end-plate. At the upper corners of the FECs an additional snap-on fixation against lateral movements is foreseen. This fixation is mounted on additional crossbars to the service support wheel. These will be dimensioned in such a way that all the mechanical stress coming from the different cables and connectors is taken away from the FECs and transferred completely to the service support wheel.

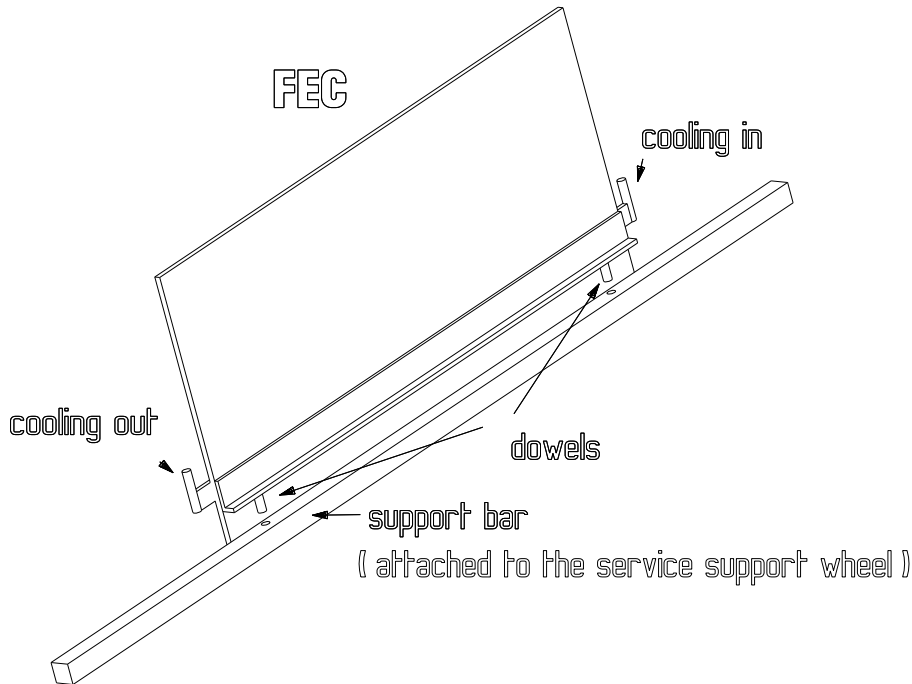


Figure 4.32: Mounting and cooling of the FEC.

4.1.4.2 Cooling system

Each of the two readout planes of the ALICE TPC consists of 18 inner and 18 outer readout chambers, equipped with 4500 FECs. Each FEC has a power consumption of up to 12 W. The TPC-FEC cooling system, therefore, has to be designed for 55 kW. The operating temperature of the TPC has to be stabilized to the level of ± 0.1 °C. To solve this problem we will use the second generation Leakless liquid Cooling System (LCS2) which is currently used in several TPC detector systems at CERN (NA49, CERES/NA45) and at BNL (STAR), and has been proposed in LHC experiments (ATLAS Calorimeter and the CMS Pixel Detector) [20].

The LCS2 fulfills the requirements for an LHC detector:

- Since the detector is located in a temporarily inaccessible area, the filling, bleeding, and draining operations are fully automated.
- The number of active components installed in the inaccessible areas are reduced to a minimum and are able to operate in magnetic fields and under radiation exposure.
- The risk of leaks is reduced as far as possible.
- All parameters are controllable from the control room.
- As a cooling medium distilled water or fluorocarbons can be used.
- The equipment will be selected in collaboration with future maintenance and operation services with the ST/CV group at CERN.

The principle of operation of the the new LCS2 cooling system developed by the SF section of the CERN/EST/SM group is sketched in Fig. 4.33. The cooling liquid, distilled water in our case, is held in a storage tank (1) positioned at the lowest point of the system. The liquid is moved by a circulator pump (2) into the heat exchangers (3). These are cooled by chilled water from the CERN network. The flow of

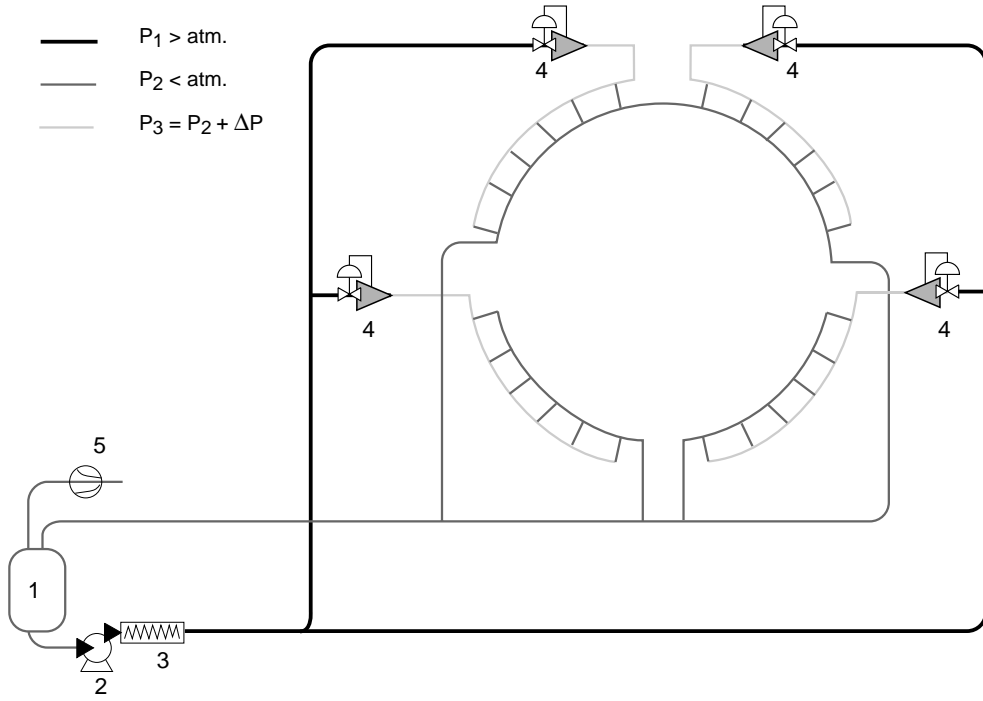


Figure 4.33: The cooling liquid is held in a storage tank (1) below atmospheric pressure by a vacuum pump (5). The liquid is moved by a circulator pump (2) into the heat exchanger (3), and then flows to the heat sources by pressure regulators (4) which maintain an equal pressure in all sub-circuits.

the cooling liquid through the cooling brass pipes which are in mechanical contact with the FECs (see Fig. 4.32), is controlled by pneumatic regulation valves (4). At the input of these regulators the system pressure is above atmospheric pressure. The regulators are located along the circumference of the TPC and feed the cooling liquid to the cooling lines which are connected to the front-end electronics. They adjust the pressure in the return lines to a value below atmospheric pressure. The regulators guarantee that in all subsections of the cooling circuits an equal pressure below atmospheric pressure is maintained. Thus, any leak in these lines and connections will not lead to a loss of cooling liquid (leakless cooling). In addition, the regulators (4) define that a constant pressure gradient of 200 mbar drives the cooling liquid through the cooling pipes which are integrated into the FECs. A vacuum pump (5) in the return line discharges any excess air collected, i.e. during drainage, and sustains a pressure below atmospheric pressure.

The cooling supply and return lines are mounted at the outer circumference of the service support wheel. The connections from the supply lines to the FEC will be made by 4 mm Viton tubes. In order to optimize the heat transfer from the cooling agent to the FEC a rectangular brass tube of dimensions $9 \times 2.5 \text{ mm}^2$ is soldered or screwed directly onto the ground plane of the FEC. In this way the heat transfer is provided by conduction. This allows the cooling system to be operated under the following conditions: With a pressure gradient of 200 mbar in the system and a serial connection of 6 FECs we get a flow of 50 l/h and a temperature gradient between the supply and return line of 1.5°C . The turbulent fluid velocity is 1.2 m/s.

The FEC thermally consists of four regions. There are the preamplifier/shapers which contribute 16% of the thermal load, the ADCs (64%), the ALTROs (14%), and finally the transducers and the voltage regulators (16%). The rectangular brass cooling tube will be mounted 30 mm above the connectors to the flexible cables at the height of the preamplifier/shapers. Thus the cooling tube is very close to the largest heat source, which minimizes the heat transfer through the pad plane into the drift volume. The very

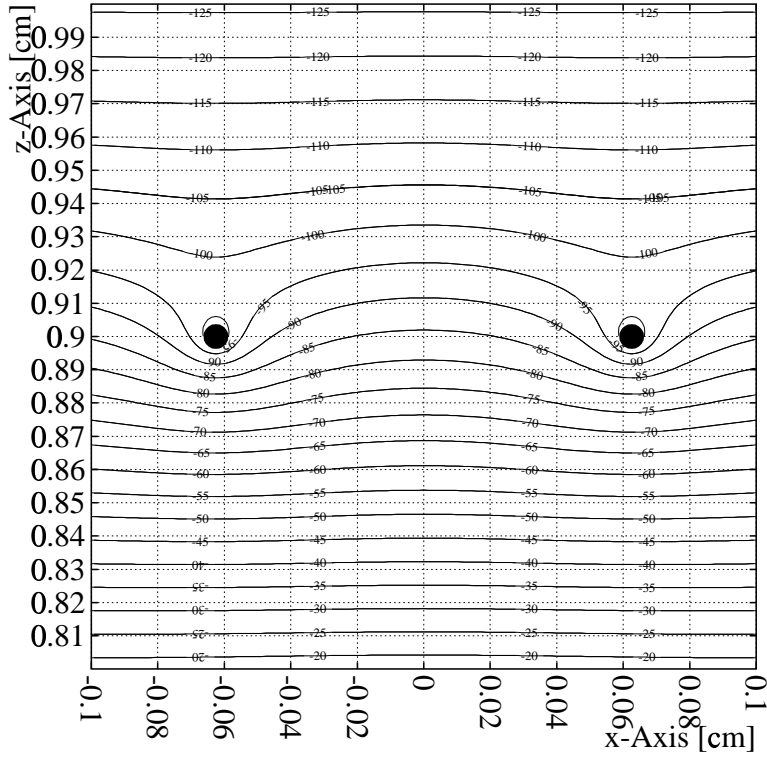


Figure 4.34: Equipotential lines close to the gating grid of the outer readout chamber: $V_{\text{anode}} = +1700$ V, $V_G = -100$ V.

stringent temperature stability in the drift volume requires a very constant and continuous operation of the front-end electronics. The overall temperature distribution will be monitored by a set of temperature sensors. In addition to sensors on the pad plane and in the drift volume, a PT100 temperature sensor will be integrated into each FEC. All this information is monitored by the slow control system. This information is then used for the fine-tuning of the temperature distribution, and necessary adjustments will be made by local heaters which are integrated into the cooling system.

4.1.5 Link between field cage and readout chambers

4.1.5.1 Electrostatic matching of readout and field cage

To obtain a smooth transition from the drift field to the readout chambers the potential on the strips of the field cage needs to be matched with the potential of the gating grid of the readout chambers. This is done by keeping the last resistor of the voltage divider chain variable, allowing the strip potential to be shifted towards that of the gating plane of the readout chamber. Furthermore, the gating grid offset voltage is adjusted by the gating grid pulser (compare Section 4.2). The correct value of the potential to be adjusted depends on the drift field itself, the position of the readout chamber in z , and the transfer fields between the wire planes of the readout chamber. Drift field distortions caused by field leakage from the amplification region are small and confined to the vicinity of the gating grid wires, as shown in Fig. 4.34 for a drift field of 400 V/cm and an anode wire voltage of 1700 V (outer chamber).

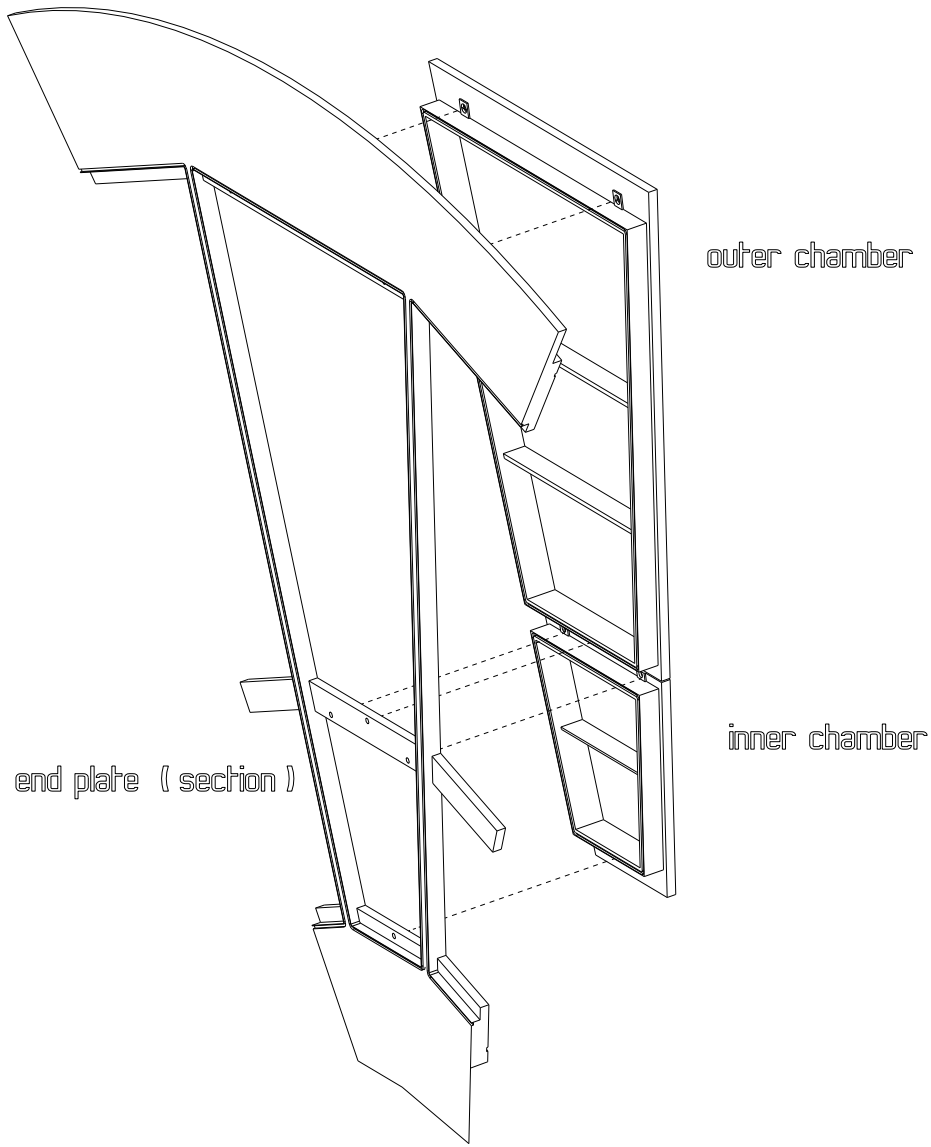


Figure 4.35: Three-point mounting of the readout chambers.

4.1.5.2 Mounting and sealing of the readout chambers

The readout chambers are mounted on end-plates closing the drift volume on either side of the TPC. Each readout plane is subdivided into 18 inner and 18 outer readout chambers. The inner chambers extend from 83.0 to 133.2 cm in the radial direction, the outer ones from 133.5 to 247.7 cm. The electronic readout components, including their cabling and cooling services, are mounted on service support wheels placed next to the end-plates. This considerably reduces the weight and, hence, the deformation of the end-plates. To reduce dead space between the readout chamber borders and the end-plate frames, a special insertion tool has been designed to mount the readout chambers from inside the field cage. During the installation procedure this tool is attached to the service support wheel. Prior to insertion of a readout chamber into the field cage volume, the readout chamber is rotated 90° around its two planar axes. Inside the drift volume the chamber will be rotated back to its original orientation and pulled back into its corresponding ‘slot’ of the end-plate. It will then be secured by three points on the end-plate (kinematically free mounting, see Fig. 4.35) and aligned with shimming (see below). This method ensures the planarity of the chamber with the central electrode to within $\leq 100 \mu\text{m}$.

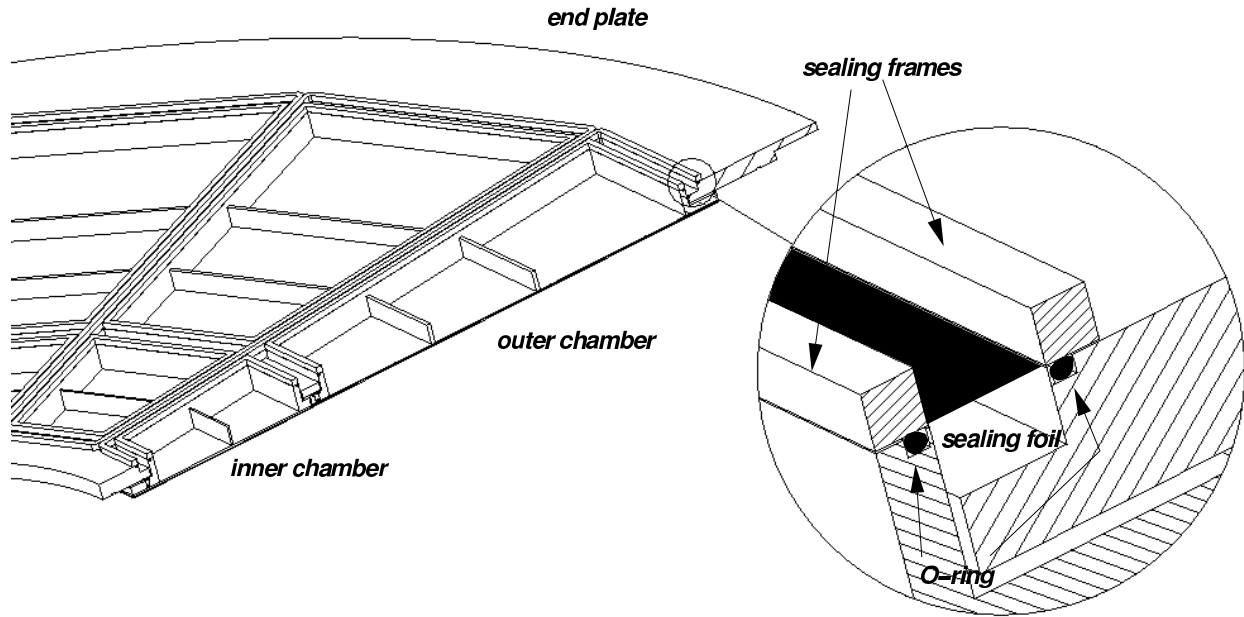


Figure 4.36: Schematic view of the end-plate with readout chamber and O-rings.

The chosen three-point mounting scheme cannot provide a gas-tight seal between the chamber and the end-plate without overconstraining the positioning of the chamber with respect to the end-plate. To close the crack between the chamber and the end-plate, a flexible Mylar gasket is mounted with two aluminium braces around the chamber border and the end-plate frame, respectively (Fig. 4.36). This sealing technique, already successfully employed in the CERES TPC [7], leaves the readout chamber stress-free in its sector of the end-plate.

4.1.5.3 Handling and replacement of readout chambers

For mounting and handling of the readout chambers, a mobile platform of a minimum size of $1 \times 3 \text{ m}^2$ is foreseen which allows access to the end-plates and service support wheels. If a readout chamber needs to be replaced *in situ*, the corresponding services mounted on the service support wheel need to be removed prior to accessing the chamber to be replaced.

4.1.5.4 Deformation of the end-plate

To estimate the deformation of the end-plate three principal load factors need to be considered in the calculations: (a) the weight of the end-plate itself and the readout chambers, (b) the weight of the ITS being supported by the TPC, and (c) a floor inclination of 1.39% (0.796°) in the experimental cavern. To this end, the static behaviour of the end plate was analysed in three-dimensional space, i.e. its deformation in its own plane (x, y) and also displacements in z , primarily due to the floor angle. The results are shown in Fig. 4.37. The conclusions are that all deformations of the end-plate are within elastic limits and do not exceed $100 \mu\text{m}$ in the xy plane and $600 \mu\text{m}$ in z . The displacements in z will be compensated by an end-plate bracket counteracting the sag force arising from the floor angle. The TPC is designed to maintain its mechanical stability and the alignment of its mounted components even when it is removed from the space frame which would be necessary for maintenance interventions at the ITS.

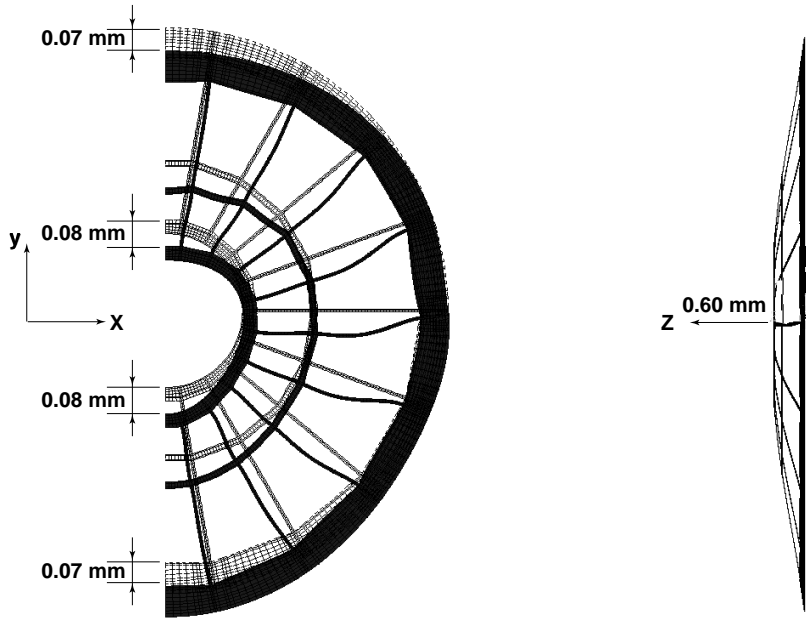


Figure 4.37: Deformation of the end-plate in the x - y plane (left panel) and in the z -direction (right panel) computed with finite element methods.

4.1.5.5 Survey and alignment

In this section we address the problem of aligning the individual components of the TPC with respect to each other. The overall survey of the TPC within the ALICE space frame and its position relative to the beam interaction point are not the subject of this study. The principal components of the TPC, the position and alignment of which need to be known with high accuracy, are the HV central electrode, the potential degrader strips and the readout chambers with their individual pad and wire planes. The intrinsic precision of all the individual components of the TPC is ensured during the manufacturing process (quality control). It is thus the knowledge of their collective behaviour within specified tolerances that leads to the expected performance of the TPC. The principal reference point for positioning all the internal TPC components with high precision is the position of the HV central electrode. This electrode, built extremely flat and stiff from composite material, is mounted into the TPC field cage with a precision of $100\ \mu\text{m}$. This precision must not deteriorate because of misaligned components mounted between the electrode and the end-plates. Thus, the positioning of the intermediate potential degrader network must be of such precision that the initial reference is preserved over the distance of 2.5 m from the centre of the TPC to the readout planes. Therefore, the placement and gluing of the strip support rods is surveyed throughout the entire installation with a high degree of accuracy. With an intrinsic precision of the rods of $< 20\ \mu\text{m}$ the internal reference position of the central electrode is thus transferred to the level of the end-plates.

The external stiffness of the composite structure of the TPC vessels lends itself to the high structural integrity of the internal, field defining, network of the TPC.

4.1.5.6 Alignment of the readout chambers

To determine the position of the readout plane within the chosen TPC reference frame, the surfaces of the end-plates serve as accessible survey points for positioning the readout chambers (Fig. 4.38). This allows the readout chambers to be aligned with respect to the strip support rods and the central electrode. Since it is known that the end-plates deform under the weight of the readout chambers (Section 4.1.5.4), the end-

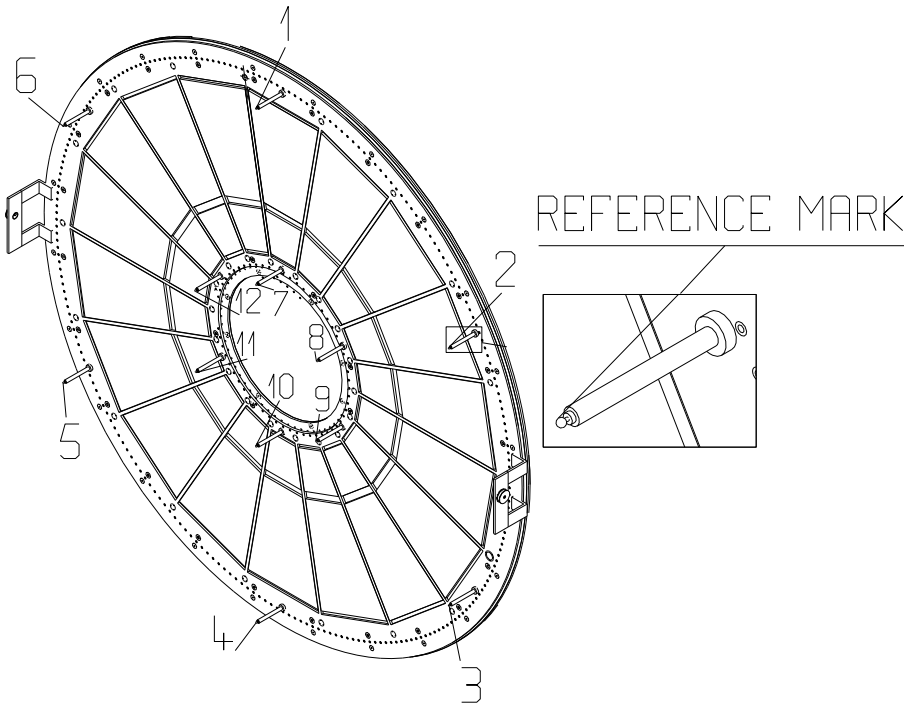


Figure 4.38: Reference marks distributed along the outer and inner circumference of the end-plate allow the orientation and planarity of the end-plate to be surveyed via photogrammetry.

plates will first be loaded with dummy chambers to estimate the amount of adjustment to be made in each individual end-plate sector prior to installation of the real chambers. This is done in the surface building with a method called photogrammetry. This method is often applied in other experiments [21] and is sensitive to a precision of $< 10^{-5}$ compared to the dimension of the apparatus surveyed. Adjustments to the chamber position are made with shim only. Thereafter, no other adjustments are possible. The isostatic three-point mounting of the chambers is designed to lead to an overall readout planarity with the central electrode of $< 100 \mu\text{m}$. Combined with the internal mechanical accuracy of the pad plane, each individual pad coordinate with respect to the central electrode will be known to a precision of $< 100 \mu\text{m}$.

4.1.6 Tests and prototyping

This section describes the steps to be taken to validate and test experimentally the optimization described above obtained from electrostatic simulations (Section 4.1.3). In addition, all the mechanical aspects of the proposed layout, e.g. the strength of the aluminium body against torsion, the mounting of the electronics and the cooling scheme etc. have to be verified. Finally, the operational parameters and characteristics of the readout chambers under realistic conditions, e.g. their stability under high particle load at a given gain, must be determined. Our strategy is to use both existing readout chambers and small test chambers to investigate aspects which appear to be independent of the final layout or dimensions of the readout chambers. In addition, full-size prototype chambers will be built. The chambers will be tested employing dedicated test beams both at GSI and CERN, as well as parasitically within CERN heavy-ion experiments (NA49, CERES/NA45) during lead beam time. Whenever appropriate, tests will be performed using laser beams, radioactive sources or cosmic rays.

Small test chambers

Several small test chambers (active area $5 \times 5 \text{ cm}^2$) with different wire and pad geometries have been built. These chambers are mounted on a 50 cm long field cage inside a steel tube of 20 cm diameter, which encloses the drift gas. The steel tube provides several ports where laser light or particles from a radioactive source can be injected into the drift volume at different positions. The readout scheme consists of standard preamplifier/shapers, which are connected to the ADC system developed in the framework of RD32 [22] and are described in Section 8.1. This set-up allows the evaluation (Section 4.1.2 and 4.1.3) of different wire and pad geometries and potential settings and their influence on the chamber performance to be verified, in particular:

- gas gain,
- gating efficiency and voltage settings,
- signal collection and shape.

Existing readout chambers

A spare readout chamber of the NA35 TPC (active area $52 \times 78 \text{ cm}^2$) has been mounted on a 15 cm long field cage and a plastic gas box. The chamber can be read out with ALEPH-type NA35 TPC electronics [23]. The purpose of this ensemble is

- to scrutinize sources of instabilities — which had been observed, but not yet understood in detail — such as discharges occurring presumably at the borders of the chambers;
- to investigate the response of the chamber to high particles fluxes; in particular the limits of stable operation should be mapped out as a function of the gas gain, particle density, mean angle of incidence and rate.

Full scale ALICE TPC readout chamber prototype

The behaviour of a chamber is specific to a particular design. Thus, some of the above tests need to be repeated with a chamber of the actual ALICE design. It is planned to build during the year 2000 two full-size prototypes of the inner chambers as described in Section 4.1.1. The chambers will be constructed at GSI. Subsequent tests will be performed employing GSI test beams. Finally the chambers will be mounted and tested in the prototype field cage, which is described in Section 3.1.5. This scheme allows us to

- investigate the mechanical properties of the chambers including the proposed sealing and mounting scheme into the end-plate;
- investigate the boundary problems (field distortions, gating) between two adjacent chambers;
- perform tests in a realistic heavy-ion environment (as the proposed ALICE TPC electronics will not be available by the end of 2000, it is planned to start with modified versions of the CERES/NA45 or NA49 TPC electronics);
- test the ALICE TPC electronics, when they become available, on the prototype chambers in conjunction with the proper cooling scheme.

4.2 Gating system

The sensitive mode of the TPC should be activated only for valid triggers and for the duration of the drift time ($100 \mu\text{s}$). Therefore, a gating grid is installed between the cathode grid and the drift region [24] (see Section 4.1). During the ‘closed’ state, potentials $V_G \pm \Delta V$ are applied on alternating wires of the grid, so that the resulting electrostatic fields render the gate opaque to the passage of charged particles. The value of ΔV depends on the magnetic field, the wire spacing, and drift field [25]. It is less than 100 V for $B < 0.5 \text{ T}$ for a cool gas, such as 90% Ne, 10% CO₂ adopted for the ALICE TPC. In the transparent state all wires of the gating grid are kept at V_G enabling the passage of drifting electrons. The gating circuit (usually called the ‘pulser’) has to place the large voltage swings ΔV on the gating grid as fast as possible with minimal pick-up on the readout electronics resulting from these swings.

4.2.1 Design considerations

For signals with a rise time greater than 100 ns the gating grids can be considered as capacitors (neglecting effects due to the finite size). Thus, we are faced with the problem of charging and discharging the capacitance of the gating grid which consists of the mutual capacitance between wires C_M , and the capacity to the ground C_0 . The voltage change on the capacitor C_M is $2\Delta V$ and therefore the capacitance ‘seen’ by the pulser is $C = C_0 + 2C_M$. For the chamber module of dimension 0.7 m^2 , and 1.25 mm wire pitch, $C_M \leq 2.75 \text{ nF}$, $C_0 \leq 0.5 \text{ nF}$ therefore we can expect a maximum capacitance of $C = 6.0 \text{ nF}$. The chambers will be connected to the pulsers via 40 m long cables so the interconnections have to be treated as transmission lines and special care has to be taken not to produce reflections caused by impedance mismatch. In order to have a gating pulse without oscillations we must have a pulser with an impedance equivalent to the impedance of the cable. The rise-time is in this case determined by that impedance and the capacitance of the gating grid. From the theoretical point of view, we have a transmission line terminated by the internal impedance of the pulser on the input end and by a capacitor of about 6.0 nF at the output end. If the output impedance of the pulser matches the impedance of the transmission line, the charging of the capacitor is determined only by its capacity and the impedance Z_0 of the cable (typically 50Ω). The voltage on the gating grid will have 95% of its maximal value in 3τ , ($\tau = CZ_0$). For $C = 6.0 \text{ nF}$ and $Z_0 = 50 \Omega$ this implies that about 900 ns are needed for the gate to be fully transparent.

The only way to reduce the rise-time for a given cable impedance is to compensate the capacitive load. This can be done by using passive elements (resistors, capacitors or coils). For our purposes the only convenient way to compensate is with an inductance because this way a reduction of the pulse amplitude is avoided and it does not introduce an additional load. The maximal value of the inductance is determined by the requirement of having a critical damping given by

$$L = \frac{Z_0^2 C}{4} .$$

In this case the voltage on the capacitor is given by

$$V = V_0 \left[1 - \left(1 + \frac{t}{\tau/2} \right) \exp -\frac{t}{\tau/2} \right] . \quad (4.7)$$

From this equation one concludes that the time for a pulse on the capacitor to reach 95% is given by 2.37τ , i.e. $2.37 \times 300 = 700 \text{ ns}$. The inductance for critical damping is $3.75 \mu\text{H}$. It follows that the coils reduce the opening time by about 20%. The compensation coils also reduce the initial capacitor charging current spike and pick-up, and hence are useful even if the switching speed is not of primary interest. The inductance is small enough to allow the use of coils without a Ferox core so that they can be used in a magnetic field.

4.2.2 Gating circuit design

Commercially available high-speed MOSFET drivers are used together with n-channel power MOSFETs as switching devices. This eliminates the need for additional adjustment of the timing of the FET opening. A block diagram of the gating pulser is shown in Fig. 4.39.

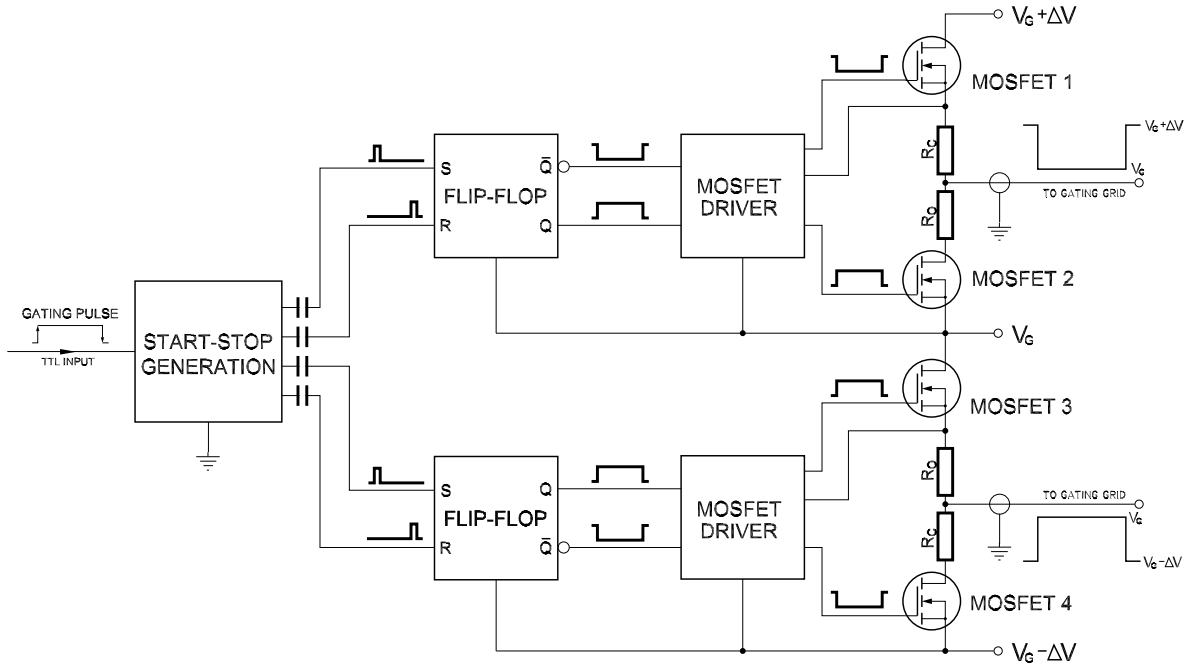


Figure 4.39: Block diagram of the gating pulser.

The input TTL pulse is transformed into short (less than 500 ns) start and stop pulses using dual mono-stable flip-flops 74HCT221. The rest of the pulser is separated from ground by capacitive coupling so that any offset voltage V_G can be applied. Its absolute maximum is limited by the voltage limit of the capacitors. The maximal ΔV is limited by the maximal V_{DS} of the MOSFET (200 V for IRF640). The gating pulse is regenerated using a resetable flip-flop (HEF 4013), and distributed into four inputs of the two dual MOSFET drivers (IR2100). Small time differences in the MOSFET switching times (of the order of 20 ns) are corrected using different values for the gate resistors. Faster turning off is achieved by adding fast diodes in parallel with these resistors. Additional fine tuning is not necessary, except for MOSFET 2, where it could be done with a 50 pF trim capacitor at the driver input. A larger mismatch in switching times can be corrected by careful selection of the components (especially MOSFET drivers).

The impedance of the pulser is determined by the resistors R_O (for gate opening), and R_C (for gate closing). The closing of the gate can be slower and it is not necessary for R_C to match Z_0 . It can be bigger in order to compensate the asymmetry of the signals caused by the time difference when opening and closing the FET (less than 50 ns). This reduces pick-up during gate opening. The optimal value is between $R_C = 150 \Omega$ and $R_C = 200 \Omega$.

4.2.3 Performance

A switching speed of less than 150 ns has been achieved (it has to be less than $2t_d$, where t_d is the cable delay, so that the pulse reflected from the chamber ‘sees’ the matching impedance on the pulser side of the cable). For a cable with 5 ns/m delay this gives a minimal length of 10 m, well below the actual cable length of 40 m. The maximal length of the cables is only limited by their ability to transmit signals with

a frequency below 10 MHz. The symmetry of the positive and negative pulses during switching from the closed to the open state can be tuned to better than 1%.

The internal delay of the pulser is less than 400 ns. This implies that the TPC gate can be opened about $1.1\mu\text{s}$ after the start of the gate signal, with possibly a small pick-up in the first two time slices. The minimal pulse duration is determined by the start-stop generation circuit and the flip-flops and is less than $1\mu\text{s}$. The maximal pulse duration is infinite. The maximal rate is determined by the maximal supply current, and pre-gating using the first level trigger is possible.

Up to now, pulsers based on this design are used for TPCs of the NA49 [6] and NA45(CERES) [7] experiments. Standard $50\ \Omega$ 20 m cables with BNC connectors are used. The cost per channel of the NA49 pulser was less than 300 CHF.

Considering the gating circuit, the readout chambers, and the necessary interconnections as a whole, the system can be designed for a switching time between $1\mu\text{s}$ and $1.5\mu\text{s}$ even for large area TPC modules such as the ALICE experiment. Owing to the simplicity of the design, the internal propagation delay could be reduced to less than half of that achieved with other existing models. The robustness of the components makes them very reliable, requiring minimal maintenance, so that they can be installed in areas which are not easily accessible. Remote control is only needed for switching and adjusting the supply voltages.

4.2.4 Implementation

It is foreseen to install the gate pulser system outside the L3 magnet on either side of the TPC. This requires cables of about 40 m length to connect to the readout chambers. Following the NA49 design the pulser cards will be housed in standard 3U Eurocrates, accommodating 10 channels and one extra module for distributing the trigger signal across the backplane. Alternatively, a 6U Eurocrate is being considered which would lead to a somewhat more compact unit with 20 channels. In both cases one complete rack will be needed on either side of the TPC which will also accommodate the remotely-controlled power supply system.

Before installation the system has to undergo stringent quality tests. As for the front-end electronics (see Section 5.1.9) a burn-in procedure lasting for about 10 h at 50° C is foreseen.

4.3 Calibration

In this chapter calibration issues related to the operation of the ALICE TPC are described. In the first part the laser system is presented addressing the determination of electron drift velocity, residual drift-field distortions, distortions related to $\mathbf{E} \times \mathbf{B}$ effects and corrections of mechanical misalignment of the readout chambers. In the second part the electronic pulser system for the gain and time equilibration of the 570 000 readout channels is described. The third part deals with the calibration of the gas amplification variations across individual readout chambers due to mechanical imperfections.

4.3.1 Laser system

4.3.1.1 Introduction

Narrow and short-duration UV laser beams can be used to simulate particle tracks in the TPC [8]. Nd:YAG lasers (1064 nm) with two frequency doublers, generating a beam with 266 nm wavelength, have been successfully applied for this purpose in NA49 and in CERES/NA45 at the SPS. The ionization occurs via two-photon absorption and thus the transverse distribution of the ionization density is in every direction $\sqrt{2}$ times narrower than the light-intensity distribution. On the other hand, the square of the fluctuation of the laser intensity will enter into the ionization.

4.3.1.2 Design considerations

The aim of the laser calibration system is to measure the response of the TPC to straight tracks at known position. In particular, the laser system should allow the TPC readout electronics and software to be tested, distortions caused by misalignment of the sectors to be measured, temporal and spatial changes of the drift velocity down to 10^{-4} to be monitored, apparent track distortions due to $\mathbf{E} \times \mathbf{B}$ and space-charge effects to be measured, and the transition region between the drift volume and wire chambers to be understood.

The first two objectives can be achieved by mere presence of several laser tracks crossing the TPC volume under various angles, based on the fact that the laser tracks are straight. We plan to have 168 beams in each of the TPC halves. For monitoring, reproducibility of the laser beam position is important, while the study of $\mathbf{E} \times \mathbf{B}$ and space-charge effects requires knowledge of absolute position. We currently assume that the absolute position will be known up to 2 mm at the entrance of the track into the TPC, and up to 2 cm at its end-point, and that the relative position will be known up to 0.2 mm and 2 mm at the entrance and end-point, respectively.

The laser installation should not contribute a significant amount of material. Following the STAR approach [26] we decided to illuminate clusters of small (1 mm diameter) mirrors by a wide beam (Gaussian profile with $\sigma \approx 2$ cm). The profile of the reflected beam is then determined by the mirror rather than the incident beam. This is an efficient way of producing many narrow beams and it does not require installation of opto-mechanical devices inside the detector.

Monitoring drift velocity will be realized by running lasers in parallel to the normal physics data-taking. The other questions will be addressed by means of dedicated laser runs. Monitoring and calibration will thus be the two modes in which the laser system will be used.

4.3.1.3 Implementation

The planned overall layout of the laser system is shown in Fig. 4.40. Each half of the TPC has its own laser. With the help of remotely controlled mirrors, and with CCD cameras and position-sensitive diodes used for diagnostics, the laser beam is transported to the edge of the corresponding end-plate.

Subsequently, the beams are reflected several times by prisms such that they follow the outer edges of the end-plates (Fig. 4.41).

At six of the 18 positions, where the beam passes close to the ends of the rods which support the field-cage, partially reflecting mirrors are used to send part of the light into the hollow rods. A mirror located at the opposite end of each rod and perpendicular to its axis helps to adjust the six beams parallel to their respective rods. This is done by requiring that the incident and the reflected beams overlap. Inside the rods, at four different depths in z , micro-mirror clusters are installed such that they do not shadow each other (Fig. 4.42). The micro-mirrors are 1 mm diameter glass fibres, cut at an angle of 45° , polished, and coated. A mirror cluster is a bundle of seven such fibres. Each fibre in a bundle is slightly rotated. This way each bundle generates a fanning-out pattern of seven beams. The rod wall has an opening such that the reflected beams can get out of the rod and enter the TPC volume.

Once the beams are aligned in the rods, the positions of all the rays in the TPC are determined by the positions and angles of the micro-mirrors. The angles of the individual micro-mirrors in a mirror bundle need to be precisely calibrated in the laboratory prior to installation of the bundle in a rod. The positions and the orientations of the bundles in the rods will be measured by photogrammetric methods. Some of these measurements will be repeated after the rods have been installed in the TPC.

The measurement of the laser beam position will be difficult because of the large beam diameter. We consider using lenses to focus the beam on the sensitive area of CCD cameras (or diodes). The cameras (or diodes) will have to be located somewhat before the position of the focus. Alternatively one can use the Poisson line technique [27].

The lasers and mirrors will be controlled via a PC. The diode data will be readout and fed into the TPC data-acquisition system.

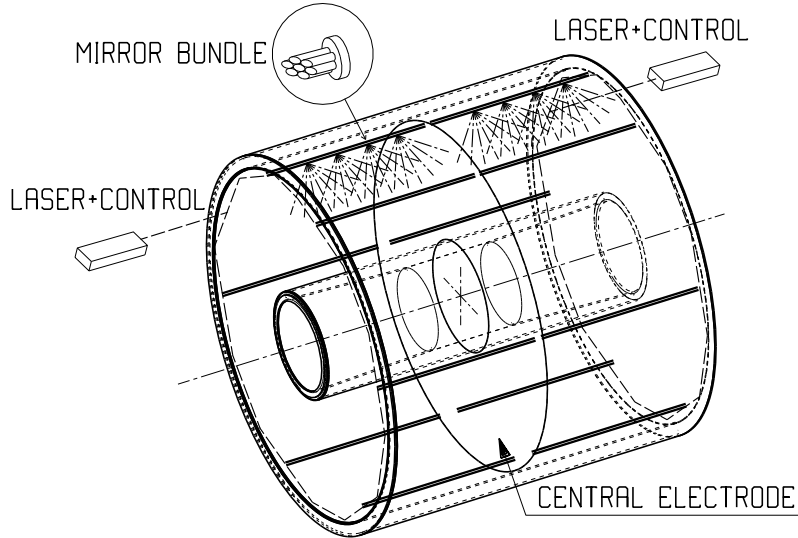


Figure 4.40: Overall layout of the laser system. Each half of the TPC has its own laser. The laser beams follow the perimeters of the end-plates, passing through partially reflecting mirrors which send part of the light into the support rods. For clarity, only tracks originating from one rod are indicated.

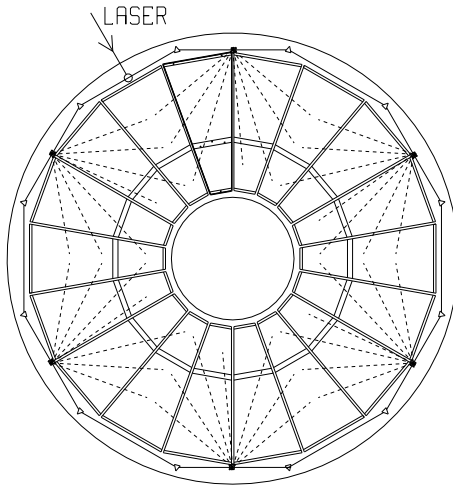


Figure 4.41: Distribution of the laser beams on the TPC end-plates. Also shown is the pattern of laser tracks at one of the four z -positions at which the mirror bundles are mounted.

4.3.1.4 Production and survey

The micro-mirror bundles will be built in collaboration with the group of A. Lebedev (STAR Collaboration). We have tested one such mirror bundle. The transverse beam profile of the beam reflected off one of the micro-mirrors, measured at different distances from the mirror, is shown in Fig. 4.43. The reflected beam profile, measured directly after the mirror, depends on the mirror shape and quality. After some 60–80 cm the beam becomes narrow and Gaussian. This is the waist of the beam; from there on the beam diameter increases.

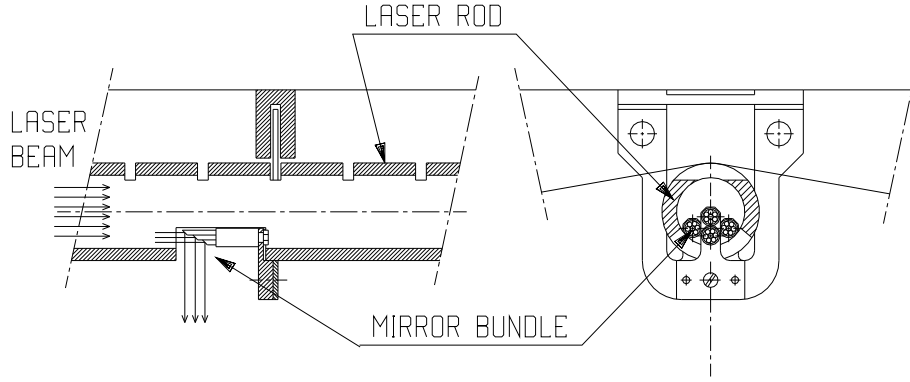


Figure 4.42: Bundles of micro-mirrors, mounted inside the field-cage support rods. The subsequent bundles are aligned such that they do not shadow each other.

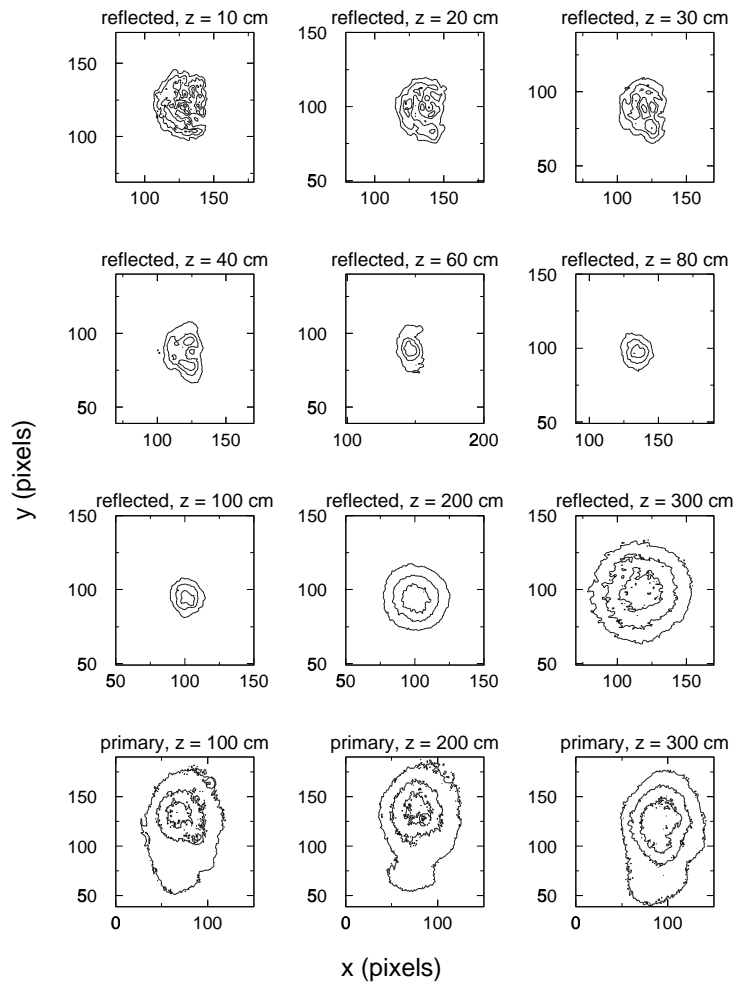


Figure 4.43: Evolution of the beam profile after a reflection off a micro-mirror. Directly after the mirror the beam has a box profile, with a size equal to that of the mirror (1 mm). About 60–80 cm later the beam acquires a perfect Gaussian shape with diameter $d \approx 0.6$ mm. (For Gaussian beams diameter is defined as four standard deviations, $d = 4\sigma$.) Subsequently, the beam stays Gaussian and its diameter increases to $d = 1.6$ mm at 300 cm, which corresponds to a divergence of 0.5 mr. For comparison, the bottom row shows the profile of the incident beam we used. (For this measurement the micro-mirror bundle was removed.)

4.3.2 Electronics calibration

The purpose of the electronic calibration system is threefold:

- **General operational tests** of the complete readout chain, i.e. preamplifier/shaper, digitizer, zero suppression, buffering, data transfer, etc. In particular, dead or defective channels should be detected.
- **Gain equilibration of all electronic channels:** The position measurement in the azimuthal direction relies on the precise determination of the cluster centroids, i.e. the weighted mean of the charge seen by neighbouring pads. In addition the requirement of 7% resolution in dE/dx puts constraints on the allowed variation of the electronics gain. The gain factors of individual channels or groups of channels should therefore not vary by more than 2%. Owing to variations in the chip manufacturing process differences in gain of 10% have been observed [28]. A relative gain calibration is therefore indispensable. In addition the pulser can be used to determine the linearity of the electronics by generating a sequence of increasing amplitudes.
- **Equilibration of the readout timing:** The determination of the drift coordinate requires a relative precision of the time measurement between different channels to be within 7 ns (200 μm). Variations in the timing are caused by varying cable lengths in the distribution of the trigger signal over the TPC readout plane and by variations in the shaping time of the preamplifier/shaper chips. The latter can easily reach 30 ns (corresponding to 850 μm).

4.3.2.1 Principle of operation

For the gain calibration the injection of an equal amount of charge into individual readout channels is crucial. One method to achieve this is the pulsing of a wire plane of a readout chamber. Owing to the mechanical precision of around 50 μm a very homogeneous capacitive coupling between the various wire planes and the pad plane is ensured. Even in the case of distance variations between cathode plane and pad plane by more than the specified value over the full width of a chamber, the local variations are only small. Therefore it is always guaranteed that the variation of charge injected into adjacent pads is in fact well within 1%.

The capacitive coupling between the cathode wire plane and the pads leads to a differentiation of the signal. Therefore the signal generated by the calibration pulser has to be the integral of the desired pulse shape at the pads. This is schematically shown in Fig. 4.44. The voltage returns to zero only after the 100 μs readout time of the TPC.

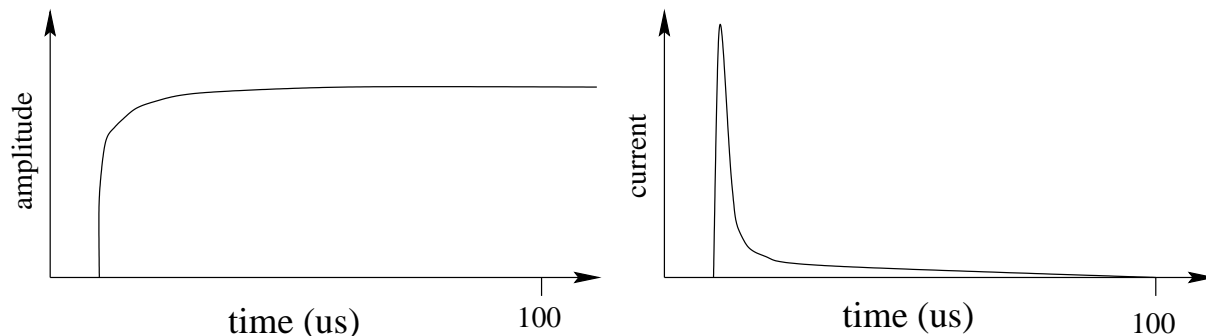


Figure 4.44: Pulse shape generated by the pulser system and fed into the cathode wire grid (left). This pulse induces a current in the pads simulating the signal from a charged particle (right).

4.3.2.2 Implementation

Because of the design of the ALICE readout chambers (see Section 4.1.1) the injection of charge is most easily done by pulsing of the cathode wire plane. Instead of connecting it directly to ground a $50\ \Omega$ resistor is introduced, acting as the termination resistor of the cable connected to the driver stage of the calibration pulser.

The pulser itself can be regarded as an arbitrary waveform generator. A schematic diagram is shown in Fig. 4.45. It is foreseen to be set up in a 3U Euro crate. It consists of the following components:

- An **interface** to the ALICE detector control system via a field bus (CAN bus, Profibus). During normal operation the pulser is switched on/off and the amplitudes are set via this communication link.
- A **field programmable gate array (FPGA)** acts as controller of the system. The pulse shape of the desired output signal is stored as a sequence of amplitudes in a SRAM. On command the FPGA switches from a dormant into a pulse-generating state taking into account the desired amplitude and the stored reference shape. The FPGA also controls which of the driver channels are actually activated.
- A **fast digital-to-analog converter (DAC)** with 16 bit resolution and 30 ns settling time generates the pulse shape according to the amplitudes stored in memory. This reference signal is distributed via a common bus line to the cable drivers.
- The **output drivers** are connected via a high-impedance input to the DAC. Their function is to drive the $50\ \Omega$ cables connected to individual TPC readout chambers. Each board accommodates

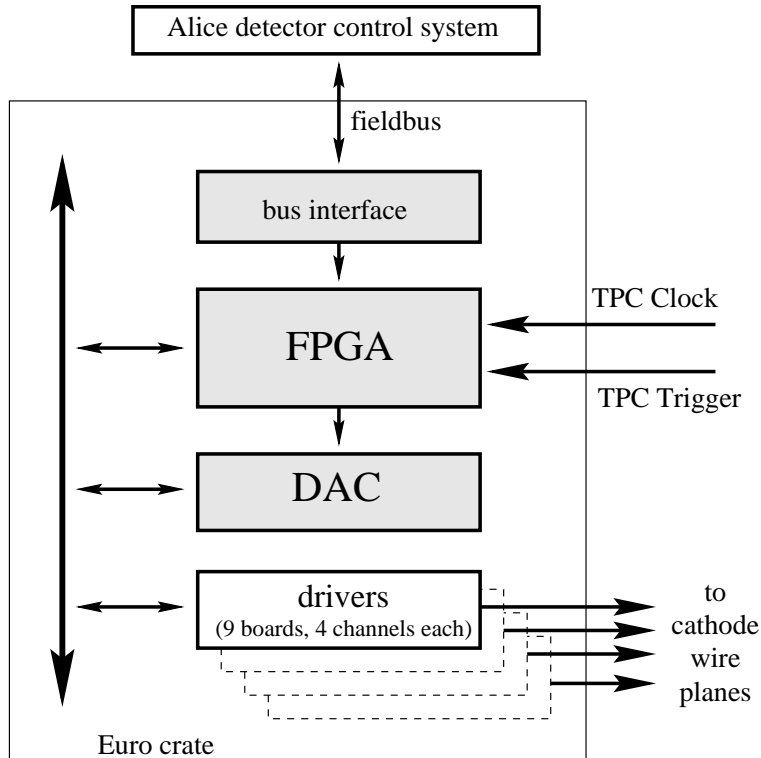


Figure 4.45: Schematic diagram of the main components of the calibration pulser system. One such unit is foreseen for each side of the TPC.

four channels. An additional control function allows the activation/deactivation of individual driver channels. This feature will allow individual chambers or groups of chambers to be pulsed.

One pulser module accommodates the 36 channels necessary to supply one readout plane of the TPC with its 18 inner and 18 outer chambers.

The pulser is connected to the clock and trigger distribution system of the front-end electronics. It is triggered by the normal TPC trigger except that the FPGA internally delays the pulse generation by a preset number of clock ticks. The use of the general TPC clock ensures that the calibration pulse is synchronized to the readout of the TPC.

A prototype of the system described has been built in Frankfurt and is at present undergoing performance tests [29]. A similar system has been built for the NA49 experiment [28], [30]. The main difference is the larger flexibility of the system under development: In the old system the shape of the output pulse is determined by a network of three RC circuits and thus the pulse shape cannot be changed easily. It is also not possible with this method to simulate properly the $1/t$ tail of the typical wire chamber output signal.

The following performance figures have been achieved in the NA49 system and are expected to be reproduced with the new system: range of output amplitudes 0–4 V with a nonlinearity of $\leq 1\%$, and a stability of $\leq 0.25\%$. The amplitude variations between different output channels are 0.04%.

It is foreseen to install the two calibration pulser systems in the rack space close to the L3 magnet in the nonaccessible cavern area UX25.

4.3.3 Krypton calibration

Variations of the gas gain due to mechanical imperfections of the readout chambers (wire sag, deformations) can be investigated by the release of a fixed amount of charge into the amplification region. The addition of radioactive ^{83}Kr to the drift gas can serve this purpose. It has been used extensively by the NA49 experiment (see Ref. [6] and references therein).

A ^{83}Rb source (produced at the ISOLDE Isotope Separator at CERN) is mounted in a bypass of the TPC recirculation system. It decays with a half-life of 124 days into an isomeric state of the stable isotope ^{83}Kr , which decays into the ground state with a half-life of 1.8 h via an excited state at 9.4 keV with a half-life of 147 ns. (A detailed description of the decay chain can be found in Ref. [31].) This decay chain provides several electron energies spread over a large dynamic range well suited for the calibration of the readout chambers. In Fig. 4.46 a Monte Carlo simulation of the resulting charge distribution is compared to the measurement in one of the TPCs of the NA49 experiment. The short lifetime of ^{83}Kr allows normal operation of the TPC several half-lives after the gas flow is cut off from the bypass housing the ^{83}Rb foil. Since it is not possible to derive a trigger from individual decays it is necessary to start the TPC readout by a random trigger. The consequence of this is that the information about the position of individual decays in the drift direction is lost. The charge measured is therefore affected also by the electron capture in the drift gas, although for reasonably small electron losses this poses no problem.

The NA49 experience shows that variations of gas gain can reach up to 10% over the surface of individual readout chambers. The application of the krypton calibration reduces this to 0.5%.

A new and thus relatively strong source of 180 MBq leads to 1000 ^{83}Kr decays during readout of 50 μs in NA49. Since the rate capability of ALICE is about a factor 100 higher than that of NA49 a data-taking period of a few hours should allow the production of high-statistics charge spectra for each channel.

It is worth mentioning that the krypton method is well suited to study long-term changes of the gas amplification, in particular ageing effects. In addition it also allows the study of gas flow pattern inside the TPC volume within certain limits. Owing to the loss of information about the drift coordinate, only a projection of the charge distribution as a function of time after injection of ^{83}Kr is possible. In Fig. 4.47 an example is shown from the NA49 Main TPC. In the top left panel the gas starts to enter the TPC from the bottom passing a deflector plate. The gas diffuses around the plate and populates preferentially one

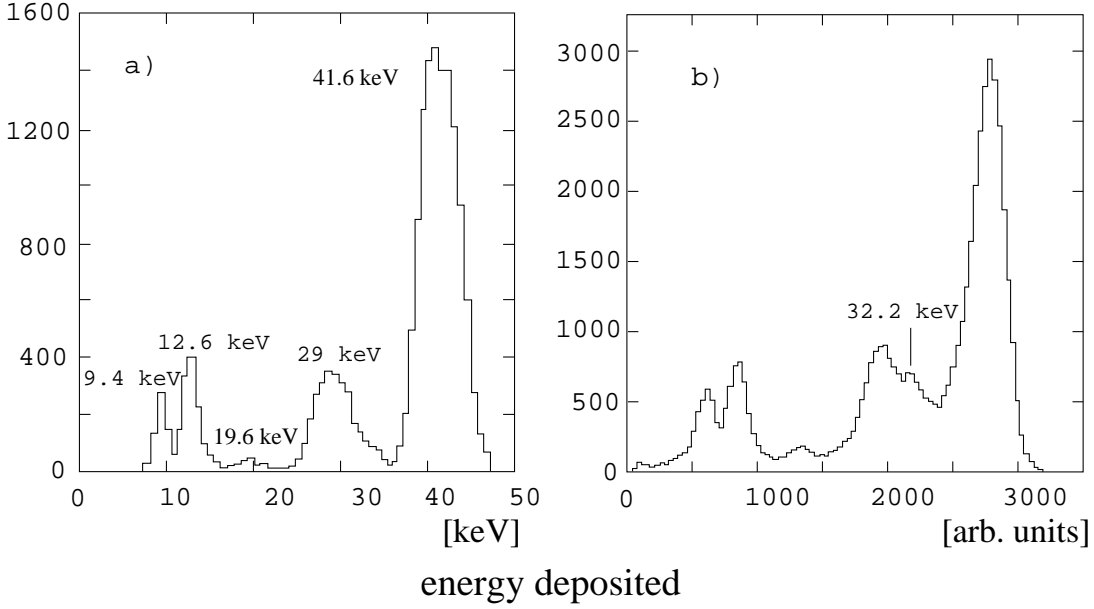


Figure 4.46: Charge spectrum from ^{83}Kr decays in the NA49 Main TPC: (a) Monte Carlo simulation, (b) data [6].

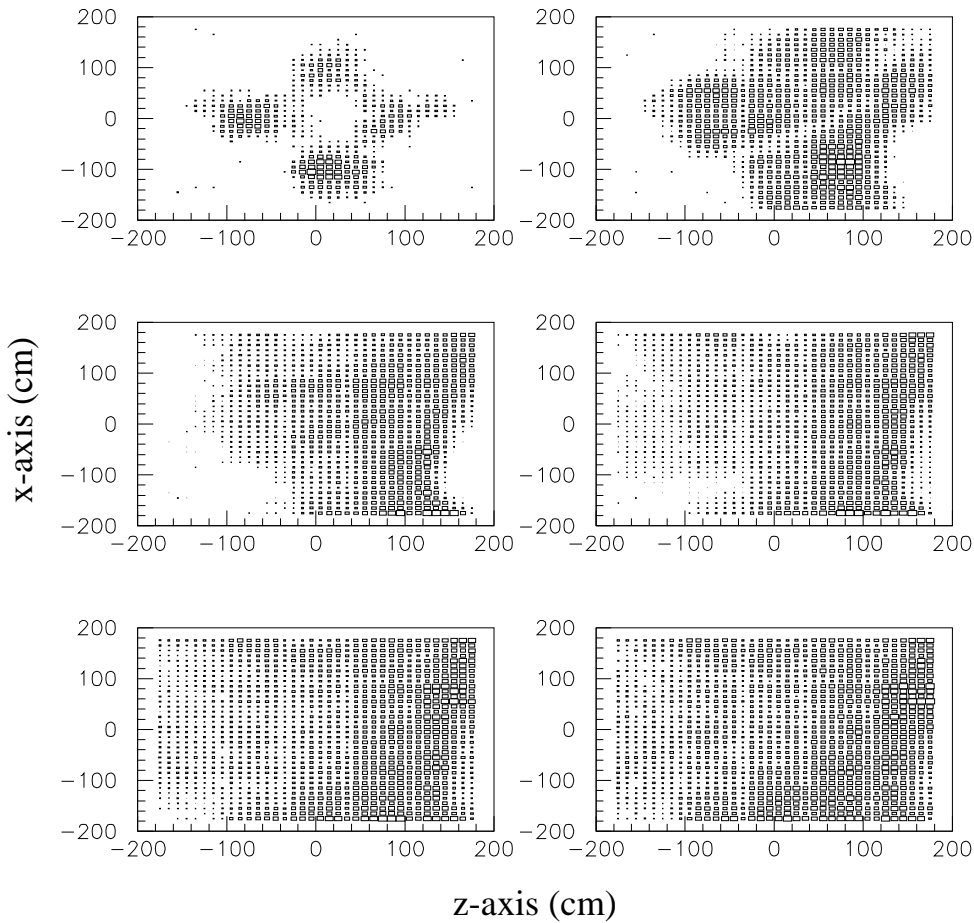


Figure 4.47: Distribution of charge inside the NA49 Main TPC at six time intervals after injection of ^{83}Kr into the gas stream. Shown is a projection of the drift volume on the readout plane. The size of the boxes is proportional to the number of clusters reconstructed. Total time covered is about nine minutes.

side of the TPC before becoming more uniformly distributed over the whole area. The TPC volume is 18 m³ and the flow rate of the gas corresponds to a 30% volume exchange per hour.

Some information about the distribution in the drift direction can be obtained by monitoring the currents in the readout chambers. Upon arrival of ⁸³Kr in the amplification regions of the wire chambers their dark current goes up. This allows an estimate of the time it takes for the gas to pass through the entire TPC volume.

5 Front-end electronics and readout

5.1 Front-end electronics

5.1.1 Introduction and overview

This section reviews the requirements for the front-end electronics and discusses briefly the general architecture and the basic building blocks.

5.1.1.1 General requirements

As detailed in Sections 4.1.2 and 4.1.4, the front-end electronics has to read out the charge detected by 570 000 pads located on the readout chambers at the TPC end-caps. These chambers deliver on their pads a current signal with a fast rise time (less than 1 ns), and a long tail due to the motion of the positive ions. The amplitude, which is different for the different pad sizes, has a typical value of $7 \mu\text{A}$. The signal is delivered on the detector impedance which, to a very good approximation, is a pure capacitance of the order of a few pF.

The main requirements for the readout electronics, listed in Table 5.1, are briefly discussed below.

- Diffusion and electron statistics limit the resolution both in the drift and azimuthal directions. Monte Carlo studies (Section 4.1.2) indicate that to reach the detector resolution limit a signal-to-noise ratio of 30 : 1 is required.
- The maximum pad and time bin for a hit corresponds typically to a charge of about 4.8 fC (3×10^4 electrons) for a minimum ionizing particle, leading to a maximum acceptable noise (r.m.s.) of about 1000 electrons.
- The ionization to be measured in a single pad can be large. The most probable proton transverse momentum is expected to be about 550 MeV/c; 280 MeV/c and 340 MeV/c protons, e.g., have

Table 5.1: Front-end electronics requirements.

Parameter	Value
Number of channels	570 132
Signal-to-noise ratio (MIP)	30 : 1
Dynamic range	900 : 1
Noise (ENC)	1000 e^-
Conversion gain	12 mV/fC
Crosstalk	< 0.3%
Shaping time	about 200 ns
Sampling rate	5.66(-7.69) MHz
Tail correction after 1 μs	0.1%
Bandwidth to DAQ/Level-3	8.4 GByte/s
Maximum dead time	10%
Power consumption	< 100 mW/channel

about 15 and 8 times the energy loss of a MIP, respectively. Owing to Landau fluctuations, another factor 2–4 in dynamic range has to be considered. Thus, the electronics should not saturate for signals up to 30 MIP (Section 7.1), leading to a desired dynamic range of at least 10 bits.

- The amplifier conversion gain has to be such that the maximum output signal matches the input dynamic range of the ADC. An ADC with 2 V dynamic range, e.g., requires a conversion gain of about 12 mV/fC.
- In general, the shaping time has to be a compromise between the need for achieving a high signal-to-noise ratio (bandwidth limitation) and for avoiding overlap of successive signals. It should be noted that, owing to longitudinal diffusion and to the track inclination, the signal spreads in time. Therefore, as soon as the shaping time becomes small as compared to the width of the pulse, the current pulses due to the different primary electrons will be visible at the shaper output. The signal width varies from 124 ns (r.m.s.), for 90°-tracks, to 400 ns (full width), for 45°-tracks. It can be shown [1] that a shaping time of about 200 ns, comparable to the signal width (FWHM), is compatible with the low-noise requirement.
- The shaping time of about 200 ns makes a sampling frequency of 5–6 MHz plausible. We therefore divide the total drift time of 88 μ s into about 500 time bins, leading to a sampling frequency of 5.66 MHz. Each of the 500 time bins corresponds to a drift distance of 5 mm. Simulations show that with 130 ns time bins a somewhat better momentum resolution can be achieved (see Section 4.1.2.3) albeit at the expense of a larger data volume. We keep the option open to run with a sampling frequency of up to 7.69 MHz, possibly just for the smaller radii.
- Owing to the high channel occupancy, in order to minimize pile-up effects, a very precise tail cancellation, at the level of 0.1% of the maximum pulse height, is required in the front-end stage. This can be done either before or after the analog-to-digital conversion.
- The large granularity of the TPC (3×10^8 pixels for 500 time bins) leads to event sizes of about 84 MByte after zero suppression (132 MByte for time bins of 130 ns). To achieve the necessary rate capability the zero suppression has to be done in the front-end before the data is transferred to the DAQ system. In Pb–Pb running, event rates will reach 10^4 minimum bias events per second, while in pp running the maximum interaction rate will be of the order of 10^5 interactions per second. A few percent of these rates correspond to central collisions that will be trigger selected. Zero suppression at the front-end will reduce the data volume by a factor 2.5, leading to a data throughput of 8.4 GByte/s (13.2 for the shorter time bins) with 100 events/s transferred to the DAQ/Level-3 processing¹. The reduction from the Level-1 rate of up to 200 Hz to 100 Hz after Level-2 is due to pileup protection against further interactions during the entire drift time of the TPC. We imagine that this could be relaxed depending on occupancy and experiences (from STAR and also our own) to a shorter protection period. Taking this into account, at least 140 Digital Data Links (DDLs) should be foreseen for the data transfer from the front-end electronics to the DAQ (as outlined in Section 5.1.1.2 actually 180 links will be used). In pp mode the detector will produce a data volume smaller by a factor 5.
- A critical aspect in the TPC operation is the temperature stability; to ensure a constant drift velocity it has to be controlled at the level of about 0.1 °C over the whole volume. The large number of channels (570 000) requires development of a system with low power consumption. The aim is to keep the total power consumption below 60 kW (100 mW/channel). We plan to remove the heat from the readout modules with a water cooling system (see Section 4.1.4.2).

¹The compression from 10-bit data to nonlinear 8-bit and according packaging could be done at the front-end level leading to 66 MByte per event. For the data format also see Section 5.1.3.5.

- The radiation load on the TPC is low, with a total dose received over 10 years of less than 300 rad and a neutron flux of less than 10^{11} neutrons/cm². Thus standard radiation-soft technologies are suitable for the implementation of this electronics. Nevertheless, some special care should be taken to protect the system against potential damage caused by Single Event Effects (SEEs).
- The electronics will be located in an area with limited access. High reliability is thus a concern.

The front-end electronics system has to satisfy many other constraints while meeting the required performance specifications. Mainly, the readout electronics needs to fit into the overall detector structure and, in particular, into the available space, which has important consequences for our requirements on reliability, power, and cooling.

The following sections provide more details on these requirements and show how we plan to meet these challenges.

5.1.1.2 System overview

The front-end electronics for the ALICE TPC consists of 570 000 channels. A single readout channel is comprised of three basic units (Fig. 5.1 and Colour Fig. IX): a charge sensitive PreAmplifier/ShAper (PASA); a 10-bit 10 MHz low-power ADC; and an ASIC which contains a shortening digital filter for the tail cancellation, the baseline subtraction and zero-suppression circuits, and a multiple-event buffer.

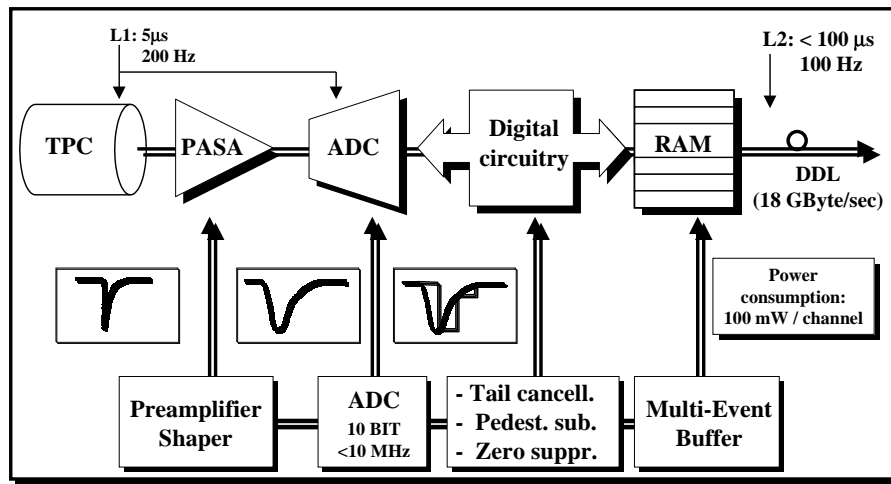


Figure 5.1: Basic components of the TPC front-end electronics.

The image charge induced on the TPC pads is amplified and integrated by a low input-impedance amplifier. It is based on a Charge-Sensitive Amplifier (CSA) followed by a semi-Gaussian pulse shaper of the second order. These analog functions are realised by a custom integrated circuit, to be implemented in CMOS technology, which will contain 16 channels with a power consumption per channel below 20 mW. The circuit has a conversion gain of 12 mV/fC and an output dynamic range of 2 V with deviations from linearity of 1%. It produces a pulse with a rise time of 120 ns and a shaping time (FWHM) of about 200 ns. The single channel has a noise value (r.m.s.) below 1000 e and a channel-to-channel crosstalk below about 60 dB.

Immediately after the PASA, a 10-bit ADC (one per channel) samples the signal at a rate of 5.66 MHz. ADCs of the required conversion time, dynamic range, and precision are commercially available. The strict limitation on the power budget (100 mW/channel) calls for low-power ADCs. Single-, double- or quadruple-channel ADCs, with power consumption below 50 mW, are available. Furthermore, most of them feature standby power consumption below 10 mW. This feature is very important since the ALICE

TPC has a duty cycle of less than 10%. A study of several commercially available ADCs has been completed, showing that the ALICE TPC requirements, in terms of performance and power consumption, are fulfilled in the frequency range of interest.

The digitized signal is processed by a set of circuits contained in an ASIC named ALTRO [2]. The ALTRO (ALice Tpc ReadOut) is a custom CMOS chip which contains the circuitry, for eight channels, to perform tail cancellation, pedestal subtraction, zero suppression, formatting, and buffering.

The circuit that removes the long tail is based on the cascade of two pole-zero shortening filters of the first order. This filter, implemented by a 16-bit fixed-point arithmetic, achieves a tail cancellation better than 0.1% of the maximum pulse height. After the tail cancellation, the ALTRO performs the subtraction of the signal baseline. This is done by a circuit, based on a look-up table, which corrects the systematic instability of the signal baseline, allowing the subtraction of (drift) time-dependent pedestal values from the input data values. Rejecting the samples of value smaller than a constant decision level (threshold) basically does the zero suppression. To reduce the noise sensitivity of this pulse detection scheme, a glitch filter checks for a consecutive programmable number of samples above the threshold. Moreover, in order to keep enough information for further feature extraction, a programmable sequence of pre-samples and post-samples can also be recorded. The zero-suppressed data are then formatted into 32-bit words according to a back-linked data structure. Trigger-related data are stored in a multiple-event buffer. The multiple-event buffer is a RAM of 1 k words, 32 bits wide, partitioned in a programmable number of up to eight fixed-length buffers. The ALTRO chip interfaces to the external world through a 40-bit control bus based on a data transfer protocol that supports a data rate of 160 MByte/s.

The complete readout chain is contained in the Front-End Cards (FEC) plugged into crates attached to the detector mechanical structure as sketched in Fig. 4.29 on page 69. Each FEC contains 128 channels and is connected to the readout pad plane by means of eight flexible cables with 16 signals each. 32 FECs are controlled by a Readout Control Unit (RCU), which interfaces the FECs to the DAQ, the trigger, and the Detector Control System (DCS). The RCU broadcasts the trigger information to the individual FEC modules and controls the readout procedure. Both functions are implemented via a custom bus, based on low-voltage signalling technology which provides a data bandwidth of 160 MByte/s. The interfacing of the RCU modules to the trigger and to the DAQ follows the standard data-acquisition architecture of the experiment [3].

In summary, for each of the 36 TPC sectors, the front-end electronics consists of 125 FECs, 5 RCUs, and 5 DDLs.

5.1.2 Interconnection to the readout pad plane

5.1.2.1 Electronics mapping

Several constraints define the mapping of the detector into front-end boards.

- The total length of the connecting wires has to be minimized.
- The cables used for this connection should be all of the same length. This should avoid the production of several types of cables and, especially, should guarantee the homogeneity of performance over the different regions of the detector.
- Cable crossing should be avoided to minimize the risk of error and a solution as uniform as possible is desirable.

These considerations lead to the interconnection scheme shown in Fig. 4.29 on page 69. The signals coming from 16 pads are grouped together and transported to the front-end cards via a cable soldered directly onto the pad plane. The high granularity in the connectivity allows to keep sufficiently short the traces by which the signals are collected from the pads and concentrated in the area where the cables are soldered (transport points). Only the pads located at the top and bottom edges of the readout chambers

which, due to the mechanical frame, are not directly accessible represent an exception and require longer traces.

As each sector is segmented into three regions with three different pad sizes, the first two requirements call for at least three different types of boards. To avoid a further increase in the number of different types of boards, we opted for a radial orientation of the boards as shown in Fig. 4.29 on page 69. The boards are grouped in five crates of (from the inside out) 20 (C1), 25 (C2), 22 (C3), 26 (C4), and 32 (C5) boards. All FECs have the same functionality and the same number of channels (128) but slightly different geometry. The FECs of the first two crates are connected to the pads of the inner readout chamber and are the smallest ones. The boards of the next two crates are connected to the central-sector pads and the last crate is connected to the outer sector. The number of different types of boards and their dimensions are summarized in Table 5.2.

Table 5.2: Classification of the front-end electronics cards.

Group	No. of boards	Dimensions [cm ²]
C1	20	19 × 14
C2	25	19 × 14
C3	22	29 × 14
C4	26	29 × 14
C5	32	40 × 14

5.1.2.2 Cables and connectors

To keep the crosstalk within the specified limit all the connections inside the connectors must be low inductance. The crosstalk of the whole chain is currently under simulation, but a finite-element 3-D model of the cable and connector has already been created and simulated.

The cables used to transfer the signals from the pads to the input of the amplifier are polyimide striplines, especially designed to minimise crosstalk, pick-up noise, and heat transfer to the pad plane. Each cable contains 16 channels and has a length of about 7 cm. As is shown in Fig. 5.2, the signal

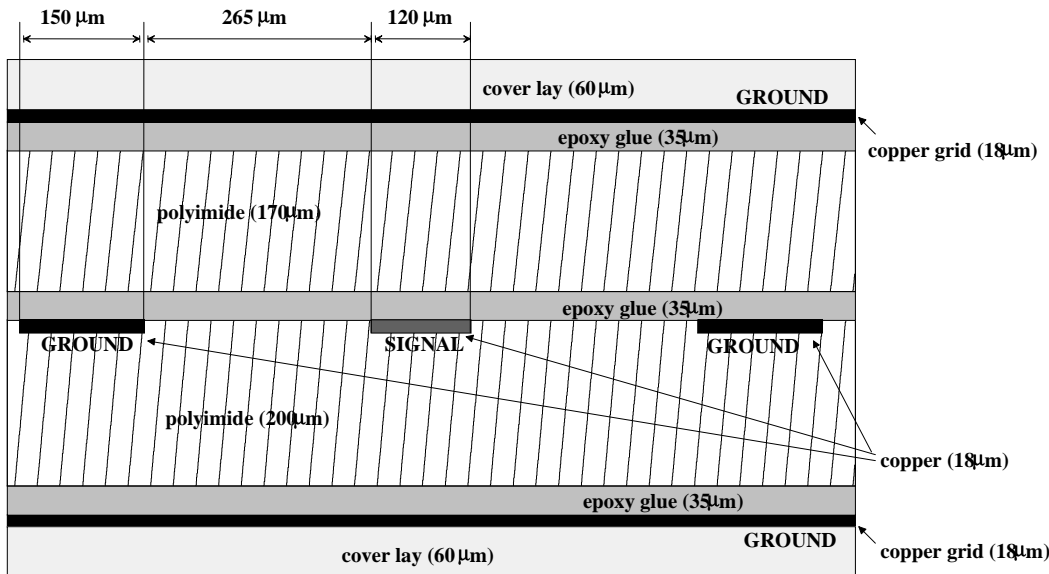


Figure 5.2: Cross-section of the front-end cable.

traces are $120\ \mu\text{m}$ wide with a pitch of $0.8\ \text{mm}$. The ground returns, $150\ \mu\text{m}$ wide, are alternated with the signal strips from which they are at a distance of $265\ \mu\text{m}$. Two solid ground planes shield completely the striplines. The crosstalk has been simulated to be less than 0.1%. The results of these simulations are shown in Table 5.3.

The proposed connector is a matched impedance connector (QSE-SAMTEC) [4] developed for high-bandwidth applications (higher than $1\ \text{GHz}$) and low crosstalk. The connector consists of a socket and terminal set with an integral ground plane running between two rows of pins. The signal pins have a pitch of $0.8\ \text{mm}$. The main characteristics are listed in Table 5.4.

Table 5.3: Electrical parameters of the front-end cable: impedance (Z_0), propagation delay (t_d), capacitance (C), mutual capacitance (C_M), inductance (L), mutual inductance(L_M), and crosstalk.

Z_0 [Ω]	t_d [ns/m]	C [pF/m]	C_M [pF/m]	L [nH/m]	L_M [nH/m]	crosstalk [%]
64	6.4	99.70	0.06	410	0.03	0.05

Table 5.4: $50\ \Omega$ connector, S-G-S configuration with center plane grounded.

0.8 mm pitch (QTE)	100 MHz	500 MHz	1 GHz
Impedance [Ω]	50.7	55.0	60
Attenuation [dB]	-0.0305	-0.2429	-0.4607
Crosstalk [dB]	-60.6	-49.0	-39.5
Propagation delay [ps]	58.4	58.4	58.4

5.1.3 Front-end basic components

5.1.3.1 Preamplifier/shaper

The basic requirements for the preamplifier/shaper chip have been outlined in Section 5.1.1.1 and in Table 5.1 on page 91. The typical number of electrons (before amplification, etc.) generating the signal on the maximum pad and time bin of a cluster is shown in Fig. 5.3 for the three pad sizes and three ranges in polar angles. As can be seen it varies systematically with pad area and for the largest pads the signals are about a factor 2 bigger than for the smallest inside pads. In comparison, the dependence on polar angle is small. In order to achieve a signal-to-noise ratio of $30 : 1$ for all pad sizes a factor 2 variation in gas gain is required. However, working with the same gas gain entails only a moderate loss in resolution as detailed in Section 4.1.2. As far as the preamplifier/shaper is concerned we envision one gain setting that puts the noise equivalent of 1000 electrons in channel 1 of an ADC with 2 V full scale. This defines the required gain as $12\ \text{mV/fC}$.

To achieve an overall system noise of 1000 electrons per channel for a typical input capacitance of about $4\ \text{pF}$ for the pads plus about $10\ \text{pF}$ for the on-board traces plus the polyimide cables requires a low-noise device.

We intend to take the design of the NA45 CERES TPC preamplifier/shaper [5] as a starting point and to optimize it for the ALICE needs, migrating from $0.8\ \mu\text{m}$ CMOS technology to $0.35\ \mu\text{m}$ and incorporating again 16 channels on one chip. The schematics of this circuit are shown in Fig. 5.4. For the ALICE application the tail-cancellation functionality will be removed from the preamplifier/shaper chip and be implemented in the digital chip (see below).

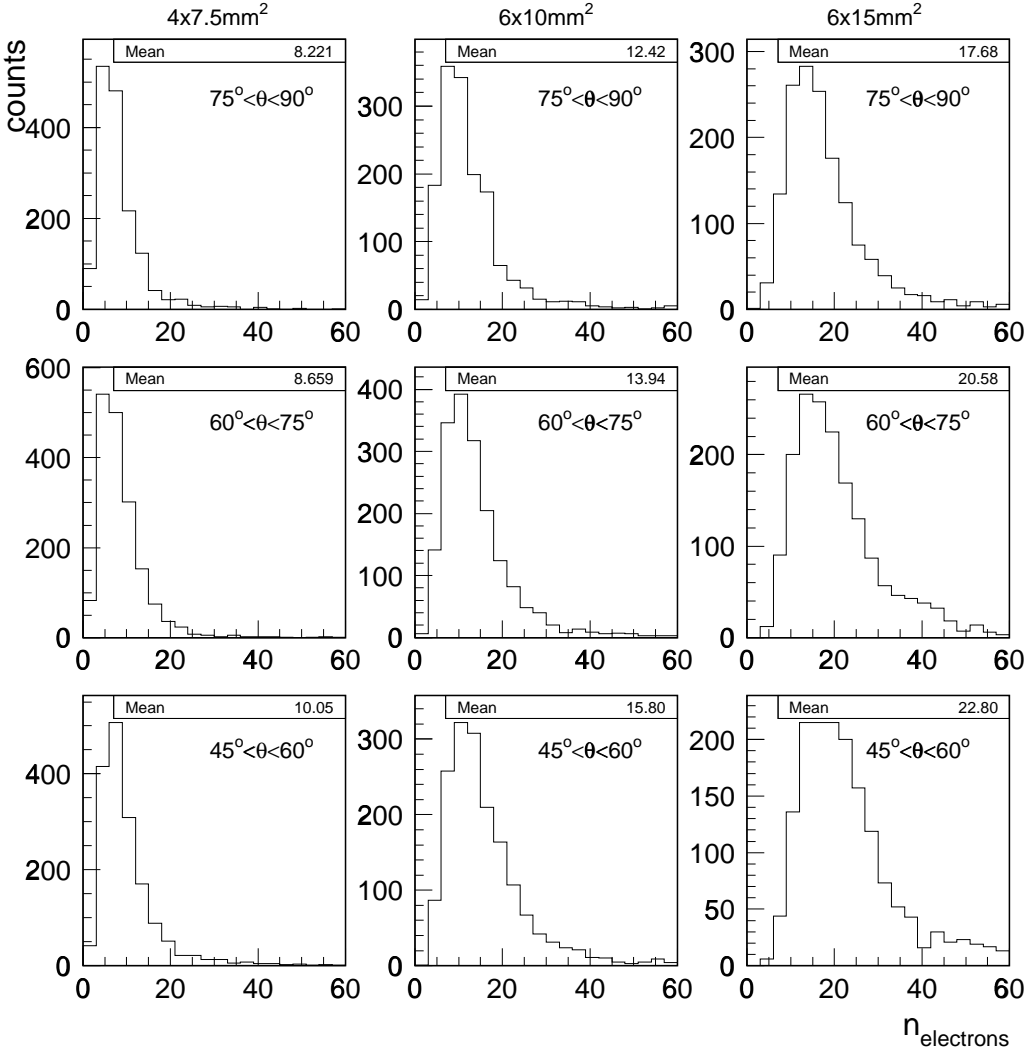


Figure 5.3: Number of electrons generating the signal in the maximum pad and time bin of a cluster for the different pad sizes and averaged over different regions in polar angle.

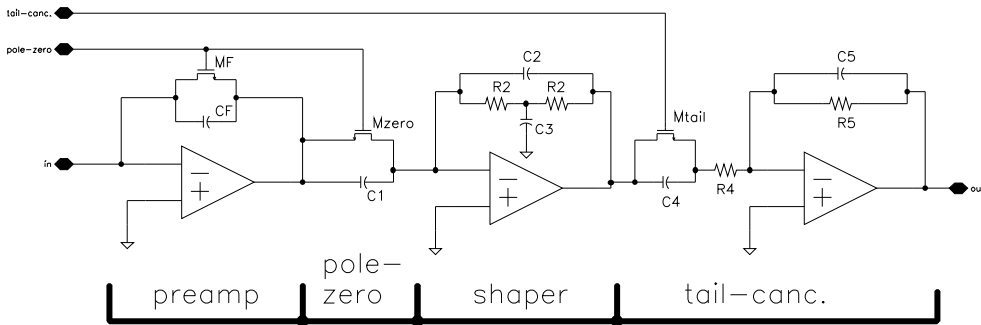


Figure 5.4: Schematics of the NA45 CERES TPC preamplifier/shaper circuit.

In contrast to e.g. the preamplifier/shaper developed for the STAR TPC which has a pulsed reset [6], the CERES design used a MOS transistor (MF) with a feedback capacitance C_F that is continuously discharged with a decay time $\tau_d = C_F \cdot R_{ds}(\text{MF})$ (see Fig. 5.4). This continuously sensitive design is particularly suitable for a detector with high occupancy. Noise considerations dictate a large feedback

resistance R_F (for e.g. a peaking time of 400 ns a value larger than $4 \text{ M}\Omega$) and the associated drain-source resistance R_{ds} of a MOSFET transistor. This has the advantage that R_{ds} depends on the biasing condition (the self-adaptive bias technique is used [7]) and that larger signals are discharged with a faster decay time (see Fig. 5.5). This is particularly relevant in an environment where signals of minimum-ionizing particles have to be measured in the presence of heavily ionizing low-energy particles. Near mid-rapidity it is expected that the abundance of protons and antiprotons is about 8% of pions and kaons with a most probable momentum of $0.56 \text{ GeV}/c$, implying that 15% of these have a mean energy loss of more than 8 MIP and Landau fluctuations will lead to even much larger signals. Therefore, beyond the question of dynamic range, in the design of the chip attention has to be payed to the response of the circuit to saturating signals.

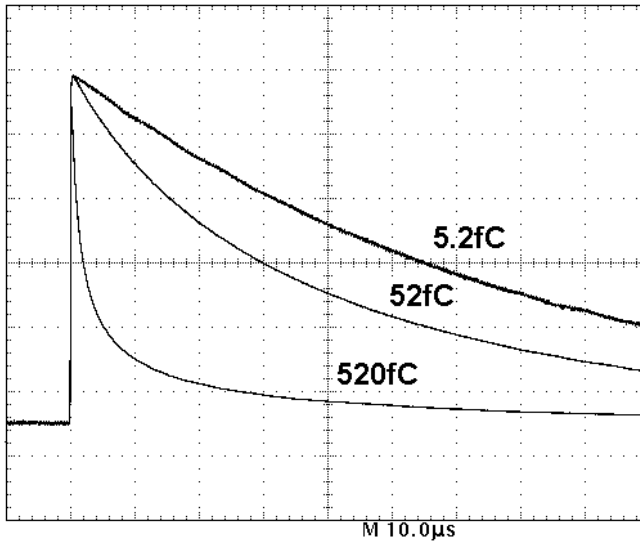


Figure 5.5: Response of the CERES charge-sensitive amplifier to input signals of increasing magnitude.

Particular attention in the design has to be given to the gain linearity in the presence of a nonlinear resistance in the feedback loop. In the CERES design this has been achieved by the self-adaptive bias technique [7] leading to a nonlinearity of the preamplifier of less than 2% for up to 350 fC input charge. For the ALICE application the maximum signal corresponds to 166 fC. In terms of noise requirements, the CERES preamplifier/shaper fulfills the requirement with an ENC of less than 600 electrons for input capacitances between 15 pF and 19 pF.

In terms of power consumption, the CERES chip requires about 60 mW per channel. For time reasons and because this was not a critical issue it has not been optimized for low power consumption. Already removing the tail cancellation and going to $0.35 \mu\text{m}$ technology should reduce the power consumption to about 1/3 and we are confident that the goal of less than 20 mW per channel can be achieved for an optimized design.

5.1.3.2 Analog-to-digital conversion

The analog signal output of the preamplifier/shaper circuit is sampled, at a rate of 5.66 MHz, by an analog-to-digital converter (ADC) with 10-bit dynamic range. Fast-conversion ADCs of the required dynamic range and precision are commercially available. Conversion times of the order of 100 ns can be achieved with flash-ADCs or with successive approximation pipelined ADCs. The requirement on the power consumption (below 100 mW per front-end channel) calls for low-power ADCs, limiting the choice to pipelined ADCs. Fortunately, due to the continuous growth in wireless communication systems and portable devices where power consumption is a major concern, 10-bit 20 MHz ADCs with low power

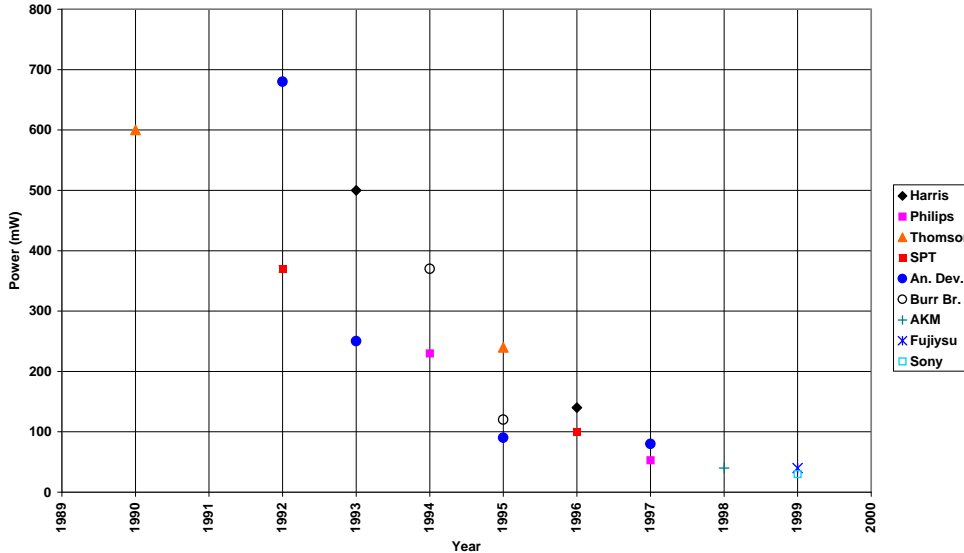


Figure 5.6: Power consumption of 10-bit 10 MHz commercial ADCs.

consumption are now widely available. Fig. 5.6 shows the reduction of power consumption, for 10-bit ADCs, over the last 10 years.

We notice that, since 1997, several commercial ADCs with power consumption below 100 mW have been available, and that in the last year a few devices with power consumption below 50 mW have appeared on the market. Moreover, the trend shown by the curve in Fig. 5.6 indicates that we can reasonably expect devices with a power consumption of 20 mW by the year 2002. In addition, most of them feature standby power consumption below 10 mW. In this respect it should be noted that the ALICE TPC has a duty cycle of about 2%, as the digitization occurs for $88 \mu\text{s}$ (TPC drift time), triggered by the Level-1 decision (200 Hz). In ‘low-power mode’ the clock signal is disabled, causing a drop in the device’s static power. From the ‘low-power mode’ the device can be recovered almost instantaneously. We will come back to this point later in this section.

Table 5.5 lists the most recent devices suitable for the TPC application. Concerning the performance of these devices, the documentation provided by the manufacturers is not always exhaustive. As a matter of fact, while the d.c. accuracy of the devices is normally well documented, often the dynamic perfor-

Table 5.5: Commercial ADCs suitable for the ALICE TPC readout.

ADC	Manufacturer	Channels per chip	Max. rate [MHz]	Power at max. rate [mW/channel]
HI5710	HARRIS	1	20	140
AD9200	Analog Devices	1	20	80
TDA8766	Philips	1	20	53
ADS901	Burr-Brown	1	20	48
MByte40C360	Fujitsu	1	25	40
CXD3300R	Sony	1	20	40
AD9201	Analog Devices	2	20	100
SPT7852	SPT	2	20	80
SPT7852	SPT	3	20	130
XRD6414	EXAR	4	20	30

mance of the device is reported only for a few values of the input signal frequency and a defined sampling frequency. Besides, the characterization of the device by the manufacturer is often done in ‘ideal’ conditions, far from the user application. In the front-end electronics for the TPC, the ADC is close to the analog circuit PASA which provides the signal to be sampled, and to the fast digital circuit ALTRO which processes the signal. Therefore, it is important to study the effect of the ADC on the analog circuit performance, and its susceptibility to the fast digital circuits. For this purpose, an ADc Evaluation Board (ADEB) [8], containing the complete readout chain, has been developed. The ADCs are mounted on small printed-circuit boards plugged into the motherboard as daughter cards. Up to four (different) ADC chips with different analog inputs can be tested at the same time in an automated test. The study of five off-the-shelf ADCs (in bold in Table 5.5) from different manufacturers has been accomplished.

There are many reasons why an ADC with N bits does not perform like an ideal N -bit converter under dynamic operating conditions. Several parameters are universally used to define these different sources of errors: Differential NonLinearity (DNL), Integral NonLinearity (INL), offset error, gain error, Total Harmonic Distortion (THD), aperture jitters, aperture delay, etc. The values of these parameters characterize an ADC and are reported on the device’s technical data sheet. To get in-depth knowledge of these devices and an independent verification of the information provided by the manufacturers, all these parameters have been measured for the five commercial ADCs under evaluation. For a detailed description of the measurements and the results we refer to [9,10]. Here we focus only on the measurement of a parameter called ‘Effective Number Of Bits’ (ENOB), which in a way includes all the effects described separately by the parameters mentioned above. This number may be considered as the number of bits in a perfect ADC whose r.m.s. ‘quantization’ error would be equal to the total r.m.s. error from all sources in the ADC under test. Figure 5.7 shows the ENOB versus the frequency of the input signal. We conclude that all the devices under test would fulfil the ALICE TPC requirements in terms of performance in the frequency range of interest.

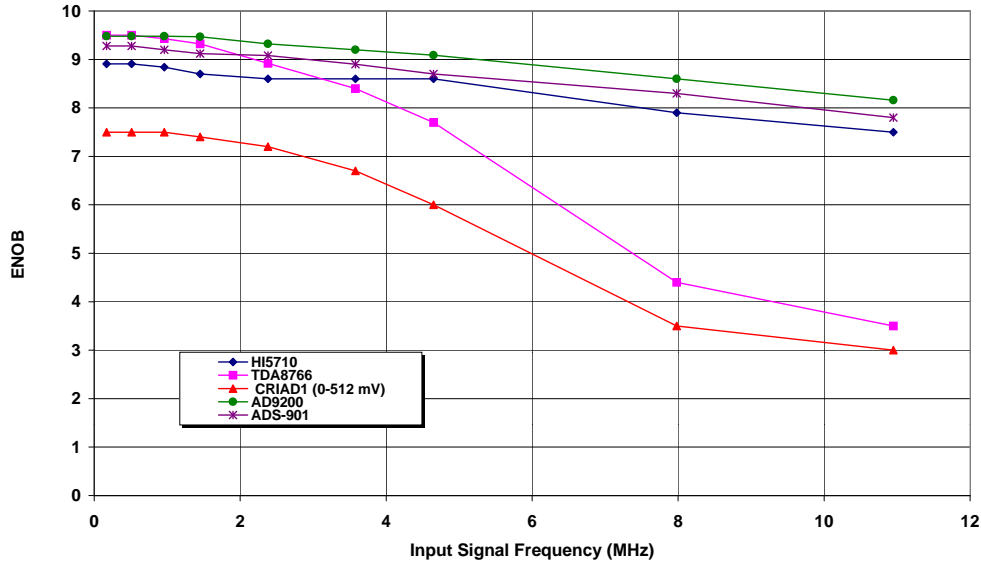


Figure 5.7: Input signal frequency versus the effective number of bits (ENOB) for five different ADCs.

One of the five ADCs (AD9200 by Analog Devices) tested has been used in the readout electronics [11] for the RCC prototype (about 1400 channels) discussed in Section 8.1. This readout electronics is based on a VME 48-channel Front-End Digitizer Card (FEDC) shown in Colour Fig. X and XI. The results achieved with this readout system, in terms of digitization resolution, are excellent. The Signal-to-Noise Ratio (SNR) measured is below 0.4 ADC counts for all channels.

In the FEDC system it is possible to put all ADCs simultaneously in ‘low-power mode’ to be activated only for 88 μ s after the trigger signal. What matters for the recovery time is how long the device has

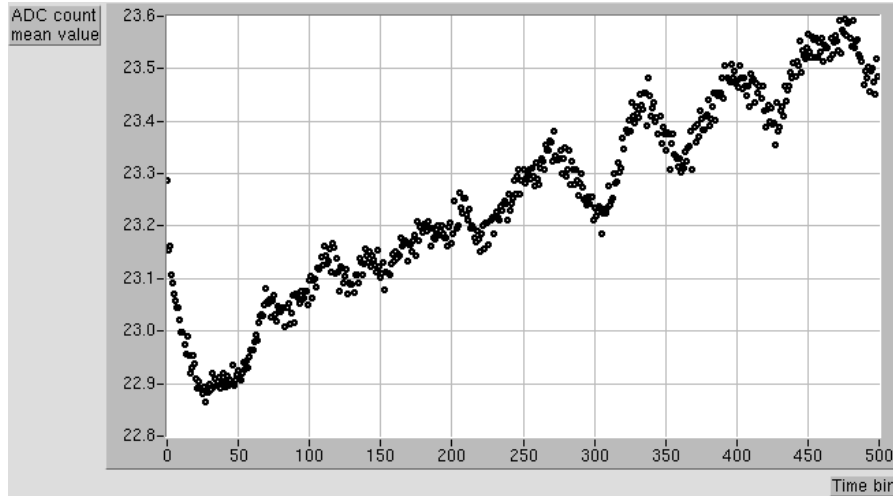


Figure 5.8: Time evolution of the signal pedestal after power-on for the ADC AD9200. Time bins are 100 ns.

been in the off-state. When the device is in ‘low-power mode’ the capacitors, which provide the reference voltages, start to discharge. When the device is switched back to running mode, the nominal value of the reference voltage is recovered in a time that depends on how long the device was kept in ‘low-power mode’. Figure 5.8 shows the time evolution of the signal pedestal when the ADC is powered on after a ‘sleeping time’ of 10 ms. It can be seen that the discrepancy is not higher than 1.4 mV even for ‘sleeping times’ of the order of 10 ms, corresponding to the typical distance between two consecutive Level-1 triggers activating the TPC readout. It should be noted that, since this error depends only on the time from the last trigger, the digital processor circuit could apply a correction before the zero suppression is performed.

Another potentially interesting option is the development of a custom ADC. A custom design provides the possibility of integrating the ADC with the rest of the readout chain, e.g. the ALTRO chip, if the technology for the two circuits is the same. Another advantage offered by a custom design is the possibility to adapt the ADC transfer function to the accuracy required in the different regions of the dynamic range. For this purpose a special version of the CRIAD [12], a low-power ADC designed at CERN for other applications, was developed for the ALICE TPC. The CRIAD is a multiple-range linear ADC with four ranges. In each range the resolution is defined by an 8-bit linear conversion performed between two references, the lower one being ground (0 V). The range selection is automatic with the signal amplitude. For comparison with the commercial ADCs, Fig. 5.7 shows also the performance of the CRIAD in the first sub-range. Despite the very promising results, this experience has shown that it is very difficult to develop, in house, a device which is competitive, in terms of performance, power consumption and price, with the commercial devices which, due to the wide market, are significantly improved year after year.

What may be more attractive here is the possibility of using a semi-custom ADC. More and more, CMOS low-power ADCs are included in the standard libraries provided by the silicon manufacturers. As an example, we mention here the case of Austria Mikro Systeme (AMS), a European silicon foundry, which includes in its 0.35 μm CMOS library a 10-bit 20 MHz ADC that, at 5 MHz, has a power consumption of 100 mW. This device features a power consumption only slightly higher than the best off-the-shelf devices.

In conclusion, at present the baseline solution is the use of a commercial ADC, however, the system design is open to the possibility of including the ADC, bought as a cell, in the ASIC (ALTRO) which contains the rest of the readout chain.

5.1.3.3 Digital readout

After the analog-to-digital conversion the TPC signal is processed by a set of digital circuits integrated in a chip named ALTRO (ALice Tpc ReadOut) [2]. The ALTRO chip is a custom integrated circuit dedicated to the processing of a 10-bit digital signal for the readout of the trigger-related data. It contains eight processing channels operating concurrently, at the ADC sampling rate (up to 20 MHz), on the digitized signal coming from eight independent inputs. Starting from a trigger signal each channel performs, on a stream of up to 1000 samples, tail cancellation, pedestal subtraction, zero suppression, formatting, and data storage in a multiple-event memory. As sketched in Fig. 5.9, the ALTRO's processing chain is based on five main units described in some detail in the following sections. First the tail cancellation occurs, followed by baseline subtraction and zero suppression. Then the data are put into a compact format in the Data Formatting Unit (DFU) and finally stored in a multiple-event buffer.

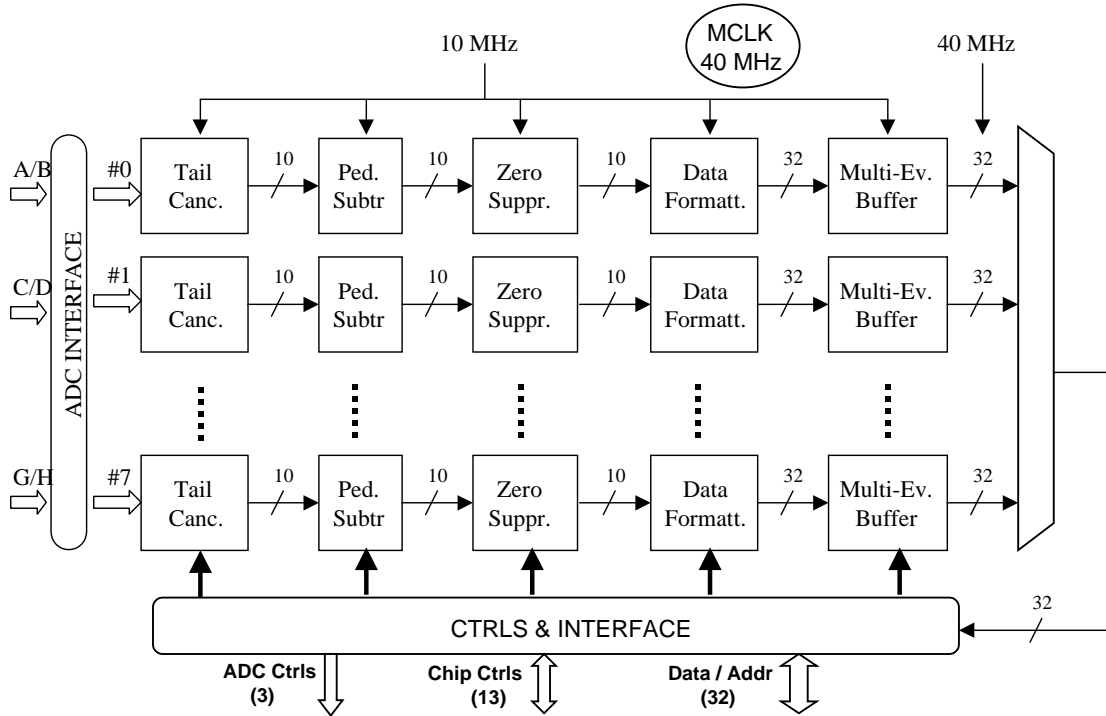


Figure 5.9: ALTRO block diagram.

5.1.3.4 Tail cancellation

As mentioned above, the signal coming from the ALICE TPC presents a long tail. A technique to cancel the tail of the signal arising from the amplification region was developed for a proportional chamber and implemented by a circuit based on discrete components [13]. The same technique underlies the tail-cancellation scheme used in the preamplifier/shaper circuit developed for the readout of the CERES TPC [5]. In this method, the measured TPC signal is approximated by the sum of three exponential terms:

$$i(t) \approx e(t) = I_0 \cdot \left[A \cdot \exp \frac{t}{\alpha \cdot \tau_1} + B \cdot \exp \frac{t}{\beta \cdot \tau_2} + C \cdot \exp \frac{t}{\gamma \cdot \tau_3} \right]. \quad (5.1)$$

Hence, the cancellation of the signal tail can be realized by a deconvolution filtering technique [13]. The signal is passed through a linear network with a response that cancels perfectly one of the exponential

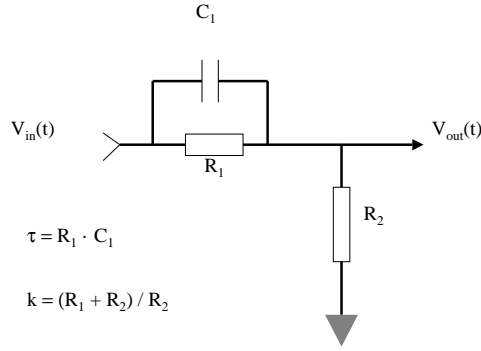


Figure 5.10: Analog pole-zero network.

terms. Let us consider a pole/zero network with transfer function

$$F_1(s) = \frac{1 + s \cdot \tau}{k + s \cdot \tau}. \quad (5.2)$$

It can be shown [13] that if the time constant τ is adjusted to be $\tau = \tau_3$, k can be adjusted in a way that all the terms containing τ/k add to zero. In this way the pole τ_3 , corresponding to the long tail ($\tau_3 > \tau_2 > \tau_1$), is perfectly cancelled. Similarly, a second pole/zero network with transfer function $F_2(s)$ can be added with constants adjusted so that the remaining terms only contain the time constant τ_1 . As a result, the convolution of the two filters with the chamber signal is

$$i_0(t) = i(t) \otimes h_1(t) \otimes h_2(t) \cong I_0 \cdot \exp \frac{t}{\alpha \cdot \tau_1}. \quad (5.3)$$

The network with transfer function Eq. (5.2) is shown in Fig. 5.10, where $\tau = R_1 \cdot C_1$ and $k = (R_1 + R_2)/R_2$. A circuit diagram of the complete tail-cancellation filter is shown in Fig. 5.11. Figure 5.12 details the behaviour of the circuit as simulated by using SPICE. The accuracy of a shortening filter realized by an analog network is limited by the tolerances of the network components. Owing to the poor precision in the matching of the passive components, provided by the actual integrated circuit technologies, the shortening filter described above cannot reach a high accuracy ($\sim 10^{-3}$) if it has to be included in an integrated circuit with no external tunable components.

On the other hand, a digital system provides much better control of accuracy requirements. This results in specifying the accuracy requirements in terms of word length, floating-point versus fixed-point arithmetic, and similar factors. Furthermore, a digital system allows flexibility in reconfiguring the digital signal-processing operations simply by changing a number of programmable coefficients. This is indeed extremely important, considering that the exact shape of the signal which depends on the details of the chamber and pad geometry is difficult to predict and is known with high precision only when the detector is operated. Also, this allows some flexibility in the choice of the gas composition and drift field depending on first running experiences. The first-order filter expressed by the Eq. (5.2) can be expressed in the discrete time domain using the z transform. We obtain the following z transform function:

$$F(z) = \frac{L_0 + L_1 \cdot z^{-1}}{1 + K_1 \cdot z^{-1}}, \quad (5.4)$$

where L_0, L_1 and K_1 are constants that are functions of $A, B, C, \alpha, \beta, \gamma$. This circuit is represented in a schematic way in Fig 5.13.

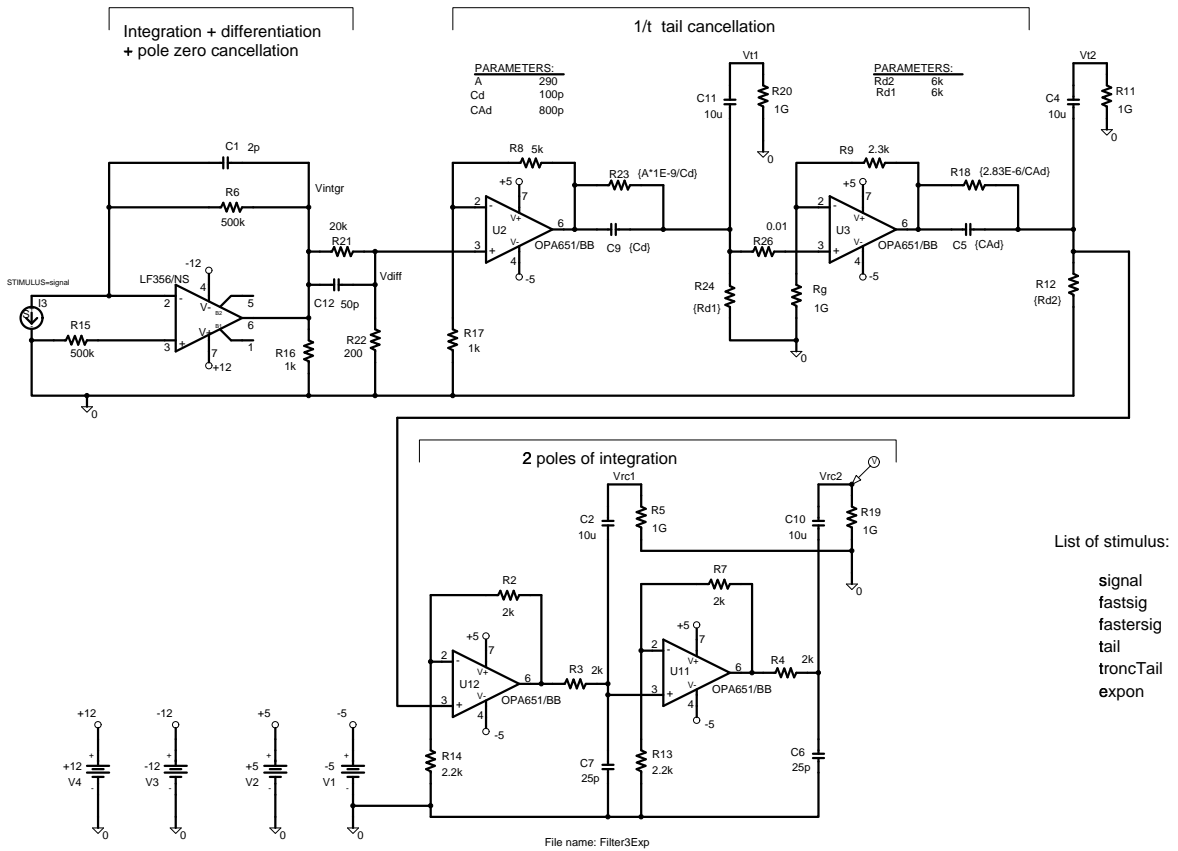


Figure 5.11: Block diagram of the analog tail-cancellation filter.

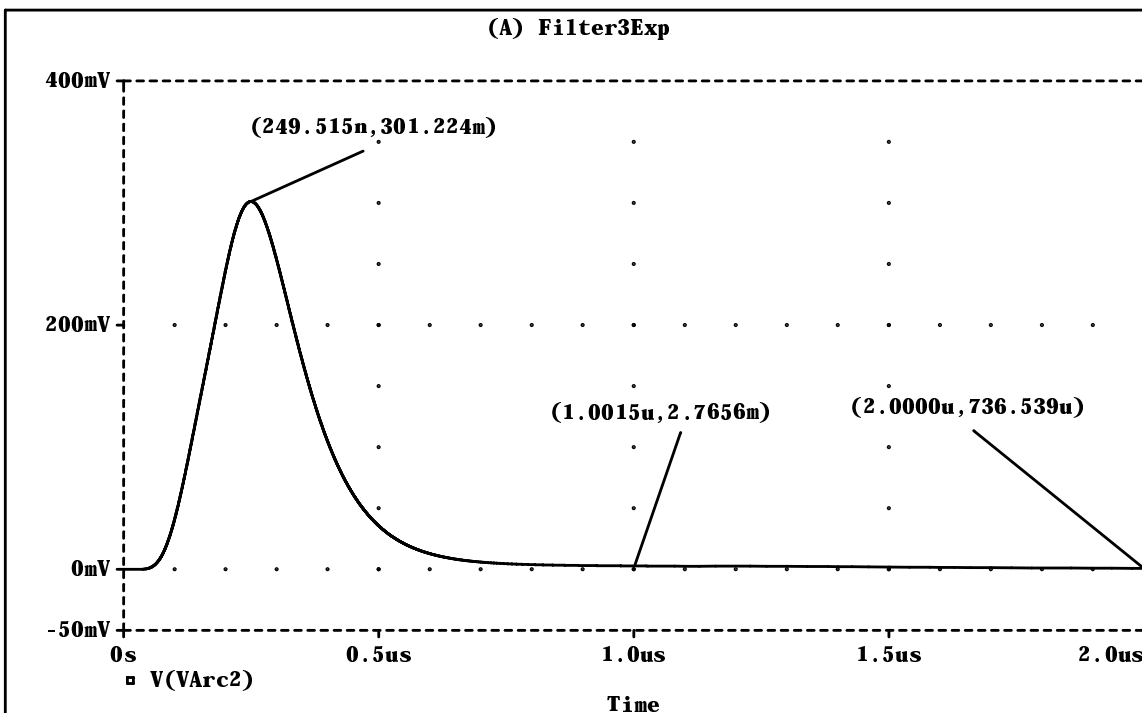


Figure 5.12: SPICE simulation of the analog tail-cancellation filter.

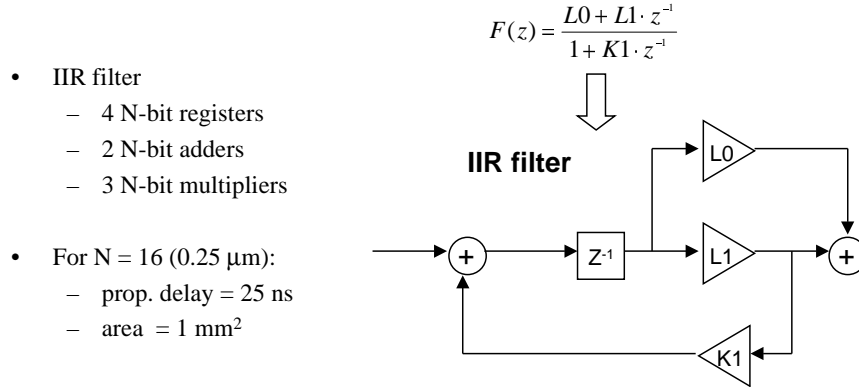


Figure 5.13: Digital pole-zero network.

It consists of three multipliers, two adders, and a register. Even though there are no negative values in the input, their use is needed for the internal calculations of the filter, therefore the two's-complement arithmetic is used. The Verilog implementation of this circuit was performed and the results are shown in this section. In order to work in the digital domain, the analog input signal according to Eq. (5.1) was sampled at 10 MHz, and 16- or 32-bit ‘quantizations’ were performed.

Figure 5.14 is an overlay of three signals: input, response after the first filter, and final output. These plots show that we can achieve a tail suppression with the three-exponential approximation. The final result was normalized so that the maximum value is equal to one. The error definition was to consider the ratio between a given sample and the maximum value. The filter coefficients were slightly adjusted to have a small undershoot providing a fast decline towards the baseline. Between the samples, there is a simple linear interpolation in order to improve readability of these plots. Only the 16-bit case is shown (see also Table 5.6).

To estimate the size of the digital filter circuit, the Verilog description has been synthesized and targeted to a 0.25 μ m CMOS technology. The results are shown in Table 5.7.

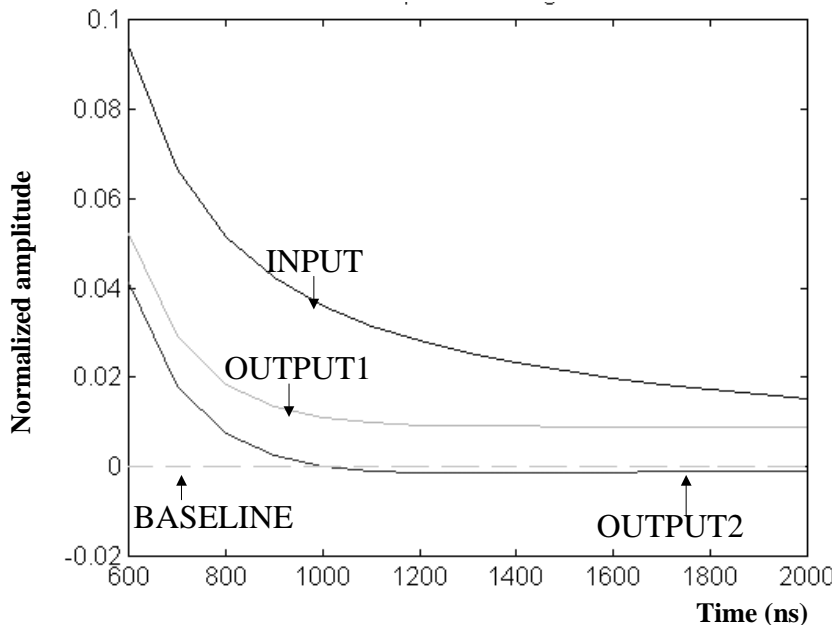


Figure 5.14: Digital filter: input signal, response after the first filter, and final output.

Table 5.6: Shortening filter performance.

	Input	Output 1	Output 2
After 1 μs	0.036	0.011	-1.83×10^{-4}
After 2 μs	0.0153	0.0088	-9.17×10^{-4}
Area [0-1 ms] AU	1.0773	0.8565	0.8270

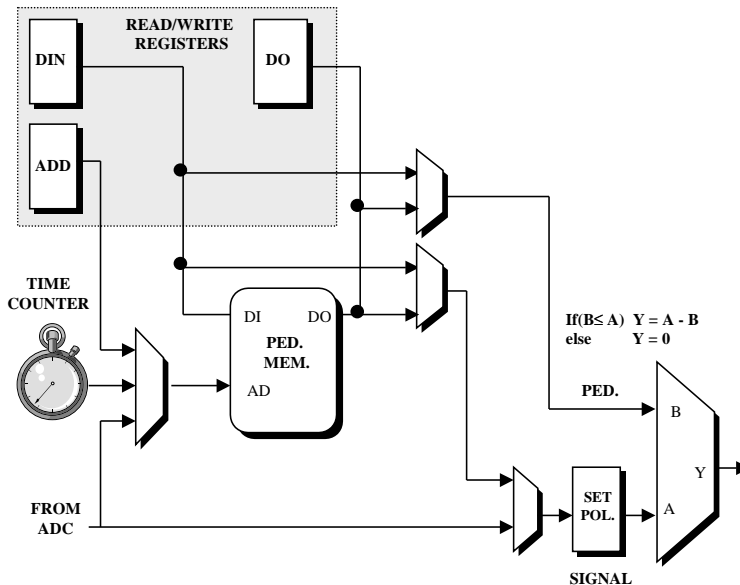
Table 5.7: 16-bit fixed-point first-order digital filter.

	Slow	Fast
Propagation delay	25 ns	10 ns
Area	0.5 mm ²	1 mm ²

5.1.3.5 Baseline subtraction, zero suppression, data formatting and buffering

The baseline subtraction is performed by the circuit schematically depicted in Fig. 5.15. It has three modes of operation:

- *Subtraction mode*. The circuit performs the subtraction of pedestal values from the input-signal values. The subtracted value can be either fixed or time-bin dependent. In the former case — *fixed subtraction mode* — the value to be subtracted from the input signal is a constant stored in a register (DIN in Fig. 5.15). In the latter case — *variable subtraction mode* — the time-bin-dependent pedestal values to be subtracted are stored in the pedestal memory which, in this configuration, is addressed by a time counter started by the trigger signal. Clearly the *variable subtraction mode* is useful whenever the signal is affected by some systematic baseline variation correlated with the readout cycle.

**Figure 5.15:** Baseline subtraction block diagram.

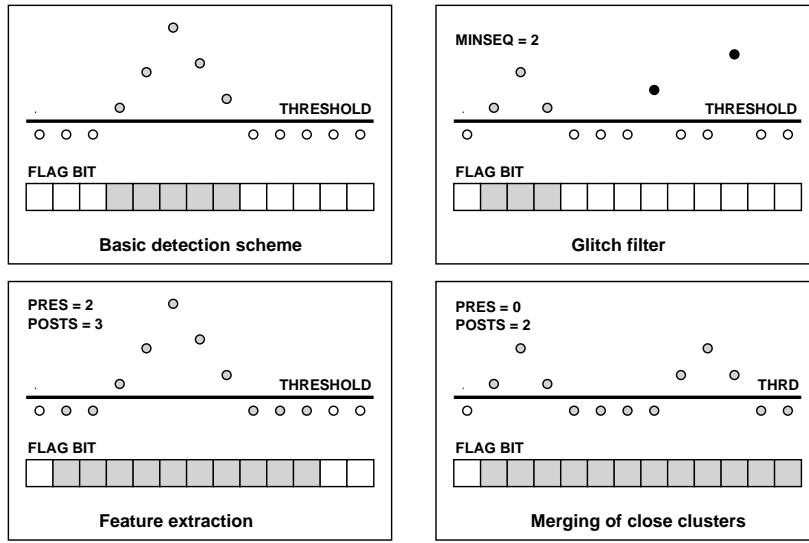


Figure 5.16: Zero-suppression scheme.

- *Conversion mode.* The circuit can perform a memoryless (static) conversion of the input signal of the type $y_n = F(x_n)$. At any instant n , the output y_n depends at most on the input sample x_n at the same time, but not on past or future samples of the input. The output values y_n are stored in the pedestal memory addressed in this case by the input x_n . Concurrently the subtraction of a fixed value from the converted signal can be performed.
- In the third mode of operation — *test mode* — the pedestal subtraction unit can be used to generate a pattern to be injected into the processing chain for test purposes. This is an important feature that allows a complete test of the overall digital readout chain.

One obvious way to compress the data stream is to discard ‘zero’ data, i.e., samples so close to the reference level (pedestal) that they are considered to contain no useful information but rather to be due to noise. The basic pulse-detection scheme is based on the rejection of samples with value smaller than a constant decision level (threshold). When a sample is found above the threshold, it is considered to be the start of a pulse (Fig. 5.16). To reduce the noise sensitivity, a glitch filter checks for a consecutive number of samples above threshold, confirming the existence of a real pulse. The minimum sequence of samples above the threshold that defines a pulse can vary from one to three. In order to keep enough information for further feature extraction, the complete pulse shape must be recorded. Therefore, a sequence of samples (pre-samples) before the signal overcomes the threshold and a sequence of samples (post-samples) after the signal returns below the threshold can be recorded. The number of pre- and post-samples can vary independently in the range between zero and four.

The data format is as illustrated in Fig. 5.17 and described in the following. The pulse thus identified and isolated must be tagged with a time stamp, in order to be synchronized with the trigger decision for validation. Otherwise the timing information would be lost by the removal of a variable number of samples between accepted pulses. This requires the addition of a time word to the set of sample data. Since 1000 is the maximum length of the data stream that can be processed by the ALTRO chip, the time information can be encoded in a 10-bit word. The principle is to label each pulse with a time stamp that defines the time distance from the trigger signal (e.g. ‘T06’ in Fig. 5.17). So the samples of the processed data stream are numbered starting from 0 to 1000.

Since the ALTRO data format does not make use of extra flag bits to distinguish the samples’ data from the time data, we introduce a further word for each accepted cluster to represent the number of words in the cluster (e.g. ‘07’ in Fig. 5.17). Since a cluster can be as long as the complete data stream

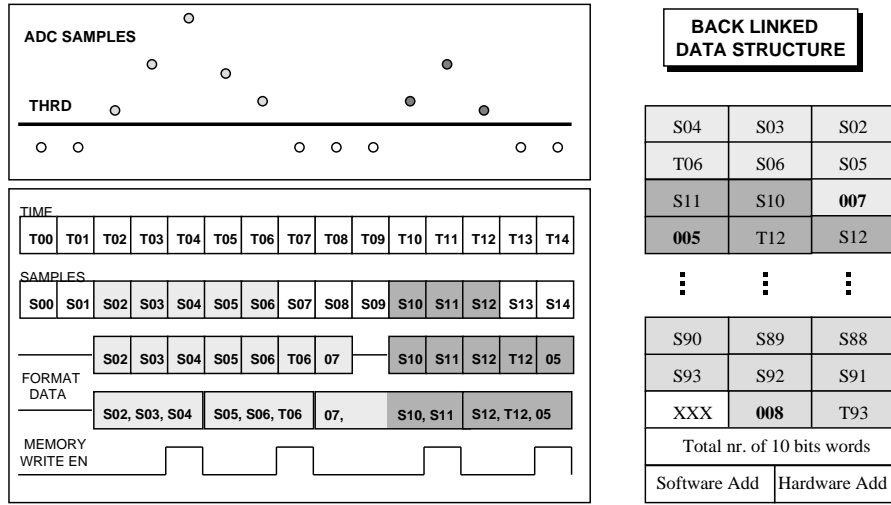


Figure 5.17: The ALTRO data format.

the new word is also a 10-bit word.

The DFU formats the stream of zero-suppressed data by adding, to each set of samples, two extra 32-bit words, and encoding the 10-bit words into 30-bit words. The two 32-bit words form the trailer of each data packet. The first word is fundamental for the decoding of the data packet and expresses the total number of 10-bit words in the packet. Indeed this word provides the position of the last 10-bit word in the data packet. Starting from the last 10-bit word the clusters are back-linked, as each set contains the pointer to the first word of the previous cluster (Fig. 5.17). The second trailer word contains in the 16 LSB a software identifier, which is read from one of the configuration/status registers, while the byte after that contains the hardware address. This address represents a geographical address and is used in the data packet to identify unambiguously to which channel the data packet is associated. The software identifier is a programmable number that can be used to specify to which data source the processing channel is connected.

Finally the data are stored in a multiple-event buffer, a 512×32 RAM that can hold up to eight events. The ALTRO chip interfaces to the external world through a 40-bit control bus based on a data transfer protocol that supports a data rate of 160 MByte/s.

5.1.3.6 ALTRO prototype

In its final version the ALTRO will be implemented in a deep sub-micron CMOS process: at the moment, $0.25 \mu\text{m}$ seems the process feature size suitable for this application. At the present phase of the project the chip functions are not frozen yet. Thus in order to have an estimate of the size and power consumption, this circuit has been studied using the standard cell library for a $0.25 \mu\text{m}$ CMOS process, leading to a die size of $8 \text{ mm}^2/\text{channel}$ and a power consumption of 8 mW/channel. With the exception of the shortening filter, all the ALTRO's functions have been implemented in a FPGA, as used in the FEDC cards [11] for the readout of the RCC (Section 8.1). Finally, for the purpose of studying the system aspects of the FEC, a four-channel prototype has been developed as a $0.6 \mu\text{m}$ double metal CMOS process featured by AMS (Austria Mikro Systeme). It has a silicon die of 40 mm^2 and is packaged into a plastic case with 100 pins (PQFP100).

The layout of the chip is shown in Fig. 5.18 where one can recognize the four channels and the common control logic. The supply voltages are distributed to the internal cells starting from two external $80 \mu\text{m}$ wide rings that surround the circuit body completely.

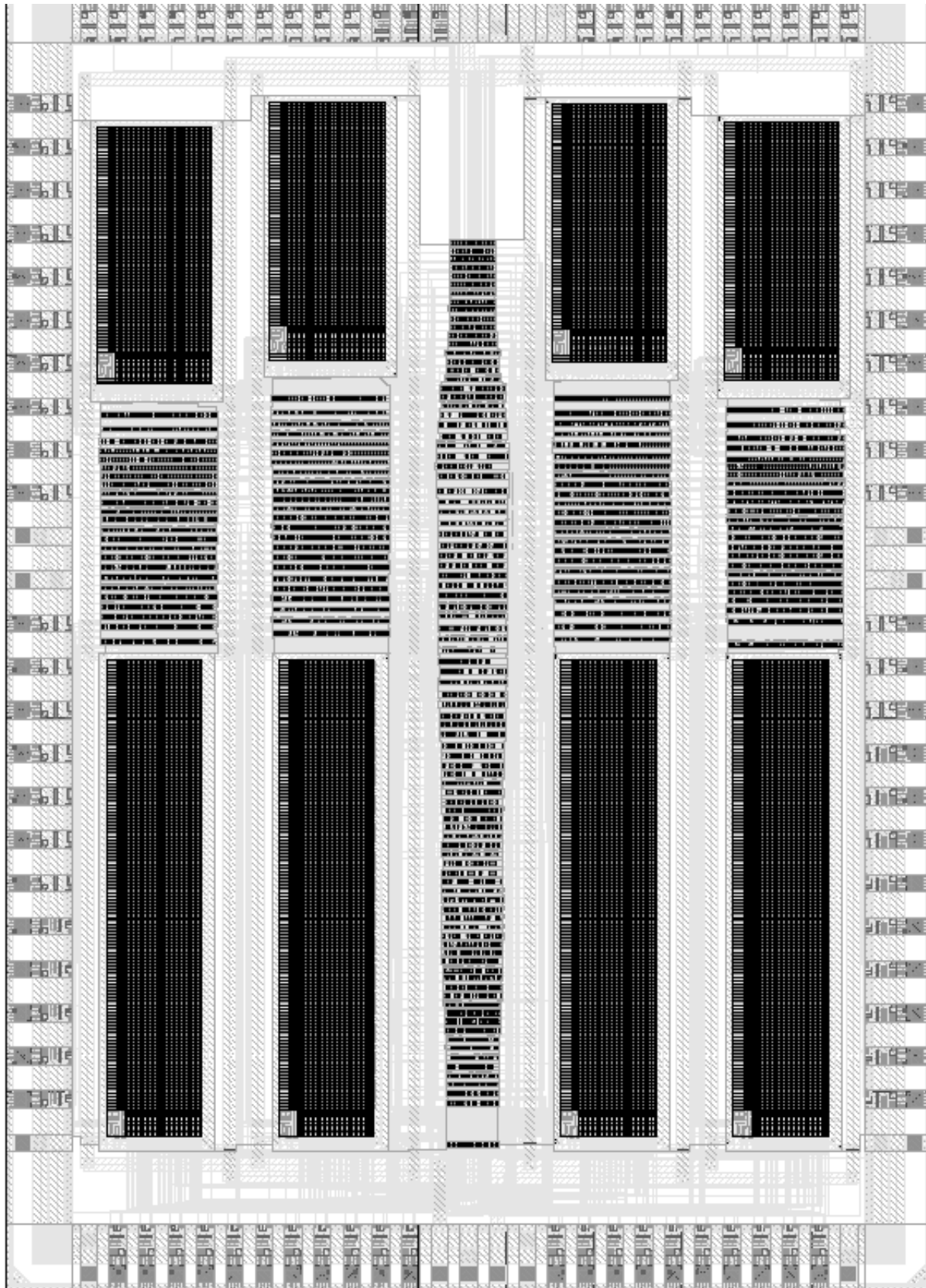


Figure 5.18: Layout of the ALTRO chip prototype.

5.1.4 Front-End Card

The Front-End Card (FEC) contains the complete readout chain for amplifying, shaping, digitizing, processing, and buffering the TPC signals. The FEC must handle the signal dynamic range of about 10 bits with minimal degradation of precision, store the signals during the Level-2 trigger latency, and provide a dead time below 10% at the maximum Level-2 trigger rate of 100 Hz. The design provides 128 channels per FEC, with an estimated maximum power consumption of approximately 12 W.

The layout of the FEC is shown in Fig. 5.19 and has the following flow. The FEC receives 128 analog signals through 8 flexible cables and the corresponding connectors as shown in the figure. The input signals are very fast, with a rise time of less than 1 ns. Therefore, to minimize the channel-to-channel crosstalk, the PASA circuits have to be very close to the input connectors. The signals are first amplified and then processed by a band-pass filter. The latter operation is done to limit the bandwidth of the ADC input signal and to reduce the signal-to-noise ratio. A 16-channel chip (PASA) contains the circuits to implement these analog functions. Each FEC contains therefore eight PASA chips. Commercial ADCs convert the PASA output signals into digital signals. ADCs with two or four converters per chip are considered suitable for this application leading to 64 or 32 ADCs per FEC, respectively.

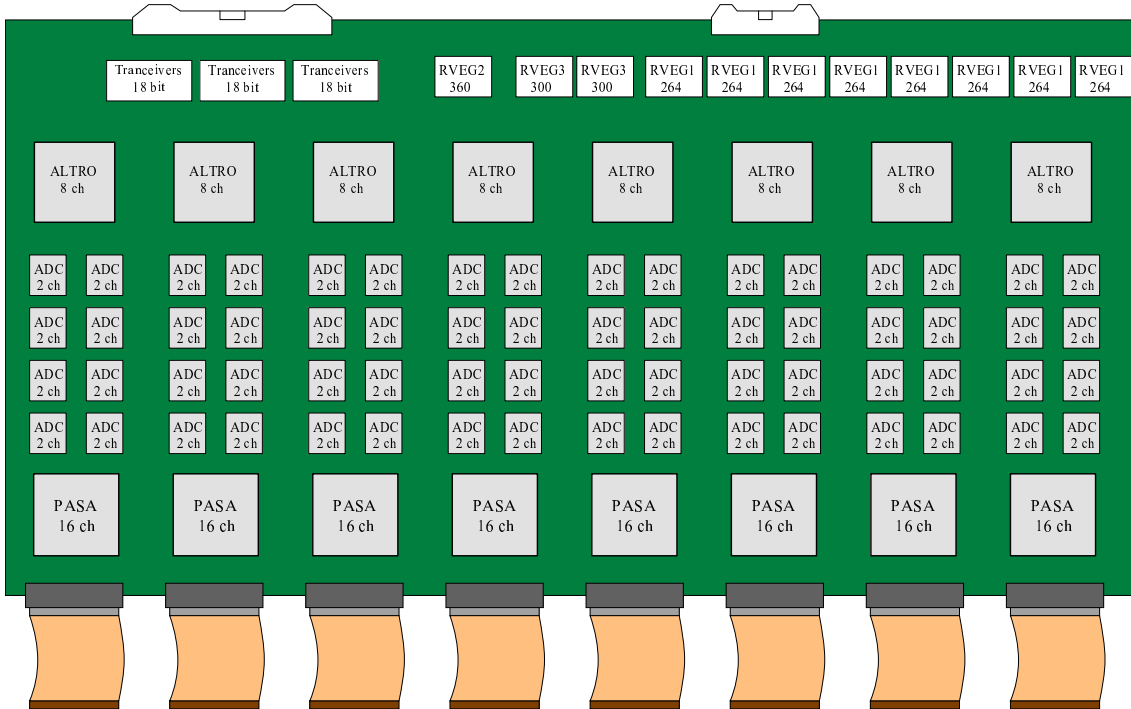


Figure 5.19: Sketch of the Front-End Card (FEC).

The digitized signals are processed and stored in a memory, where they wait for a Level-2 trigger, to be either read out or discarded. In the former case, the buffer will be frozen and protected against overwriting until the data are transferred to the Readout Control Unit (RCU). The details of the data transmission protocol are discussed in Section 5.1.5.2. In the latter case, the buffer is made available to store a new data set. All the digital circuits are implemented in the ALTRO chip that contains eight channels and the output multiplexing circuitry.

The FEC channels are multiplexed, at the board level, via a LVTTL (Low-Voltage TTL) bus. It features an asynchronous VME-like protocol, which is enhanced by a Clocked Block Transfer (CBT) that provides a bandwidth of 160 MByte/s. The FEC is interfaced to the RCU through a 40-bit bus that is based on the GTL (Gunning Transceiver Logic) standard. At the board output the bus signals are translated from LVTTL level to GTL level by bidirectional transceivers. The configuration, readout and

test of the board are done via the GTL bus. However, the FEC contains a circuit, named Board Controller (BC), implemented in a FPGA, which provides the RCU with an independent access to the FEC via a field-bus. Although this secondary access is normally used to monitor the board activity, power supplies and temperature, it can also be used for the configuration and readout of the FEC at a slower rate.

The board offers a number of test facilities. As an example, a data pattern can be written into the ALTRO chip and read back exercising the complete readout chain. It is also possible to perform a boundary scan test of the ALTRO chips under the control of the BC. The BC allows the bus activities, the presence of the clock, and the number of triggers received to be verified.

The ALTRO chips and the BC work synchronously under a master clock frequency of 40 MHz. The ALTRO circuits usually perform the same operations simultaneously under the control of the RCU which can also control a single channel at a time. This is performed in the configuration phase and for test purposes. The RCU broadcasts the trigger information to the individual FEC modules and controls the readout procedure. Both functions are implemented via the GTL bus.

The board layout of the FEC can be seen as partitioned in nine different sections. The first eight sections are identical, each one containing the readout chain for a group of 16 channels. Each chain is comprised of one PASA, eight (or four) ADCs, two ALTROs and four voltage regulators. The last section contains the LVTTL–GTL translators and the BCs. As detailed in Section 5.1.8 the FEC is powered by means of four power cables carrying three supply voltages ($+4.3\text{ V}$, $\pm 2.5\text{ V}$) and a common ground. From the three main supply voltages, for each of the eight sections, four supply voltages are derived and distributed ($+3.3\text{ V}$ for the ADCs, $+3.3\text{ V}$ for the digital circuits and $\pm 1.5\text{ V}$ for the PASA). The last section is powered independently with $+3.3\text{ V}$. The voltage regulators feature a power mode that is remotely controllable. The ON/OFF pin of the voltage regulators related to the same section is controlled via the BC which monitors the current supplied by each voltage regulator. It can be programmed to power down the sections where the monitored quantities exceed an upper limit.

The actual layout of the FECs has just been completed. This is an important step because it demonstrates that even for the smallest boards on the inner chamber with dimensions of only $19 \times 14\text{ cm}^2$ all components for 128 channels can fit on the board. The actual layout for the two sides of the board is shown in Fig. 5.20 and Fig. 5.21.

5.1.5 Readout bus

5.1.5.1 Requirements

The communication between the RCU and the FECs is implemented via a custom bus (front-end bus) based on a shielded ribbon cable and a custom protocol. The front-end bus is essentially an extension of the FEC's internal bus that allows the RCU to access the FEC's internal components. It is a multiple-drop single-master bus where the RCU is the master unit and the FECs are the slaves. In order to minimize the length of the bus cables the bus controller supports two branches running in opposite directions as shown in Fig. 5.22.

The front-end bus has to satisfy the following requirements.

- From the functional point of view the front-end bus is the means by which the RCU broadcasts the Level-1 trigger information to all the FECs in a crate and steers the readout procedure. Besides these basic functions, the RCU will also download the FEC's configuration parameters (pedestals, thresholds, tail-cancellation coefficients, etc.) and run test procedures via the same bus.
- To match the performance of the DDL it has to provide a bandwidth of at least 100 MByte/s.
- It must contain a number of slots that ranges from 21, for the innermost crate, to 33 for the outermost one. Physically the front-end bus is composed of two branches, each one with half the number of slots.

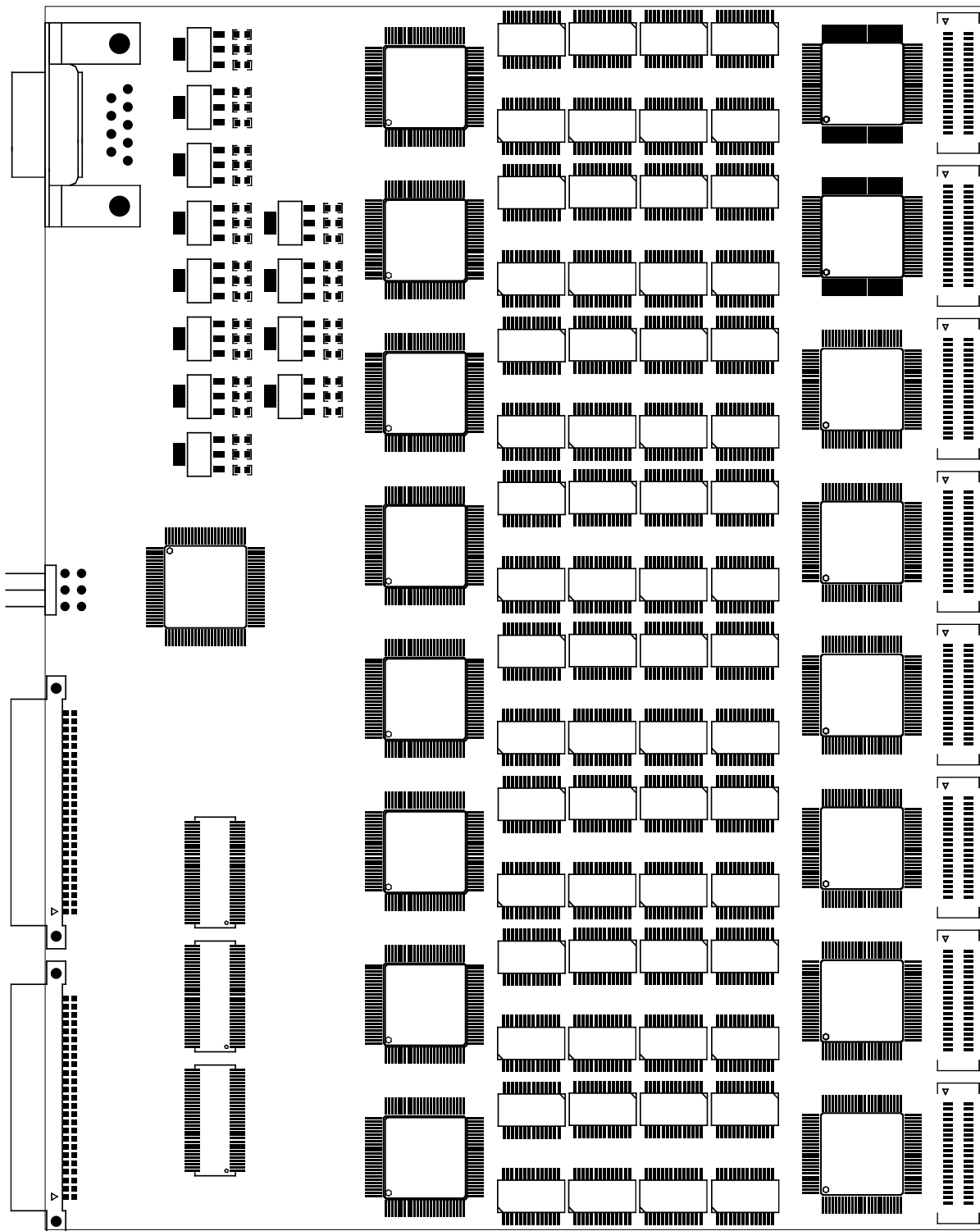


Figure 5.20: Top view of the layout of the small FEC.

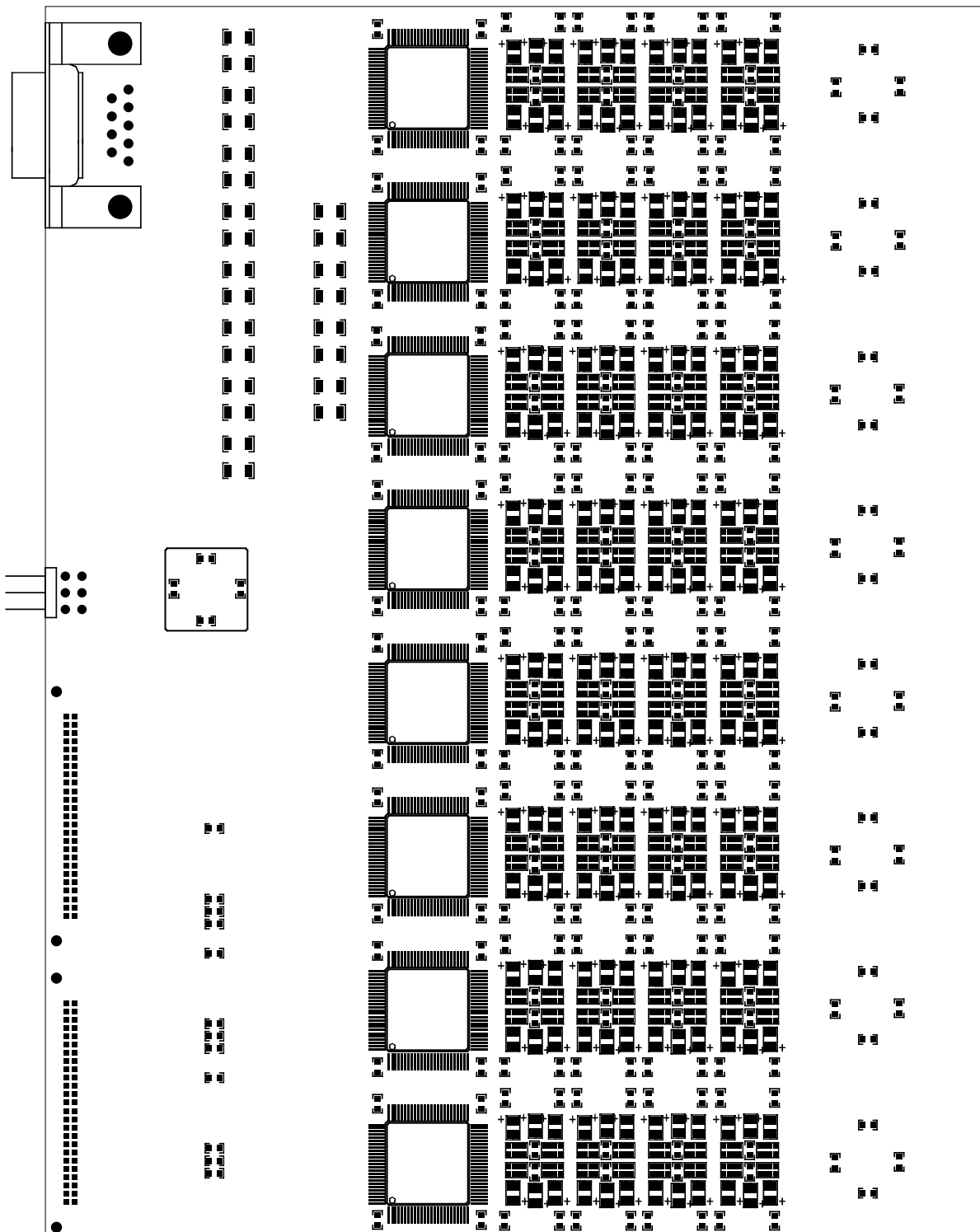


Figure 5.21: Bottom view of the layout of the small FEC.

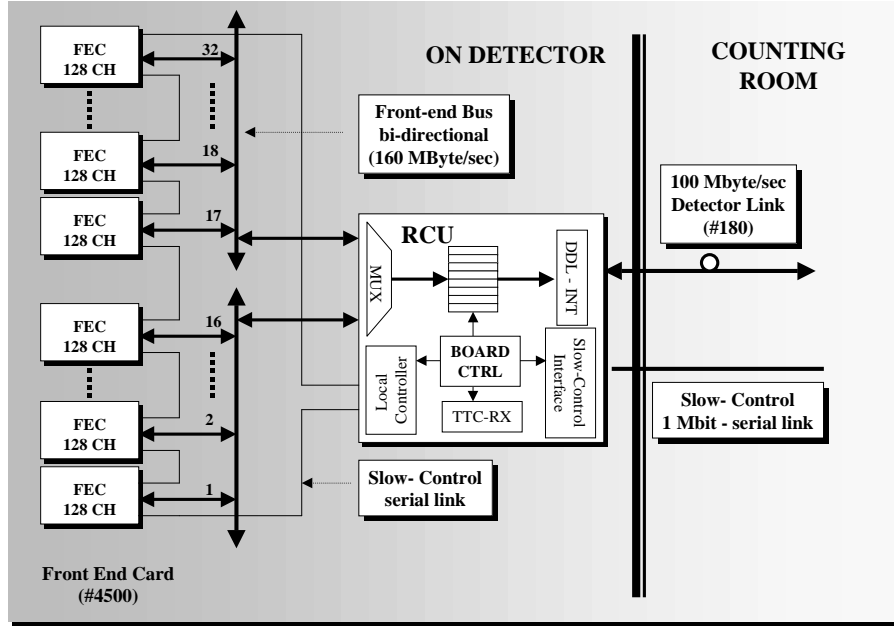


Figure 5.22: Front-end electronics system architecture.

- The front-end bus cables are very close to the analog front-end electronics; therefore low signal noise and ElectroMagnetic Interference (EMI) are an issue.

5.1.5.2 Readout protocol

The readout of one event is performed in two separate phases which are consecutive for a given event, but can otherwise be activated concurrently. In a first phase, the trigger information is received by the RCU and broadcast to all modules in the subsystem, starting the digitization of each channel, which lasts for $88 \mu\text{s}$ (the TPC drift time). During this phase tail cancellation and zero suppression are performed. In the second phase, information is moved from the multiple-event buffers to the RCU. The time needed to complete the second phase depends on the size of the event, but other triggers can be processed during the readout of the previous event, as long as the multiple-event buffers in the FEC are not full. Dead time can be generated only when this condition occurs. The transfer of data words is synchronous and modules containing valid unread data are enabled to assert data on the bus by individual addressing. To be able to perform online hardware data compression, the order in which the data are presented for optical transmission is not arbitrary. The best sequence is to send all time bins of one channel in a channel-by-channel fashion with neighbouring channels being also transmitted adjacently. However, the detailed data format may have to be revised when more detailed studies of the possible data-compression scenarios have concluded.

The front-end bus implements a VME-like protocol with an asynchronous handshake between the RCU and the ALTRO chips in the FECs. A synchronous block transfer enhances the protocol whereas words are transferred without any acknowledgement. The bus consists of 32 bidirectional lines for the transmission of data and addresses, and six control lines. Special lines are used to distribute the trigger (Level-1) and clock signals. The ALTRO chip recognizes a set of eight instructions. By means of these instructions the RCU can access each ALTRO chip in the system to

- write/read a Configuration/Status Register (CSR),
- issue a COMMAND,
- read the multiple-event buffer.

The ALTRO chip acknowledges the execution of any instruction. A special case is represented by the data readout procedure where the ALTRO acts as MASTER and strobes data on the RCU FIFO (SLAVE) synchronously without any acknowledgement. The signals used for the implementation of the protocol are BD[31:0], WRITE*, CSTB*, ACKN*, TRSF*, DSTB*, GRST*, TRG*, MCLK.

In the CSR access or COMMAND instructions, the most significant 16 bits of the BD bus specify the chip and channel addresses, the CSR address or the COMMAND code. The least significant 16 bits are used to input data in the CSR WRITE and COMMAND instructions, and to output data in the CSR READ instructions. The write/read access to a CSR is defined by the WRITE* signal. A rising edge on CSTB* (Command STroBe) informs the ALTRO chip that the addressing and data information in the BD[31:0] lines is stable and can be captured. On a WRITE* or COMMAND cycle, the ALTRO drives the ACKN* signal to indicate that it has successfully received all the data called for by the instruction type. On a read cycle, the ALTRO drives the ACKN* signal to indicate that it has placed data on the data bus. During the readout of the multiple-event buffer the chip announces the data transfer by means of the signal TRSF* (TRanSFer) which is kept low until the data packet has been completely transferred. The data transfer is not necessarily continuous and for this reason each single word being transferred is validated by the signal DSTB* (Data STroBe). The GRST* (Global ReSeT) initializes all the internal registers, counters, and state machines. The TRG* (Level-1 TRiGger) signal starts the processing of the digitized signals. The MCLK (Master CLocK) is a clock signal generated by the RCU and distributed to all FECs, which is used only by the readout circuits.

A second clock signal SCLOCK (Sampling CLOCK), with much tighter constraints on the maximum skew and jitters, is distributed via a dedicated point-to-point connection. This is the clock signal distributed to the ADCs and it has a frequency between 5 MHz and 10 MHz.

The front-end bus provides, with a clock frequency of 40 MHz, a bandwidth of 160 MByte/s on each of the two branches, leading to an aggregate bandwidth of 320 MByte/s. It is clear that a bus master-clock frequency of 20 MHz which corresponds to a bandwidth of 160 MByte/s would be adequate to match the bandwidth currently foreseen for the DDL. However a front-end bus with a higher bandwidth will allow to support possible future upgrades of the DDL performance.

5.1.5.3 Electrical and physical specifications

For the electrical implementation of the bus transceivers we plan to use GTL+. GTL, invented by W. Gunning at Xerox Corporation and standardized by JEDEC, is a low-swing input/output driver technology. It has been further modified by Intel and TI (Texas Instruments) who have increased the voltage swing to create GTL+. The typical swing for GTL+ is from 0.6 V low (VOL) to 1.5 V high (VOH) at most. TI uses tighter threshold regions to provide better signal integrity in its stand-alone devices.

It has been shown [14] that the newest TI GTL+ devices (GTL161612A) can operate up to 100 MHz, providing bit rates of 3.2 Gbit/s in a 32-bit wide backplane. They are designed with a slow rising and falling edge to offer significant system frequency improvement in heavily loaded backplanes. The GTL output consists of an edge-control circuit that provides optimized rise and fall times, typically 2.6 ns (20% to 80%), for backplanes under various loading conditions. Device power can be switched off without having to remove the device from the system because the inputs and outputs are at high impedance and, therefore, are able to tolerate active bus signals.

The basic GTL output structure is an open-drain transistor, whereas the input is a differential driver. Besides, the GTL I/Os have been designed to minimize their capacitance, an extremely important factor for distributed-load high-performance backplanes. Figure 5.23 shows the backplane electrical model for a 17-slot system located in the outermost crate (C5).

For the TPC front-end electronics a rigid backplane is not a practical solution as the FECs are mounted on the detector first, and the backplane should be plugged onto 17 boards simultaneously. Therefore we plan to implement the front-end bus in a polyimide flexible cable. The 40 bus lines are alternated with ground lines, with a pitch of 1.27 mm, and lie above a solid ground plane. The electrical performance of

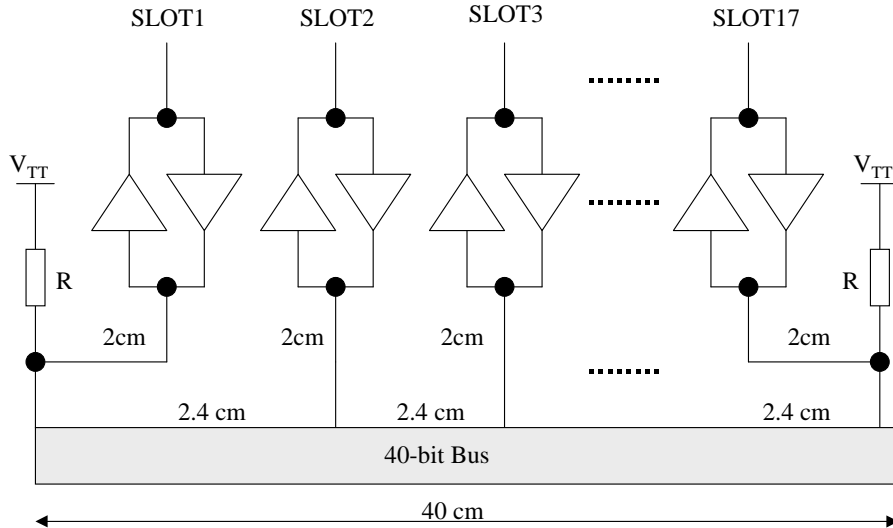


Figure 5.23: Backplane model for one branch of the front-end bus for the outermost crate.

this system is equivalent to a standard rigid backplane.

5.1.6 Readout control and services

The overall TPC electronics architecture is sketched in Fig. 5.22 on page 114. The electronics for 128 channels is mounted on a Front-End Card (FEC) as described in Section 5.1.4. The functionality performed here includes, aside from amplification and digitization, digital filtering, zero suppression, and buffering of up to four black events. For a motivation why four events are adequate refer to Section 5.1.7. Basically the FEC hosts all electronics necessary for one channel. In addition, it also performs necessary power management, which has to be as close as possible to the analog circuitry.

There will be a total of about 4500 FECs. Assuming black events and the maximum 200 Hz TPC readout each card will produce a data stream of about 11 MByte/s if the data not falling into the nominal acceptance (32%) are not read out (otherwise 16 MByte/s). The accepted ALICE data transmission standard off the detector is DDL [15, 16] supporting 1 Gbit/s. Therefore multiple TPC FECs can be merged into one DDL. This functionality is performed by the readout control unit sketched in Fig. 5.22 on page 114. However, depending on the radial position, not the total depth of the chamber will be read out and also position-dependent compression factors are expected. Therefore the number of FECs per readout controller varies from 20 to 32 such that the average throughput per link is constant. There are going to be five readout controllers per sector.

The readout controller has the following functional requirements

- merge digitized data from FECs into the DDL data stream in ordered form (time bin, pad number, pad row);
- distribute trigger and clock signals to FECs;
- interface detector control system (DCS) to FECs;

The following paragraphs discuss the functionality and interfaces of this device.

5.1.6.1 Clock and trigger interface

The accepted ALICE standard how to distribute trigger and clock information is the RD12 TTC system which will be used here [17]. Every readout controller implements an appropriate receiver (TTCRX)

which produces the phase-corrected LHC clock, Level-1 trigger and Level-2 accept/reject; these have to be forwarded to all FECs via the readout bus. Due to the multiple-drop nature of the readout bus there will be some clock skew between the different FECs. With a cable length of less than 30 cm per readout bus link the clock skew between any FEC relative to the TTCRX chip which can be individually phase corrected, can be kept below 5 ns with less than 200 ps electronic jitter. This corresponds to a systematic position error of less than 200 μm with a contribution to the position resolution of less than 10 μm .

In addition, a 4-bit trigger type needs to be provided to the FECs which can be used to issue pulser or test readout triggers, such as the readout of a pre-loaded event for test purposes of the data path. These triggers can be issued as broadcast commands through the TTC. Normal physics Level-1 triggers have the default readout type zero.

ALICE implements a multiple-deadtime system allowing triggers to some subdetectors while others, such as the TPC, are busy. Therefore, an event number is not an unambiguous means to identify an event and to ensure data integrity. The TTC receiver provides a bunch-crossing number which, however, is only unique for one LHC turn. Therefore it was decided to use the combination of the bunch-crossing number and an orbit counter. Here 24 bits correspond to 20 minutes of real time, which is longer than any event is expected to remain within the DAQ and therefore adequate to ensure uniqueness of the event ID. The orbit counter has to be implemented externally to the TTCRX and be able to run at 12 kHz.

5.1.6.2 Interface to the digital optical links

The ALICE standard to transmit data off the detector is the DDL technology developed by the DAQ group [15, 16]. It implements a gigabit optical link which is driven by a Source Interface Unit (SIU) on the readout controller. Since this device is being used by multiple subdetectors this SIU will be built by the DAQ group and be implemented as a mezzanine card on the readout controller. The protocol between the readout controller and the SIU is a synchronous 40 MHz 32-bit bus.

The readout controller will start sending an event as soon as it has received a Level-2 accept for the event guaranteeing that the event will not be aborted. Since the order of events is maintained by the Level-2 accept or reject commands no special event identification logic is required but rather the queued events can be handled in the order they were triggered. The whole architecture can be implemented as a simple push architecture. Any Level-2 decision received by the TTC will be forwarded immediately to the FECs which then will start sending the next event upon an accept or will free the appropriate buffer in their round-robin buffer scheme. Therefore the readout controller acts mainly as a multiplexer for the optical transmitter (SIU).

The data format to be shipped is variable length. Every event will be encapsulated by at least three command/status words, the begin-of-event, the begin-of-data and the end-of-event commands. The begin-of-event command is followed by a fixed-length header that further defines the event type and size. Following standard practice, the first bytes of the subevent header define the total subevent size. The second 32-bit word defines the subevent type and subtype including some version number. In addition the event header has to contain the trigger type, event ID (the bunch-crossing number and orbit number), and the readout controller ID. Following the header are the zero-suppressed raw data. The exact header data format is not critical and will be defined jointly by the TPC and DAQ groups.

5.1.6.3 Detector control related interfaces

The readout controller has to have two detector control related interfaces. One is the connection to the FECs, which is required in order to configure and monitor the devices, and the other is the DCS interface itself. The functional requirements for the DCS interface are the following

- configure power state on all FECs;
- monitor power and temperature on all FECs;

- read/write any configuration parameter in the front-end, including zero-suppression thresholds, and configuration of the digital filter;
- asynchronously fire exceptions or warnings out of the front-end;
- read status parameters, such as error conditions;
- upload an event into the front-end for testing;
- download an event from the front-end as redundant fall-back.

The largest data items for up/download are complete events. However, since this is done for testing purposes only, there are no particular performance requirements here and it would be acceptable if the event data transmission took several seconds. All other parameter sets are comparatively small. The slow control interface has to be full duplex supporting the ability to address individual registers in the front-end. It is the goal to implement any front-end configuration register in read/write mode so that the as is status can be read back and verified. Further, the front-end needs to be able to assert asynchronous events such as alarms like over-power, current or temperature.

One accepted ALICE standard for slow control is the fieldbus CAN (ISO 11898–2). The maximum CAN data transmission rate is 1 Mbit/s at a maximum distance of 40 m. This would correspond in case of a central Pb–Pb event to less than 20 seconds for the readout of a complete sector. CAN is a multi-master multiple-drop serial bus implementing the CSMA/CD arbitration. There are low-cost, single-chip devices available today, such as the Siemens C167 16-bit microcontroller, which have an integrated CAN interface. This or a similar microcontroller will be hosted on the readout controller to perform all necessary detector-control functionality. The particular protocol to address the various control and status registers is not yet defined in detail as is the case for the CSR registers. This will be done in collaboration with the detector control systems group. There are no particular technological challenges. In order to reduce the single point of failure risks there will be one CAN bus per TPC sector.

The readout controller needs to be able to communicate commands to and receive status from the FECs. Most of the control and status registers will be part of an FPGA on the FEC. Therefore a simple synchronous serial interface would be adequate and would allow to keep the number of signals and cables to a minimum. This simple interface will be part of the programmable logic on the FEC and also be implemented on the readout controller as interface to the CAN microcontroller. The details of this serial interface are not defined yet and will be finalized as the prototyping of the FEC progresses. Given the speed of less than 10 MHz, there are no particular technological challenges here.

5.1.7 Front-end electronic readout efficiency

This section deals with the readout efficiency of the front-end electronics. In particular, it will be shown how the system dead time depends on the dimensions of the front-end multiple-event buffer.

We assume here that the TPC will be operated at a rate (Level-1 trigger) of about 200 Hz for Pb–Pb central collisions. At the receipt of a Level-1 trigger, the front-end electronics processes the TPC signals for 88 μ s, storing the zero-suppressed data into a multiple-event buffer. We assume that the Level-2 trigger (accept/reject) has a fixed latency which corresponds to the TPC drift time. It should be noted that, owing to the trigger past–future protection, for the TPC a new Level-1 trigger only comes after the Level-2 trigger related to the previous event.

In the case of a Level-2 accept, the memory region where the event data has been stored is protected against overwriting until the data has been shipped to the RCU. Otherwise, in the case of a Level-2 reject, this region is immediately freed to store a new data set. Therefore the multiple-event buffer is not a pipelined memory but rather a memory subdivided in regions (buffers) to be accessed randomly. To avoid fragmentation each buffer is deep enough to contain a black (non zero-suppressed) event. When all memory regions are occupied the front-end electronics generates dead time.

The dead time generated by the TPC has therefore two contributions: detector dead time, i.e. the drift time, and front-end electronics dead time (readout dead time). While the multiple-event buffer scheme can reduce the second contribution, it cannot eliminate or reduce the first. This obvious fact implies that the total dead time has a lower limit determined by the detector drift time.

In order to study the readout performance of the front-end electronics and to dimension properly the multiple-event buffer, a Verilog model of the front-end chain has been created. Verilog is a hardware description language suitable for the stochastic analysis of digital systems. The results are displayed in Figs. 5.24 and 5.25 which show how the system dead time depends on the number of buffers for two different Level-1 rates: 1 kHz and 200 Hz, respectively. The simulations assume a Level-2 rate of 100 Hz and an average occupancy of 25%.

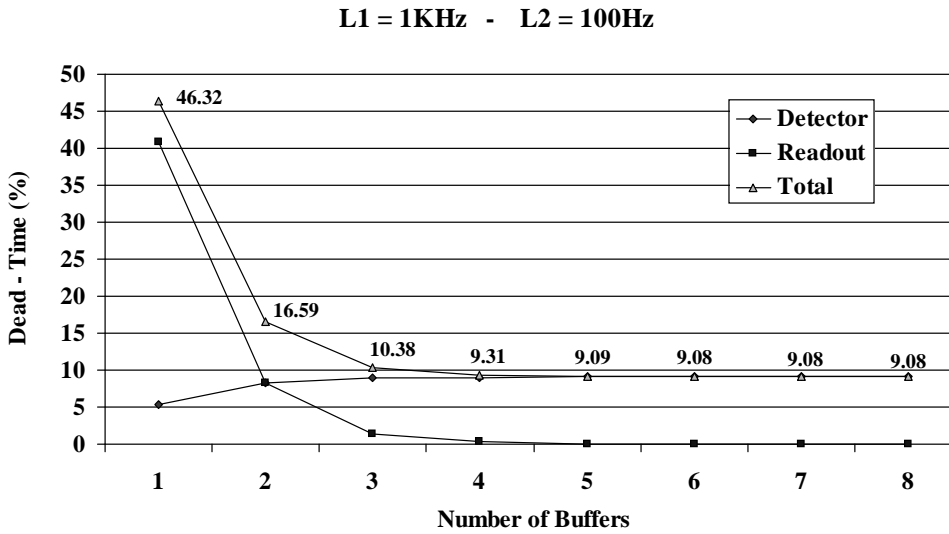


Figure 5.24: TPC dead time versus the number of buffers in the front-end memory. The simulation is made under the following assumptions: Level-1 rate = 1 kHz, Level-2 rate = 100 Hz, average occupancy = 25%.

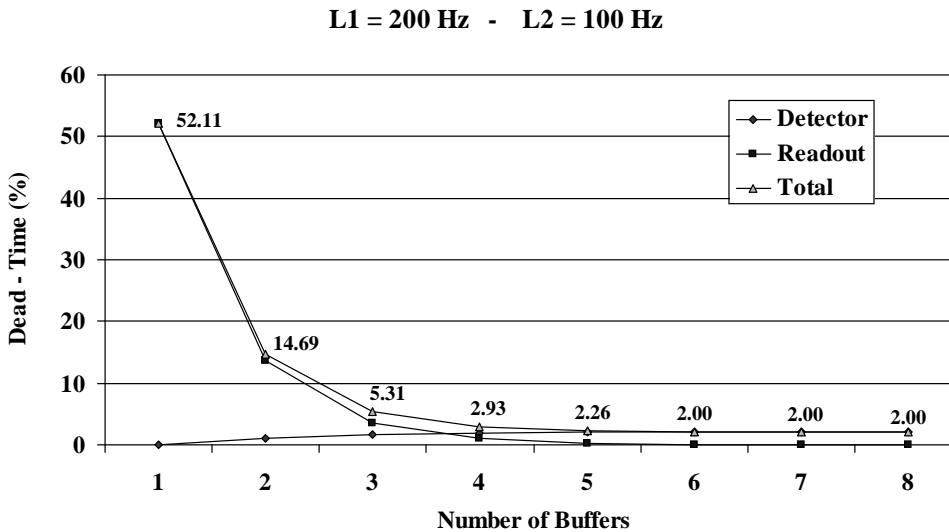


Figure 5.25: TPC dead time versus the number of buffers in the front-end memory. The simulation is made under the following assumptions: Level-1 rate = 200 Hz, Level-2 rate = 100 Hz, average occupancy = 25%.

5.1.8 Low-voltage power supplies and distribution

For the calculation of the number of low-voltage supply lines for the FECs and their cross section, it is assumed that each card dissipates at most 100 mW/channel of power (in total 12.8 W), where 20% are consumed by the preamplifier/shaper at ± 1.5 V and 80% are consumed by the digital part at +3.3 V. In total the supply system has to supply about 21 kA of current. It is assumed that the power supplies are located outside the L3 magnet on both sides of the TPC in the area not accessible during LHC operation. The cable length required in this scenario is 40 m.

To avoid cooling of the cables but keep the cost of cables moderate a voltage drop of 0.5 V has been assumed as a design value leading to acceptable levels of heat dissipation in the L3 cavern. In Table 5.8 the characteristics of the cables are listed.

Table 5.8: Characteristics of the low-voltage supply cables. The voltages are nominal voltages at the load. The power dissipation quoted refers to the power dissipated in 40 m of cables.

Parameter	Analog supply	Digital supply
Nominal voltage	+1.5 V/-1.5 V	+3.3 V/GND
Cross section	$2 \times 4 \text{ mm}^2$	$2 \times 10 \text{ mm}^2$
Current	$2 \times 0.85 \text{ A}$	$2 \times 3.1 \text{ A}$
Power	1700 W	6200 W

Two scenarios are considered. In the first the power for each FEC is provided individually via a separate cable with four wires and a common shield (in total 2232 cables per end-plate). This assumes that the cables have to pass through the existing gaps at the L3 magnet doors with its chicane and thus have to be flexible enough to accommodate a bending radius of less or about 5 cm. If the openings can be enlarged the need for flexible cables is alleviated. In the second scenario, therefore, the supplies for about five cards are combined into a thicker, less flexible but more economic cable. There would be a transition from the thick cable to individual cables at a patch panel mounted at the service support wheel (see below).

To allow access to the inner tracking system the TPC and its supply lines have to accommodate movements of about 4.5 m along the beam direction. Due to space limitations no distribution scheme allowing such a movement while at the same time keeping the supply lines permanently connected could be found. It is therefore foreseen to connect the low-voltage cables via patch panels mounted on the service support wheel. For service interventions all cables have to be disconnected at the patch panel.

The cross sections of all low-voltage cables connecting the patch panel with the individual FECs can be reduced easily by a factor of two compared to the 40 m long main sections. The estimated power dissipation close to the end-plate is then 200 W per end-plate.

To avoid ground loops it is foreseen that the power supplies are left floating on the supply side and connected to ground only at the detector side. A schematic layout of the low-voltage system with its grounding scheme is shown in Fig. 5.26. Since each FEC is connected to the pad plane with eight cables, each of which carries the ground for each of the 16 channels plus a common shield, a relatively large cross-section is available in case of an interruption of the ground return line.

The DCS will monitor the voltages on the FECs before regulation. If a voltage drop is detected the power supplies can be powered down sufficiently fast (on a time-scale of ms) to avoid damage due to excessive currents.

With regard to the stability of the power supplies no special requirements are necessary since the final regulation is done on the FECs themselves. Quite strict limits on noise have to be adhered to the given sensitivity of the preamplifier/shaper part. The cables are therefore shielded between the power supplies and the patch panel. At this point no analysis has been performed regarding the best grouping of power-supply lines and therefore the maximum output currents required per supply module.

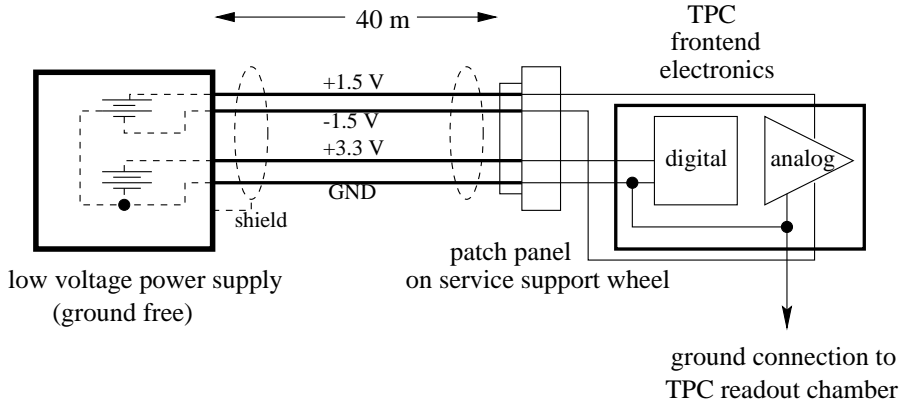


Figure 5.26: Connection of the low-voltage power supplies to the front-end electronics of the TPC.

5.1.9 System implementation

5.1.9.1 Quality assurance

The inaccessibility of the ALICE experiment during the entire year of LHC running makes stringent quality tests of the readout electronics mandatory before installation. To minimize the failure rate all FECs will be tested in a dedicated test set-up. A schematic diagram of this tester is shown in Fig. 5.27. An important part of the test procedure is a burn-in process, which will be made in an oven at a temperature of 50 °C for a period of approximately 10 hours. All crucial functions of the circuits will be cycled according to a preselected scheme. During the 10 hours of burn-in typically thousands of cycles will be completed. The results of the tests will be automatically logged to file for later investigation of the errors occurring. A malfunctioning component will be replaced with a new one and the full test will be

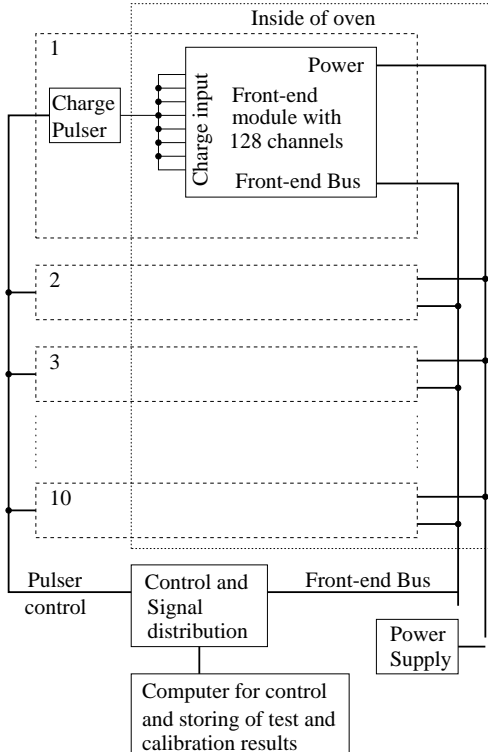


Figure 5.27: Functional diagram of the FC tester with burn-in feature.

repeated before accepting the board for installation. Special care has to be taken to control the external noise influence on the analog circuits.

The test set-up foreseen will hold ten units to be tested and two test rounds could be completed per 24 hours. A total number of 570 000 readout channels grouped in about 5000 FECs (including 10% spares) then requires about 240 days to complete the burn-in acceptance test using one test station. It is foreseen to duplicate the test set-up in order to speed up the burn-in process.

Once the boards are accepted and installed on the TPC an *in situ* testing procedure has to be implemented. All the digital parts can be tested through the DAQ and/or the DCS. To test the analog part (preamplifier/shaper and ADC) it is necessary to include the TPC itself or use the calibration pulser. During operation the full system has to be monitored for malfunctioning channels.

5.2 Readout

The ALICE Trigger/DAQ architecture was initially designed for a set of requirements described in the Technical Proposal [3]. These requirements and the corresponding Trigger/DAQ architecture have been relatively stable since then and have been refined for the preparation of the first TDR. This architecture is now facing two important modifications of the original requirements. First, the occupancy of the TPC is expected to be higher than originally assumed. Second, a new trigger detector (the TRD) has been introduced into the ALICE detector system. Both modifications require revisiting the baseline architecture in order to ensure that the changing requirements can be met by the Trigger/DAQ architecture. In the new scenario the TPC and TRD detector data are sent directly into the host processors of a Level-3 Trigger/DAQ processor farm. The system is scalable in terms of processing power and bandwidth in order to meet the computing requirements of the various physics programmes. It is absolutely mandatory that zero-suppressed raw data are recorded without any further processing, especially in the first year of running in order to ensure a complete understanding of the TPC response. The intelligent readout system (Level-3) guarantees the readout of unprocessed full TPC events at a rate of 10 Hz. Having understood the TPC response to central Pb–Pb collisions, the Level-3 system will take over more functionalities. Almost lossless data compression and selective readout for TRD events can be implemented easily, since these techniques do not need large computing power. Finally, by adding more computing power, online track finding in the whole TPC and therefore very effective data compression methods and TPC-based selective readout schemes become feasible. Should there be a need for a higher rate of unprocessed full TPC events, the bandwidth of the system can be increased. This system is referred to as Level-3 trigger, Level-3 filter and Level-3 processors in various places, depending on the functionality addressed in the context.

Extensive simulations of track-finding methods and data flow have been performed for the proposed Level-3 Trigger System of the STAR [18] experiment at RHIC. A large scale prototype of an Level-3 system is currently being installed. There is a large overlap in the physics objective, detector design, readout electronics and personell between the STAR and the ALICE Level-3 systems.

5.2.1 Physics requirements

5.2.1.1 Event size

The latest simulations for central Pb–Pb collisions indicate that the average TPC occupancy will be about 25% (see Table 5.13 on page 132 in Section 5.2.3). The readout chambers have a granularity of 570 000 pads, the number of time buckets per channel is assumed to be 512. The exact number of time buckets will be determined after the first Pb–Pb collisions have been recorded and the cluster shapes have been analysed. Depending on occupancy it may increase to 768 at the most. The 10-bit amplitude can be compressed into a nonlinear 8-bit number. This corresponds to a raw event size of 292 Mbyte. The event size can be reduced by roughly 30%–50% by removing the two inner 45° cones of the TPC volume

during readout. Different solutions for coding the zero-suppressed data are currently being investigated. Assuming a 15%–40% overhead for encoding the zero-suppressed data yields an event size of about 66 Mbyte $\pm 15\%$ per central collision. Minimum-bias events are assumed to be smaller by roughly a factor of two (in NA49: central Pb–Pb 100%, medium bias 85%, p–A 30% and pp 20%).

5.2.1.2 Event rates

In general, the required central event samples for various physics topics vary between $< 10^6$ for most inclusive hadronic observables to $> 10^7$ for rare processes such as open charm and open bottom production, quarkonia production, and the detection of direct real and virtual photons [3, 21–23]. The detailed event rates to be taken undergo continuous discussion within the collaboration.

In the following we present, for a quantitative evaluation of the proposed readout schemes, an illustrative set of event rates expected for hadron and electron physics in the TPC. However, the proposed readout scheme is sufficiently general that physics motivated variations in the rates should be accommodated without changes in the architecture.

An event rate of about 1 Hz leading to more than 10^6 events per ALICE year is currently considered sufficient for most hadronic observables. An example for an observable that would require higher event rates (≥ 10 Hz) is the reconstruction of D mesons via their hadronic decay products. The ALICE DAQ was originally dimensioned to handle up to 50 Hz of events with full readout and in addition up to 1 kHz of muon triggers, with a total bandwidth to mass storage of up to 1.3 Gbyte/s. With the introduction of the TRD and the increase of occupancy in the TPC, the event size has grown substantially since the publication of the Technical Proposal and would currently limit the data rate to less than 30 Hz within the foreseen bandwidth.

As discussed above, the final bandwidth of the system can be increased beyond 10 Hz if the corresponding physics requirements are there. However, by introduction of the Level-3 system, online tracking will make it feasible to perform partial readout, event rejection and sophisticated data compression. It can significantly reduce the event size for full TPC readout (potentially by more than one order of magnitude) and/or reduce the event rate (by online filtering) and therefore restore the originally foreseen rates within or below the originally foreseen bandwidth to mass storage. Typical event rates and the TPC event size for different compression schemes (discussed in detail below) and different trigger samples are given in Table 5.9.

The required event rates for the full dielectron programme and an improved open-charm programme with a Level-3 trigger are as follows.

Full dielectron programme:

- TRD triggers TPC readout at $\simeq 60$ Hz;
- Selective inspection of a few TPC sectors;
- Online processing of electron track candidates, limited processing compared to full TPC tracking;
- Output rate is $\simeq 30$ Hz, event size 0.5 Mbyte.

Improved open charm (hadronic decays) programme:

- TPC readout at 10 Hz–100 Hz;
- Online processing of full TPC data, large processing power needed for cluster and track finding;
- Selecting high-transverse-momentum tracks;
- Output rate is 10 Hz–100 Hz, event size is 4 Mbyte.

Table 5.9: Typical TPC event rates and data rates. It has to be noted that all other detectors contribute 10 Mbyte to the size of an event for a central collision. The muon programme will increase the bandwidth by approximately 250 Mbyte/s.

	No. of events	Event rate [Hz]	Event size [Mbyte]	Bandwidth [Mbyte/s]
1 — no Level-3, full TPC readout				
Hadronic observables	10^6	1	66	66
Open charm (hadronic decays)	10^7	10	66	660
2a — Level-3, lossless data compression				
Hadronic observables	10^6	1	47	47
Open charm (hadronic decays)	10^7	10	47	470
2b — Level-3, slightly lossy data compression				
Hadronic observables	10^6	1	19	19
Open charm (hadronic decays)	10^7	10	19	190
3 — Level-3, TRD trigger and selective TPC subsector readout				
Dielectrons	6×10^7	60	1 – 2	60 – 120
4 — Level-3, TRD trigger, selective TPC tracking and event rejection				
Dielectrons	3×10^7	30	0.5 – 2	15 – 60
5 — Level-3, TPC tracking and high- p_t track selection (> 0.5 GeV/c)				
Open charm (hadronic decays)	10^7	10	20	200
6a — Level-3, TPC track/cluster modeling and full data compression				
Open charm (hadronic decays)	10^7	10	4	40
6b — Level-3, TPC tracking and data compression, DE tracks, TPC summary event for correlations				
Dielectrons	3×10^7	30	5	150

5.2.2 Data rate reduction

From a trigger point of view the detectors in ALICE can be divided into two categories: fast and slow. Fast detectors provide information for the trigger system at every LHC bunch crossing. Decisions at trigger Levels-0, -1 and -2 are made using information from these detectors. Fast detectors are the Forward Multiplicity Detectors (FMD), the Zero Degree Calorimeter (ZDC), the Transition Radiation Detector (TRD) and the muon trigger chambers.

The slow detectors are tracking drift detectors and need a longer time span after the collision to deliver their data. The Time Projection Chamber (TPC) and the Inner Tracking System (ITS) are slow detectors. Their slowness is compensated for by the detailed information they provide. The Level-3 system is intended to take advantage of TPC information (up to 66 Mbyte/event at rates of up to 200 Hz) in order to reduce the data rate as far as possible to have reasonable taping cost. The data are then recorded onto an archival-quality medium for subsequent offline analysis.

A key component of the proposed system is the ability to process the raw data — performing, for example, track finding in real time — besides its baseline requirement of forwarding zero suppressed events into the DAQ data stream. Level-3 is designed to utilize the information from the TPC and the fast detectors, e.g. the TRD. The system will be flexible enough to be expanded to include other tracking devices.

Data reduction can be achieved in different ways:

- Generation and application of a software trigger capable of reducing the input data stream.

- Reduction in the size of the event data by selecting subevents. By analysing the tracking information or by utilizing TRD information, Regions Of Interests (ROI) can be defined. The data volume is significantly reduced by recording only summary information and raw data of the ROIs (e.g. electron tracks).
- Reduction in the size of the event data can also be achieved by compression techniques. General lossless or slightly lossy methods can compress TPC data by factors 2–3 [20]. By online tracking and a compressed data representation an event size reduction by a factor of 15 can be achieved [24]. This data compression method is based on a cluster model and a local track model. It is assumed that all TPC information can be reduced to a local track with its helix parameters and a mean charge, the corresponding cluster information (charge per cluster, cluster position) is stored as the (quantized) deviation from the local model. The result may be further compressed by a Huffman coding scheme (see e.g. [25]). Since all necessary information is preserved, TPC data can later be once more reconstructed by the offline chain. This method may be useful in the later phase of the experiment when the detector and the reconstruction performance are well understood.

5.2.2.1 Volume reduction

The raw data volume per event can be reduced by compression techniques or by selective or partial readout. These subevents contain only the raw data of a few tracks. Zero suppression is performed in the front-end electronics by pedestal subtraction (a threshold operation) and one-dimensional (time direction) hit-finding. The resulting long zero sequences between hits can then be compressed by, for example, run-length encoding, which is equivalent to storing only the hits and their positions. This technique achieves compression ratios which are roughly inversely proportional to the TPC occupancy. The thresholding and hit-finding operations are lossy techniques which could lead to a loss of small clusters or tails of clusters. The following encoding methods of hit sequences are lossless. All these operations are performed on the front-end electronics board (see Section 5.1.3.5).

Selective or partial readout

Subevents or ROIs can be defined on the basis of rough tracking information, including a PID supplied by the TRD. All raw data inside these regions are written on tape and all other data are dropped. For the lepton measurements the data volume can be reduced to candidate e^+e^- tracks, which would yield a few tracks per event.

Data compression

General data compression techniques have been applied to TPC data, i.e. both the NA49 raw data [20,26] and the STAR simulation data [18,19,27]. Zero suppression reduces the TPC data by a large margin (depending on occupancy). Lossless transformations like variable length codes (e.g. Huffman coding) or lossy compression methods like vector quantization can compress the ADC data by factors of up to 3. The data volume can be reduced even further by using data modelling techniques, and storing only quantized differences to a data model, i.e. a cluster and a local track model. This results in reduction factors of about 15.

Lossless compression – variable length coding The crucial observation to reduce the size of the data is that the ADC values are not equally probable. Small ADC values occur very often in the data stream but larger ones are rare (Fig. 5.28). The distribution is approximately exponential. The expected size of the data can be reduced if short words are used for frequent values and longer ones for rare values. Another advantage of this technique is that one is no longer restricted to 256 symbols — as one is with bytes — or powers of two. One can choose as many codes as necessary. This means that if one enhances

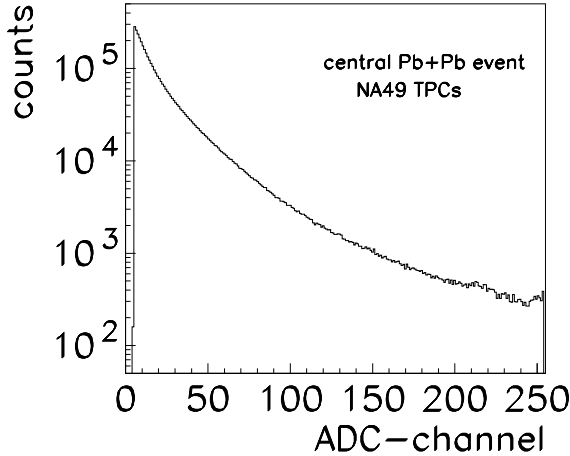


Figure 5.28: Distribution of ADC values for a central Pb–Pb collision.

the ADC resolution from 8 to 9 bits the size of the data is no longer doubled, but increased by 1/8 in the worst case.

There is a theoretical lower bound on the average word size that can be achieved by this strategy. This lower bound is called entropy E of the data source and can be computed as

$$E = \sum_{x \in \Sigma} p(x) \log p(x), \quad (5.5)$$

where Σ is the set of all possible words that are output by the data source, p is the probability of the occurrence of an ADC value x . It can be shown that this bound is tight for stochastic data sources [28]. There are compression techniques that approach this bound arbitrarily close. An example is arithmetic encoding, which is rather complex and also patented. An alternative to arithmetic encoding are Huffman codes. They are easier to implement, need less processing power and achieve good results unless the distribution of input values is too extreme. It is important to note that the average size of an event will be reduced by this approach, but one has to consider that sometimes events can become larger than uncompressed.

A TPC is obviously not a stochastic data source, as adjacent ADC values are highly correlated. Therefore it is possible to compress the data to a lower bit rate than the entropy of the ADC values. In other words, there are representations of the TPC data that have a lower entropy than the formats described above. Various methods like differentiation, prediction, etc. have been evaluated, but none of these approaches yields results that are much better than the plain Huffman coding [25, 29].

Lossy compression There is some gain in using the lossless techniques such as simple Huffman encoding. Better results can be achieved when very small, noise-like changes of the data are tolerated. This leads to the so-called lossy compression schemes. One kind of lossy compression, the zero suppression together with a run-length encoder, is already in use at the front-end. The following section focuses on the further reduction of the remaining data.

- **Vector quantization**

Vector quantization [30] is a sophisticated type of quantization. Here, statistical dependencies between successive data samples are exploited: Instead of quantizing data samples independently, several samples are grouped together to form a vector of data samples. Then this vector is compared to entries in a codebook and the number of the best matching vector from this codebook is

output, where best matching means lowest distance using Euclidean or any other metric, as best suited for the application. If the distribution of the input data is known in advance, the vector quantizer can produce data with a very low distortion relative to the bitrate. To be optimal, the codebook has to be trained on statistical properties of typical input data. This is usually done before the codebook is applied with an algorithm known as the modified LBG algorithm [31]. The adapted codebook then remains unmodified throughout the actual quantization.

- **Vector quantization with residual encoding**

Though this approach offers a very low bitrate, it is obvious that there is almost no possibility for the vector quantizer to change behaviour: Since the codebook is preproduced, only the given vectors are available to represent the output data. Even if the codebook were well adapted to the data, sometimes large quantization errors could occur (Fig. 5.29). To prevent this, we need to store the differences between the input data and the selected codebook entry, the so-called residuals. These residuals are then quantized and entropy encoded to achieve an even lower bitrate. A quantization of the residuals is especially effective, since the distribution of errors between codebook entry and input data is very steep: If the codebook is sufficiently trained, the vector quantizer will already absorb much of the input signal energy, so the residual encoder will mostly get values around zero. When these values are quantized, even more values are mapped to zero. Here, arithmetic compression [25] is the method of choice.

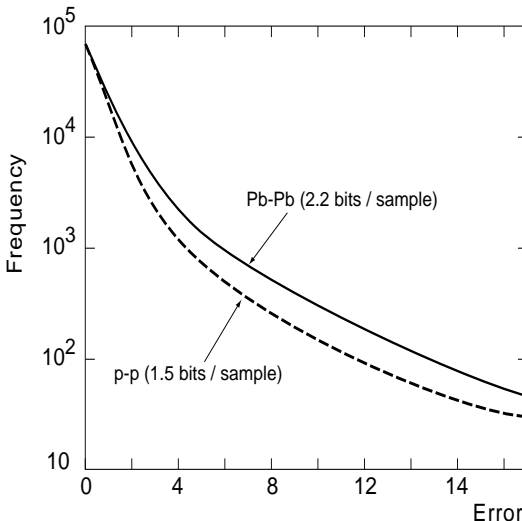


Figure 5.29: Error distribution of vector quantization.

- **Cluster and track Modelling**

The best compression method is to find a good model for the raw data and to transform the data into an efficient representation. Information is stored as model parameters and (small) deviations from the model. The relevant information given by a tracking detector is the local track parameters and the clusters belonging to this track segment. The local track model is a helix; the knowledge of the track parameters helps to describe the shape of the clusters in a simple model [33, 34]. The track finder reconstructs clusters and associates them with local track segments. Note that track recognition at this stage can be redundant, i.e. clusters can belong to more than one track and track segments can overlap. Once the track recognition is completed, the track can be represented by helix parameters. These are curvature r , starting point (x, y, z) , dip angle λ , azimuthal angle ϕ , track length, average charge, χ^2 of the helix fit and the number of clusters belonging to this track segment (see Table 5.10).

Table 5.10: Track parameters

Parameter	Size [byte]	Type
Curvature r	4	float
Begin x	4	float
Begin y	4	float
Begin z	4	float
Dip angle λ	4	float
Azimuthal angle φ	4	float
Track length	2	integer
Cluster charge (average)	2	fixed point
χ^2	2	fixed point
Number of clusters	1	integer
Total	31	

Table 5.11: Cluster parameters

Parameter	Size [bit]
Flag empty cluster	1
Δ time	6
Δ pad	6
Δ cluster charge	7
Δ shape	4
Total	24

In a second step, the deviation of the cluster centroid position from the track model (residuals), the deviation from the average charge and deviations from the expected shape (based on the track parameters) are calculated for each cluster. These numbers are then quantized by a nonlinear transfer function adapted to the detector noise and detector resolution (see Table 5.11). Remaining clusters can be optionally kept as raw data arrays.

The compression method discussed above allows for a later second pass of calibration and distortion corrections, track and vertex finding and fitting, and dE/dx analysis. Since the aim of the track finding is not to extract physics information but merely to build a data model, which will be used to collect clusters and to code cluster information efficiently, any inefficiencies in track finding e.g. due to an unprecise track model will result in an inefficient compression, but not in a loss of clusters; no relevant data are lost. By fast and redundant online track recognition, reduction factors of about 15 can be achieved [24].

Experimental results The described algorithms were applied to a set of TPC events from the NA49 Pb–Pb collisions as well as to pp data. The results for central heavy-ion collisions are shown in Table 5.12. Compression factors for pp data with a much lower occupancy are higher by 30%–40%. In our experiments we used a vector quantizer of length three, so that two vectors model the majority of hits of lengths up to six time bins. The size of the codebook is 256 entries (VQ3). This leads to a data rate of 2 bit/sample for the vector quantizer alone. The algorithm RVQ3 is a vector quantizer of length three with quantized residuals. Allowing an absolute error of one in the residual quantization, the change of the number of clusters was less than 10^{-4} and no change in the number of tracks was observed. First preliminary test with ALICE simulated data are in accordance with the above results [32].

Table 5.12: Performance of different compression algorithms on NA49 TPC data.

Type of encoder	Entropy bit/sample	Relative event size Pb–Pb (NA49) [%]
Zero suppressed raw data	8	100
Huffman	5.8	72
Transformations e.g. differentiation (gif)	5.3 – 6.1	66 – 76
RVQ3 lossless	4.8	60
VQ	2.3	
Residual value	2.5	
RVQ3 lossy (error 1 ADC value)	3.8	48
VQ	2.3	
Residual value	1.5	
VQ3 lossy	2.3	29
Cluster and track Modelling		7

5.2.2.2 Event rate reduction — Level-3 trigger

Based on the results from the TRD analysis and the online tracking information, the (sub)event building can be aborted. The Level-3 system is responsible for deriving such a trigger decision. The relevant tracks are identified by the TRD, and a processing command is sent to the appropriate sector processors of the TPC. The Level-3 processor receives this information via its Level-3 network from the TRD global trigger. This can easily be implemented at a rate of a few hundred Hz without presenting any particular technological challenges.

5.2.2.3 Modes of operation

The Level-3 system will incorporate all data compression methods mentioned above. The TPC raw data are shipped directly to commercial off-the-shelf computers, which have FEDC (Front-End Digital Crate) and LDC (Local Data Concentrator) functionalities (see Section 5.32). The number of machines is mapped to the natural granularity of the TPC (36 sectors, 180 fibre connections). This local layer of the Level-3 system is part of a hierarchical system. Data compression, subevent selection and track recognition are performed on the local level, the global layer is responsible for track merging across detector boundaries and different detectors and for deriving software trigger decisions. The mode of operation for a combined dielectron/open charm programme is shown in Fig. 5.30. The Level-3 system utilizes the full luminosity, while producing manageable data rates.

No Level-3 activity — full TPC zero-suppressed data readout

Zero-suppressed raw TPC data is passed on to DAQ without any processing beyond standard data compression. This is the baseline assumed in the Technical Proposal.

Full readout and almost-lossless data compression

In this model, the receiver processors function exactly the same way as the GDC processors in the Technical Proposal. The compression for each sector is made in parallel and the reduced data is then transmitted. The event building would take place after the compression. Thereby, the event headers would not be compressed, but the additional overhead for all the headers can be neglected.

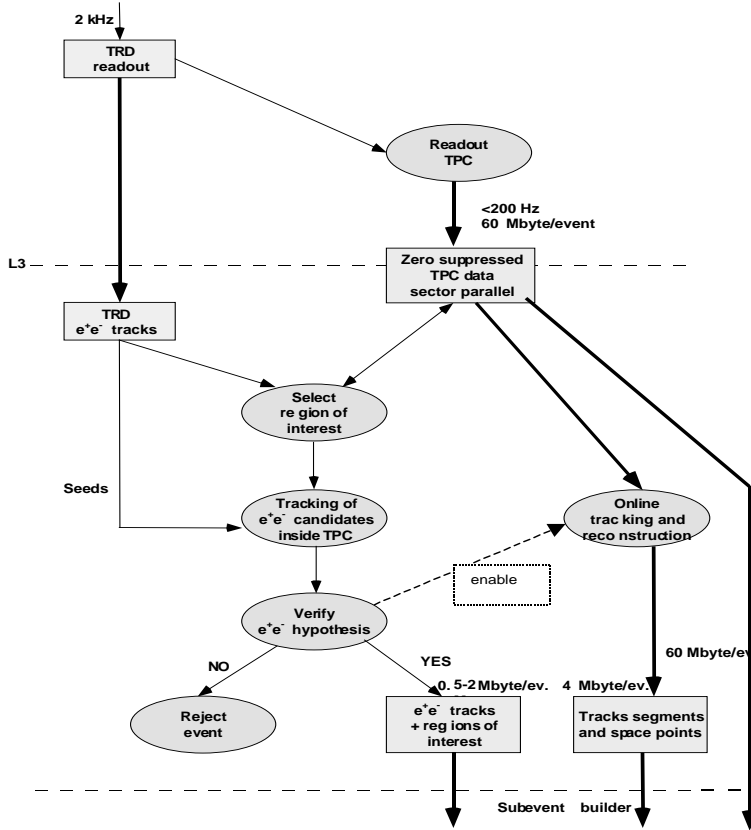


Figure 5.30: Level-3 data flow.

Full readout — data exchange with other detectors

In principle, the new architecture does not need to have an influence on other subdetectors. The raw data of other detectors can easily be distributed to the relevant processors within the Level-3 farm. It is also possible to combine the data from the receiver processors into one overall data flow after the trigger has been received and to send it to the DAQ. This ensures that, at any time, zero-suppressed and even non zero-suppressed raw data can simply be read out, though limited by the tape bandwidth.

TRD Level-3 trigger and selective readout (without tracking)

The electron tracks are identified by the TRD, and a processing command is sent to the appropriate sector processors of the TPC. The coordinates of the track candidates are distributed through the Level-3 network. After having received the event in memory, the sector processor calculates roads in the raw-data space (pad number and time bin) based on the track parameters given by the TRD trigger. If an event is to be read out, the processor receives an appropriate network message and the ROIs are transferred. If not, the internal data are marked available again in the FEDC tables and overwritten later by another event.

TRD Level-3 trigger and selective Level-3 processing

Even if the TRD should perform as designed, it will produce, for example, 40 Hz triggers but only 20 Hz of them will be good events. The intention here is to achieve this reduction by tracking the high- p_t candidates in the TPC. If the TRD selectivity is not as high as planned, the same method could be used for increasing the selectivity by tracking the track candidates in the TPC so that the resulting trigger rate would not exceed 10 Hz–20 Hz. However, this does not require the full event. The relevant tracks are identified by the TRD, and a processing command is sent to the appropriate sector processors of the

TPC. After having received the event in memory, the processor starts tracking the defined track candidate only together with the processing command. Which track candidate to use has to be distributed through the Level-3 network. During these calculations, the processor can already receive another event to make maximum use of the CPU time. The Level-3 processor receives the information concerning the candidate via its network from the TRD global trigger. This can easily be implemented at a rate of a few hundred Hz without presenting any particular technological challenges. The tracking is done relatively fast.

Level-3 processing for ROI selection and partial readout

Owing to the data, each receiver already knows what needs to be done with the data record. Up to 16 TTC commands accompanying the data can be defined. In case of a full readout and Level-3 processing, the cluster finder algorithm has to be executed first in order to determine space points, a task that typically requires the longest time. This can be done in parallel for each sector. The receiver processors would take on this task. The architecture offers enough leeway to be able to provide adequate computing power. For example, four- to eight-fold processor modules could be used instead of simple processors. After the space points are determined, they could then be sent to a second layer for tracking. This is only one scenario, many other solutions are possible. The receiver board, for example, can be configured in such a way that a certain part of the events (every second, three out of four, etc.) are sent directly to the network to obtain a higher degree of parallelism. All these scenarios can be put into practice or even be changed long after the installation.

Level-3 processing for data compression

This is similar to the above, but tracking has to done only locally, though redundantly, i.e. with very open parameters, since track parameters are only used for compression purposes. The aim of the track finding is not to extract physical information but merely to build a data model, which will be used to collect clusters and to code cluster information efficiently. Therefore, the pattern recognition algorithms are differently optimised or even different methods may be used, as compared to the offline tracking.

5.2.3 Architecture

The basic idea is to add an intelligent layer to the TPC readout and to move the data only if necessary. Data moving costs money and data storage is location independent. Custom designs should be avoided wherever possible and mass-produced electronics shall be used wherever possible. The updated architecture will allow a very high degree of flexibility by reducing the requirement for custom hardware to a minimum and using standard interfaces instead. In the new scenario the TPC and TRD detector data are sent directly into the host processors of a Level-3 Trigger/DAQ processor farm, thus avoiding the necessity for custom front-end systems. By using a standard bus, which is common in any commercial off-the-shelf computer system today, a very large degree of freedom is achieved with regard to the processor architecture.

The intelligent Level-3 layer will make use of the inherent granularity of the TPC and TRD readout. Each sector is processed in parallel, results are then merged on a higher, global level. 36 TPC sectors are processed in parallel by a single Level-3 processing farm per sector. For a Level-3 trigger (e^+e^- inspection) only a few tracks in a few sectors have to be analysed. A complete event reconstruction (Level-3 processing) results in 12 000 trackable tracks total, 333 tracks and 125 000 clusters per sector (see Table 5.13 and Section 7.2).

The TPC granularity is adapted to the granularity of the TRD. Therefore there will be 2×18 sectors, which are composed of two segments each (inner and outer). The analog data is preamplified, shaped, and digitized (10 bits). A digital filter will be used to achieve a better tail correction. After this, zeroes will be suppressed, and the data will be shipped to the counting room. In order to optimize fibre utilization the front-end electronics implements a small elasticity buffer.

Table 5.13: Number of tracks and clusters and size of raw data of a central Pb–Pb event ($dN_{ch}/dy = 8000$, 570 000 channels, 160 pad rows, approximately 66 Mbyte/event).

	Total	Per sector	Per optical link
TPC raw data	292 Mbyte		
Without inner cone	146 – 208 Mbyte		
After zero suppression	37 – 52 Mbyte		
Including coding overhead	≈ 66 Mbyte	1.8 Mbyte	0.37 Mbyte
Total trackable tracks	12 000	333	
Total clusters	4 500 000	125 000	25 000
Track summary (total)	0.4 Mbyte	11 kbyte	
Compressed data (total)	4.2 Mbyte	120 kbyte	

The TPC raw data are shipped optically to the counting room. The protocol proposed here is the ALICE development DDL [16]. Appropriate mezzanine cards are available in the PMC form factor. Assuming a total of 180 optical links or five links per sector, the data rate per link corresponds to about 67 Mbyte/s (at 200 Hz) leaving plenty of head room.

In the following, we will show that the FEDC functionality presented in the ALICE TP can be achieved by using an architecture, where a new RORC plugs directly into the backplane of a commercial off-the-shelf computer, such as a PC. The corresponding overall architecture of a sector is shown in Fig. 5.31. The raw data are directly transmitted to a processor’s main memory via the widely used standard PCI bus (assuming the use of a fast 66 MHz/64-bit version, which is available today), while the LDC task runs on the processor’s CPU. The elasticity buffers on the PCI FEDC and the main memory of the computer functions as the event buffer in this case.

The processors that hold the PCI RORC are called receiver processors in Fig. 5.31. They are generic standard processing units, which could be operated as such, ignoring or disabling the RORC, or be part

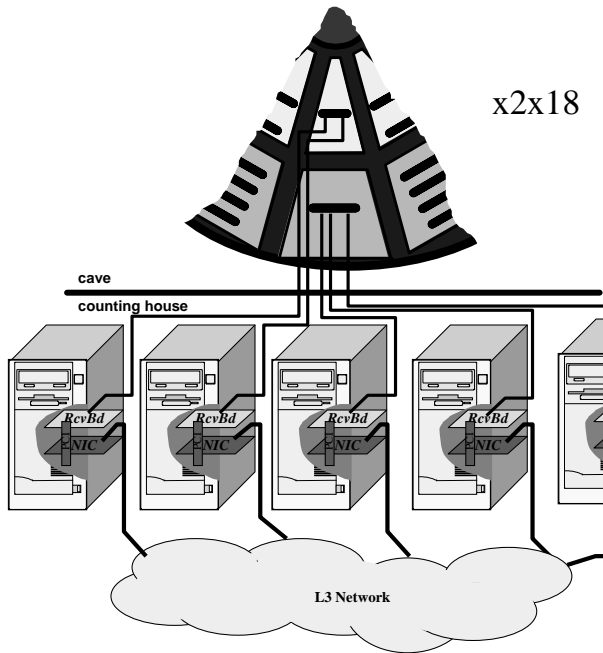


Figure 5.31: Schematic view of the readout electronics installed on a sector.

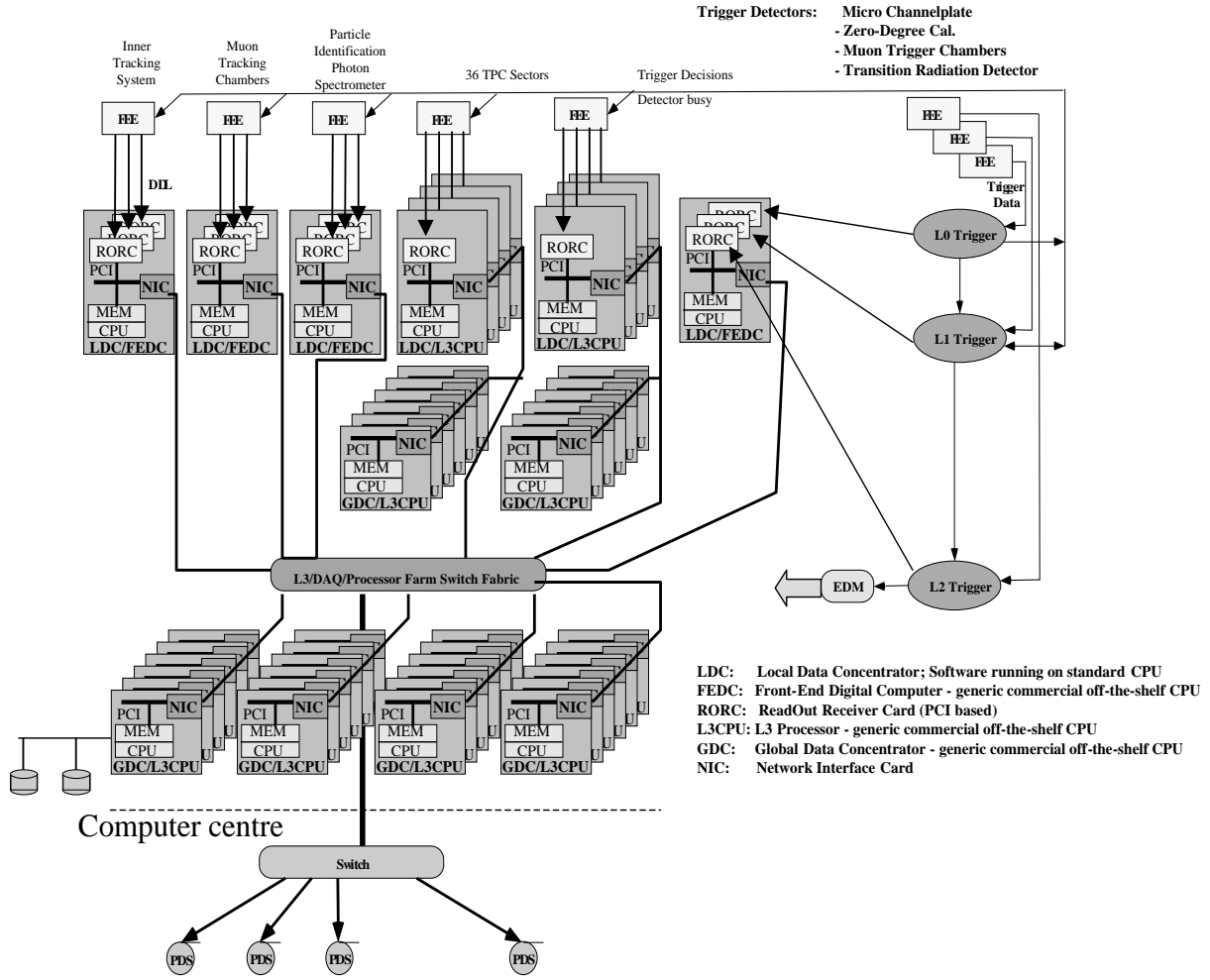


Figure 5.32: Level-3 architecture.

of the whole system or even further operate as a stand-alone single-sector DAQ system. These different configurations are only software switches.

Figure 5.32 shows a sketch of the Level-3 architecture. The receiver processors are all interconnected by a hierarchical network. The bus standard used to interface to these Network (Interface) Cards (NIC) is labelled as PCI as this is the standard that would be used if the system were to be built today. However, in the unlikely event of another standard becoming as widely accepted by the time the design has to be frozen, it would be used. At present, neither the precise network topology nor the networking technology are defined. However, it is obvious that the TPC sector granularity is reflected in the architecture processing the TPC data. There are various promising candidates and as in the case of the computing nodes the best standard network will be chosen at the latest time possible. This requires the use of portable standard network APIs. Following this Level-3 network, there are only further processors. Note that the GDC and LDC functionality can be performed on identical processing nodes. LDC and GDC functionality can even be performed on the same CPU running different tasks. Note that the permanent data storage is performed by the computer centre through an appropriate link. This very same link can be used to feed this general-purpose processing cluster when ALICE is not running in order to allow the utilization of this system as an analysis processing farm.

The system architecture provides an overall unit that can also be operated offline. In this mode, only some processors have an additional card, which may or may not be used (RORC). If the TPC is to be tested offline, an appropriate readout process could then run simultaneously in the background (similar to

a computer in a network which, today, can receive and send data in the background) or a corresponding group of receiver PCs could be taken out of the Level-3 cluster. All of this can be controlled by software, without any need to make changes to the hardware. It is possible that the online and offline operation will be using different operating systems, something which could be done easily. Each computer should be equipped with a small hard disk for paging and swapping in the offline mode.

5.2.3.1 Estimated computing power

Track recognition in tracking detectors like the TPC is usually done sequentially. After finding clusters, the position and charge of the clusters are corrected for gain differences, distortions, time offsets, etc. These space points are then passed on to a track finder which builds track pieces out of clusters. Track pieces are finally merged to global vertex and nonvertex tracks.

A fast cluster finder has been optimized for speed [35]. Preliminary timing tests in the STAR environment [19, 36] showed that cluster finding for 600 clusters including deconvolution can be done in 10 ms on a 66 MHz version of a i960 microprocessor [37]. The second step in the sequential track recognition scheme is a track finder. The tracker combines a number of space points to form track segments. Track segments are then merged to form vertex and nonvertex tracks. The track finder currently used in STAR is based on an algorithm described in Refs. [38, 39]. Its main features are an optimized data organization and a conformal mapping to speed up fitting procedures. It takes about 90 ms on an ALPHA XP1000 (500 MHz) to find 400 tracks.

The processing power needed could be estimated on the basis of these benchmarks for the STAR Level-3 system [36]. A farm of the order of about 500 PCs (year 2005 PCs, assuming scalability according to Moore's law) would suffice for full tracking. Partial readout needs even less computing power. In view of the high occupancy a sequential track recognition approach may not work. Track finding on raw TPC data by transformation techniques followed by a cluster fitter is a possible alternative [40, 41]. Should there arise a need for more computing power for the track recognition, more nodes could be added to the sector Level-3 system, or PCI boards with DSPs or FPGAs could be added to perform special functions at very high speed on the data stream.

5.2.3.2 Network bandwidth and latency

The receiver processors and all other Level-3 processors are interconnected by a hierarchical network. At present, neither the precise network topology nor the networking technology are defined. The network has to have a low latency, a high bandwidth, and should allow remote access to data with low processing overhead.

5.2.3.3 Simulations and Prototyping

Extensive simulations of track recognition methods and data flow have been performed for the proposed Level-3 Trigger System of the STAR [18] experiment at RHIC. A large scale prototype of an Level-3 system is currently being installed. There is a large overlap in the physics objective, detector design, readout electronics and personell between the STAR and the ALICE Level-3 systems.

The RHIC accelerator at Brookhaven National Laboratory, USA, will start to investigate Au–Au collisions with $\sqrt{s} \leq 200$ A·GeV and pp collisions with $\sqrt{s} \leq 500$ GeV in 2000. The STAR experiment is a large scale, cylindrical, symmetric 4π -detector at one of the RHIC interaction points. Data taking will start in 2000 with a full size TPC (Time Projection Chamber, $r_{in} = 0.6$ m, $r_{out} = 2$ m) with 24 TPC sectors, 6912 pads each. The STAR Level-3 trigger is a distributed ALPHA processor farm, performing online tracking of $N_{track} \geq 8000$ particles with a design input rate of $R = 100$ Hz. The components (cluster finder, track finder) have been benchmarked, a large scale prototype system (1/3 of the final design, $R = 20$ Hz) is envisaged for STAR data taking in 2000.

The STAR trigger system is subdivided into 4 hierarchic levels. The Level-0 input rate is 10⁵ Hz, the first three levels reduce the rate by one order of magnitude each. The Level-3 trigger is supposed to reduce an input rate of 10² Hz to the final DAQ rate of $R_{\text{tape}}=1$ Hz at an expected TPC event size of $\simeq 15$ Mbyte. The tasks of the Level-3 trigger are event selections based upon the online reconstructed track parameters of each particle. Two examples are: for Au–Au collisions the online invariant mass reconstruction of $J/\psi \rightarrow e^+e^-$, and for pp collisions the filtering of 700 pile-up events in the TPC per one Level-0 trigger.

The Level-3 trigger design is embedded into the STAR DAQ system [19]. Each physical TPC sector is mapped onto one VME crate, containing a Sector Broker, i.e. Motorola MVME-2306 VME board, carrying a PowerPC 604 (300 MHz, VxWorks), as the TPC sector master controller and a low latency, high bandwidth network interface for the raw-data transfer to the main STAR event builder and the connection to the Level-3 track finder CPU. Moreover, each DAQ crate also contains six VME receiver boards, each carrying three mezzanine cards with one Intel i960 CPUs (66 MHz, VxWorks) for data formatting, initiating the VME raw-data transfer and running the Level-3 cluster finder, and 4 Mbyte of dual-ported VRAM for buffering and pipelining of raw data for 12 events.

The Level-3 trigger scheme consists of two main parts: The sector Level-3 part is mapped onto one physical TPC sector. It contains the Level-3 cluster finder and the Level-3 track finder. The global Level-3 part consists of one master CPU for the whole STAR TPC, collecting all track data and issuing the Level-3 decision. The development of the Level-3 trigger can be subdivided into two main stages. In the first stage, envisaged for 2000, eight TPC sectors are connected. The Level-3 trigger will employ TPC data only, and the input trigger rate is estimated to be 20 Hz. In the second stage, all 24 TPC sectors will be connected. The Level-3 trigger will employ additional information from the SVT (Silicon Vertex Tracker) and the EMC (ElectroMagnetic Calorimeter), and the final design value for the input trigger rate is 100 Hz. Probably more than one CPU per TPC sector will have to be used, implying programming parallelization techniques.

The cluster-finder algorithm runs on the Intel i960 CPUs, implemented on the DAQ receiver boards. The number of i960s is 18 per TPC sector, 432 for the whole TPC. Input to the cluster finder are zero-suppressed TPC raw data, stored in the VRAM. The output cluster data, i.e. cluster center-of-gravity and cluster total charge (ADC sum), are sent via VME to the Sector Broker, which itself ships the data via the network to the Level-3 track finder CPU (expected data transfer rate of $\simeq 3$ Mbyte/s per TPC sector). The time constraint is $\tau_{\text{cluster}} \leq 10$ ms (input rate 100 Hz). Benchmarks on the i960 were performed for 600 clusters (realistic Au–Au scenario) on the TPC’s innermost pad row. The position resolution (difference between reconstructed and Monte-Carlo generated cluster positions) of $\Delta(r\phi) \simeq 37 \mu\text{m}$ and $\Delta z \simeq 13 \mu\text{m}$ could be obtained with an algorithm within $\tau_{\text{cluster}} = 7.5$ ms. If two clusters are merged, an additional deconvolution subroutine must be started, consuming 6.0% more CPU time than in the case of two separated clusters.

In case of an Au–Au collision, the track finder algorithm must be able to fit at least $N \simeq 400$ tracks per event per TPC sector, each consisting of $N_{\text{point}} \leq 45$ points (given by the number of pad rows). The fast track finder algorithm has specifically been developed for the Level-3 trigger project [39]. It employs conformal mapping (transformation of a circle² into a straight line), followed by a fit with a follow-your-nose method. Cluster data are the input to the track finder. The track finder time constraint of $\tau_{\text{track}} \simeq 110$ ms is given by the buffer time of 12 pipelined events (12×10 ms), minus the time being necessary for cluster finding $\tau_{\text{cluster}} \leq 10$ ms. The track finder code was benchmarked on several Linux CPUs. According to the benchmark results, the ALPHA XP1000 500 MHz workstation was the only CPU to be able to fulfill the time requirement, if one restricts the number of CPUs per TPC sector to one. Based on these results, the ALPHA 21264 was chosen for the first Level-3 track finder implementation. Other architectures (e.g. Pentium III 733 MHz) are candidates for future Level-3 extensions.

One global Level-3 CPU receives the track data from all sector Level-3 CPUs. It is connected to

²In the STAR solenoid magnetic field of $B = 0.5$ T charged particle tracks can be parametrised as helices, being visible as circles in xy -projection.

the network. The global Level-3 CPU performs track merging for tracks of different sectors, a Level-3 decision algorithm based on the track data (e.g. invariant mass reconstruction) and issues the Level-3 yes/no decision.

5.2.4 Interfaces

This paragraph outlines the peripheral interfaces of the ALICE Level-3 intelligent readout system. The overall architecture has been outlined in the previous section.

5.2.4.1 Interface between TPC readout electronics and Level-3.

By far the largest amount of data is produced by the TPC. The shipping of the data has to be done optically in order to avoid any ground potential problems. In order to minimize risk, all unnecessary electronics on the detector should be avoided. 180 optical links (five per sector) will ship the raw data off the detector into the counting room. In order to utilize the optical links optimally a small eight-event elasticity buffer will be implemented on the front-end digital chip in order to support a very streaming data transfer across the optical fibre. The estimated aggregate data rate is expected to be about 73 Mbyte/s (at 200 Hz). For a detailed description refer to Section 5.1.

The decision about the Level-3 processor type and architecture will be delayed as long as possible in order to benefit from the rapidly evolving markets. On the other hand an interface is required to allow these computers, which are currently not yet defined, to receive the TPC data for processing. The most obvious approach is to use the most widely accepted peripheral bus standard in industry, PCI [42], as interface or whatever becomes the PCI replacement at the time the design has to be frozen. Basically all computers today use this bus standard as their internal peripheral bus. Given the availability of a PCI receiver card, which connects to the optical fibres being fed by the TPC front-end, it is conceivable to mount this card into a Level-3 CPU and to directly receive the TPC data into the processor's main memory. This scenario avoids the requirement for any front-end bus systems, such as VME, and uses the inexpensive host memory as elasticity buffer.

General description of the data transfer components

The only data being transmitted from the counting room to the TPC are slow controls, calibration and monitoring data. These data, however, are to be provided by the Detector Control System (DCS). It is an essential system requirement that the DCS be independent of any other system such as DAQ or trigger in order to have the necessary redundancy to debug such a complex system. Therefore an additional path to the front-end will have to be implemented in any case in order to enable downloading of test or calibration data, and to read out typical slow-control data such as temperature, voltage and current within the system. This existing data path is an ideal method for redundant but slow readout of any TPC sector, allowing simple offline detector testing without the requirement of a DAQ system. Given these arguments there is no requirement for a full duplex TPC data up-link. For a detailed description of the TPC front-end system please refer to Section 5.1.

The TPC counting room data link consists of three major components: the network feed, which is part of the front-end readout cards on the detector, the actual optical link itself and the optical receiver card in the Level-3 host. The network feed is part of the TPC front-end electronics. However, in order to achieve maximum flexibility while permitting continued progress on the TPC front-end electronics, the fibre transmitters in the front-end will be mounted on appropriate mezzanine cards using a standard bus. Prototype optical transmitters have already been designed, as has an appropriate prototype of a PCI optical receiver.

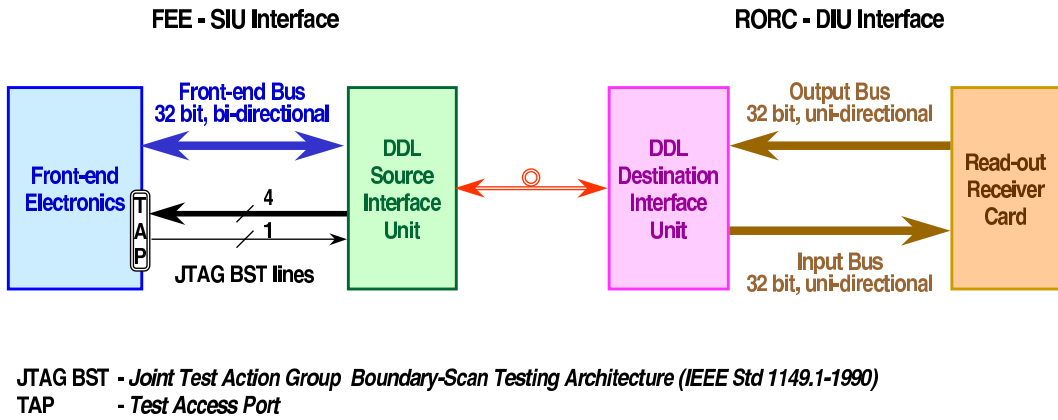


Figure 5.33: DDL logical interface. Note that this interface can be operated in full-duplex mode with handshake as sketched above, which, however, is a feature, which is not being required by the ALICE TPC.

Detector Data Link

The Detector Data Link (DDL) [16] is the proposed standard for optically transmitting data within ALICE. The logical interface of the DDL can be seen in Fig. 5.33. The DDL is composed of three hardware items: the Source Interface Unit (SIU), the fibre, and the Destination Interface Unit (DIU). It can be operated in full-duplex and half-duplex modes. The operation mode for the TPC is half duplex. The SIU is designed to be plugged into the front-end electronics of most of the detectors. The fibre will be the only medium used to ship the data between the ALICE detectors in the experimental area and the computing room located in the access pit. The DIU will be inserted on a mother card (the RORC) inside a computer located in this computing room.

A prototype of the DDL DIU and of a VME-based receiver card have been developed. A prototype of the DDL SIU is currently under design. Its main characteristics correspond to the needs of the TPC. A test of integration of the TPC readout system and of the DDL will be performed in 2000. The specifications of the DDL will be frozen after a successful integration test with the TPC and the other major ALICE detectors. Two modules have been produced to allow an easy stand-alone test of the front-end electronics. These two modules simulate a complete DDL and DAQ system by simple and cheap electronics boards [43, 44].

Read-Out Receiver Card (RORC)

A prototype Front-End Digital Crate (FEDC) housing several RORCs has been developed and tested in the NA49 Forward TPC detector system. The current prototype of the FEDC consists of a VME crate. In this prototype, the data transfer system is performed through the VME backplane by the Local Data Concentrator (LDC). The LDC is currently implemented as a single-board computer running the UNIX operating system. The physics data transferred by the DDL are buffered in a prototype RORC, built as a VME module and carrying two DDL DIUs [45].

PCI is the proposed standard interface between the detector electronics and the Level-3 system. Almost every modern computer uses PCI as a peripheral interface bus. The processor choice for the Level-3 system is not restricted by this requirement. Should another bus standard become as widely used

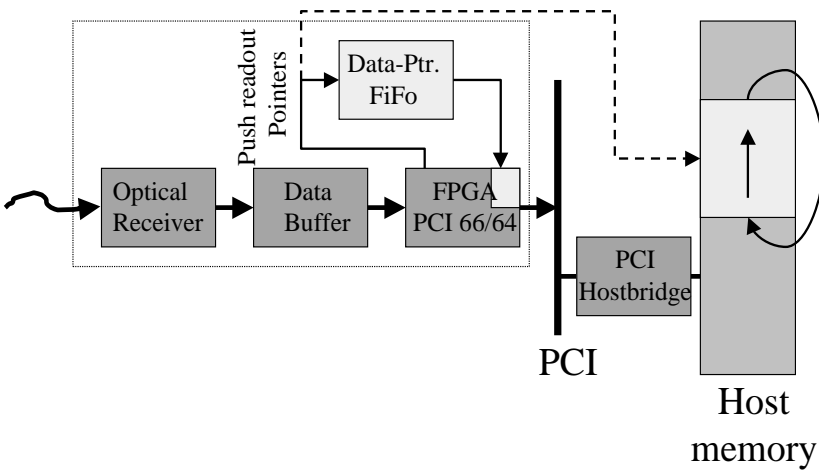


Figure 5.34: The functional blocks of the TPC receiver card (PCI-RORC).

by the time the ALICE electronics has to be frozen it would be chosen instead.

The PCI receiver card basically consists of a data converter which writes the optically arriving data to the main memory of the host computer (receiver processor) after some additional buffering. The interface is PCI 66/64 (theoretical bandwidth of 528 Mbyte/s). At present, PCI is the baseline bus interface.

Figure 5.34 shows the functional blocks of this card as it is integrated in the computer. The data which are received optically are converted into electronic signals. A small elasticity buffer follows behind, which is only necessary in order to cover PCI latencies. The arriving data is then copied directly into the main memory of the receiver processor via the PCI bus using a DMA engine on this card. The host's main memory, which now also acts as data buffer, can easily be considerably enlarged without producing significant additional costs. The target memory area is marked light grey and works like a cyclic memory buffer. The start and end long-term addresses are configurable. The receiver card copies the arriving data sequentially into the cyclic memory buffer of the host. These memory models are supported by all common operating systems, including Windows NT and Linux. The buffer principle of an Ethernet interface, for example, is very similar. For every newly started event, the start address of this event is written into a second buffer memory, which is here also implemented as a FIFO for the sake of simplicity. The host processor(s) only need(s) to read the start address of an event from the FIFO. An empty FIFO defines the absence of further data. If an event has been either transmitted to the DAQ or has been rejected, the corresponding read pointer in the CSR area of the receiver card is updated, thus freeing the corresponding memory area.

This architecture does not require any flow control between the detector front-end and the receiver modules. At every point, there are large enough elasticity buffers to absorb maximum reaction times. The data buffer in the receiver processor can easily be enlarged to ensure that there will be no dead-time under normal operating conditions. In case of extremely long trigger bursts or false trigger thresholds, a simple model, such as high/low-water marking, would allow to generate Level-3 dead-time through software. Alternatively, a busy signal can be generated on the PCI-RORCs and daisy-chained into one TPC counter box, which sends a busy signal to the trigger. This ensures that no data can be overwritten, while the requirement for flow control hardware is nevertheless minimal. The resulting system can be debugged very easily.

The PCI interface itself can be integrated into the RORC FPGA. There are commercially available

FPGAs which, today, all support 64 bits and 66 MHz operating speed. For example Xilinx, Lucent and Altera specifically offer such chips today, which demonstrates the industry's large interest in supporting such architectures. All FPGAs named above have a gate count of or exceeding 30 000.

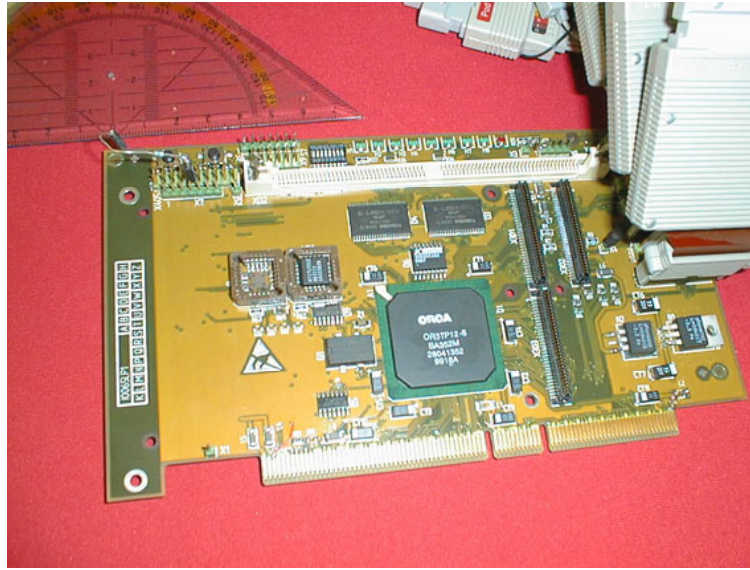


Figure 5.35: The PCI–RORC prototype

In order to test the functionality discussed above and to design the necessary software, a PCI–RORC prototype was built. Figure 5.35 shows a picture of the device. It contains the discussed functional blocks. The interface to the optical receivers (DIU) is implemented as a common mezzanine card CMC. Appropriate DDL modules are currently being built. Should other optical transports become attractive they could easily be implemented as all data signals to the mezzanine card are freely programmable.

The design of the device is complete, including necessary driver software. First performance tests show 90–100 Mbyte/sec of data being moved by the DMA engine on the card directly into the host memory of the processor using a 32-bit, 33 MHz PCI system. Further tests with a 64-bit and 66 MHz system are planned for the spring of 2000.

5.2.4.2 Interface to DAQ and trigger

The remaining interfaces are those to DAQ and trigger. Neither of the two have particularly challenging requirements. The TPC group is currently working closely with the DAQ and trigger group in order to detail these interfaces.

Interface to DAQ

The detailed interface between the Level-3 system and DAQ is not yet finalized. In the following a few scenarios are presented to illustrate the feasibility and functionality of this interface. Although the data acquisition system and the Level-3 trigger are functionally different systems, the processors and networking hardware are expected to be identical. The software executed on a particular node at a particular time may have Level-3 trigger or DAQ functionality. For example the processors hosting the TPC receiver cards will first perform Level-3 cluster finding on the received zero-suppressed raw data and forward the space points to another node within the Level-3 farm, which then performs tracking. Having accepted the event the same processor may then go on to perform the necessary event building

steps running DAQ routines. Ultimately the whole Level-3 farm can be used as a generic processing farm during times when ALICE is not running. This scheme requires the data structures and data flow architecture to be well defined between the Level-3 trigger and DAQ.

Given the architecture of the Level-3 system outlined above the resulting requirements present no particular technological challenges. This is mainly due to the fact that Level-3 activity commences only after an Level-2 accept. In the ALICE detector system all data is copied into elasticity buffers upon an Level-2 accept. Therefore, there is no explicit maximum latency for Level-3. The raw data of the TPC is received directly into Level-3, where the buffers can be made easily large enough to accommodate the appropriate latencies. Then the data, which has to be moved from the Level-3 receiver processors, are only the space points and track segments in case of Level-3 processing or some derivative of the raw data in case of an accept. The Level-3 space points, however, are small and the data shipped to DAQ after an Level-3 accept are either compressed further or appropriately reduced with appropriate trigger selectivity. However, at any point in time the system can be scaled up such that it operates exactly as described in the TP.

The flow control and synchronization between Level-3 and DAQ require the definition of a multiprocessor network software interface, supporting the following functionality. After the raw data have been received by a receiver processor it will start processing them according to event type, which is part of the data stream. After completion, the resulting space points may have to be shipped to the next processing layer, handling a complete sector for track segment processing. This requires the ability to move bulk data. The processor node needs to know the next available target node downstream, which is another network message to be received and processed. At some point later the Level-3 decision has to be multicast to all receiver processors holding the appropriate raw data. After reception of the Level-3 decision for a given event it is discarded upon a reject, or the Level-3 compression and the DAQ process is activated upon an accept. Once the subevent is built it is shipped to the appropriate processor upstream, which again has to report its availability via the network. Other requirements for Level-3 are the interfaces to other detector subsystems in order to allow processing of a complete event. Therefore a data input path into Level-3 needs to be provided.

Interface to trigger

Since the Level-3 system is activated only upon an Level-2 accept there is no direct feedback required to the lower trigger layers. The processing farm could operate completely data driven. But in order to have some redundancy and the possibility of error checking, the Level-3 system will implement a TTC receiver like any other ALICE subdetector. This receiver will allow matching of the events arriving at the various receiver processors to the triggers as issued by the Level-1 trigger system.

5.2.5 Data acquisition and Level-3 software

Several aspects of the proposed architecture influence the software of the Level-3 system. The proposed Level-3 system will be built from standard low-cost components. The connection between the nodes will be via a standard network. The connection to the detector front-end electronics will be designed around whatever bus is widely accepted at the time. Since it is highly desirable to use the Level-3 farm for real-time and offline processing it is mandatory to make switching between these modes as simple as possible. The expected low price for each node and the high number of nodes will limit the choice of operating systems. The Level-3 trigger algorithms are likely to change frequently and are unlikely to be implemented by real-time experts. The input rate into the system is in the order of a few hundred Hz and there are several levels of elasticity buffers throughout the system allowing simple flow control mechanisms to be used. Assuming a network that does not create a large number of interrupts the real-time requirements for such a system are moderate. A possible software architecture that addresses these boundary conditions is described in the following.

5.2.5.1 Operating systems

The ALICE collaboration has not yet selected a common operating system. However, for the time being we will illustrate that the requirements for such a system can be met by at least one currently available system. We choose RT-Linux for this purpose. Whatever commercially available cost-effective systems will be used, it is very likely that Linux will be running on them. Several real-time extensions to Linux can be used. Interrupt latencies better than $20\ \mu\text{s}$ have been reported for Intel-based machines (see, for example, Ref. [46]). However, because of the design of the Level-3 system, no interrupts will be generated for the process of moving the data via the RORCs into the memory of the machines. The large possible buffer size in the main memory of the nodes will reduce the need of real-time behaviour even further.

All required tools for software development are available on Linux and owing to their similarity to common UNIX systems minimal training for systems programming will be required. The stability and robustness of the kernel have been demonstrated in many farm and cluster applications. A UNIX-like operating system has the additional benefit that offline reconstruction codes will run with only minimal changes on the Level-3 farms. This will allow for a dual use of the system for triggering and reconstruction work. Because of the wide distribution of Linux systems, machines for development will be widely available.

5.2.5.2 Online processing

Two principal groups of tasks will run on the Level-3 systems. One that controls transport of data and communication and manages the processing of the events, and one that performs data analysis tasks. While the first will be quite stable from the beginning, the second has to be modified frequently to cope with changes in running conditions and the physics programme. The first group will have to deal with some real-time aspects and has to run only on the Level-3 systems. This part of the software structure can be called control tasks.

The second will more closely resemble offline code and it is highly desirable to use almost identical code in Level-3 and in the simulation of Level-3. This group of tasks can be referred to as processing tasks, which should not be aware of time. They should be called inside a framework provided by the control tasks and in case of exceeding the allowed time limits the control task will abort the processing and start the clean-up code of the processing task. This clean up code will be the main difference between the online and the offline versions of the Level-3 processing code. The controller tasks will make heavy use of portable standard network APIs to allow flexible and early implementation of the system.

A key component of the proposed system is the ability to process the raw data, performing track recognition in real-time. It is designed to utilize the information from the TPC and fast detectors. The system should be flexible enough to be expanded in a natural manner to include the other tracking devices. Track recognition of tracking detectors like the TPC is usually done sequentially. After finding clusters, the position and charge of the clusters are corrected for gain differences, distortions, time offsets, etc. These space points are then passed on to a track finder which builds track pieces out of clusters. Track pieces are finally merged to global vertex and nonvertex tracks. If track densities especially in the inner pad rows get too high, clusters start to overlap so that a simple cluster finder cannot recognize or resolve merged clusters. Track recognition methods for track finding on raw data like template matching or adaptive generalized Hough transforms [40, 41] have to be employed. These methods have been used in NA35 and tested in NA49.

5.2.5.3 Implementation

The control tasks with their complicated structure will benefit from modelling the system using a software engineering methodology like OMT. To allow a large number of participants in the Level-3 effort to understand and maintain software, a widely accepted and available programming language has to be

used. At the moment the candidate is ANSI C++, which is used for the online tracking in STAR and on which the ALICE simulation framework (AliRoot) is based.

Some of the computational tasks can be realized in hardware. Huffman compression chips are commercially available. The vector quantizer can be heavily pipelined with several parallel stages and a tree-enconding scheme which reduces comparisions between data words by a factor of four. Rough estimates show that a vector quantizer with arbitrary, table based metric and table based residual encoder can be implemented in one rather large XILINX XC4000 FPGA and a small external RAM at a rate of about 60 million samples per second [47]. Even track recognition procedures, e.g. Hough transformation, can be implemented in a FPGA if necessary.

6 Material budget

The performance requirements of the ALICE TPC are more stringent than for any other TPC ever built. The major goal is to handle the harsh LHC environment, in particular, the high particle density and the high interaction rate. Since the amount and position of material traversed by particles in the inner detectors has an impact on the performance of the outer detectors and consequently on the physics, it represents a major optimization issue in the definition of the TPC layout, as well as in several technical choices. The simulation of the TPC material must be very accurate in order to provide a careful determination of the material in terms of radiation and interaction length. In order to estimate the importance of different contributions and hence the targets for optimization, the analysis of the material budget is split into two parts:

1. The cylinder material that is uniformly distributed around the beam pipe, i.e. the inner containment and field-cage vessels, and the outer containment and field-cage vessels. This is indicated in Fig. 6.1a.
2. The field cage material that is not homogeneously distributed over the cylinder, i.e. in the ϕ direction, for example the Mylar strip support rods. This is shown in Fig. 6.1b.

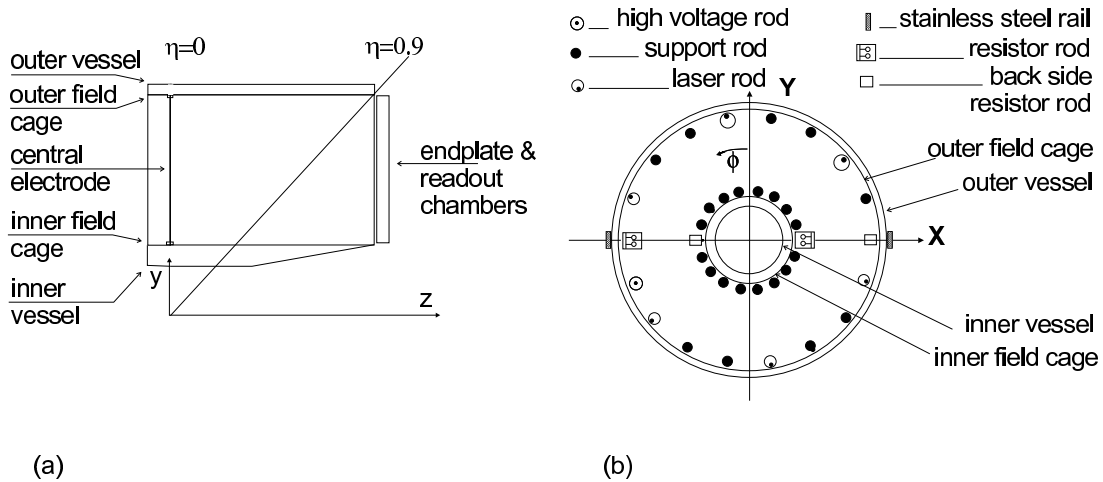


Figure 6.1: Schematic of the TPC material in η (a), and ϕ (b), space.

Viewed from the interaction point, the material in the path of particles is ‘scanned’ in η and ϕ slices, taking into account the density and composition of the material traversed (shown in Tables 6.1, and 6.2) and its position in space. This was performed with the CAD tool Euclid, and the results in terms of X/X_0 are given in the next sections.

6.1 Estimate of radiation length in η space

As can be deduced from Fig. 6.1a the material distribution in η space is generally smooth and homogeneous. The only step-like mass concentration in η space comes from the central electrode located at $\eta = 0$. Since its volumetric occupancy is small compared to the maximum η acceptance of the TPC, we scan the material with and without the presence of the central electrode. Furthermore, to avoid singularities in the material distributions from individual components, the origin of particle trajectories has been smeared over the LHC beam interaction diamond, i.e. $-5.3 \text{ cm} \leq z \leq 5.3 \text{ cm}$. The results are shown in Figs. 6.2a and 6.2b.

Table 6.1: Properties of the material of the TPC vessels, gas and outer thermal screen.

Material	Thickness [cm]	ρ [g/cm ³] ([g/l])	X_0 [g/cm ²] ([cm])	λ_0 [g/cm ²] ([cm])	X/X_0 [%]	λ/λ_0 [%]
Field-cage structure						
Tedlar	0.04	1.71	44.77 (26.18)	84 (49.12)	0.15	0.08
Fibre (Kevlar)	0.24	1.45	44.86 (30.94)	83.9 (57.86)	0.60	0.41
Nomex (29 kg/m ³)	7.5	1.45 × 0.02	41.28 (1424)	85 (2931)	0.52	0.25
Air (within Nomex)	7.5	(1.293)	(30420)	90 (107305)	0.02	0.01
Mylar	0.05	1.39	39.95 (28.7)	85.7 (61.65)	0.17	0.08
Al	0.05	2.70	24.01 (8.9)	106.4 (39.4)	0.56	0.12
H ₂ O	0.1	1.00	36.1 (36.1)	84.9 (84.9)	0.27	0.01
Ne–CO ₂ [90–10]	178	(1.116)	(30755)	(101152)	0.58	0.17
CO ₂	32	(1.977)	(18310)	90.5 (45776)	0.18	0.07
Total					3.05	1.20

Table 6.2: Properties of the material of the TPC field defining network.

Item/Material	Thickness [cm]	ρ [g/cm ³]	X_0 [g/cm ²] ([cm])	λ_0 [g/cm ²] ([cm])	X/X_0 [%]	λ/λ_0 [%]
Support rod sector						
Support rod (i) ^a	2.5	1.20	41.84 (34.6)	83.9 (69.9)	7.225	3.57
Support rod (o) ^a	2.5	1.20	41.84 (34.6)	83.9 (69.9)	7.225	3.57
HV sector						
HV cable/polyethylene	2.7	0.93	44.7 (48.15)	78.8 (84.7)	5.61	3.4
HV cable/copper	0.31	8.96	12.9 (1.43)	134.9 (15.5)	21.67	2
HV rod (hollow) ^a	1	1.20	41.84 (34.6)	83.9 (69.9)	2.89	1.43
Support rod (i) ^a	2.5	1.20	41.84 (34.6)	83.9 (69.9)	7.225	3.57
Resistor rod sector						
Resistor rod ^a	2.5	1.20	41.84 (34.6)	83.9 (69.9)	8.71	3.57
Strip hook/copper	0.01	8.96	12.9 (1.43)	134.8 (15.5)	0.69	0.06
Resistor/iron	0.05	7.87	13.84 (1.76)	131.9 (16.7)	2.84	0.29
Resistor/graphite	0.3	2.27	42.7 (18.8)	83 (36.5)	1.59	1.64
Support rod (i) (hollow) ^a	1	1.20	41.84 (34.6)	83.9 (69.9)	2.89	1.43
Laser rod sector						
Laser rod (hollow) ^a	1	1.20	41.84 (34.6)	83.9 (69.9)	2.89	1.43
Support rod (i) ^a	2.5	1.20	41.84 (34.6)	83.9 (69.9)	7.225	3.57
Field-cage structure					3.05	1.20

^aMacrolon

(i) — inner

(o) — outer

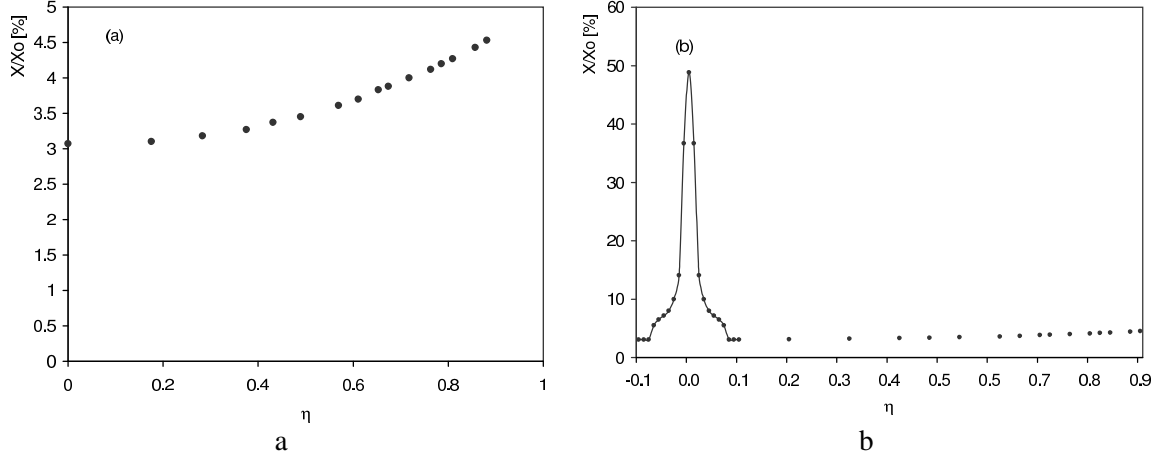


Figure 6.2: Fractional radiation length of the TPC in η space without (a) and with (b) the central electrode.

6.2 Estimate of radiation length in ϕ space

Unlike the smooth material distribution in η space, there are distinct high-mass concentrations within the ϕ acceptance of the TPC (see Fig. 6.1b). These are due to the presence of the electric field defining network, in particular, the support rods of the Mylar strips. Some of these rods are hollow and have therefore a different mass because of additional functions, such as housing the voltage divider resistor chain, the high-voltage feed, and the optics for the laser calibration system. We are investigating whether the other support rods, which are made of solid Macrolon, can also be replaced by Macrolon tubes, to reduce passive material in these regions even further. The individual mass and position within the TPC volume are taken into account for the calculations over the entire ϕ range (0° to 360°). In Fig. 6.3a we give an account of the material concentration as seen by particles of infinite momentum traversing the TPC in all ϕ directions. The ϕ -scan includes the steel rails of the TPC located at $\phi = 90^\circ$ and 270° .

Figure 6.3b gives a detailed view (zoom) of the equivalent radiation length of a laser rod placed at $\phi = 130^\circ$ in Fig. 6.3a.

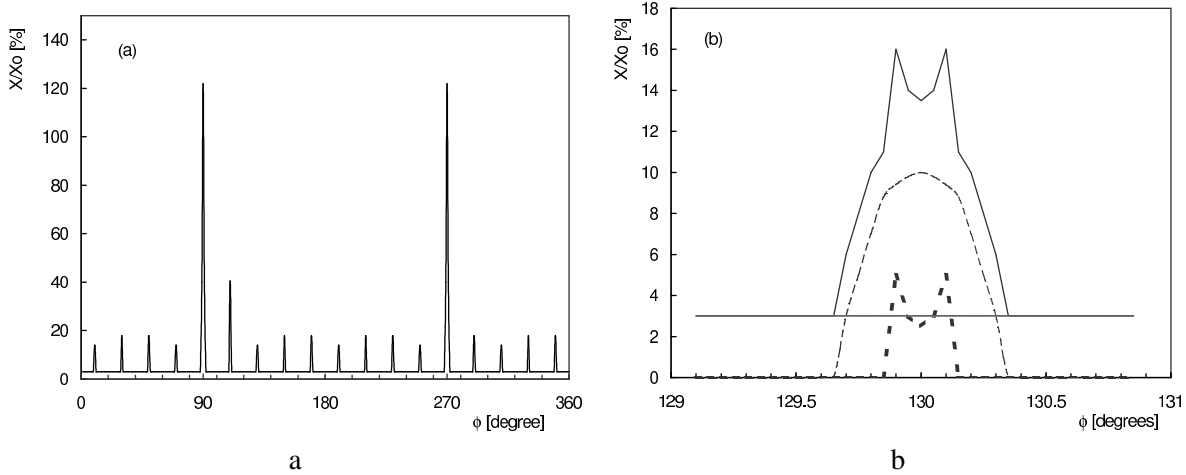


Figure 6.3: Map of the fractional radiation length of the material in ϕ space (a), and an expanded view of the peak located at $\phi = 130^\circ$, showing the detailed mass distribution of the individual components of one of the laser rods (b). The top distribution is the sum of the three distributions below.

7 Detector performance

7.1 Requirements and detector parameters

The Time Projection Chamber (TPC) is the main tracking device of the ALICE experiment. Its tasks are track finding, momentum measurements and particle identification by dE/dx . A good two-track resolution, required for correlation studies, is also one of the main design goals. Besides, significant attention should be paid to the possibility of track matching with other detectors. These requirements are conflicting. Higher readout granularity required for good track-finding efficiency is limited by the data volume and by the signal-to-noise ratio. Good momentum resolution calls for a ‘cold’ drift gas of low diffusion (diffusion constants should not significantly exceed $200 \mu\text{m}/\sqrt{\text{cm}}$). This however requires a high drift field (400 V/cm) to secure an acceptable drift time of $\sim 100 \mu\text{s}$. Large signal-to-noise ratio requires a drift gas with large ionization (large Z). On the other hand, a gas with a large Z leads to a large space-charge in the drift volume and thus to larger distortions. Also multiple scattering is larger for such gases. More detailed discussion on the choice of the drift gas can be found in Ref. [1].

The TPC design should secure the following detector performance in an environment corresponding to $dN_{\text{ch}}/dy = 8000$:

- drift time $\leq 100 \mu\text{s}$, which imposes a 10% upper limit for the CO_2 content;
- $dp/p \sim 1.2\%-1.5\%$ for MIP and about 5% for a $5 \text{ GeV}/c$ electrons (stand-alone);
- $dE/dx < 10\%$ in the high track-density region;
- signal-to-noise ratio for MIP better than $\sim 20:1$ in the case of small pads in inner sectors and $30:1$ for larger pads in outer sectors;
- track-finding efficiency larger than 90%;
- track matching to other detectors $\sim 90\%$;
- two-cluster resolution $\sim 1 \text{ cm}$ in both $r\phi$ and z directions;
- the distortions, in general, should not be significantly larger than the space-point resolution (a few hundred microns) which calls for the uniformity of both electric and magnetic fields and also for a gas with a low Z and large ion mobility.

7.2 Simulation of TPC response

7.2.1 Microscopic simulator

The ALICE TPC is supposed to operate in rather extreme conditions, because of very high particle multiplicity, the event geometry (inclination angles of tracks), and a large drift length. The detector performance (i.e. resolutions, tracking efficiency, data volume, etc.) depends on many parameters, such as

- energy loss per unit length;
- diffusion of electrons during the drift;
- electron attachment;

- gas gain, including fluctuations;
- pad and time response, determined by the readout-chamber geometry and electronics parameters.

In order to study the influence of these parameters and to choose the optimal ones, a reliable Monte Carlo simulation is required. This led to the development of a microscopic simulator described in Ref. [2]. In AliRoot [3], the simulation code used by the ALICE Collaboration, this simulator is incorporated into the GEANT3.21-based tracking package. Below, the details of the microscopic simulator are described.

7.2.1.1 Physics of the AliRoot Monte Carlo

Ionization in gas

The ionization in the gas proceeds in two stages. Firstly, electromagnetic interactions of the primary particle with the TPC gas lead to the release of primary electrons. The statistics of the primary interactions implies a Poisson distribution of a number of primary electrons, as shown in Fig. 7.1. The distance

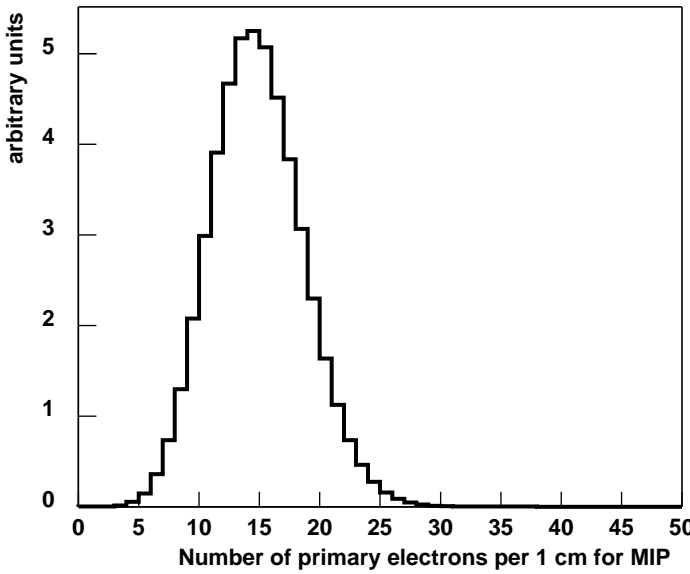


Figure 7.1: Distribution of number of primary electrons per 1 cm for MIP in 90 % Ne, 10 % CO₂.

between collisions leading to the primary ionization is described by an exponential distribution (see, for example, Refs. [4, 6])

$$P(s) = \frac{1}{D} \exp \frac{-s}{D},$$

where s is the distance between two successive collisions and D is the mean distance between primary ionizations:

$$D = \frac{1}{N_{\text{prim}} \cdot f(\beta\gamma)},$$

where N_{prim} is the number of primary electrons per 1 cm produced by a MIP, and $f(\beta\gamma)$ is the Bethe–Bloch curve. In Fig. 7.2 the energy-loss data for 90 % Ar, 10 % CH₄ [5, 6] are plotted together with the parametrization proposed by the ALEPH Collaboration [6],

$$f(\beta\gamma) = \frac{P_1}{\beta^{P_4}} \cdot \left\{ P_2 - \beta^{P_4} - \ln \left[P_3 + \frac{1}{(\beta\gamma)^{P_5}} \right] \right\},$$

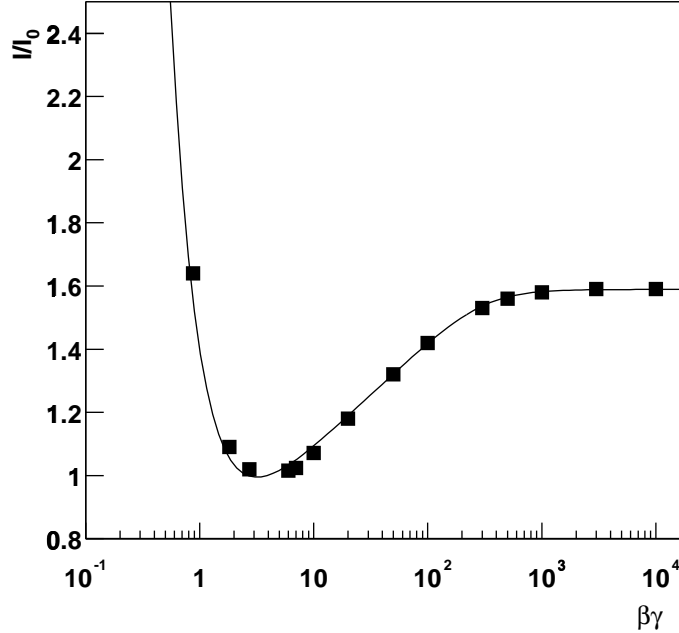


Figure 7.2: Bethe–Bloch curve for 90 % Ar, 10 % CH₄, data from Ref. [6]

where $P_{1\dots 5}$ are free parameters. The fit to these data gives

$$P_1 = 0.762 \times 10^{-1},$$

$$P_2 = 10.632,$$

$$P_3 = 0.134 \times 10^{-4},$$

$$P_4 = 1.863,$$

$$P_5 = 1.948.$$

This parametrization is also used in our simulation, as the energy-loss data for Ne in the $1/\beta^2$ region are rather poor and the behaviour of the Ne-based mixtures is very similar to that of Ar-based ones [5].

The energy transfer to atomic electrons can be described by the PhotoAbsorption Ionization model (PAI) — see for example Refs. [7, 8]. In most cases, if one neglects the atomic shell structure, it obeys the $1/E^2$ rule. However, for light gases the data indicate a slightly steeper dependence [6, 9]. In our simulations we use $1/E^{2.2}$ for 90 % Ne, 10 % CO₂. The lower energy cut-off is equal to the first ionization potential, the upper one is equal to 10 keV. Above this energy, the GEANT simulation package generates δ -rays. The comparison of our simulations with those using the PAI model shows satisfactory agreement.

Generation of secondary electrons

With sufficient kinetic energy, the primary electron can ionize atoms and produce secondary electrons, creating an electron cluster. The total number of electrons in such cluster is given by

$$N_{\text{tot}} = \frac{E_{\text{tot}} - I_{\text{pot}}}{W_i} + 1,$$

where E_{tot} is the energy loss in a given collision, W_i is the effective energy required to produce an electron–ion pair and I_{pot} is the first ionization potential. The clusters are assumed to be point-like, and

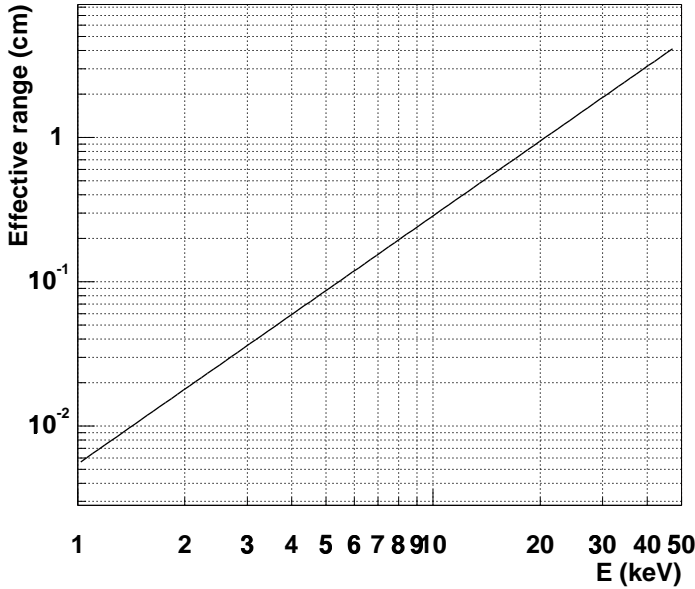


Figure 7.3: Effective range of an electron in Ne.

no distinction between primary and secondary electrons is made. This seems to be justified, as most of the fractional energy losses in a given step are small (on average about 3–4 electrons are produced in a single collision) and the effective range of low-energy electrons is small (see Fig. 7.3) compared with the length scale of diffusion during the drift towards the readout chambers. Even the most energetic electrons, i.e. those with energy equal to the upper cut-off (10 keV), create in the magnetic field of 0.2 T a blob of radius $\sim 160 \mu\text{m}$ only. The energy loss and total number of electrons per 1 cm for MIP (π with a total momentum equal to 400 MeV/c) in 90 % Ne, 10 % CO₂ are plotted in Fig. 7.4 and in Fig. 7.5, respectively.

Diffusion of electrons

During the drift, the electrons are subject to diffusion. The electron cloud, after drifting over a distance L_{drift} , can be described by the 3-D Gaussian distribution:

$$P(x, y, z) = \frac{1}{\sqrt{2\pi}\delta_T} \exp\left[-\frac{(x-x_0)^2}{2\delta_T^2}\right] \cdot \frac{1}{\sqrt{2\pi}\delta_T} \exp\left[-\frac{(y-y_0)^2}{2\delta_T^2}\right] \cdot \frac{1}{\sqrt{2\pi}\delta_L} \exp\left[-\frac{(z-z_0)^2}{2\delta_L^2}\right],$$

where (x_0, y_0, z_0) is the electron creation point and

$$\delta_T = D_T \sqrt{L_{\text{drift}}}$$

$$\delta_L = D_L \sqrt{L_{\text{drift}}},$$

D_T and D_L are the diffusion constants in the transverse and longitudinal direction, respectively.

Electron attachment

During the drift, electrons can be absorbed in the gas by the formation of negative ions. This is due to the presence in the drift gas of substances with large electron affinities such as oxygen. According to

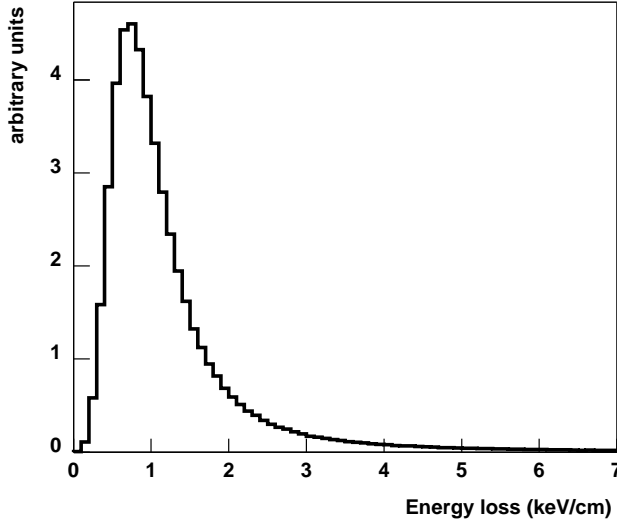


Figure 7.4: Energy loss of electrons per 1 cm for MIP in 90 % Ne, 10 % CO₂.

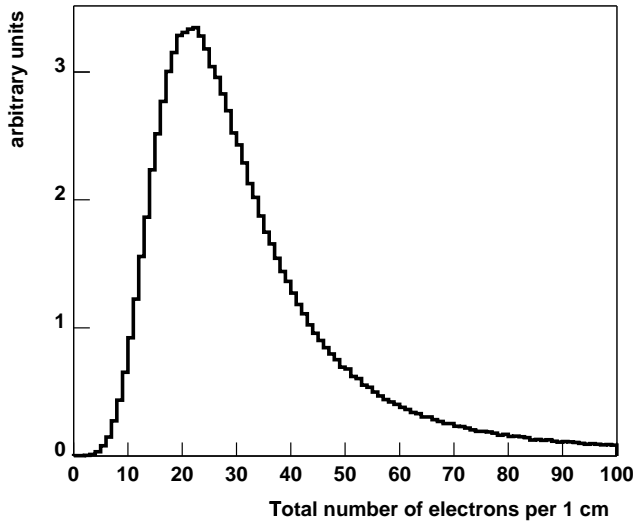


Figure 7.5: Total number of electrons per 1 cm for MIP in 90 % Ne, 10 % CO₂.

experience from NA49 [9], the probability for an electron drifting in our gas to be captured by an O₂ molecule is 1% per 1 m drift per 1 ppm of O₂ (at the level of a few ppm of O₂). This value has been used in the simulations.

E × B effect near the anode wires

It has been assumed that the electric and magnetic fields in the drift volume are uniform and parallel. This, however, is not true close to the anode wires, where the electric field becomes radial with respect to each wire. Thus the electrons experience, because of the Lorentz force, a displacement along the wire direction. If an electron enters the readout chamber at the point (x_0, y_0) , it is displaced in the x -direction (assuming that the wires are placed along the x -axis). The new x -position of the electron is then given by

$$x = x_0 + \omega \tau \cdot (y - y_0),$$

where y is the coordinate of the wire on which an electron is collected, and $\omega\tau$ is the tangent of the Lorentz angle.

7.2.1.2 Signal generation

Avalanche at the anode wire

An electron arriving at the anode wire creates an avalanche, the amplitude of which is determined by the high voltage applied to the wire. This amplitude is subject to fluctuations, which can be described, according to Refs. [4, 6], by an exponential distribution

$$P(q) = \frac{1}{\bar{q}} \cdot \exp -\frac{q}{\bar{q}},$$

where \bar{q} is the average avalanche amplitude. The resulting avalanche is the convolution of single-electron avalanches.

Shaping and sampling time signal

The time signal is obtained by folding the avalanche with the shaping function of the preamplifier/shaper. This signal is then sampled with a given frequency. In the present simulations a 3σ truncated Gaussian has been used to describe the preamplifier/shaper response. The preamplifier/shaper efficiency, i.e. the ratio of integrated charge to that on the preamplifier/shaper input, was assumed to be equal to 0.4. The measurements by the STAR Collaboration [10] indicate that it should be possible to obtain larger values. This would be very welcome as it could lead to a better signal-to-noise ratio.

Charge induced on pads and pad response function

An electron collected on the anode wire induces a charge on the pad plane. This charge is integrated over the pad area. It is the pad response function (PRF) which characterizes the readout chamber and determines the intrinsic resolution. If the charge induced on the pad plane has a distribution given by $Q(x, y)$, the PRF is defined as

$$\text{PRF}(x, y) = \int_S Q(x', y') dS,$$

where S is the pad area.

The 2-D induced-charge distribution has been calculated according to Ref. [11], and is shown in Fig. 7.6 and Colour Fig. V. The 2-D pad response function for rectangular pads is shown in Fig. 7.7 and Colour Fig. VI. The steps in one direction indicate the position of the anode wires.

The method we adopted for the PRF calculation is a general one and can be used for classical wire chambers with different pad geometries (rectangular, chevron, radially oriented) as well as for the GEM-type readout. (The details of the GEM readout can be found in Section 8.2.) This algorithm also allows the signal coming from the wires on the neighbouring pad rows ('crosstalk') to be taken into account.

Electronics noise and the conversion gain

It has been assumed that the electronics noise can be described by a Gaussian with r.m.s. equal to $1000 e$. The conversion gain was chosen such that σ_{noise} corresponds to 1 ADC count.

Digitization

The analog signal, obtained by integration of signals created by individual electrons, is digitized using a given dynamic range of the electronics and applying zero suppression.

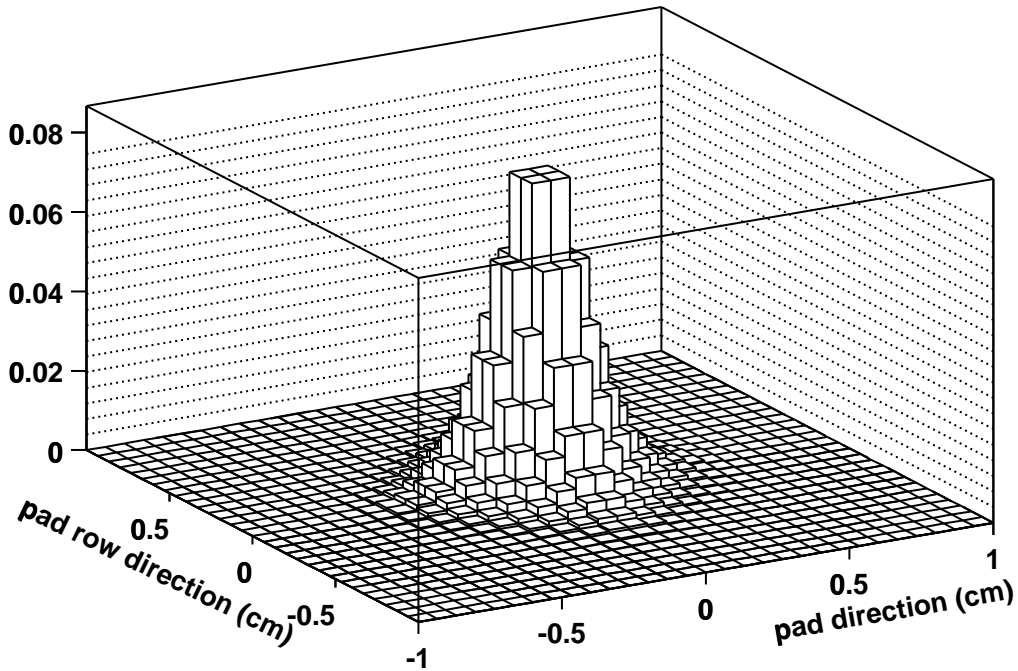


Figure 7.6: Induced-charge distribution according to Ref. [11]. Normalization is arbitrary.

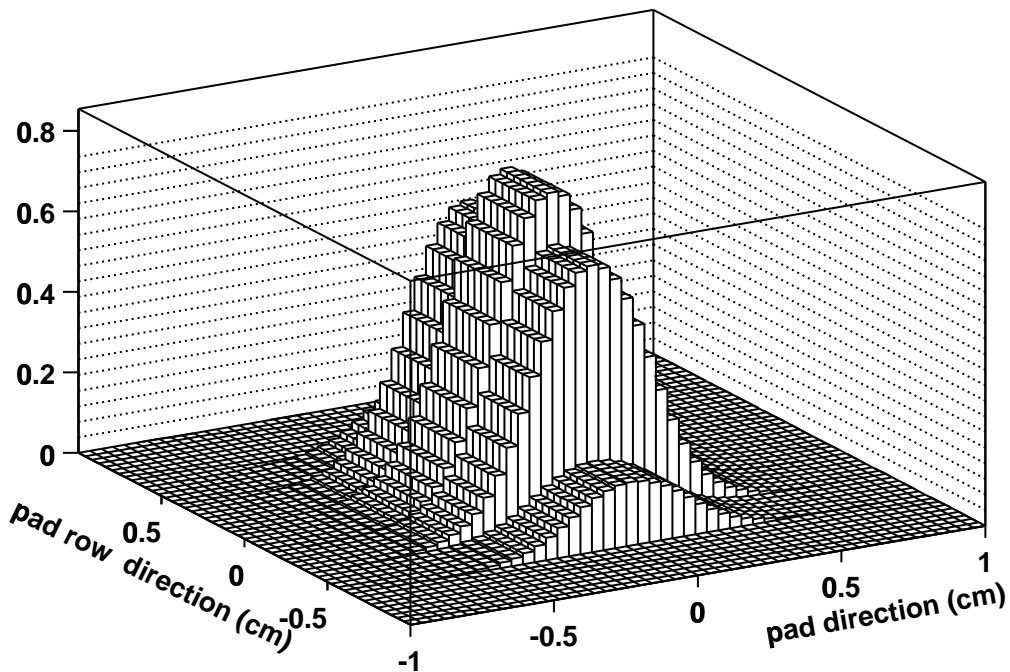


Figure 7.7: Pad response function for rectangular $4 \times 7.5 \text{ mm}^2$ pads. Normalization is to unity.

7.2.1.3 Parameters used in the simulations

In this section the main parameters of the drift gas (Table 7.1), readout chambers (Table 7.2), and electronics (Table 7.3) are listed.

Table 7.1: Parameters of the drift gas.

Item	Value
Number of primary electrons for MIP	14.35
First ionization potential	20.77 eV
Effective energy for e–ion pair creation	35.97 eV
Drift velocity at 400 V/cm	2.83 cm/ μ s
Diffusion constants ($D_T = D_L$)	220 μ m/ $\sqrt{\text{cm}}$
Tangent of Lorentz angle ($\omega\tau$)	0.15
Oxygen content	5 ppm

Table 7.2: Parameters of the readout chambers.

Item	Value
Pad dimensions:	
$84.1 \text{ cm} < r < 132.1 \text{ cm}$	$4 \times 7.5 \text{ mm}^2$
$134.6 \text{ cm} < r < 198.6 \text{ cm}$	$6 \times 10 \text{ mm}^2$
$198.6 \text{ cm} < r < 246.6 \text{ cm}$	$6 \times 15 \text{ mm}^2$
Anode wire spacing	2.5 mm
Anode wire to pad distance:	
$84.1 \text{ cm} < r < 132.1 \text{ cm}$	2 mm
$134.6 \text{ cm} < r < 246.6 \text{ cm}$	3 mm
Gas gain	2×10^4

Table 7.3: Parameters of the electronics.

Item	Value
Noise (r.m.s.)	1000 e^- (in the system)
Dynamic range	2 V, 10 bits
Conversion gain	12 mV/fC
Shaping time	190 ns FWHM
Sampling time	200 ns
Zero suppression	3 ADC counts

7.2.2 Background and detector load

The total load on the readout chambers is estimated from the obtained ionization density in the drift volume in central collision events. The charge dose per centimetre of wire and per year of operation can then be calculated by integrating in time along with the electron amplification and the trigger rate for each kind of events. The results are summarized in Table 7.4 for both lead and proton beams. All heavy-ion beams are considered to be lead beams. A charged-particle multiplicity for central collision events of 8000 per unit of rapidity has been assumed. Minimum-bias events, about 90% of the total

Table 7.4: Estimation of the maximum dose per cm of anode wire for different cases.

	Charge/cm ^a [mC/cm]	Trigger rate ^b [Hz]	Run time [s]	Dose [mC/cm.yr]	Current ^c [nA]	Current ^d [μA] (ROC)
Pb–Pb	2.3×10^{-13}	200(1+1/5)	10^6	1.1	3.36	7.2
Pb–Pb ROC	5.8×10^{-16}	8000(0.1+0.9/5)	10^6	0.018		0.19
pp	2.3×10^{-16}	400	10^7	0.018	0.15	0.0012
pp ROC	6.4×10^{-19}	10^5	10^7	0.013		0.008

^aPer central collision event, averaged along the innermost region $82 < R < 102$ cm, before amplification.

^bIncludes the multiplicity correction (on average one fifth of central) for minimum bias events (90% of all interactions).

^cTotal current in the drift volume corresponding to one inner chamber.

^dCurrent in one inner readout chamber after amplification.

interactions, are considered to have on average one fifth of this multiplicity. The average multiplicity for pp interactions is taken to be 1000 times lower than for Pb–Pb minimum-bias events. The charge released in the 0.7 cm gap between the pad plane and the gating-grid electrode of the inner chambers, which is always active irrespectively of the trigger, is taken into account separately (columns labeled Pb–Pb ROC and pp ROC in Table 7.4). The overall expected dose, about 12 millicoulombs per centimetre of wire in 10 years, is rather moderate. Given the gas mixture and the materials foreseen in the detector assembly, such a charge load does not challenge either the short-term or the long-term stability of the readout chambers.

The currents in the inner volume of the TPC are also given, both in the drift volume (trigger independent) and in the readout chambers, after amplification.

7.3 Track reconstruction

7.3.1 Tracking environment

7.3.1.1 Detector occupancy

The performance of the TPC working in the high track-density environment strongly depends on the detector occupancy. The latter should be reduced to the level that secures the performance mentioned in Section 7.1. Thus, detailed studies of the dependence of the occupancy on the detector parameters of were performed. The occupancy O can be defined as the probability of having a signal (digit in the pad–time-bin plane) above threshold (zero suppression). In these studies we defined (see also Section 4.1.2.2) occupancy as the ratio

$$O = \frac{N_{\text{ABOVE}}}{N_{\text{ALL}}},$$

where N_{ABOVE} is the number of digits above threshold, N_{ALL} is the total number of digits.

The number of digits above the threshold depends on the particle density F and on the effective (mean) cluster area s_{eff} . Neglecting correlation between clusters one obtains

$$O = 1 - \exp(-F \cdot s_{\text{eff}}).$$

Notice that in the low particle-density environment, the occupancy depends linearly on F and s_{eff} , while for a high particle density saturates exponentially.

The particle density at the position \mathbf{r} from the interaction point can be expressed as

$$F \sim K(\alpha) \frac{1}{r^2} \cos \alpha,$$

where $K(\alpha)$ is given by the interaction mechanism, $\alpha = \triangleleft(\mathbf{dS}, \mathbf{r})$, \mathbf{dS} being the unit area in the pad plane. The r^{-2} dependence suggests the possibility of decreasing occupancy by increasing the lower radius of the TPC sensitive area. However, because of the saturation in the high particle-density environment, the reduction of occupancy by 50% at the inner-pad-row radius would require its increase from 84 to 140 cm. This is incompatible with the requirement of good track matching with the Inner Tracking System (ITS). Therefore, one has to reduce the occupancy, reducing the effective cluster area. Assuming a Gaussian shape of the clusters, the effective area s_{eff} can be expressed as

$$s_{\text{eff}} = 2\pi\sigma_t\sigma_p \ln\left(\frac{K_{\text{Max}}}{\text{threshold}}\right),$$

where σ_t, σ_p are the r.m.s. of the cluster width distributions in the time and pad directions, respectively. The maximal amplitude within a cluster is given by

$$K_{\text{Max}} = \frac{Q_{\text{ch}}}{2\pi\sigma_t\sigma_p},$$

where Q_{ch} is the integrated charge of a cluster.

The effective area of a cluster and thus the occupancy can be reduced by decreasing the cluster width in both pad and time directions. This width, in general, depends on the diffusion, on the response functions, and on the pad length. For a given gas and drift field the diffusion is no longer a variable factor. Thus, in order to decrease the cluster size one can optimize the last two parameters only. This led to the present choice of pad geometry and preamplifier/shaper width, and to the reduction of the PRF in the inner part of the TPC down to about 2 mm. A detailed discussion is presented in Section 4.1.2.1

In Fig. 7.8 the occupancy as a function of z -coordinate is plotted for different pad-row radii. It reaches, for small η (central region), 44% for the pad row at a radius of 90 cm and drops to 10%–15% for 250 cm. In Colour Figs. VII and VIII the simulated clusters are shown in the innermost and outermost pad rows, respectively. The average occupancy is about 22%.

7.3.1.2 Distortions

In general, the distortions of the electron trajectory in the drift volume are due to imperfections of the electric and magnetic fields and their relative orientation. In the calculations presented in this section we took into account

- the nonuniformity of the electric field because of the positive charge pile-up in the drift volume;
- the nonuniformity of the magnetic field of the L3 magnet.

The nonuniformity of the electric field because of imperfections of the field cage and to edge effects is discussed elsewhere (see Sections 2.1 and 4.1.5). Here, the nonuniformity of the electric field results only from the positive charge pile-up.

An electron created in the ionization process drifts in the electric (**E**) and magnetic (**B**) fields inside the TPC volume with velocity

$$\mathbf{v}_{\text{drift}} = \frac{\mu}{1 + (\omega\tau)^2} \cdot \left(\mathbf{E} + \omega\tau \frac{\mathbf{E} \times \mathbf{B}}{B} + (\omega\tau)^2 \frac{(\mathbf{E} \cdot \mathbf{B}) \cdot \mathbf{B}}{B^2} \right),$$

where μ is the electron mobility and $\omega\tau$ is the tangent of the Lorentz angle. For both fields uniform and parallel, the drift velocity is

$$\mathbf{v}_{\text{drift}} = \mu \mathbf{E}.$$

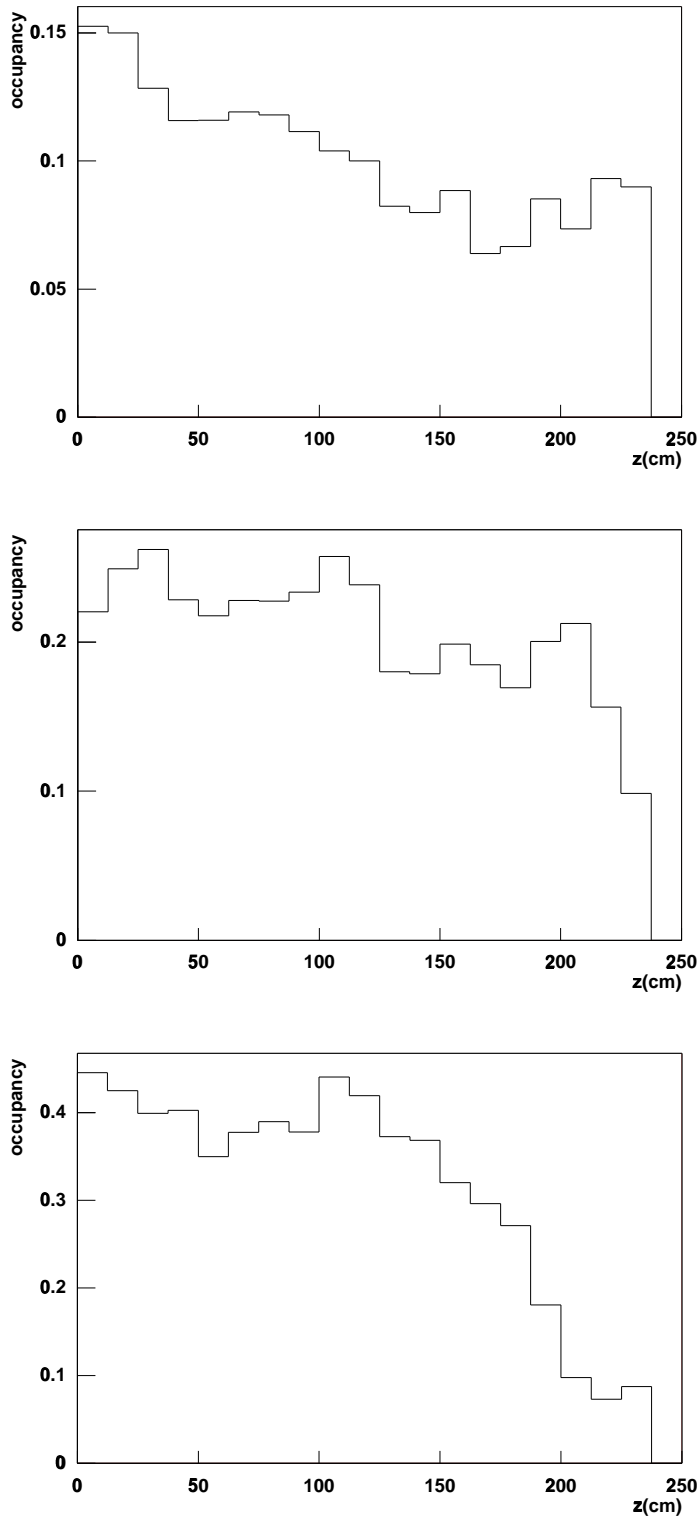


Figure 7.8: Occupancy in different TPC regions as a function of z -coordinate. The lower plot was obtained for a pad-row radius of 90 cm, the middle one for 130 cm and the top one for 250 cm. Values of the parameters used in these simulations are presented in Section 7.2.1.3.

Positive charge pile-up

There are two sources of the positive charge in the drift volume of the TPC: the ionization caused by the ionizing particles and the positive-ion feedback from the readout chamber. The latter is reduced by the implementation of the gating grid, while the first leads to a build-up of positive charge in the drift volume. This is because the ion mobility is smaller by 3–4 orders of magnitude than that of electrons, which, in practice, results in the permanent presence of a positive charge in the TPC drift volume, affecting the drift field. The electric field due to the space-charge has been calculated through the following steps.

- The primary charge density $\rho_{\text{prim}}(r, z)$, where r is the radial coordinate and z is along the drift, has been calculated using the HIJING event generator tuned to $dN_{\text{ch}}/dy = 8000$ at midrapidity for central Pb–Pb events. The multiplicity of minimum-bias events which produce the major contribution to the space-charge creation has been scaled by an appropriate factor (1/5).
- The build-up of the positive charge in the drift volume, resulting in the charge density $\rho(r, z)$, has been calculated for
 - luminosity $\mathcal{L} = 1 \times 10^{27} \text{ cm}^{-2}\text{s}^{-1}$,
 - ion mobility $\mu_{\text{ion}} = 4 \text{ cm}^2\text{V}^{-1}\text{s}^{-1}$.
- The potential $\Phi(r, z)$, and thus the extra electric field, has been obtained by solving the Poisson equation

$$\nabla^2 \Phi(r, z) = -\frac{1}{\epsilon_0} \rho(r, z),$$

ϵ_0 being the electrical permittivity of vacuum.

Results

The numerical values for the distortions have been obtained by integrating the equation for the drift velocity during the drift time and comparing the obtained electron position with the initial one.

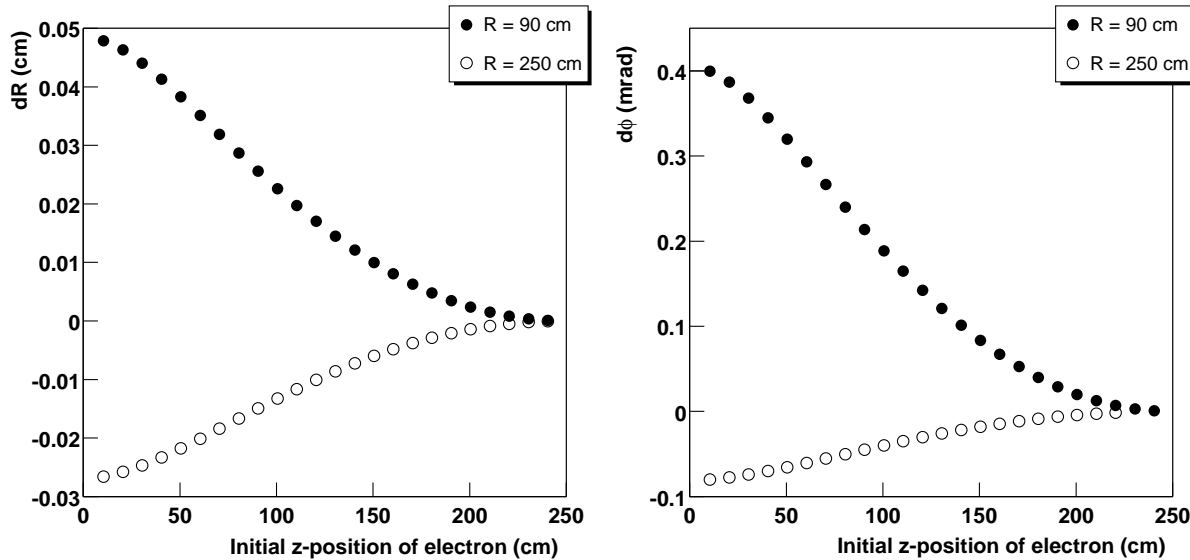


Figure 7.9: Radial and azimuthal distortions due to space-charge in 90 % Ne, 10 % CO₂. Magnetic field is uniform and parallel to z -axis.

Distortions due to the space-charge In Fig. 7.9 the radial and azimuthal distortions due to the space-charge in the drift volume are shown. The magnetic field is assumed to be uniform and parallel to the z -axis. Note that the distortions of this type for Ar-based gas mixtures would be larger by a factor of about 5 with respect to Ne-based ones. This is because of the higher ionization in argon and the lower Ar-ion mobility.

Distortions due to the nonuniformity of the magnetic field The uniformity of the magnetic field plays a crucial role in the track reconstruction. It determines the validity of the track model and thus the possibility of online tracking.

We have studied two configurations of the magnetic field:

(oo) L3 magnet + the Muon Arm dipole^{*}

(cc) L3 magnet + the Muon Arm dipole + extra iron plugs in the L3 magnet door.

One should keep in mind that the ALICE reference system is placed 30 cm above the L3 magnet axis, which results in a ϕ -asymmetry of the magnetic field inside the TPC volume. The electric field was assumed to be uniform and parallel to the z -axis. The results are shown in Figs. 7.10 and 7.11 for the (oo)-configuration, and in Figs. 7.12 and 7.13 for the (cc)-configuration. One can see that the iron plugs improve, in general, the quality of the magnetic field, reducing the distortions by up to a factor of 2. Further in this Section the (cc)-configuration of the magnetic field has been used.

Overall distortions The realistic case, where the drift field \mathbf{E} is distorted by the space-charge and \mathbf{B} is the real magnetic field of the L3 magnet with the Muon Arm dipole, is shown in Figs. 7.14 and 7.15.

It should be noted that, although radial distortions can exceed 1 mm, the effective shift of the cluster along the pad row is smaller by a factor of $\tan \alpha$, where α is an angle between the track and the pad axis. Azimuthal distortions reaching 1 mrad lead to a large shift along the pad row of about 1 mm at the lower (90 cm) and 2 mm at the upper (250 cm) radius of the TPC. This necessitates of corrections. However, as the experience of the NA49 and CERES experiments shows, distortions of this magnitude can be corrected. We are aware that distortions due to the imperfection of the magnetic field (the most common in present-day fixed-target experiments) and those due to the space-charge are of a different nature: The

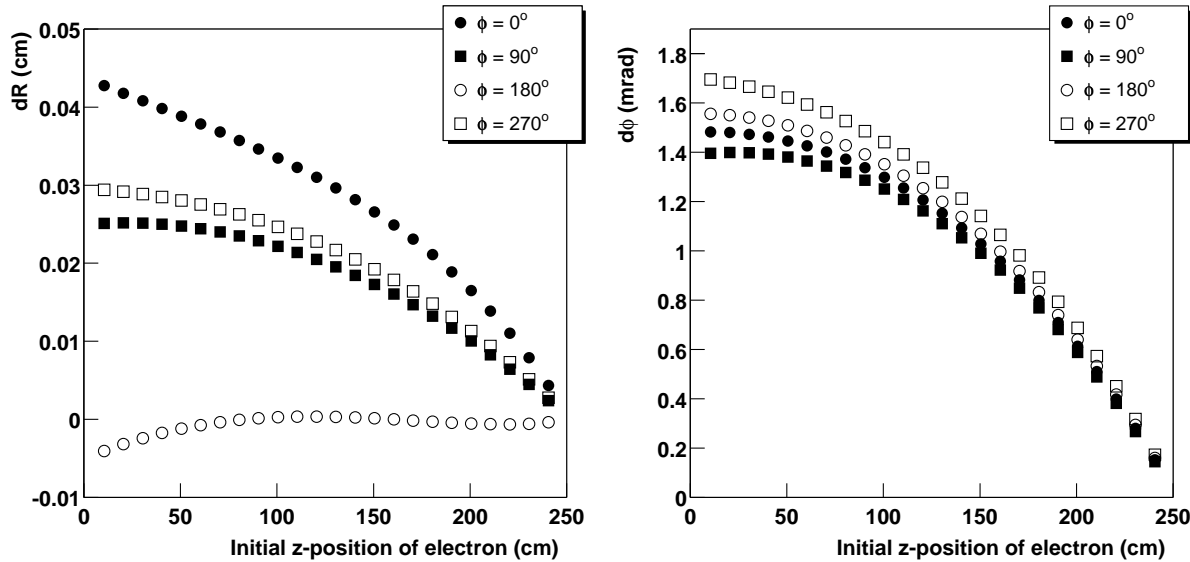


Figure 7.10: Radial and azimuthal distortions at lower TPC radius (90 cm) due to nonuniformity of magnetic field ((oo)-configuration). Electric field is uniform and parallel to z -axis.

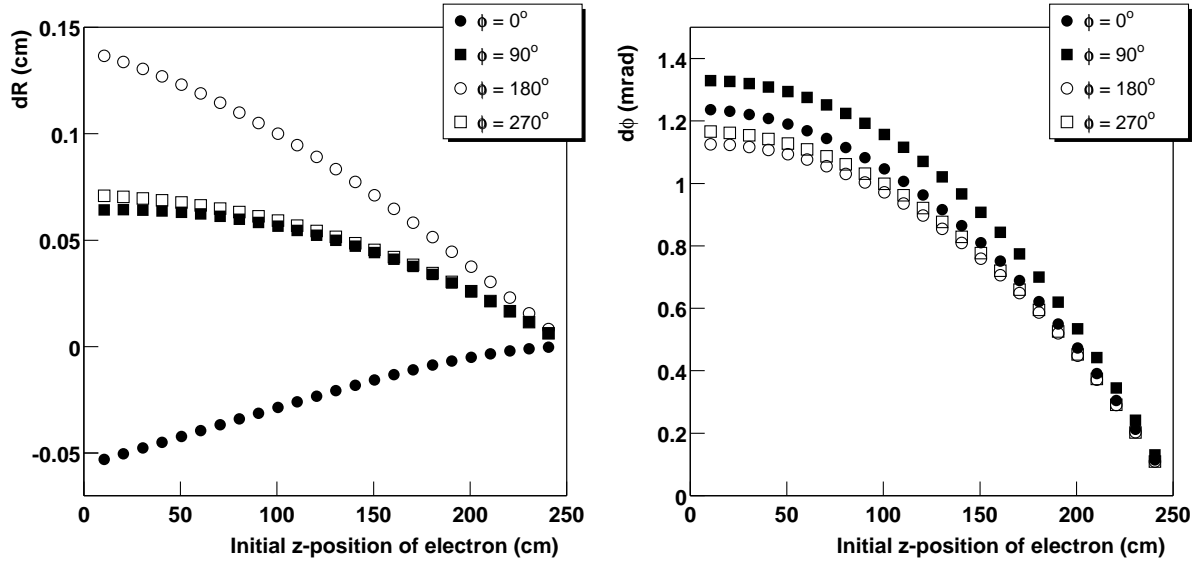


Figure 7.11: Radial and azimuthal distortions at upper TPC radius (250 cm) due to nonuniformity of magnetic field ((oo)-configuration). Electric field is uniform and parallel to z -axis.

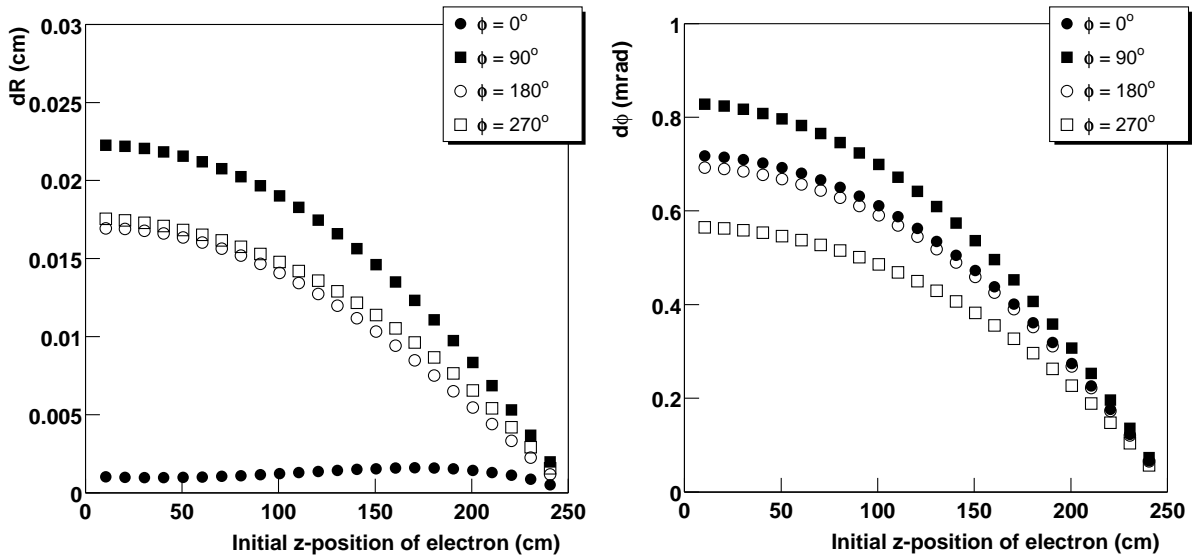


Figure 7.12: Radial and azimuthal distortions at lower TPC radius (90 cm) due to nonuniformity of magnetic field ((cc)-configuration). Electric field is uniform and parallel to z -axis.

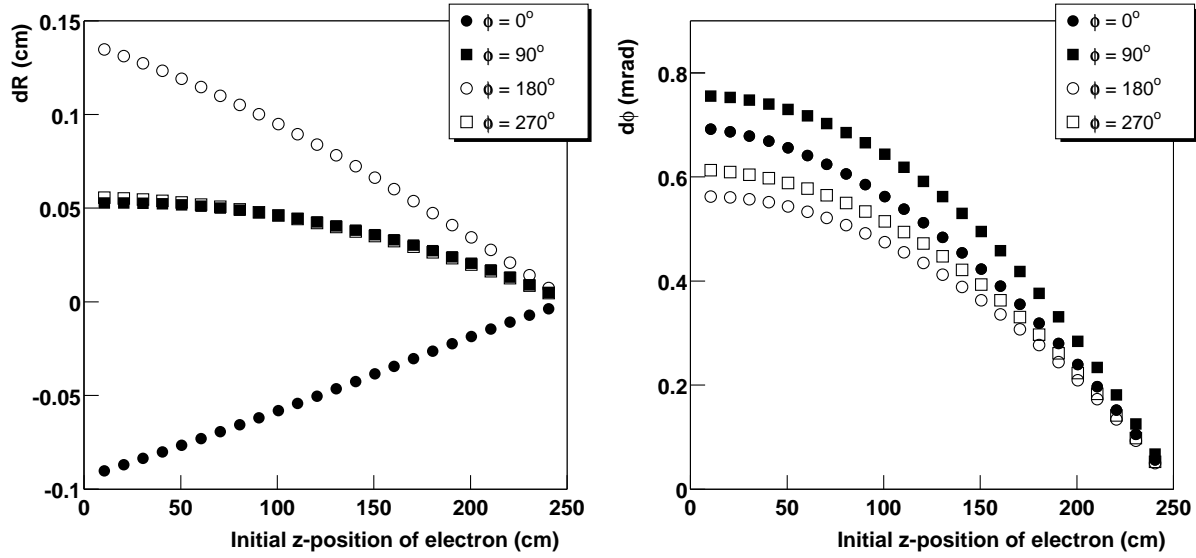


Figure 7.13: Radial and azimuthal distortions at upper TPC radius (250 cm) due to nonuniformity of magnetic field ((cc)-configuration). Electric field is uniform and parallel to z -axis.

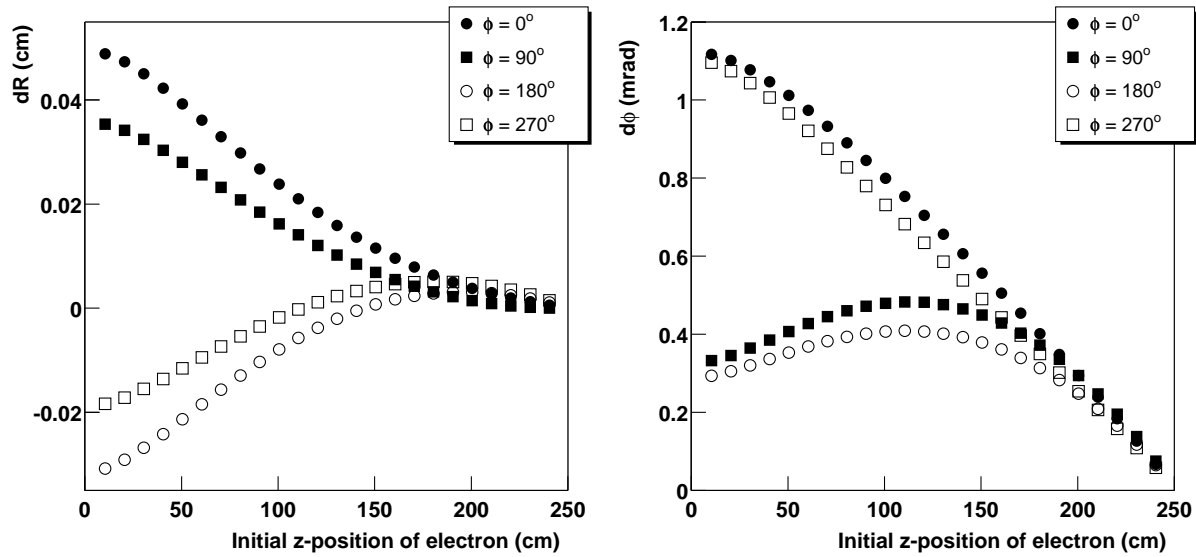


Figure 7.14: Radial and azimuthal distortions at lower TPC radius (90 cm) due to space-charge and nonuniformity of magnetic field.

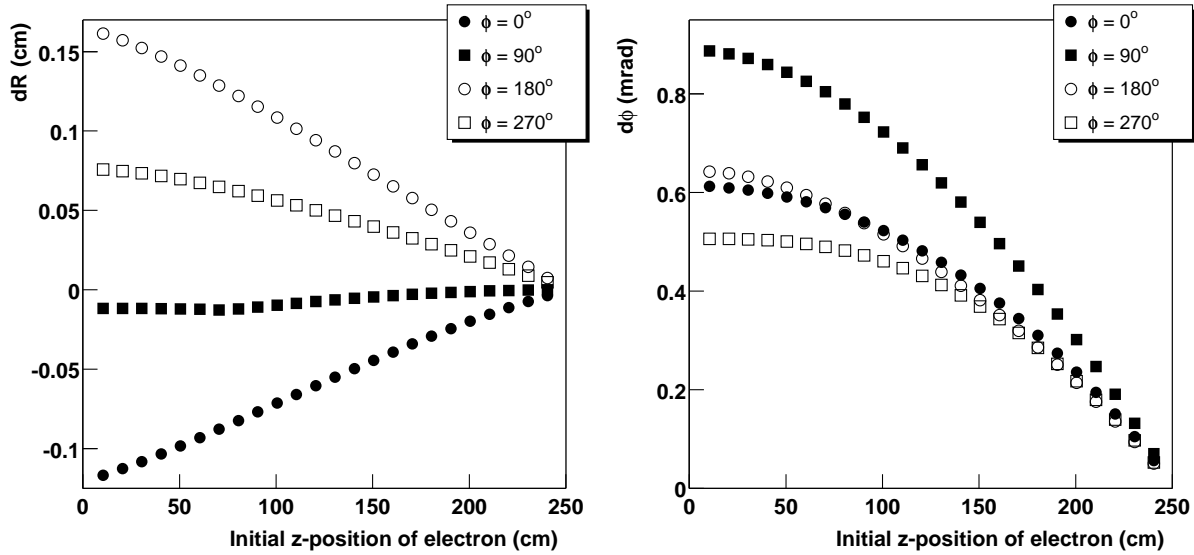


Figure 7.15: Radial and azimuthal distortions at upper TPC radius (250 cm) due to space-charge and nonuniformity of magnetic field.

first are static while the latter are, in the best case of a stable luminosity, quasi-static. This would probably require a more sophisticated approach to the corrections than in the experiments mentioned above.

Distortions in the drift (z) direction are significantly smaller and do not exceed few tens of microns.

7.3.2 Cluster finding

We have chosen a classical approach for the tracking in the ALICE TPC. This means that, before the tracking itself, we have to find two-dimensional clusters in pad-row-time planes. Then we reconstruct the positions of the corresponding space points, which are interpreted as the crossing points between the tracks and the centres of the pad rows.

Up to now we have used a simple variant of the cluster finder. First we look for ‘preclusters’, i.e. the groups of adjacent cells in a pad-row-time plane which have, after digitization, the signal above the zero-suppression threshold. The two distinct preclusters are hence separated from each other by a gap where the signal is less than the zero-suppression threshold. For each precluster we then find all its local maxima. If there is only one local maximum we assume that such a precluster has been initiated by one track only. In this case we store as the space-point coordinates the centre of gravity of the precluster. If there are several local maxima we split this precluster into the corresponding clusters in the following way: For each local maximum we search for a group of adjacent cells with the signal greater than the signal of the cell at the nearest saddle point. In other words, we cut the peaks at the signal level of the nearest saddle point. Then we take the centres of gravity of these groups of cells as the reconstructed positions of the corresponding space points.

Another important piece of information, which has to be provided by the cluster finder, is the estimate of the errors of the reconstructed space points in both the pad-row and the drift directions. For tracking we will need, however, two types of error (for details see the description of the tracking algorithm below). After extrapolating a track from one pad row to the next we have to define a window around the predicted point in terms of the standard deviations, which comprise the extrapolation errors and the expected space-point errors. These types of space-point error, which depend on the track parameters, are called ‘potential’ space-point errors. When, during the filtering step, we try to assign a definite space point to the track, it is better to use an actual estimate for the errors of this particular space point, which depends on the parameters of the corresponding cluster. These types of error are called ‘actual’ space-point

errors. Because of the complicated way of cluster forming in a TPC, it is impractical to calculate both these errors theoretically. Instead, we rely on the results of our microscopic simulations.

In addition to the raw data, the microscopic simulator gives the exact coordinates of the tracks' crossing points with the centres of the pad-row planes. Comparing the reconstructed space-point positions with the generated ones and parametrizing the corresponding deviations as a function of the track parameters and the pad-row number, we get the parametrization for the potential space-point errors. This was done using several simulated events with a very low track density, when the number of overlapping clusters was negligible.

Concerning the actual space-point errors, we found that they are approximately proportional to the dispersions (second central moments) of the corresponding clusters. This is not true in general. However, at least for tracks which cross the entire TPC (i.e. for pions with $p_t > 80 \text{ MeV}/c$ and $45^\circ < \theta < 135^\circ$) it is a good approximation. The cluster dispersions can be calculated for each cluster and, after multiplication by constants (which have been found again using the microscopic simulator, separately for the two directions), are used as the errors of the reconstruction of this cluster.

The precision of the reconstruction of the cluster positions depends on the track parameters and on the pad-row number; in other words, it is a function of the drift length and the angles at which tracks cross pad-row-drift planes. This precision is also a function of the properties of the drift gas, the particular design of the readout chambers, and parameters of the front-end electronics. In Table 7.5 the space-point resolutions for well-separated tracks are summarized. These results are averaged over pad rows in the inner and outer TPC sectors, as well as over all tracks which cross the entire TPC. During the simulations all the TPC parameters were set to the values discussed above. The values reported here are about 10% better than those shown in Fig. 4.13 on page 55 for MIPs, because here we also averaged over particle momenta.

Table 7.5: Averaged space-point resolutions.

	Pad direction [mm]	Drift direction [mm]
Inner sectors	0.87	1.28
Outer sectors	0.72	1.13

An additional quantity, which we have to know after the cluster finding, is the charge deposited in the clusters. We need this information for particle identification by dE/dx measurements. There are at least two ways to determine this charge. As a measure of the charge in a cluster, we can use either the sum (in ADC counts) of all digits which are associated with this cluster or just the largest digit in the cluster. We have found that in our case the latter option gives better results (see below).

In order to better unfold the overlapping clusters one has to fit them to a given shape, which we have not yet done. The first reason for this is that the fitting is a rather slow procedure. The other difficulty with the fitting is the following: Before starting to fit, we would like to know, at least, how many tracks contribute to the given cluster. It would also be very useful to have an estimate of the angles at which these tracks cross the particular pad row. Otherwise, we have to fit too many parameters, and so the fitting procedure becomes very unstable.

Unfortunately, we have no information about tracks during the cluster finding. Nevertheless, we think that this straightforward cluster ‘unfolding’ could be very promising, if one managed simultaneous track finding and cluster finding. This approach is currently under study.

7.3.3 Track finding

Track finding for the predicted particle densities is one of the most challenging tasks in the ALICE experiment. It is still under development and here we report the current status. Track finding is based on the

Kalman-filtering approach. Kalman-like algorithms are widely used in high-energy physics experiments and their advantages and shortcomings are well known [12].

There are two main disadvantages of the Kalman filter, which affect the tracking in the ALICE TPC. The first is that we have to reconstruct clusters before applying the Kalman-filter procedure. As has already been noted, this is in the present situation not a trivial task. We have about 40% occupancy in the inner sectors of the TPC; therefore a certain number of the clusters get lost, and the others may be significantly displaced. These displacements are rather hard to take into account. The other problem with the Kalman-filter tracking is that it relies essentially on the determination of good ‘seeds’ to start a stable filtering procedure. Unfortunately, for the tracking in the ALICE TPC we have to construct the seeds using the TPC data themselves. The TPC is a key starting point for the tracking in the entire ALICE set-up. Practically none of the other detectors can provide the initial information about tracks. Therefore, we have to make the seeds in a straightforward combinatorial way, and this more than doubles the computing time.

On the other hand, there is a whole list of very attractive properties of the Kalman-filter approach.

- It is a method for simultaneous track recognition and fitting.
- Within this method there is a possibility to reject incorrect space points ‘on the fly’, during the only tracking pass over a track. Such incorrect points can appear as a consequence of the imperfection of the cluster finder. They can be due to noise or they can be points from other tracks accidentally captured in the list of points to be associated with the track under consideration. In the case of a global tracking approach one usually needs an additional fitting pass to get rid of these incorrect points.
- In the case of substantial multiple scattering, track measurements are correlated and therefore large matrices (of the size of the number of measured points) need to be inverted during a global fit. In the Kalman-filter procedure we only have to manipulate up to 5×5 matrices (although many times, equal to the number of measured points), which is much faster.
- Using this approach one can handle multiple scattering and energy losses more easily than in the case of global methods.
- Kalman filtering is a natural way to find the extrapolation of a track from one detector to another (for example from the TPC to the ITS or TRD).

In the following we briefly describe our implementation of the Kalman-filter algorithm.

The first and most time-consuming step is seed finding. It begins with a search for all pairs of points in the outermost pad row and in a pad row n rows closer to the interaction point ($n = 20$ at present) which are projecting to the primary vertex. The position of the primary vertex is reconstructed, with high precision, from hits in the ITS pixel layers, independently of the track determination in the TPC. When a reasonable pair of such points is found, we calculate the parameters of a helix going through these points and the primary vertex, and take the parameters of this helix as an initial approximation of the parameters of the potential track. The corresponding covariance matrix can be evaluated by taking the point errors, which are given by the cluster finder, and applying an artificially large uncertainty to the primary-vertex position. At this step we assign an uncertainty of the size of the beam pipe, in order to take into account multiple scattering and not to lose the tracks from decays close to the primary vertex. This is the only place where we introduce a certain (not too strong) vertex constraint, and later we allow tracks to have any impact parameters in both the z -direction and $r\text{-}\phi$ plane. Using the calculated helix parameters and their covariance matrix we start the Kalman filter from the outer point of the pair to the inner one. If at least half of the possible points between the initial ones were successfully associated with this track candidate, we save it as a seed and continue to look for another pair of initial points.

To avoid a bias of the seed through cluster distortions (owing to overlaps and δ -rays) and subsequent loss of the track candidate, a second seed-finding is performed (using another pair of pad rows, at present the 10th and $(n+10)$ th).

At the end of the seed finding we sort the seeds according to increasing track curvature. Then we proceed with the Kalman filter through the entire TPC, starting with the stiffest tracks, removing assigned clusters and continuing with softer ones.

For each seed we calculate the track parameters, as well as their covariance matrix, at the next pad row. During this extrapolation step we take into account multiple scattering (by adding the corresponding matrix to the track covariance matrix) and mean energy loss (by means of the Bethe–Bloch formula), assuming that the actual particle is a pion. Then on this pad row we define a ‘window’ along the pad direction inside which we look for a cluster to be associated with the track. To calculate this window we do the following steps. First, the formula which parametrizes the errors of the cluster reconstruction as a function of the track parameters and pad-row number gives us an expected value for the errors of the cluster reconstruction — the potential space-point errors. Then we take the element of the track covariance matrix, which describes the uncertainty of the track position in the pad direction, compute the square root of the sum of this element and the square of the potential space-point error, and multiply the result by a constant, which is a parameter of the tracking program. Since the residual distributions are, unfortunately, essentially not Gaussian, we use as a constant a factor of 5 (instead of 3, which would be good enough in the case of Gaussian errors).

After the window is defined we check all the clusters which appear within it. Here we have three possibilities.

- There are no clusters in the window. In this case we try to find necessary clusters on the next pad row. If there were already several consecutive pad rows without clusters associated with this track, we terminate the tracking for this candidate and remove it from the corresponding list, but keep all of its clusters in the event. Consequently we allow the track to miss as many as half of all pad rows in a particular TPC sector. This is because we have rather large dead zones between the TPC sectors.
- There is one cluster inside the window. If the χ^2 value calculated for this cluster is small enough (at present we use as an upper limit 12 per two degrees of freedom), we attach this cluster to the track and update the track parameters according to the standard filtering procedure. If the χ^2 value is too large, we continue as in the first case.
- There is more than one possible cluster. In this case we choose the cluster which gives the smallest χ^2 value and go to the previous case.

From time to time it happens that the track leaves a TPC sector and enters another. In this case we recalculate the track parameters and the covariance matrix so that they are always expressed in the local coordinate system of the sector within which the track is at that moment.

When a current track candidate reaches the inner boundary of the TPC, we check if there are at least 40% of all possible clusters attached to it. If so, we consider the track candidate as a found track and remove its clusters from the event. Otherwise, we remove the track candidate and the corresponding clusters are left in the event.

7.4 Tracking performance

In this section we present the tracking efficiency, momentum and dE/dx resolutions. The angular and impact-parameter resolution, involving the tracking in the ITS are discussed elsewhere [13].

7.4.1 Tracking efficiency

In order to determine the tracking efficiency within the TPC acceptance we define the following quantities.

1. ‘Generated good track’ — a track which crosses at least 40% of all pad rows and produces at least one hit on the pad rows chosen for the seed-finding procedure.
2. ‘Found good track’ — a track for which the number of assigned clusters is larger than 40% of the total number of pad rows. In addition we require for such tracks that no more than 10% of clusters are incorrectly assigned and that at least half of the innermost 10% of clusters were assigned correctly.
3. ‘Found fake track’ — a track with the sufficient number, but incorrect assignment, of clusters.

The tracking efficiency is then defined as the ratio of the number of ‘found good tracks’ to the number of ‘generated good tracks’, while the probability to find a ‘fake’ track is expressed by the number of ‘found fake tracks’ normalized in the same way. The tracking efficiency was determined only for primary tracks.

No significant dependence of the tracking efficiency on the transverse momentum of the particles or on their dip angle was found (see Fig. 7.16). This confirms earlier estimates given in Ref. [1].

In order to study the dependence of the tracking efficiency on the particle density we have performed simulations for three different values of dN_{ch}/dy . We used the HIJING generator with the total multiplic-

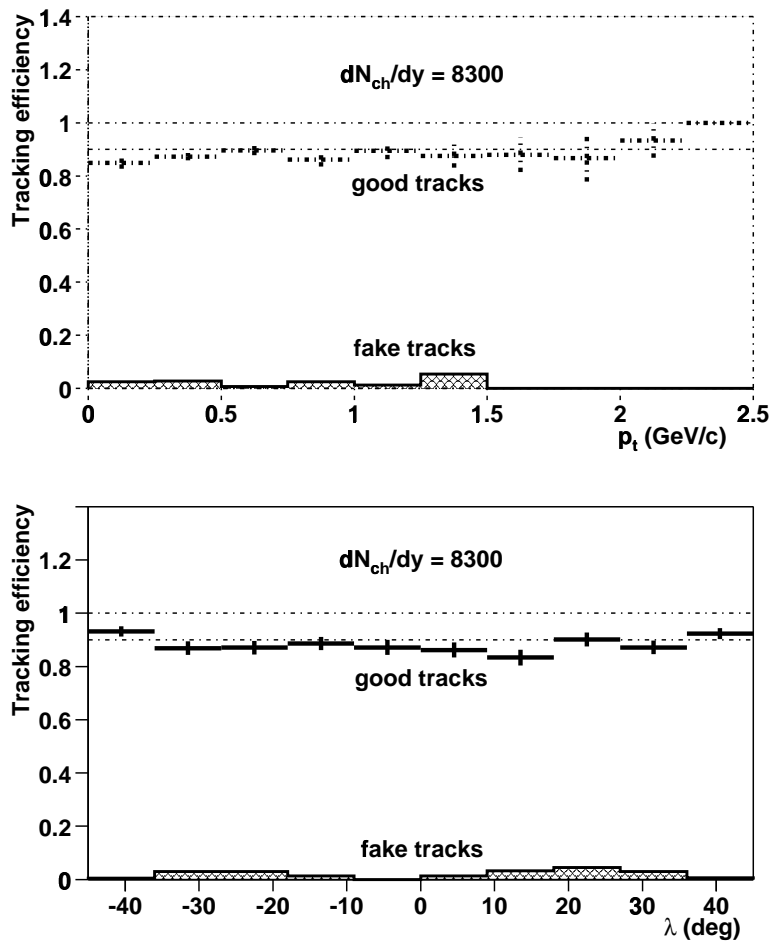


Figure 7.16: Tracking efficiency as a function of particle transverse momentum and dip angle.

ity scaled by appropriate factors to obtain the right rapidity density in the central region. The results are presented in Table 7.6.

Table 7.6: Tracking efficiency for different track densities.

dN_{ch}/dy	Efficiency for real tracks	Probability of fake tracks
1300	0.98	0
4300	0.94	0
8300	0.88	0.02

7.4.2 Two-track efficiency

In order to evaluate two-track efficiency we modified the standard HIJING event generator. For every second generated particle the momentum of the next particle was generated with a small difference with respect to the momentum of the previous one. This difference was uniformly distributed within a sphere of radius $0.03 \text{ GeV}/c$ (in momentum space). In this way we increased artificially the number of particles with close momenta.

After the reconstruction of such an event, the two-track efficiency can be calculated as a ratio of the number of found particle pairs to the number of generated ones. This ratio, as a function of the absolute value of the (generated) momentum difference of the two particles, is shown in Fig. 7.17. This result has been obtained for the particle density $dN_{ch}/dy = 8300$.

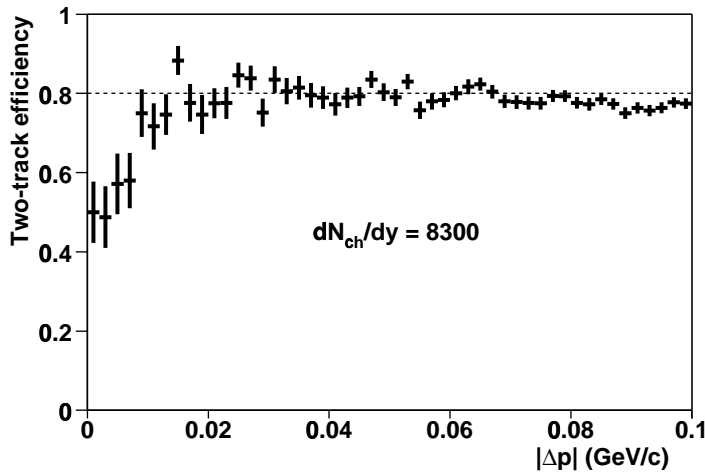


Figure 7.17: Two-track efficiency for particle density $dN_{ch}/dy = 8300$ as a function of absolute value of generated momentum difference of two particles.

One can see that we lose pairs of particles if their momenta differ by less than $0.015 \text{ GeV}/c$. However, the two-track efficiency never falls to zero even when momentum difference is close to zero. This is because multiple scattering in the material crossed by particles with close momenta between the interaction point and the TPC sensitive volume (beam pipe, ITS, inner vessel of the TPC) tends to separate them. This effect increases the probability to detect such pairs of particles, but at the same time it deteriorates the two-track momentum resolution. Nevertheless, if a pair of particles was successfully registered in the TPC, the actual momentum difference at the vertex can then be reconstructed using the ITS information.

We have estimated that for the present ITS and TPC design the two-track momentum resolution is only slightly worse than that presented in the ALICE Technical Proposal [1]. The results are summarized

Table 7.7: Two-track momentum resolution.

dN_{ch}/dy	δq_{long} [MeV/c]	δq_{side} [MeV/c]	δq_{out} [MeV/c]		
			$p_t = 0.2$ MeV/c	$p_t = 0.5$ MeV/c	$p_t = 1.0$ MeV/c
1000	1.0	0.5	3.7	7.4	13
6000	1.1	0.5	3.9	8.5	16

in Table 7.7 where the two-track momentum resolutions are given separately, for the three components of the momentum difference, and for low and high charged-particle densities. The resolutions of the longitudinal (in the z -direction) component and of the ‘side’ (the direction in the transverse plane, perpendicular to the total momentum of the pair) component are practically momentum independent. The resolutions of these two components are determined by the angular resolution at the interaction point. On the other hand, the resolution of the ‘out’ (the direction in the transverse plane, parallel to the total momentum of the pair) component deteriorates with increasing p_t , because in this case the main contribution is due to the momentum resolution itself.

7.4.3 Momentum resolution

The momentum resolutions for the three track densities are shown in the Table 7.8. Because of particular interest in high-momentum electrons in ALICE, 10% of electrons with $p_t = 5$ GeV/c were artificially added to the HIJING generated events.

Table 7.8: Momentum resolutions averaged over the HIJING spectrum and for high-momentum electrons only ($p_t = 5$ GeV/c).

dN_{ch}/dy	$\Delta p_t/p_t$ [%]	
	averaged	$p_t = 5$ GeV/c
1300	1.6	5.1
4300	2.0	7.6
8300	2.1	8.5

It can be seen that for lower track densities the obtained resolutions are consistent with those predicted in the ALICE Technical Proposal. However, the resolutions deteriorate (especially for high-momentum tracks) when the track density increases. This is mainly due to the cluster overlappings which are more probable for higher particle multiplicities. Nevertheless, we hope to improve the momentum resolutions by refitting clusters using information about tracks already reconstructed.

From these numbers it is obvious that (for electron physics) the required momentum resolution of 2.5% at 4 GeV/c can only be obtained in conjunction with the ITS and TRD and for running with increased magnetic field. The improvement in $\Delta p_t/p_t$ which is expected when combining information from the TPC and ITS for tracking and when running at $B = 0.5$ T is demonstrated in Fig. 11.13 of the ALICE Technical Proposal [1].

7.4.4 dE/dx resolution

As mentioned above, we compared two methods for obtaining dE/dx information. The most natural way is to use the total charge deposited in clusters. However, it has also been found that, for the tracks which are within the TPC acceptance, one can successfully use the maximal digits in a cluster for the evaluation of dE/dx . We divide the charge, or the maximal digit, by the length of the corresponding track segment; then the dE/dx value is calculated using the truncated mean method. The best resolution in our conditions

can be achieved if we discard 5% of the smallest signals and 25% of the largest ones. The corresponding results for minimum-ionizing pions are presented in Table 7.9.

Table 7.9: dE/dx resolution for total-charge and maximal-digit methods.

dN/dy	dE/dx (total charge) [%]	dE/dx (maximal digit) [%]
1300	7.8	7.0
4300	12.6	8.6
8300	17.3	10.0

In the conditions of low multiplicity, both methods give approximately the same result. However, for higher track densities the difference becomes more obvious. As we do not, in fact, unfold overlapping clusters, the total charge is often more distorted than the signal at the peak, which is why in this case the maximal-digit method yields better results. We would also like to emphasize that for well-separated tracks, having assigned at least 90% of all possible clusters, the dE/dx resolution is 5.5%, which is in agreement with the estimate given in Ref. [1].

We observed a slight dependence of the dE/dx resolution on the polar track angle. The resolution for the most inclined tracks is worse than that for the tracks which are perpendicular to the beam direction. The difference, however, does not exceed 1%. This effect is due to the variation of the cluster shape with polar angle of the track.

Therefore, despite the better performance of the maximal-digit method, we would consider the total-charge method to be less dependent on peculiarities of the simulations, and thus more reliable. Taking this into account, we are planning to repeat the total-charge method calculations when we implement a more reliable cluster separation.

The results of the simulation indicate that the requirements in dE/dx resolution can be fulfilled even at the highest multiplicity densities expected in Pb–Pb collisions

7.5 Track matching

The charged-particle tracks found in the TPC have to be connected to other ALICE detectors in order to improve the momentum resolution and particle identification. We describe here the connection to the ITS and to the TRD.

7.5.1 Connection to ITS

The method used for the TPC–ITS track matching is described in Ref. [13]. The tracks, after the track-finding step in the TPC, are more or less ordered according to track curvature (because we have started from the seeds ordered according to stiffness). Nevertheless, before actual matching we check and when necessary repair the ordering.

During tracking in the ITS (as well as in the TPC) we do not allow for hit/cluster sharing among different tracks (we always remove assigned hits). Therefore it is better to start the track finding with more accurate tracks. The dominant contribution to the extrapolation errors comes from multiple scattering in the TPC field cage, HV degrader and vessel. The multiple-scattering contribution of course increases with decreasing momentum. Therefore we start from tracks with the lowest curvature (i.e. the highest transverse momentum), because the extrapolation to the outer ITS layers for these tracks will be more accurate than for those with smaller momenta.

The distance between the TPC and the ITS sensitive volumes is rather large (about 45 cm) and the track density inside the ITS is so high (the occupancy in the outer ITS layers can reach up to 3%–4%) that simple continuation of the tracking procedure used for the TPC would be ineffective. The hit multiplicity in a $\pm 3\sigma$ window around the extrapolated position of the track is on average 3–4, and there are cases in

which it reaches 20. If we used only the criterion of minimal χ^2 for the hit assignment there would be a high probability of incorrect assignments. Therefore, we have implemented some improvements to the Kalman-filter procedure used for the TPC tracking.

First, we do not decide whether a hit inside the $\pm 3\sigma$ window belongs to the track or not after each track step. Instead, we assign to the track, one by one, all the hits within the predicted window having reasonable χ^2 (not only the one with minimal χ^2). In this way we build for each track found in the TPC the tree of candidates through all of the ITS. The decision is made, and thus the matching is done, only after we can use the information from all of the ITS layers. We choose the candidate (i.e. the path along the tree), and corresponding hits, which for the maximal number of assigned hits has the minimal sum of the χ^2 .

Another change in the algorithm, with respect to the TPC Kalman-filter procedure, is that we use explicitly the vertex constraint. The primary-vertex position is known, prior to the actual tracking, from the ITS pixel detector measurements with an accuracy better of than 20 μm (see Ref. [13]) for central Pb–Pb collisions. During tracking, at each ITS layer, we propagate the track from the nominal vertex position towards the ITS layer concerned, using its current parameters. In this way we project the vertex position on the measurement plane, obtaining two additional ‘measurements’ (two coordinates). Effectively we then have a four-component measurement vector, which we use in the Kalman procedure.

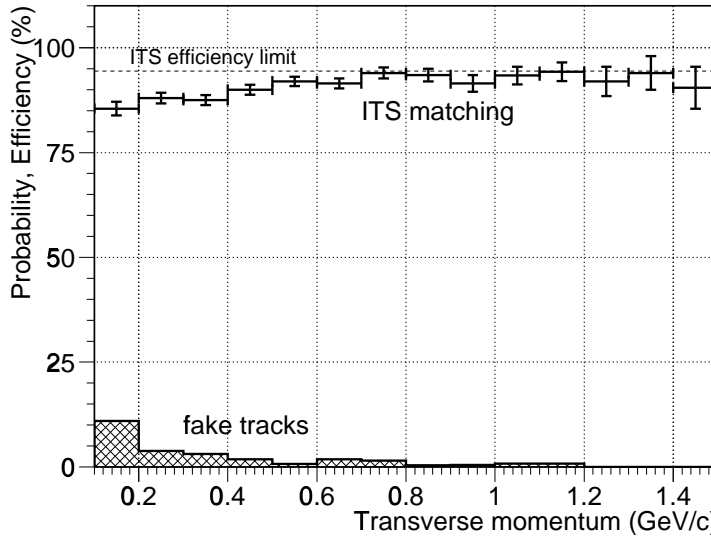


Figure 7.18: Efficiency and fake-track probability for the track matching between the TPC and the ITS.

In Fig. 7.18 the efficiency of the algorithm described above is shown. The presented values include the track-matching efficiency as well as track-finding efficiency in the ITS (they cannot be easily separated). For a track to be reconstructed in the ITS we require that at least five of the six points be found. Because we assume a certain detection efficiency for the ITS layers (98% for the pixel layers and 95% for the other four layers), there is some maximal achievable track-finding efficiency in the ITS (94.5%). The reconstructed track is considered good if all assigned points are correct, otherwise the track falls in the fake-track category. For tracks with transverse momenta above 400 MeV/c we achieve an efficiency of only a few per cent below the maximum achievable. For lower p_t the efficiency is slightly worse because of the larger influence of multiple scattering.

7.5.2 Connection to TRD

Because the TRD design, and also the TRD detailed simulation, are under development, we have used the fast simulation approach (similar to the one used in the Technical Proposal for the TPC–ITS matching),

to estimate the efficiency of the matching of the TPC tracks with the TRD tracking information. In fact, if we compare the results obtained with this simplified method and those obtained with the Kalman filter in the case of the ITS, we will find very good agreement. Therefore, we are confident that when we include the detailed TDR description, the results will not change substantially.

In order to estimate the track position and angular resolution at the TRD inner surface we have used the estimate of the track-parameter errors after the TPC tracking and we take into account multiple scattering in the material between the TPC sensitive volume and the TRD (outer field cage, HV-degrader and outer TPC vessel). Knowing the average TRD occupancy and its point resolution, we can by a simple Monte Carlo program calculate the probability to correctly (or incorrectly) match the TRD hits to the track extrapolation. The results, as a function of transverse momentum, are shown in Fig. 7.19.

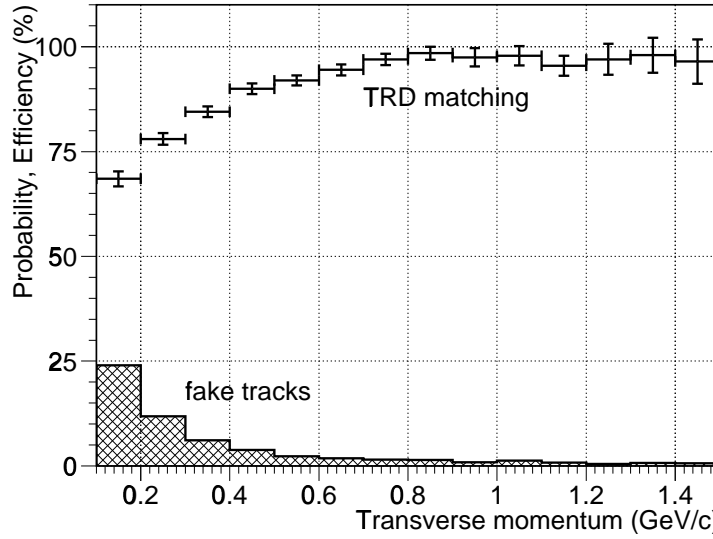


Figure 7.19: Estimated efficiency and fake-track probability for the track matching between the TPC and the TRD.

Again, for the high- p_t tracks, the estimated matching efficiency is excellent, about 98%. On the other hand, for tracks with transverse momentum below 700 MeV/c the efficiency starts to deteriorate even faster than in the case of the TPC–ITS connection. This is the consequence of the larger bending angles for the same p_t in the place further from the interaction point and the higher TRD occupancy.

8 R&D for alternative readout chambers

The conditions in the ALICE experiment [1] are such that the chambers have to be operated at rather large gains ($> 10^4$) and track densities. In the course of evaluating all options for readout chambers we have, consequently, also investigated a number of different technologies. Among the alternatives to wire-based readout chambers are Ring-Cathode Chambers (RCC) and Gas Electron Multipliers (GEM). The results obtained in these R&D studies are discussed below.

8.1 Ring-Cathode Chamber

In 1992 the research project RD32 [2] was started at CERN to investigate low-diffusion gas mixtures and novel designs, both for readout chambers and analog front-end electronics. Furthermore new techniques for high-volume data readout and data reduction were explored. One of the results of these investigations was the development of a readout scheme for wire chambers incorporating ring-shaped cathode elements. This readout architecture would allow easy construction due to only one wire plane. Owing to the better coupling of the charge signal to the readout, the signals observed on the pad elements are larger by about a factor four compared to the classical TPC readout (NA49 geometry, see Ref. [3]) for a given gas gain. A new four-channel preamplifier/shaper in bipolar technology optimized for low power consumption and high baseline stability completed this development.

In the course of further studies it was demonstrated on small prototypes that the original concept using small closed rings could be replaced by open C-shaped structures making it easier to insert the anode-wire plane without losing the advantages of the ring design. In addition, a scheme was developed to produce a sufficient number of rings to equip a reasonably large prototype.

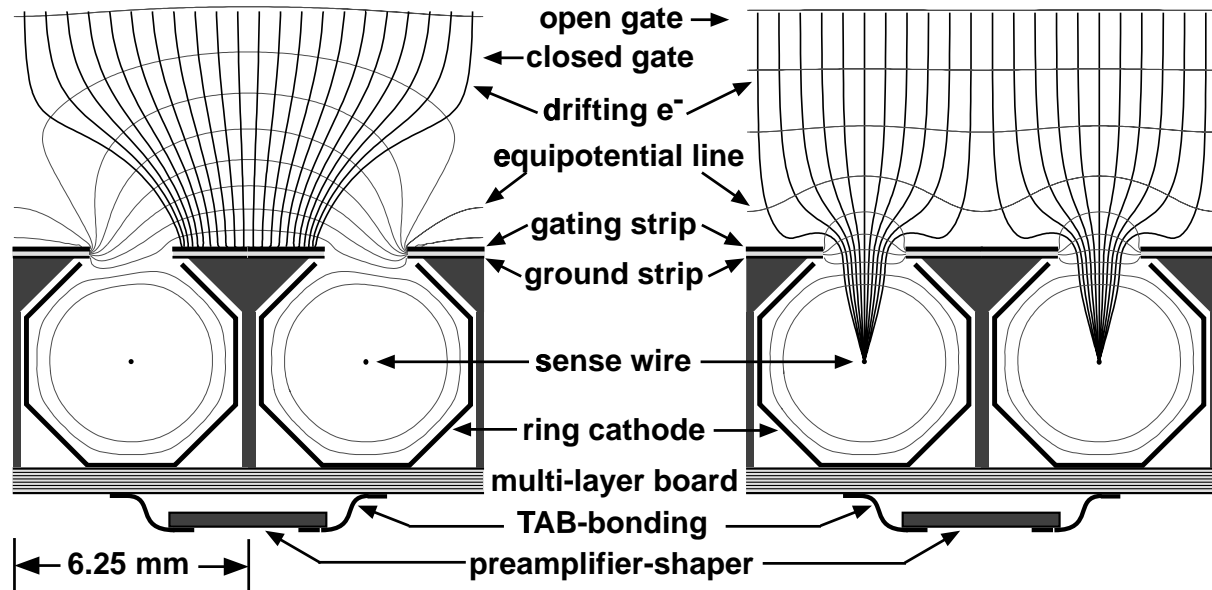


Figure 8.1: Schematic cross-section of the readout board with ring-cathode elements and preamplifier/shaper chips. In addition equipotential lines and drift lines for electrons are shown: left, gate closed; right, gate open.

In 1996 work started to incorporate the new developments into a fully operational detector prototype and test it under realistic conditions. An agreement was reached with NA49 to set up the detector in front of the Main TPCs of NA49 with the lead beam passing through the detector. Part of the phase space not covered by NA49 would become accessible. As a consequence the readout of the prototype had to be matched to NA49 requirements. In 1998 the RCC prototype with an active area of $\approx 40 \times 23 \text{ cm}^2$ and ≈ 1200 active electronic channels was operated successfully within the NA49 environment. In the following text only the principle functionality of the RCC is explained and documented. More detailed information, especially on the analog and digital electronics, can be found elsewhere [4].

In Fig. 8.1 a schematic cross-section through the RCC ALICE prototype is shown. The ring elements are positioned on a multilayer board. Four rings are coupled electrically to one preamplifier/shaper channel which is bonded directly to the backside of the board. Thus a single pad element has a size of $25.0 \times 2.65 \text{ mm}^2$. Conducting strips are inserted between the open sides of the rings. Variation of their potential allows to gate the RCC.

8.1.1 Preamplifier/Shaper

The preamplifier/shaper is optimized for the characteristic signal which is induced by the positive ions created during the amplification process close to the wire of the RCC. The basic design of the chip was developed within the RD32 project starting in 1992. The aim was to design a circuit with a baseline restoration better than 1 permille after $2 \mu\text{s}$. Furthermore a very low power consumption that allows the mounting of the chip very close to the detector readout plane (pad plane) was envisaged. For the production of the chip the radiation hard bipolar process from HARRIS was chosen. In November 1997 the first four-channel chips were cut from the wafers of a multichip project and tested at CERN. From this run approximately 350 chips were finally selected according to specification and later used for the RCC prototype. The technical specifications of the chip are summarised in Table 8.1.

The circuit diagram of the chip is shown in Fig. 8.2. The response of the preamplifier/shaper chip when connected to a small prototype readout chamber is shown in Fig. 8.3.

Table 8.1: Parameters of the preamplifier/shaper chip.

Process	UHF1	Number of channels	4
Die size	$2.6 \text{ mm} \times 2.7 \text{ mm}$	Package	S024/TAB
Supply voltage	$+2.5 \text{ V}/-2.5 \text{ V}$	Number of Adjust pot	4
Power consumption (total)	30 mW	Power consumption/channel	7.5 mW
Input impedance (DC)	150Ω	Input impedance (at 1 MHz)	300Ω
Conversion gain	5 mV/fC	Output dynamic range	2 V
Noise (on detector)	$\sim 2600 e$	PSRR on VEE	-10 dB
Linearity	1%	Crosstalk	50 dB
Shaping time	225 ns	Shaping capacitor/channel	1 external
Tail cancellation (1 to 4 us)	$< 2 \times 10^{-3}$	Tail cancellation ($> 4 \text{ us}$)	$< 0.5 \times 10^{-3}$

8.1.2 TAB bonding

The tape automated bonding (TAB), see Ref. [4], is a technology usually applied for production of big series where high reliability is required. In principle the TAB process in our application can be divided in the following steps :

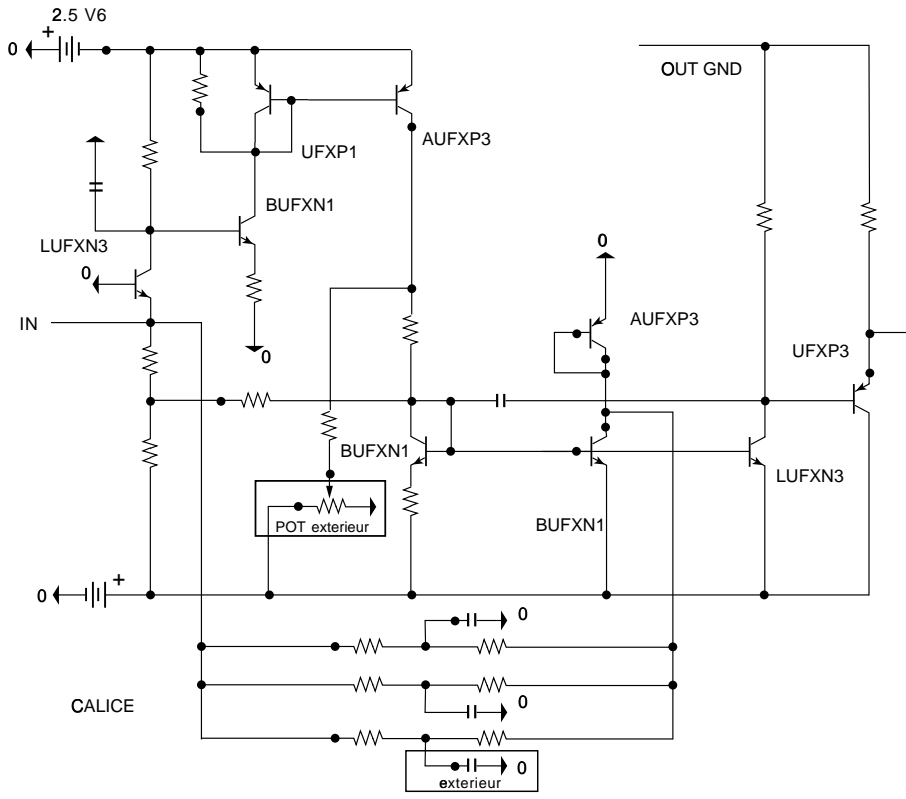


Figure 8.2: Circuit diagram of the preamplifier/shaper chip.

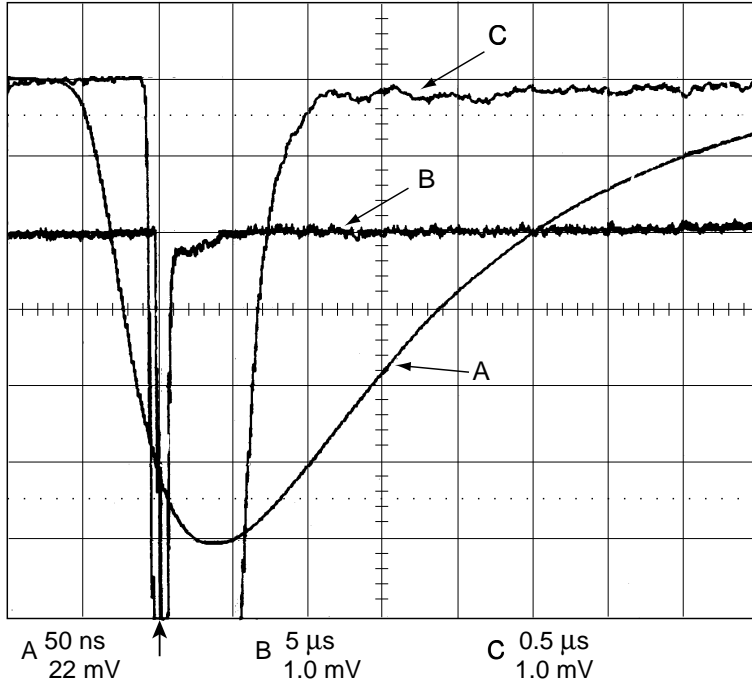


Figure 8.3: Signal from a preamplifier/shaper connected to a small prototype readout chamber.

- a) Delivery of dice from the foundry to the company providing TAB.
- b) ILB (inner lead bonding i.e. mounting of dice on tape) which allows to perform a full performance test (AC + DC).
- c) Selection of dice which perform within certain quality limits (possibility to select different classes).
- d) Transfer of selected dice from ILB tape to the substrate (detector back plane or PCB).

Step a) to d) would be done by the same company which delivers finally a fully functional and guaranteed device according to specifications.

Application of TAB for the production of the RCC prototype

For the RCC prototype we decided to bond the chips directly onto the backside of the readout plane of the RCC. As this was done by the company it had the advantage that fully tested readout segments were delivered. Furthermore, the electrical connection from the preamplifier/shaper to the buffer amplifier was done with flexible cables (FLEX TAB).

8.1.3 Pad response function

Several high-precision measurements have been performed to determine the width of the pad response function (PRF) for the specific wire pad geometry of the RCC. It has to be mentioned that the natural PRF is only determined by the charge coupling of the electrons/ions to the cathode plane while the reconstructed PRF is dependent on the sampling, i.e. the chosen pad width. For the measurements an alpha source was used which ensures a high ionization deposit with a minimum of fluctuations. Angular wire/pad effects were minimized by using a trigger counter to select particles that were emitted from the source parallel to the readout plane. Figure 8.4 shows the fit of the PRF with the models of Gatti [5] and Endo [6]. Applying a Gaussian fit to the data measured with the RCC structure (ring radius of 3 mm) a σ_{PRF} of 2.0 mm was obtained.

The smallest residual were obtained with the Gatti function which might be explained by the higher number of degrees of freedom compared to Gauss and Endo. The measurements show that the width of the measured PRF is approximately 66% of the radius of the cathode ring. More details about the measurement with the small prototype TPC can be found in Ref. [7].

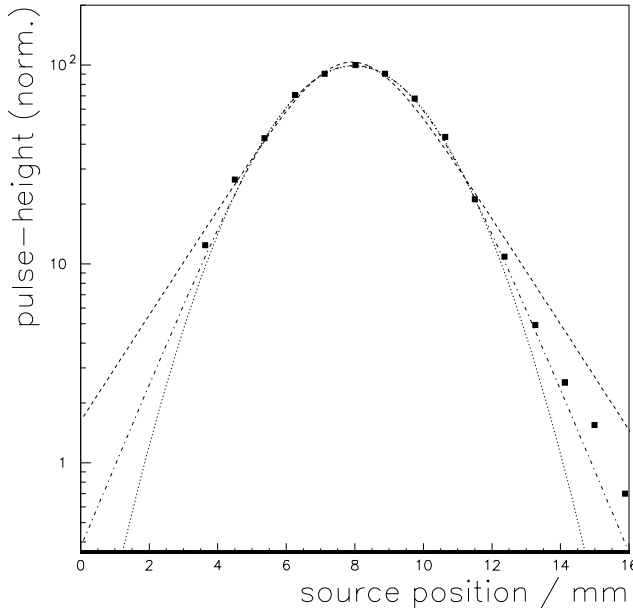


Figure 8.4: Pad response function of the ring-cathode chamber. The curves are Gatti (dash-dot), Gauss (dots) and Endo (dash) estimates.

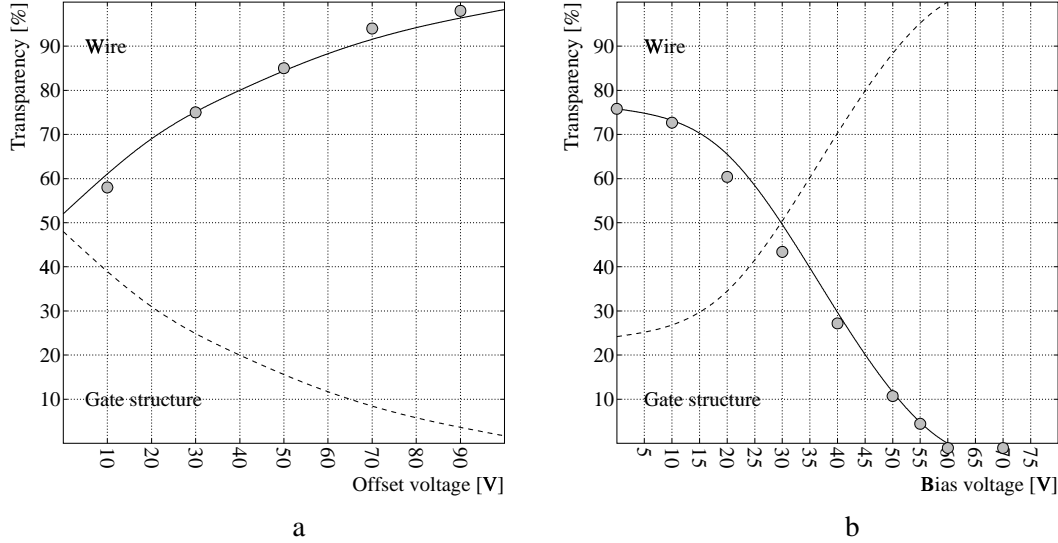


Figure 8.5: Transparency for electrons compared to measurement (full dots) as a function of the offset voltage V_G (a) and as a function of bias voltage ΔV with offset voltage $V_G = -30$ V (b). Solid line: electrons arriving on the anode wire; dashed line: electrons arriving on the gate structure.

8.1.4 Gating

The transmission for electrons of the gate structure depends on the offset voltage that is applied to the gating strips. The voltage setting for a given transparency, which is defined as the fraction of electrons that arrive on the amplification wires, depends on the drift field strength. The higher the drift field, the higher must be the offset voltage.

For the gate transmission measurements of the RCC a beta source was glued to the Mylar window of the field cage. The current in the sense-wire circuit was measured as a function of the gate-offset voltage for different drift fields. It has to be mentioned that the drift field strength was kept for safety reasons far below the 400 V/cm necessary for the operation of the ALICE TPC. The closing characteristic of the gating structure for electrons was measured with a beta source and with the lead beam.

A detailed simulation of the behaviour of the RCC has been performed using GARFIELD (see Ref. [4]). For the simulation the RCC has been modelled as closely as possible to the actual design. Electrons approach the wire through the opening. The anode wires have a diameter of 20 μm , and a 90% Ne, 10% CO₂ gas mixture is assumed.

Transparency for electrons

Assuming a wire potential of 850 V and a drift field of 125 V/cm, the transparency in the open gate state varies from 50% at an offset potential of 0 V to nearly 100% for an offset of -100 V. This agrees well with measurements of this quantity as shown in Fig. 8.5a. Good agreement with the measurement is also obtained for the bias voltage variation with an offset voltage V_G of -30 V, see Fig. 8.5b.

Transparency for ions

Ions go, under most angles, to the ring cathode. These are the ions produced under angles that do not face the ring-cathode exit. When the gate is open, the ions produced in a 30° sector facing the ring-cathode exit will enter the drift zone. When the gate is closed, this sector vanishes. The gating structure is reached by some ions irrespective of the state of the gate: when the gate is open, slightly under 20° give access

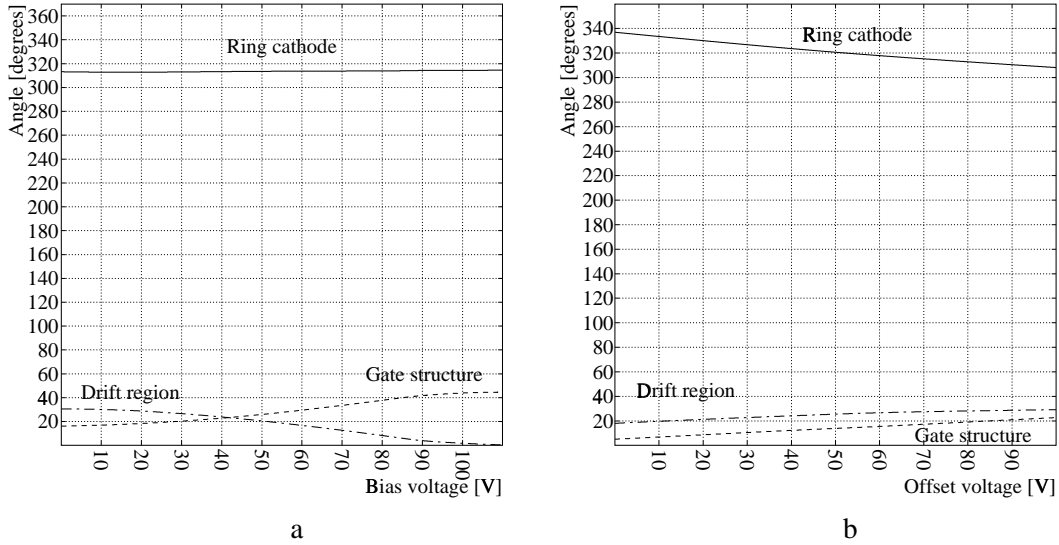


Figure 8.6: Angular region around the sense wire from where positive ions end up on the gating grid, the ring-cathode or the drift volume, respectively, as a function of bias voltage ΔV (a) and offset voltage V_G (b).

to the gating electrodes, an angular range that increases to nearly 45° when the gate is closed (Fig. 8.6).

Since the gating efficiency for ions depends strongly on the assumptions about the initial distribution of the ion cloud around the sense wires, no predictions on the permille level can be made. In addition diffusion effects may play an important role when the gate is closed. These effects are also difficult to calculate with the required precision.

8.1.5 Isochrony

Neon (Ne) ions need 45–55 μs to reach the ring cathode, while CO_2 ions need 25–35 μs . Once past the gate, ions enter the drift region where the field is 180 V/cm, with drift velocities of only 800 cm/s. In Fig. 8.7 lines of isochrony are shown for positive Ne ions.

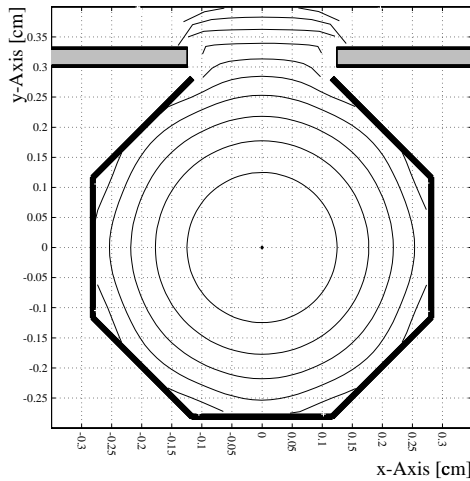


Figure 8.7: Isochrones (10 μs) for drift of positive ions away from the sense wire (offset voltage $V_G = -100$ V, bias voltage $\Delta V = 0$ V, drift field = 185 V/cm).

8.1.6 Lead-beam tests

For the lead-beam test the prototype TPC, shown in Colour Fig. XII, was mounted downstream of the Vertex II magnet of NA49 directly in front of one of the Main TPCs. The size of the prototype was $40 \times 35 \times 40 \text{ cm}^3$.

Pedestals

After complete installation of the system in the experimental area and connection to the DAQ system pedestal data (empty events, gating pulser on) were taken. The result is shown in Fig. 8.8. The noise behaviour was as expected and measured to be around 1.1 ADC counts which corresponds to ~ 2600 electrons. The baseline shows a very small systematic tendency to drop over the readout time by about 0.1 ADC counts.

Baseline stability

A qualitative impression of the baseline stability can be obtained from inspection of the signals of a single pad with the online monitor. An example is shown in Fig. 8.9. However, for a more quantitative

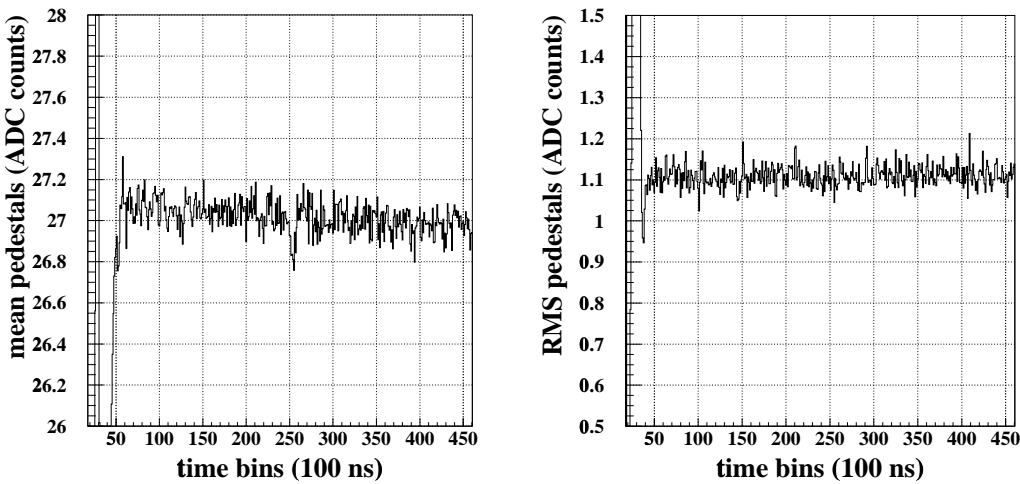


Figure 8.8: Mean value and r.m.s. of pedestals as a function of time bin (average over 128 pads from one row).

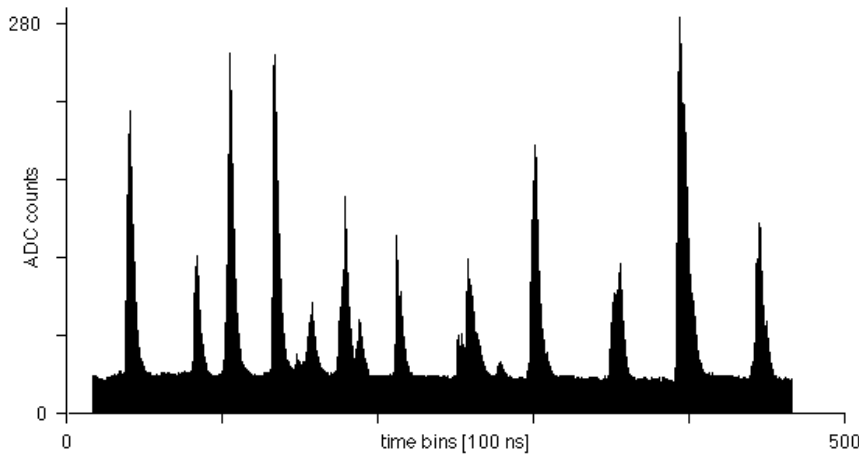


Figure 8.9: Digitized signals from one ring-cathode element recorded from a central Pb–Pb interaction (40 GeV/nucleon). The full range corresponds to 45 μs .

evaluation of the baseline stability with sub-permille resolution radioactive ^{83}Kr has to be used. Pb–Pb interactions could not be used for this purpose because of the rather high occupancy which results in more than one hit during the readout time.

8.1.7 Conclusions on RCC

The bench tests and in particular the lead-beam tests have shown that the system in general works quite well. In the following the weak and strong aspects of every component are briefly summarized.

- The **ring cathodes** work according to expectation: the coupling of the signal is found to be around 90%, i.e. about a factor 4 better than classical TPCs with field wires (NA49) and about a factor 2 better than TPCs without field wires (CERES, STAR).
- The **baseline shift** is much smaller than in classical TPCs when operated with Ne/CO₂ (NA49). Simulations suggest that a readout without field wires (CERES, STAR) though would be rather similar to the RCC. Unfortunately its baseline behaviour could not be measured over the full time range relevant for ALICE (100 μs) because of a limitation in the readout.
- The width of the **pad response function (PRF)** is as expected from the ring diameter and about appropriate for an application in ALICE. Ideally one would use a somewhat larger PRF of about 3 mm matching the expected cluster size given by diffusion. The position resolution could unfortunately not be determined in the tests.
- For the **mass production** of rings, promising techniques have been developed. However, more studies are needed to evaluate a final production scheme.
- The new gating scheme using **gating strips** instead of a wire plane works in principle quite well. Its limits in terms of electron transmission could only be determined down to the per-cent level. The behaviour at the 10^{-4} level has to be known though for ALICE applications. The closing properties for positive ions have not been measured. From simulations it is concluded that for Ne/CO₂ gas it is not possible to close the gate while the positive ions are still inside the ring cathode. Owing to the high drift velocity the positive Ne ions pass the opening after around 70 μs . The gate opening time in ALICE will be 100 μs , therefore the present gating scheme needs to be optimized to ensure that no positive ions enter the drift volume.

8.2 GEM-based readout chambers

8.2.1 Principle of operation of GEMs

Essentially, the Gas Electron Multiplier (GEM) is a double-sided metallized Kapton foil perforated with holes typically of 70 μm diameter and 140 μm pitch [8]. The application of a potential difference across the foil creates a high field region in the holes and enables the collection, amplification and transfer of ionization electrons as illustrated in Fig. 8.10. A cascaded structure of several foils produces a high effective gain at a relatively low amplification of a single foil. Differently from wire chambers, the signal is produced by the motion and collection of electrons, which are produced in the last foil above the anode pads. Ions do not contribute to the signal thus avoiding the tail cancellation problem. Furthermore, the lateral size of the charge cluster collected on the pads (the PRF) is predominantly determined by the diffusion in the gas and not by the readout geometry. The feedback of positive ions into the drift volume is suppressed to 10^{-1} – 10^{-2} by the GEM structure itself [9].

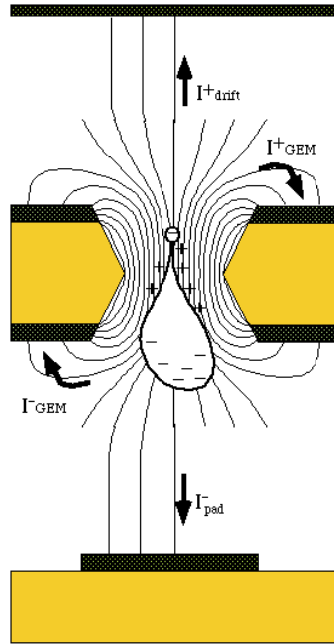


Figure 8.10: Schematic view of the amplification principle in a GEM hole.

8.2.2 Basic properties of GEMs relevant for TPC readout chambers

8.2.2.1 Gain and electron-collection efficiency

Electron amplification of a factor of $> 10^3$ for a single GEM foil has been observed. Hence a gain of 10^4 is possible for moderate amplification voltages ΔU in a double GEM set-up. Our measurement (Fig. 8.11) shows, in agreement with Ref. [10], that a gain $> 2 \times 10^4$ is reached at a voltage $\Delta U = 425$ V in each of the GEM foils. Another important entity, which depends on the value of the drift field, is the transparency of the GEM, in other words the collection efficiency for primary electrons. At TPC operating conditions ($E_{\text{drift}} \approx 200\text{--}400$ V/cm) the collection efficiency was measured to be around 95% [9, 11].

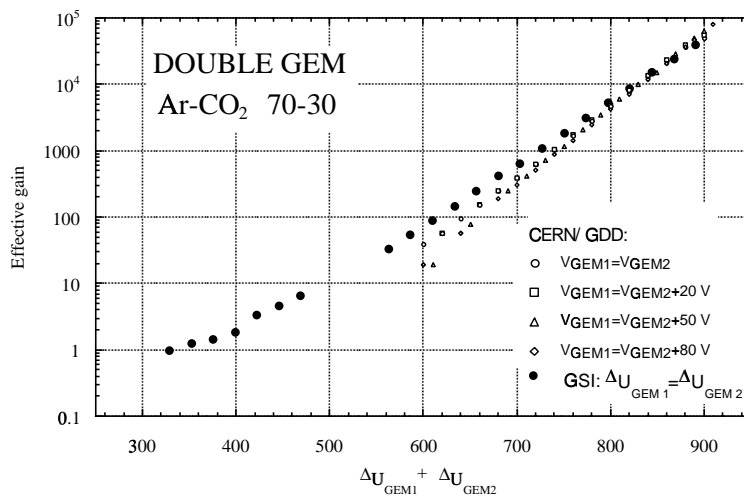


Figure 8.11: Comparison of the effective gains achieved in various GEM configurations at CERN (open symbols [10]) and at GSI (closed symbols [12]).

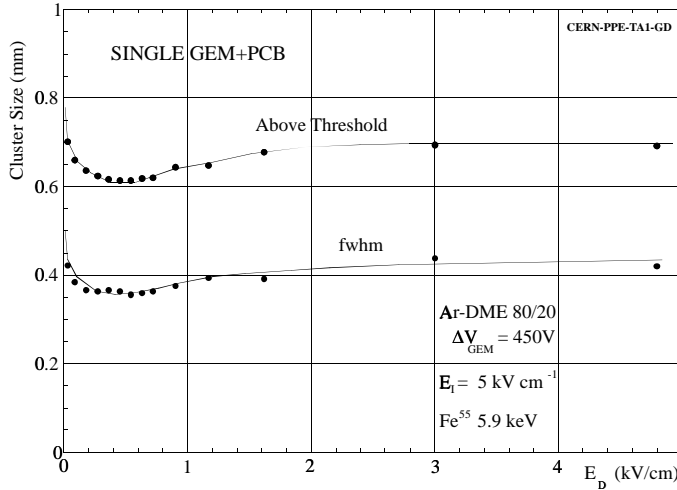


Figure 8.12: Dependence of the cluster size on the drift field for a single GEM detector, operated at constant gain and induction field.

8.2.2.2 Pad response function

Differently from conventional wire chambers, the signal for a GEM stems mainly from the electrons collected on the pad (assuming the appropriate integration time of the amplifier). This suggests that the cluster size, and hence the PRF, is dominantly given by diffusion of the electron cloud during the drift. The measured cluster size (at the base above threshold and FWHM) as a function of the drift field for a given induction field (5 kV/cm) and gap (2 mm) is shown in Fig. 8.12. The typical behaviour of diffusion in argon-DME is found, with a minimum cluster size of 0.35 mm (FWHM) around 500 V/cm [13], indicating that the spread of the electron cloud by the GEM intrinsic properties is negligible relative to the diffusion contribution in the ALICE TPC. This, however, means that the $r\phi$ -resolution is worse for short drift distances (< 50 cm), i.e. when the lateral size of the electron cloud becomes comparable to the pad width.

8.2.2.3 Energy resolution

A pulse-height spectrum from a ^{55}Fe source measured in a double GEM structure in conjunction with a field cage is shown in Fig. 8.13. The detector was operated in this case with an 90% Ar, 10% CO_2 mixture and was illuminated with 5.9 keV photons perpendicular to the drift direction. The spectrum exhibits an energy resolution of $\approx 23\%$ FWHM. This resolution is comparable to standard wire-chamber readout.

8.2.2.4 Ageing

Ageing measurements have been performed for GEM–MSGC structures and did not show any deterioration of detector gain up to 15 mC/mm^2 wire accumulated charge [14]. A priori, however, it is not clear whether this behaviour holds as well for double GEM structures operated for high gains, where high charge densities occur in particular at the second GEM foil. In order to investigate the ageing behaviour at high gains a double GEM [gas: 70% Ar, 30% CO_2] was irradiated with an intense ^{55}Fe source for about four weeks corresponding to an integrated charge of 0.7 mC/mm^2 [15]. This corresponds to about 10^2 years of ALICE heavy-ion operation. In summary, we can state that, within the accuracy of the measurement, no significant drop in gain has been observed. Inspection of the GEM foils under an electron microscope shows no deposits from polymerization; the occurrence of Newton rings, however,

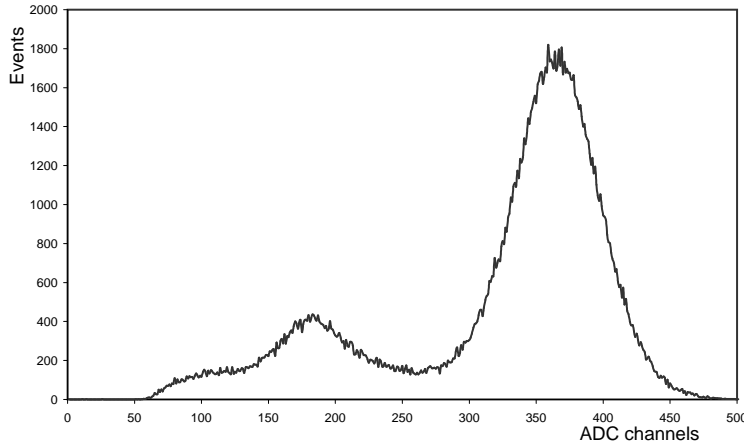


Figure 8.13: Pulse-height distribution for 5.9 keV photons in a 90% Ar, 10% CO₂ gas mixture obtained with a double GEM detector in conjunction with a field cage.

indicates the build-up of a thin ($\approx \mu\text{m}$) polymer film. The conclusion, which can be drawn from this relatively simple test, is that the observed ageing behaviour would not preclude the use of GEM foils from an application such as ALICE-TPC readout chambers.

8.2.2.5 Ion feedback

Because of the asymmetric electric fields above and below a GEM foil the transmission for ions and electrons is different, i.e. ions created in the amplification zone are preferentially directed towards the upper layer of a GEM foil (Fig. 8.10 on page 181). This feature could, in case the ion feedback is suppressed to a level of 10^{-4} , avoid a gating grid.

The ion feedback relative to the electron signal has been measured by comparing the currents on the readout pad and the GEM cathode [9]. It was found that for symmetric operation of a double GEM (both GEMs at the same ΔU of 450 V) the ion feedback is of the order of 5%–10%, depending on the details of the operating conditions, i.e. the drift, transfer and induction field settings as shown in Fig. 8.14. This value could be improved for a — less desirable — asymmetric operation of the two GEM foils (e.g. $\Delta U_{\text{GEM}1} = 350$ V and $\Delta U_{\text{GEM}2} = 550$ V) to a level of $\approx 1\%$ [10].

8.2.2.6 Sparking

High-gain operation involves also for GEMs high charge densities (in particular from slow, highly ionizing particles) which could lead to sparks. These sparks could be harmful as they might destroy the GEM foil. In fact, discharging the large capacity of a $10 \times 10 \text{ cm}^2$ GEM foil leads to amplitudes (measured at $1 \text{ M}\Omega$ directly at the pad) of more than 60 V.

Figure 8.15 shows the spark rate without source for different voltages. The spark rate is a rather steep function of the applied voltage and is of the order of one spark per hour at a total voltage of $\Delta U_{\text{GEM}1} + \Delta U_{\text{GEM}2} = 900$ V. It seems to saturate at above 960 V at a rate of about 3 Hz. A random spark rate of the order of several sparks per hour is also reported from CMS [16], Hera-B [17] and in Ref. [18]. In order to simulate a worst-case scenario we irradiated a double GEM with an intense alpha source (²⁴¹Am, 5.4 MeV). We find a spark probability per incident alpha particle of the order of 10^{-3} (see Fig. 8.16) when the alpha particle is stopped close to the GEM foil, i.e. when the ionization density corresponds to the Bragg peak. The spark probability decreases by two orders of magnitude if the source is positioned such that the energy loss close to the foils is smaller.

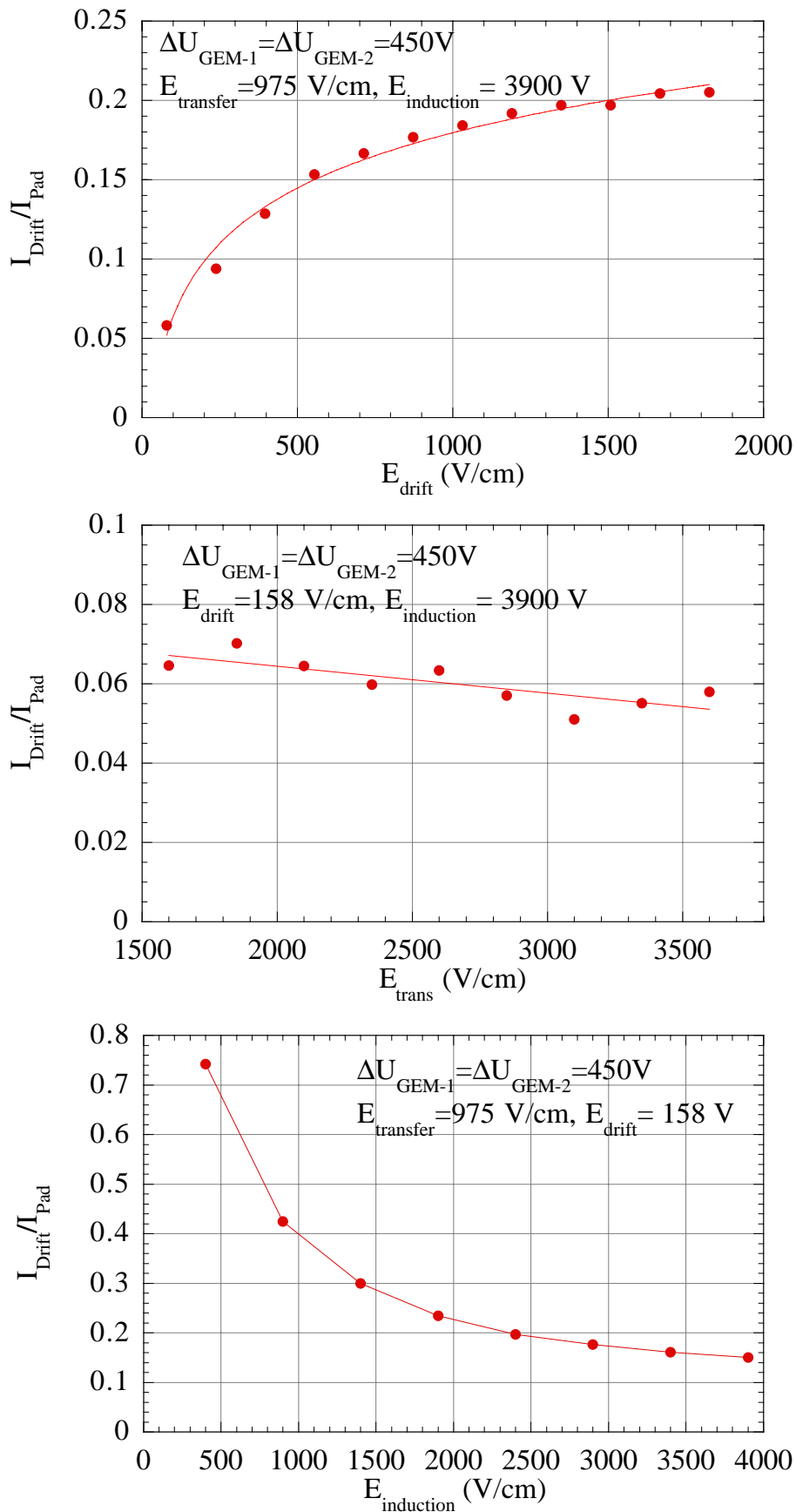


Figure 8.14: Ratio of ion current to electron current as a function of drift (top), transfer (middle), and induction (bottom) fields.

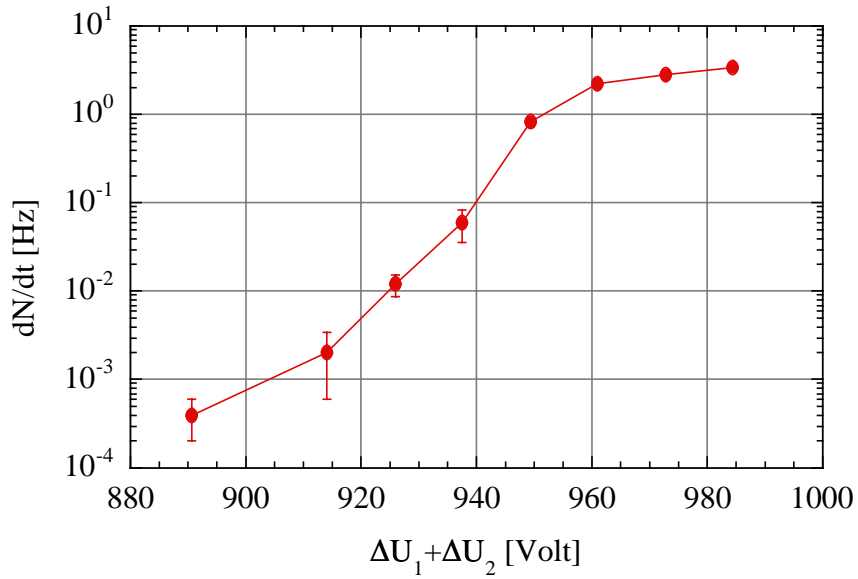


Figure 8.15: Sparking rate without source as a function of high voltage.

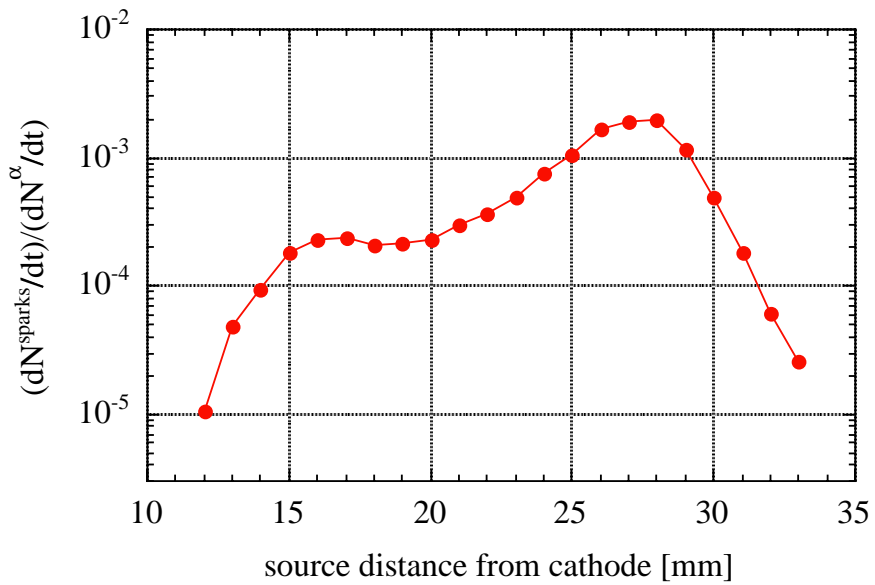


Figure 8.16: Spark probability per incident alpha particle as a function of distance of the source from the cathode at a voltage across each GEM foil of $U = 457$ V.

8.2.3 Conclusions on GEMs

The measurements clearly indicate that additional gating is mandatory for the application of a GEM as TPC readout chamber in order to reach the required suppression of ion feedback into the drift region. Both the gain achieved and the primary-electron collection efficiency do not indicate any severe problems with respect to a potential application as TPC readout chamber. An integrated charge corresponding to about 10^2 years of ALICE heavy-ion operation has been accumulated without any observable deterioration of the chamber performance. The observed ageing behaviour would thus not preclude the use of GEM foils as TPC readout chambers. We measure a moderate background spark rate of $10^{-4} - 10^{-3}$ Hz (per 100 cm^2 foil) at TPC operating conditions. The irradiation with slow alpha particles yields 10^{-3} sparks per alpha particle. The large capacity of the GEM foil gives rise to very large amplitudes in case of a spark. This might have a destructive impact on the GEM foil itself. Moreover, these energetic sparks could produce unfavourable conditions for the front-end electronics or other detectors in a densely packed experiment. Generally, the GEM holds as a potential alternative to conventional readout chambers. However, for a large-scale application more experience, in particular about the long-term effects of sparks, is mandatory.

9 Installation, slow control and safety

9.1 Implementation and infrastructure

9.1.1 ALICE experimental area

The ALICE detector will be installed at Point 2 of the LHC accelerator: the experimental area designed for the L3 experiment. The main access shaft, 23 m in diameter, provides a $15 \times 7 \text{ m}^2$ installation passage and space for counting rooms. The counting rooms are separated from the experimental area by a concrete shielding plug (see Fig. 9.1). The experimental cavern is 21.4 m in diameter and will be re-equipped with a $2 \times 20 \text{ t}$ crane having a clearance of about 3 m over the L3 magnet.

The L3 magnet provides a 11.6 m long and 11.2 m diameter solenoidal field of up to 0.5 T. The end-caps have a door-like construction. The door-frames will support large beams traversing the L3 magnet, from which the ALICE central detectors will be supported.

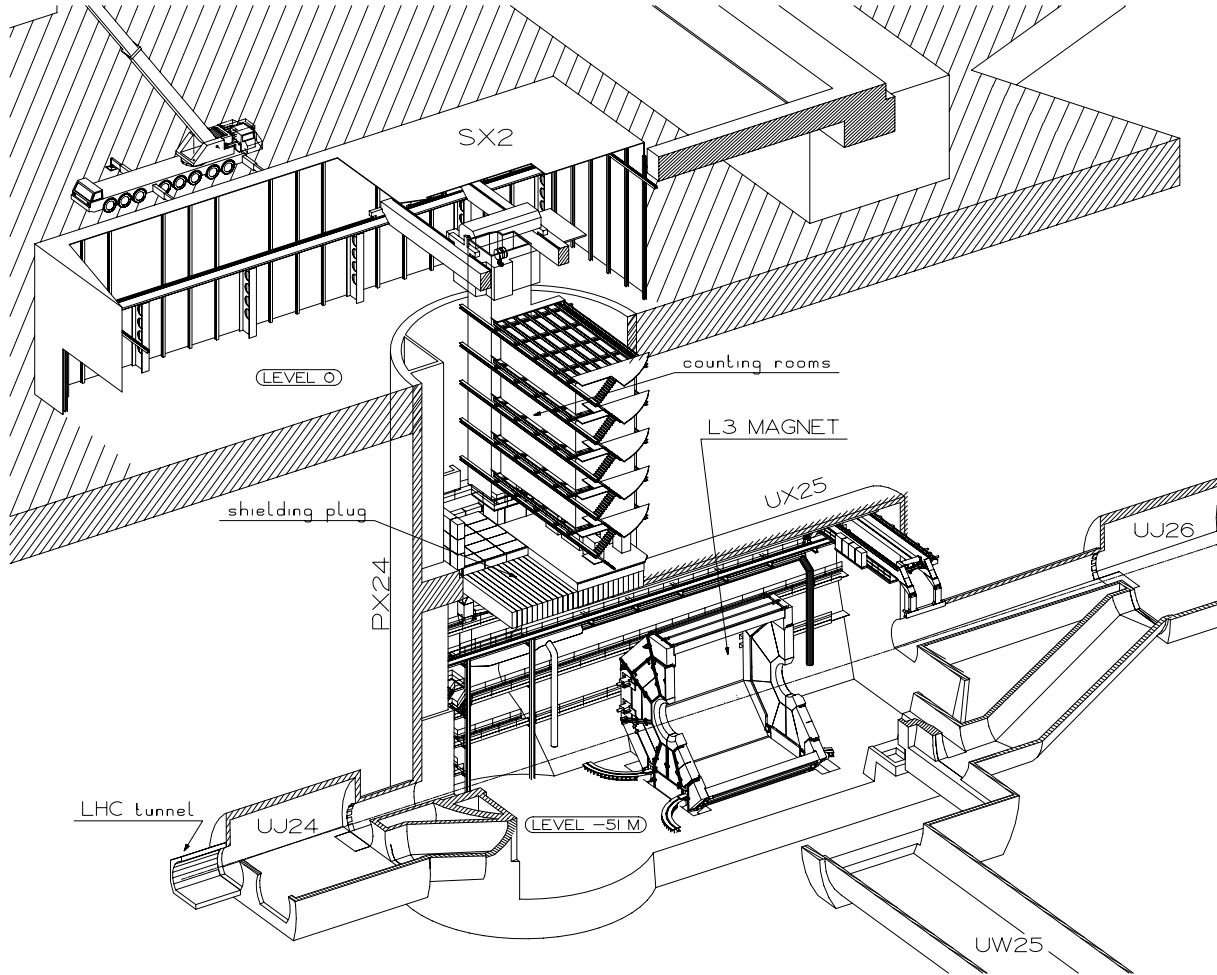


Figure 9.1: General layout of the basic underground structures at Point 2, showing the L3 magnet and the counting rooms.

9.1.2 Implementation of the TPC detector

9.1.2.1 General integration considerations

The TPC detector is supported by a cylindrical space frame construction, which also serves as a support for all the central detector units. The space frame is placed on large support beams straddling the coil section of the L3 magnet. (see Fig. 9.2). This allows the complete assembly of the central detector units outside the L3 magnet.

The overall ALICE installation scenario requires that the TPC can be displaced independently of the space frame, in order to gain access to the ITS detector and the central vacuum chamber. The TPC detector will, therefore, be supported from two rails fixed to the space frame, which can be prolonged outside the space frame.

It is conceivable that the complete space frame, with the TPC detector installed, is lowered down as one unit into the experimental area. However, the present installation scenario foresees a separate installation of the TPC detector.

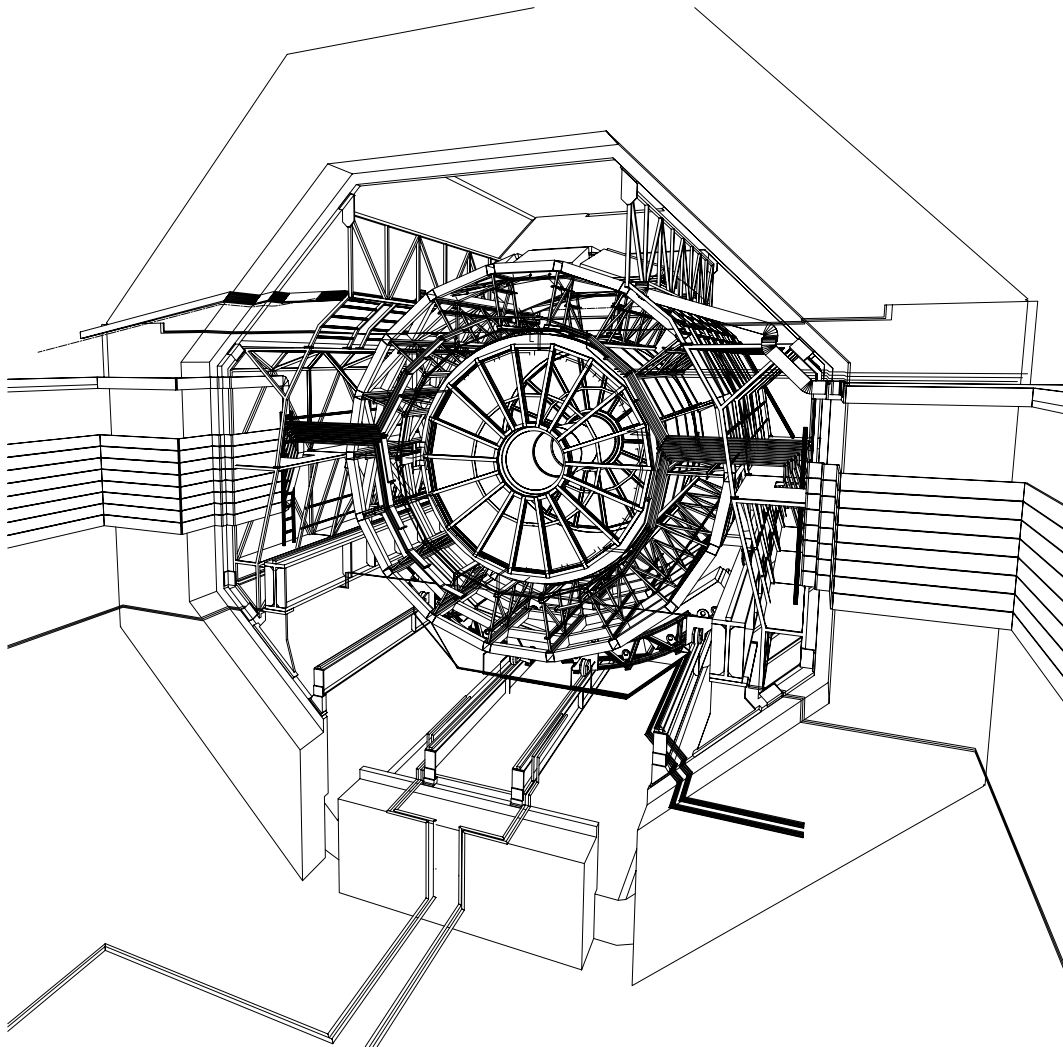


Figure 9.2: General view of the TPC detector and the space frame inside the L3 magnet.

9.1.2.2 The space frame

The space frame is divided into 18 sectors of 20° following the agreed sectorization of the central detectors. All material has been concentrated at the sector boundaries and two concentrically placed support rings as indicated in Fig. 9.3.

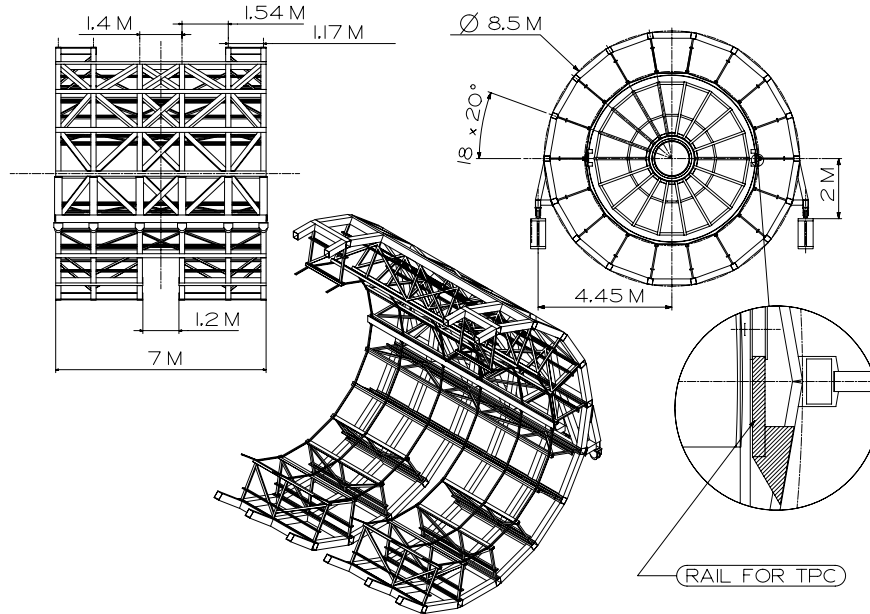


Figure 9.3: General layout of the space frame showing the position of the TPC support rails.

The frame is supported on two support beams. There are two support points on each beam, which assures the same vertical displacement of the frame and the beams at all support points. The horizontal displacement of the frame is blocked on one side and free to move on the other side. The support beams are 12.1 m long and supported at their extremities by the L3 door structure.

The combined space frame and support beam structure has been calculated for a total load of 50 t [1]. The calculations were based on reducing the deformation of any two points on the space frame to a few mm and limiting the overall vertical displacement to < 5 mm. Furthermore, the support members of the frame in front of the PHOS and HMPID detectors were removed¹ in order not to introduce any additional material in the acceptance of these detectors.

The calculations show that the movements of the TPC support rails can be limited to 4 mm in the vertical direction and 5 mm in the horizontal direction, with a corresponding highest stress level of 140 MPa. The total weight of the space frame is 14 t and each support beam has a weight of 11 t.

9.1.2.3 Pre-assembly phase

The present surface zone at Point 2 includes sufficient assembly hall space to meet the ALICE requirements and no new hall construction will be necessary for the detector assembly. The overall ALICE schedule foresees a pre-assembly phase for the complete TPC detector in the SXL2 assembly hall prior to the installation in the underground area, as indicated in Fig. 9.4. The detector will be fully assembled together with the space frame structure. This will allow an early preparation of the various detector services and permit the installation and access scenarios to be analysed and corrected before lowering the TPC into the experimental cavern. All handling of the TPC outside the space frame will be done using a transport frame. The transport frame will allow the TPC to be transported to Point 2 and will also be used during the installation of the TPC into the space frame.

¹A decision about the existance of holes in the space frame will be taken in spring 2000.

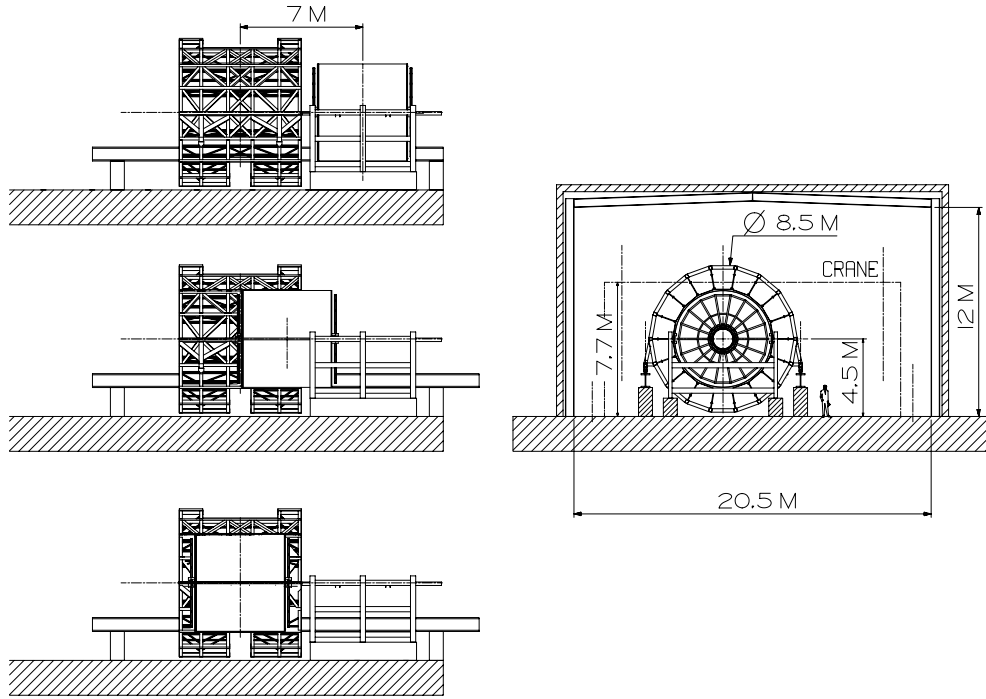


Figure 9.4: Pre-assembly of the TPC in the SXL2 assembly hall at Point 2. The left part of the figure shows the TPC being moved from the transport frame to the space frame.

9.1.2.4 Installation in the underground cavern

The ITS detector is located inside the inner aperture of the TPC and held in place by the inner containment vessel. This will allow stable alignment between the two detectors and avoids introducing a special support structure for the ITS detector.

Before proceeding with the installation of the TPC it is necessary to install the space frame into the L3 magnet volume and complete the installation of the Dipole magnet and the absorber structures. At this stage the TPC, supported by the transport frame, can be lowered down into the experimental area and placed on the extension rails used for the installation of the space frame, as indicated in Fig. 9.5.

The TPC will be positioned about 4.5 m away from the intersection point and a set of rails will be fixed to the inner containment vessel Fig. 9.6. This will allow the ITS and the vacuum chamber to be installed. A detailed description of the installation of the ITS detector and the fixing to the TRD can be found in the ITS TDR [2].

Once the installation of the ITS and vacuum chamber is complete the TPC will be moved over the ITS into its final position, where the ITS will be fixed to the TPC. This is achieved by a set of eccentric levers, accessible from the outside, which transfer the support points of the ITS from the rails to the TPC inner vessel.

9.1.3 Access, maintenance and services

9.1.3.1 Access for maintenance and repair

Access for maintenance to the various parts of the TPC detector is relatively straightforward. Both readout planes and support wheels are easily accessible from the platforms placed at several levels on both sides of the space frame. The access platforms will be equipped with support points for the chamber extraction tools. The installation or removal of a readout chamber, particularly on the absorber side, must however be regarded as relatively complicated and time consuming. All access to the ITS detector or the region between the ITS and the front absorber will necessitate a displacement of the TPC.

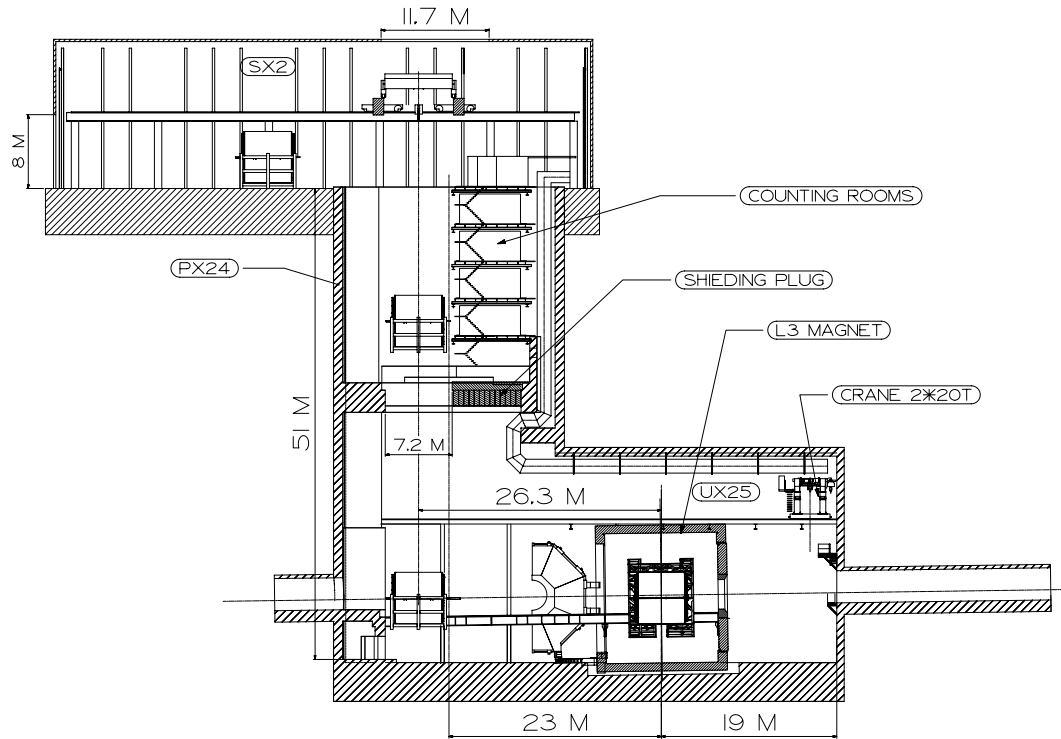


Figure 9.5: Lowering the TPC detector into the experimental area. It should be noted that the access shaft has a maximum opening of 15.0 m × 7.2 m.

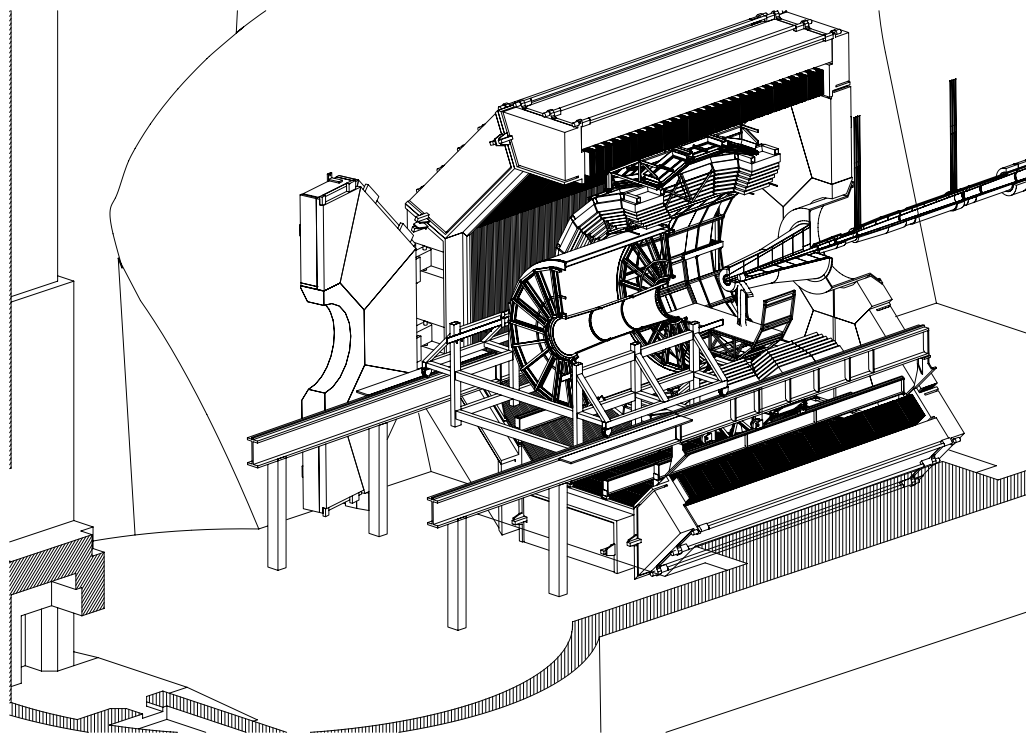


Figure 9.6: Position of the TPC detector during installation of the ITS detector and the vacuum chamber.

9.1.3.2 Services

The TPC services are described in Chapter 3. All services will have to pass through the narrow chicane-shaped clearance (100 mm) between the magnet doors and the door frames (Fig. 9.7). In order to install the services the door will have to be opened, which prohibits any further service installations on the absorber side, once the Muon spectrometer is installed.

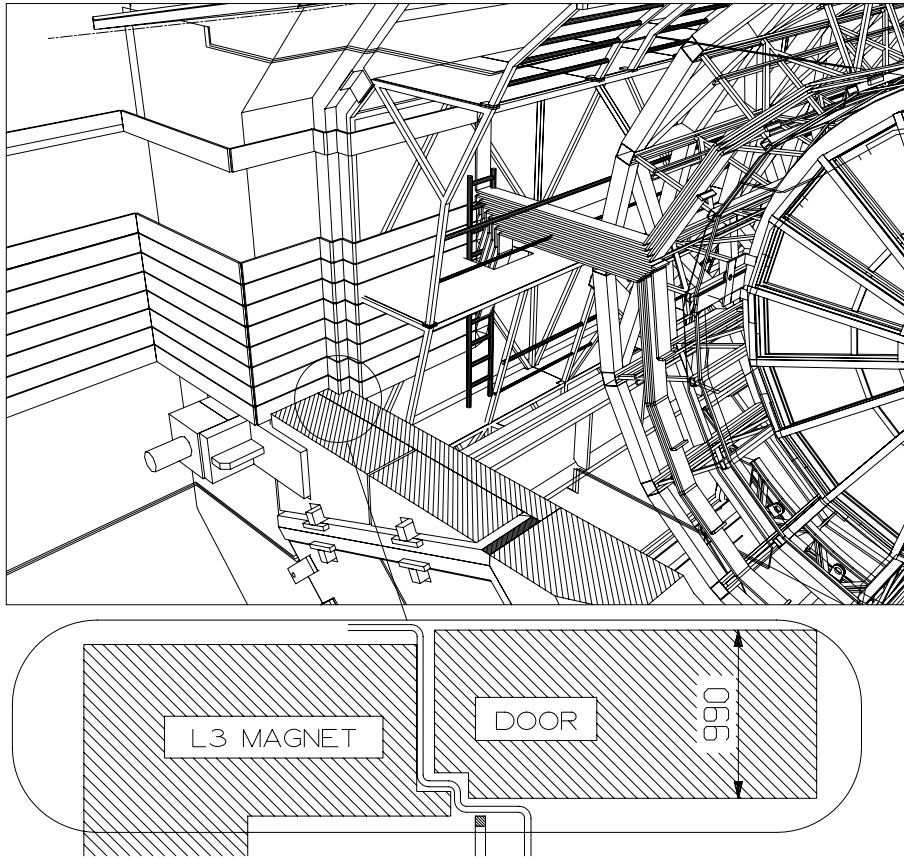


Figure 9.7: Routing of cables from the central detectors through the gap in the L3 magnet doors.

The gas supply will come from the existing surface building, and the distribution units will be located on the shielding plug in PX24.

To keep the losses and cost of cable installation to a minimum the racks for the power supplies will be installed as close as possible to the L3 magnet. They will be located at both sides of the L3 magnet at floor level, as indicated in Fig. 9.8. Monitoring of the power supplies will be carried out remotely from the control room, since access to the power supplies will not be possible during LHC operation.

In the event of a displacement of the TPC detector all services will have to be disconnected. This is facilitated by installing ‘patch-panels’ on the support wheels. An alternative possibility would be to arrange all services in ‘garlands’, which would avoid any disconnection. This possibility has, however, not yet been studied.

9.1.4 Assembly and installation schedule

The installation of the TPC detector is integrated with the general schedule for the ALICE project. Figure 9.9 shows the overall schedule for the TPC project. The TPC will be pre-assembled in the SXL2 assembly hall at Point 2 between August 2003 and June 2004, and the installation in the experimental area will take place in September 2004.

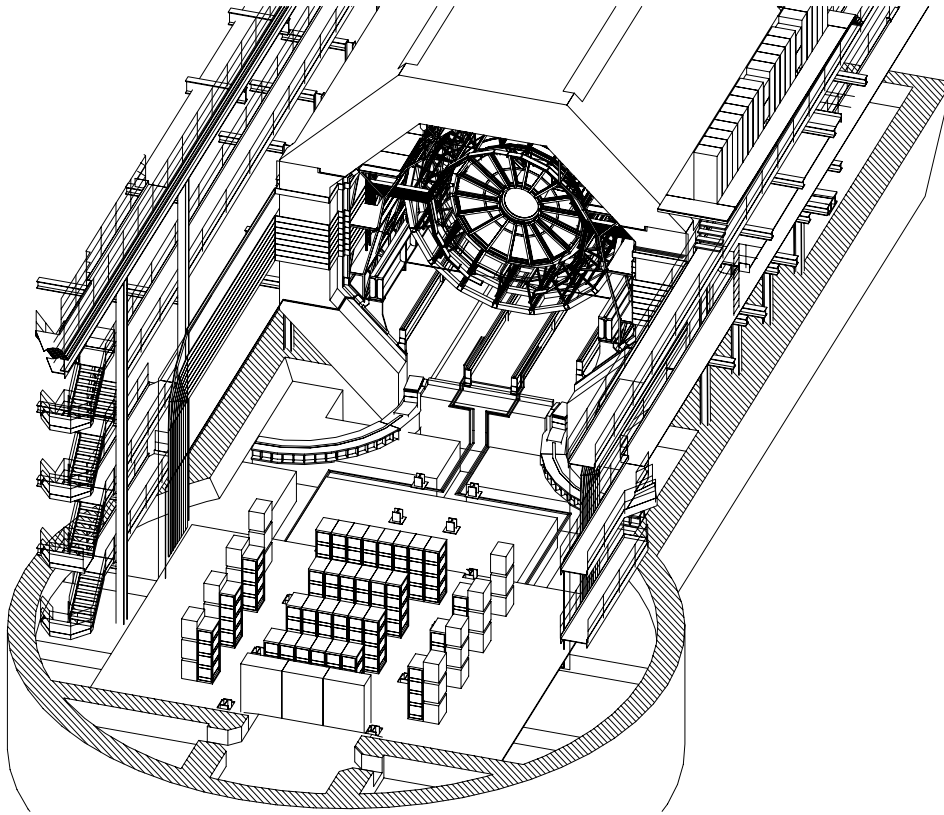


Figure 9.8: Principal routing of services, showing the position of the racks in front of the L3 magnet. The Muon platform and L3 magnet door structures are not shown.

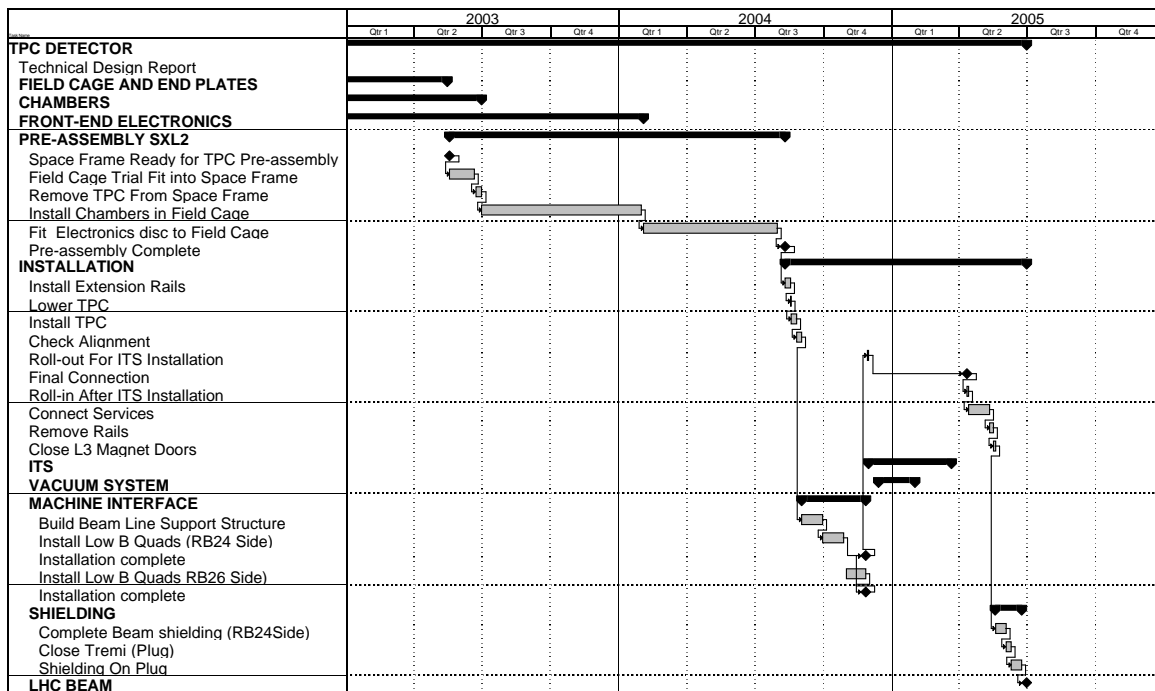


Figure 9.9: Overall schedule for the TPC assembly and installation.

9.2 Slow control

The ALICE Detector Control System (DCS) is responsible for the monitoring and control of the correct operational conditions of the subdetectors. As this task also involves safety aspects, the hardware links used are independent of the DAQ. The ALICE DCS is presented in Ref. [3] and will be described in detail later in the ALICE Computing Technical Proposal. Its functionalities include (see also Ref. [4]):

- starting or shutting off a detector, or components of a detector, in a controlled way;
- monitoring of characteristics (analog and/or status values) which are necessary for detector operation and/or the physics data analysis;
- reporting of alarm conditions;
- logging and archiving of characteristics, alarms and operator interactions;
- retrieving archived data for trend displays or detector analysis;
- uploading and downloading complete events to and from the front-end (see Section 5.1.6).

In addition, interactions are required with a number of external systems like the area safety system, cooling and ventilation system, electricity mains supply, LHC, and magnets. However, these systems, with the exception of the magnets, will only provide informative links to the DCS. Such functionalities have to be implemented in two operating conditions.

- During normal physics data-taking the DCS will control starting and operation of all the ALICE subdetectors. For this purpose standard operator commands will be available. Malfunctioning will be signalled through centralized alarms and to the detector-dedicated control station.
- During installation and/or maintenance periods it will be necessary to run different detectors, or partitions of them, separately but simultaneously. In this case interference among detectors or between them and external services must be screened.

To satisfy the above requirements the DCS architecture will have two essential features –scalability and modularity– and will be based on distributed intelligence. The slow control system will be designed and organized in layers, corresponding to different levels of visibility and access rights. The higher levels will have a more global view, and will only be allowed to make a limited set of macroscopic actions. At the other end, lower layers will have access to more detailed information and control. At the highest level of the experiment a Supervisory Control layer will provide the communications among the main ALICE subsystems such as: the Data Acquisition Control (DAQC), the Trigger Control (TRC) and the DCS. The DCS will be accessed through the Supervisory Control layer and no peer-to-peer connection between DCS and DAQ is envisaged. The Supervisory Control will have the following features.

- It will provide a global view of the whole experiment to the operator.
- It will allow the control of the experiment through commands to the DCS, the DAQC and the TRC. It will be capable of generating the sequence of operations in order to bring the experiment to a given working condition. However, detailed actions will be the responsibility of the subsystems.
- It will collect and dispatch all the communications between the subsystems.
- It will monitor the operation of the subsystems, generate alarms, and provide the interlock logic where necessary.

- It will allow the dynamic splitting of the detector into independent partitions and the possibility of concurrent data-taking from the partitions.

Hardware protection of TPC components will be implemented wherever possible. This is the case, for example, for the ramp-down of sense wire high voltages in the presence of sustained over-currents.

9.2.1 Hardware

As for the general ALICE DCS, the hardware structure of the TPC DCS will include three layers.

- **Process layer.** This is the layer of field instrumentation such as sensor heads, actuators, etc. The field instrumentation has to comply with the requirements of the detector hardware. However, the interfaces to the control equipment will follow well-established electrical standards like 0–10 V for voltage interfaces or 4–20 mA for current-loop interfaces. The signals to be monitored for the TPC detector are listed in Tables 9.1 and 9.2.
- **Control layer.** This corresponds to multipurpose-control computer equipment of the PLC (Programmable Logic Controller) type, in compliance with the relevant recommendation [5]. However, wherever convenient in the case of a large number of field-instrumentation channels to be controlled, VME-based controllers may be used. This hardware layer also includes self-contained intelligent instruments like high- and low-voltage power supplies.
- **Supervisory level.** The equipment on this layer consists of general-purpose workstations which will be linked to the control layer through the TCP/IP. The workstations will provide the Man-Machine Interface (MMI) to the DCS and will behave as server stations for detector monitoring and data logging, or as client stations for detector control. At the level of general supervisory control, the workstations will be dedicated to the management of configuration data for all the detectors and equipment, partitioning, alarms, logging and archiving, and data communication.

9.2.2 Communication

The data transmission links can be categorized in layers equivalent to the hardware architecture. At the field-instrumentation level, point-to-point links for voltage or current signals will be the general case. An exception will be the large number of FEE temperature sensors (two per board, i.e. 9360 in total), which are read by dedicated on-board ASICs. Similarly, the voltage for the FEE is regulated on-board. The ASICs will be connected to the controller level via one of the proposed standard fieldbuses. This does not change the hardware architecture since the bus system will be seen as an extension of the controller station. In addition it is foreseen to allow the up- and download of complete events to and from the FEE via the DCS interface (see Section 5.1.6). This provides the ability to test the entire TPC without invoking the general DAQ. The connection between different subsystems will be established by a fieldbus or a dedicated LAN which is also connected to the supervisory level. Access to the equipment will be allowed from remote locations. However, access restrictions are planned depending on the locations in order to avoid conflicts.

9.2.3 Software

The controller-level software, which will reside in the control computers that are directly linked to the process, will be configured individually for each subdetector. For development and maintenance of the detectors each group will also configure a personalized MMI. This software will be based on the same product(s) as for the ALICE DCS system and will therefore allow integration in the overall system during operation of the experiment and, separate access and control of each subsystem during other periods. It

Table 9.1: Main parameters of the Detector Control System for the TPC.

Systems/sub-systems	Location	Controlled parameters	Number	Link type	Parameters	Control
FEE cooling	UX25	inlet and outlet liquid-coolant temperature inlet and outlet liquid-coolant pressure liquid-coolant valve control gas temperature temperature threshold for cooling alarm pressure threshold for cooling alarm	36	analog analog analog analog analog analog	temperature pressure voltage temperature voltage voltage	R/W R/W R R/W R/W R/W
	UX25 end-cap pad plane		4 72 2			
	UX25 UX25 PX24		2 1			
FEE control	detector detector detector detector	FEE temperature FEE voltage regulation interface (status, exceptions, pedestals, events) board on/off	2 × 130 × 36 3 × 130 × 36 130 × 36 1	bus bus bus bus	temperature current complex bit pattern	R R/W R/W on/off
	UX25 UX25 UX25 PX24	FEE power supply FEE power supply temperature FEE power supply status/enable word safety switch	2 × 36 2 × 36 2 × 36 1	serial analog serial binary	current temperature bit pattern voltage	R/W R R/W on/off

Table 9.2: Main parameters of the Detector Control System for the TPC, cont'd

Systems/sub-systems	Location	Controlled parameters	Number	Link type	Parameters	Control
Thermal screen	detector	thermal screen plate temperature	72 + 36	analog	temperature	R
	detector UX25	inner-cylinder temperature	18	analog	temperature	R
	UX25	inlet and outlet liquid-coolant temperature	2 × (72+36)	analog	temperature	R/W
	PX24	liquid-coolant valve control	72 + 36	analog	voltage	R/W
Field cage HV	drift volume	gas temperature	72	analog	temperature	R
	UX25	safety switch	1	binary	voltage	on/off
	UX25	HV supply on/off	1	serial	voltage	R/W
Readout chambers	UX25	HV settings and readings	1	serial	complex	R/W
	UX25	external resistors	4	analog	voltage	R
	UX25	safety switch	1	binary	voltage	on/off
Gas system	PX24	HV supply on/off	1	serial	voltage	R/W
	PX24	HV settings and readings	1	serial	complex	R/W
	PX24	safety switch	1	serial	voltage	on/off
Detector	PX24	primary inlet and outlet gas temperature	2	analog	temperature	R
	PX24	primary inlet and outlet pressure	4	analog	pressure	R
	PX24	primary inlet and outlet gas flow regulation	2	analog	flow	R
	PX24	safety switch	5	serial	complex	R
	PX24	purity control	1	serial	voltage	on/off
	detector	primary inlet and outlet gas temperature	2 × 18	analog	complex	bit pattern
	detector	primary inlet and outlet pressure	2 × 18	analog	temperature	R
	detector	primary inlet and outlet gas flow	2 × 18	analog	pressure	R

is planned that the driver software for the controller stations to interface the field instrumentation to the ALICE DCS architecture will be based on the OPC [6] standard. OPC, i.e. Object Linking and Embedding (OLE) [7] for Process Control allows Windows applications to access control data in a controlled way. It means that hardware and applications from different manufacturers can be connected more easily. OPC is currently being evaluated in the context of the CERN JCOP project. It is based on the Microsoft technology DCOM (Distributed Component Object Model) and provides a standardized access method and unified interface between the field level and a SCADA (Supervisory Control And Data Acquisition) system or office applications running under Windows. It is therefore possible, for example, for an Excel macro to read data from a PLC via the OPC Interface and to display it graphically. The OPC interface standard is defined and developed by the OPC Foundation which includes the major companies in the automation sector (Siemens, Fisher-Rosemount, National Instruments, Rockwell Software, et al.). A wide range of OPC servers and applications is already available and additional companies have announced their adherence.

9.3 Safety and quality management

9.3.1 Mechanical

In the bidding process a detailed set of specifications for the TPC cylinders and end-plates will be proposed to the manufacturer. This will contain appropriate conditions in order not to increase the prices inordinately with respect to choice of material and very extensive testing by the manufacturers. As a matter of production follow-up, dimensional checks will be carried out at any point during the construction and prior to shipment and delivery to CERN. The supplier is expected to be capable of working to quality assurance standard ISO 9001 or an equivalent national standard.

Although the TPC detector will be operated at a pressure of 1 mbar above atmospheric, the vessels are designed for a maximum over-pressure of 5 mbar.

9.3.2 Gas

In addition to adherence to mechanical tolerances, the fabrication, finishing, and choice of materials must ensure an adequate gas purity in order to run the detector with the desired performance and within operational cost. Excessive leaks lead to intolerable gas flows and the injection of fresh gas. It is therefore foreseen that detailed leak tests will be performed at the constructor's site with a complete trial assembly of the detector. The procedure of these tests is described in Section 3.1.2.6.

All the gases used in the TPC are nonflammable. However, because of its large volume, the drift vessel will have to be flushed with air prior to any intervention - such as replacing a readout module - which involve opening the detector in order to avert an oxygen deficiency situation in the environment. The use of a moderate dose of a short-lived gaseous isotope (200 MBq, half-life 1.9 h) complies with the existing rules of radiation protection. As far as the containment vessels are concerned, redundant and stand-alone safety mechanisms have been implemented in order to protect the TPC from under- or over-pressures.

9.3.3 Radiation protection

The two main mechanisms that may induce radioactivity in the TPC are low-energy neutron activation and inelastic hadronic interactions at high energy. The maximum neutron fluences over a period of ten years at the inner and outer radii of the TPC are $3.5 \times 10^{11}/\text{cm}^2$ and $1.1 \times 10^{11}/\text{cm}^2$, respectively. Scaling from the equivalent dose rates induced by the high-luminosity pp interaction regions [8] to those of the ALICE experimental conditions (approximately a factor of 100 lower), we do not expect any radiation hazards to be caused by the accumulation of radionuclides in the TPC.

9.3.4 RF shielding

Both surfaces of the inner and outer TPC containment vessels are coated with a $\sim 50 \mu\text{m}$ thick layer of aluminium foil. Thicker metallic shielding is incompatible with our requirements for a low-mass structure for the TPC.

9.3.5 Electrical system protection

9.3.5.1 High voltage for the field cage

When assessing the risks of operating the very high-voltage circuitry of the TPC field cage, it becomes evident that any component failure in the system must automatically lead to high-voltage shut-off. On the other hand, the possibilities to recognize component failure are very limited, usually restricted to measuring the current through the voltage divider resistor chain. For example, shorted paths and connections are recognized when there is an increase in the divider current, whilst open connections are indicated by a decrease of current. In both scenarios the HV supply system will be shut down before corrective action can be taken.

Given the limited access and the mechanical fragility of the system, it is also clear that corrective measures to the voltage divider network itself are extremely difficult, if not impossible, to make. Since in situ interventions on the resistor chain are basically excluded, the voltage dividing network inside the resistor rod must be very robust and undergo stringent quality control and test procedures prior to its installation. Therefore, every single component (e.g. the resistors), and each stage during the assembly of the rod are carefully inspected and tested. Upon completion of the work the entire resistor rod will be operated above nominal rating ($> 100 \text{ kV}$) and burnt in by thermal cycling for several weeks. Furthermore, as outlined in Section 3.1.2, the voltage dividing network will be tested at regular intervals during assembly.

9.3.5.2 High voltage for readout chambers

The readout chambers require an operating voltage of around 1700 V. For the outer sectors two separate voltages are foreseen, whereas the inner sectors require only one voltage. In total, 108 supply lines are needed. The installation is based on standard coaxial high-voltage cables rated for 3 kV, together with standard high-voltage connectors.

Standard, remotely-controlled power supplies with voltage and current monitoring will be used. If an over-current is detected, the corresponding voltage will be ramped down at a preset rate. No parts of the readout chambers under high voltage are accessible once the chambers have been installed. Therefore, no special provisions such as interlocks are foreseen.

9.3.5.3 Low voltage

The front-end electronics of the TPC is a typical low-voltage high-current system (about 21 kA in total), which may run the risk of fire in case of uncontrolled currents. To avoid any danger to the TPC and its readout system, the following strategy has been adopted.

Firstly, the power supplies themselves are ground-free. The ground reference is obtained only at the detector side. This avoids any accidental parasitic currents in the conducting paths (not adapted to such large currents) flowing back to the power supply if one of the ground lines is broken.

Secondly, the powering of the system will be monitored by the DCS. Each front-end card provides a measurement of all the incoming voltages. If there is a voltage drop, the system can be powered down on a time-scale of milliseconds. By monitoring also the temperature of each front-end card, the DCS can react to temperature excursions, and shut off the relevant section of the system.

Furthermore, the design of the front-end cards and their connections to the ground of the readout chamber is such that the copper cross-section is sufficiently large to accommodate high current densities

(see Section 5.1.8). This would be the case if the ground return line was accidentally connected to the general ground, which would lead to a parasitic current through the TPC support structure.

9.3.6 Laser

The TPC laser calibration system uses two pulsed Nd-YAG lasers both having an energy of about 40 mJ per pulse at a wavelength of 266 nm. The lasers will be placed as close as possible to the TPC outside the L3 magnet. The laser light will be guided by a mirror system to the end-plates of the TPC. The light path will be totally enclosed by light-tight tubes. A similar light-tight system is also foreseen for the distribution of the laser light at the perimeter of the support wheel (see Section 4.3.1). The light enclosure and light paths will only be accessible to authorized personnel. Once the laser light has entered the TPC drift volume through the quartz windows no further protection is needed. All parts of the laser system will be labelled with proper warning symbols.

9.3.7 Safety aspects

The TPC detector has been the subject of a recent Initial Safety Discussion [9]. The outcome of this ISD was that the design of the TPC detector did not include any major safety risks.

The TPC detector uses nonflammable gas mixtures and the absence of toxic, corrosive, or flammable components makes the TPC an intrinsically safe detector. The operation of the two Nd-Yag lasers will be inhibited during access periods and the laser beams will be guided through steel tubes. Apart from the initial construction period the handling of the TPC will always rely on the mechanical stability of the space frame or the transport frame, which will reduce the probability of any mechanical failure.

The closed volume inside the dipole magnet and the part of the Muon spectrometer that penetrates into the L3 magnet will be separately monitored for both flammable gas and oxygen deficiency. The access to the inside of the L3 magnet will be restricted and regarded as a confined volume.

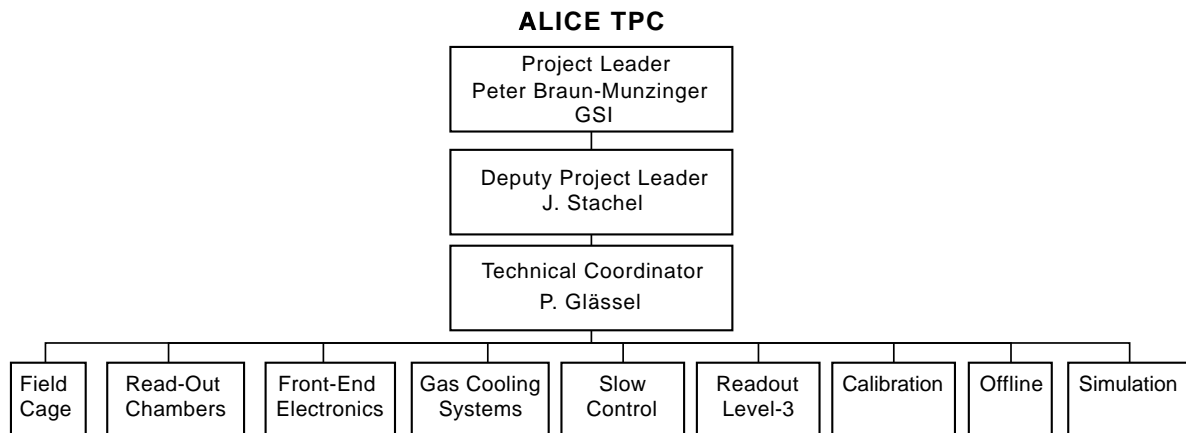
The high-voltage (> 100 kV) applied to the detector will not be accessible once it is installed in its final position, but could constitute a safety hazard during tests and stand-alone operations. An appropriate outer protection layer for the high-voltage cable will be included in the final design.

All construction materials and electronic printed circuit boards will conform to the CERN safety instruction TIS IS41 and IS23 concerning the use of plastic and other non-metallic materials at CERN with respect to fire safety and radiation resistance.

10 Organization

TPC organization

The ALICE TPC organization is constituted by a project leader, a deputy project leader and eight sections: Field Cage, Read-Out Chambers, Front-End Electronics, Gas System, Slow Control, Readout and Level-3, Test Beams and Simulation.



TPC task force

The following persons have contributed to the work presented in this Technical Design Report.

H. Appelshäuser, J. Bächler, J.A. Belikov, C. Blume, P. Braun-Munzinger, H.W. Daues, R. Esteve Bosch, Z. Fodor, P. Foka, C. Garabatos, C. Gregory, H.A. Gustafsson, J. Hehner, M. Hoch, M. Ivanov, M. Kowalski, L. Leistam, V. Lindenstruth, D. Miśkowiec, T. Meyer, L. Musa, R. Renfordt, M.J. Richter, D. Röhrich, K. Šafařík, A. Sandoval, H. Sann, E. Schäfer, H.R. Schmidt, S. Sedykh, A. Sharma, B. Skaali, J. Stachel, H. Stelzer, R. Stock, D. Swoboda, P. Vande Vyvre, R. Veenhof, D. Vranic, B. Windelband and the ALICE TA2 engineering group.

TPC TDR editorial committee

The TPC TDR editorial committee was composed of the following persons:

P. Foka (Chair), H. Appelshäuser, P. Braun-Munzinger, H.A. Gustafsson, M. Kowalski, T. Meyer, A. Sandoval, H.R. Schmidt, J. Stachel, R. Stock

Participating institutions

The following institutions will participate in the construction of the TPC detector.

- Bergen, Norway, Department of Physics, University of Bergen.
- Bratislava, Slovakia, Faculty of Mathematics and Physics, Comenius University.
- Budapest, Hungary, KFKI Research Institute for Particle and Nuclear Physics, Hungarian Academy of Sciences.

- CERN, Switzerland, European Laboratory for Particle Physics.
- Cracow, Poland, Henryk Niewodniczanski Institute of Nuclear Physics, High Energy Physics Department.
- Darmstadt, Germany, Gesellschaft für Schwerionenforschung (GSI).
- Frankfurt, Germany, Institut für Kernphysik, Johann-Wolfgang Goethe Universität.
- Heidelberg, Germany, Kirchhoff Institut für Physik, Ruprecht-Karls Universität.
- Heidelberg, Germany, Physikalisches Institut, Ruprecht-Karls Universität.
- Lund, Sweden, Division of Cosmic and Subatomic Physics, University of Lund.
- Marburg, Germany, Fachbereich Physik, Philipps Universität.
- Copenhagen, Niels Bohr Institute.
- Oslo, Norway, Department of Physics, University of Oslo.

Responsibilities

Table 10.1 presents the sharing of responsibilities for the construction of the TPC detector.

Table 10.1: Sharing of responsibilities for the construction and installation of the TPC detector.

Item	Institution
Field cage	CERN
Readout chambers	Bratislava, Budapest, Frankfurt, GSI, HD (Stachel)
FEE and readout	Bergen, Budapest, CERN, Frankfurt, GSI, HD (Herrmann), HD (Lindenstruth), HD (Stachel), Lund, Marburg, Oslo
Gas system	GSI
Slow control	CERN, GSI, Marburg
High voltage and low voltage	Crakow, Frankfurt, HD (Stachel)
Laser system	Copenhagen, GSI

Construction programme

The design of the field cage will be finalized at the end of 2000. It will be constructed during 2001, assembled and tested in 2002 and by May 2003 it will be ready for installation. The R&D of the field cage and gas envelope will extend until the end of 2001 to develop the best assembly and certification procedures.

A full-size prototype readout chamber will be constructed and tested by the third quarter of 2000. The production and testing of the full set of readout chambers will commence during the first quarter of 2001 and will continue until March 2003.

Regarding the gas system, the R&D on a recovery plant will continue until the end of 2000, at which time it will be decided whether or not it is needed.

The components of the front-end electronics will be designed and prototyped until the fourth quarter of 2001. Their production, starting in the fourth quarter of 2001, will be finished by the end of 2002. Testing of the components will run in parallel with the construction, and the system integration and system test will be done from the fourth quarter of 2002 until May 2003.

The design, construction, test and installation schedule of the TPC components is summarized in Fig. 10.1.

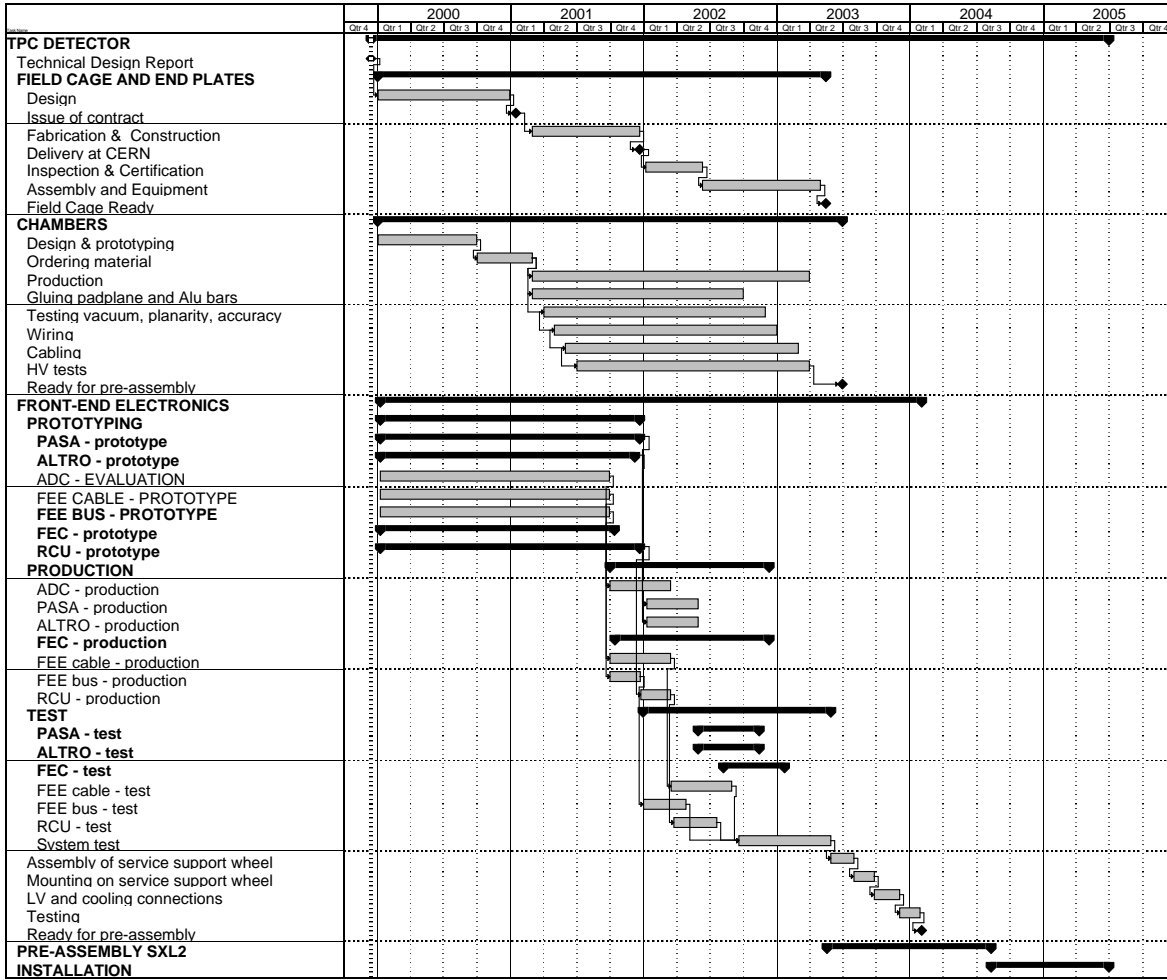


Figure 10.1: Chart of the time-line for the construction of the TPC.

Cost estimate and resources

The total cost of the TPC has been estimated taking into account realistic yields for the electronic chips. Industrial quotes were used as much as possible. Table 10.2 gives the global cost of the TPC in kCHF.

Table 10.2: Global cost of the TPC in kCHF.

Item	Cost
Field cage	1 660
Readout chambers	1 665
High/low voltage	950
Front end electronics	9 000
Readout	2 040
General	1 531
Total	17 046

The Level-3 farm, doing the local pattern recognition and data compression during the Pb period and used for offline reconstruction outside of it, has been costed at 1980 kCHF and is budgeted under the common projects.

The resources of the participating institutions cover the costs of the construction, installation and commissioning of the TPC.

References

Chapter 1

- [1] ALICE Collaboration, Technical Proposal, CERN/LHCC/95-71.
- [2] A. Mueller, in Proc. of the INPC 98; Nucl. Phys. **A654** (1999) 37; hep-ph/9902302.
- [3] ALICE Collaboration, Technical Proposal, Addendum 2, CERN/LHCC/99-13.
- [4] ALICE Collaboration, Technical Proposal, Addendum 1, CERN/LHCC/96-32.

Chapter 2

- [1] H.G. Fischer, Private Communication.
- [2] ALICE Collaboration, ALICE TDR 4, CERN/LHCC 99-12.
- [3] ALICE Collaboration, Technical Proposal, Addendum 2, CERN/LHCC 99-13.

Chapter 3

- [1] S. Afanasiev et al. (NA49 Collaboration), Nucl. Instrum. Methods **A430** (1999) 210.
- [2] R. Bouclier et al., Technical Note CMS-TN/96-038.
- [3] J. Bächler, Internal Note ALICE/99-25.
- [4] D. Vranic, Internal Note ALICE/97-22.
- [5] J. Harris et al., Nucl. Instrum. Methods **A315** (1992) 33.
- [6] F. Hahn, Private Communication.
- [7] I. Lehraus and W. Tejessy, Internal Note ALEPH 97-009, TPCGEN 97-001.
- [8] A. Marín (CERES/NA45 Collaboration), First Results from the CERES Radial TPC, in Proc. of the Quark Matter'99 Conference, Torino, Italy (to be published in Nucl. Phys. A).
- [9] S. Wenig, Nucl. Instrum. Methods **A409** (1998) 100.

Chapter 4

- [1] H. Wieman et al. (STAR Collaboration), Nucl. Phys. **A638** (1998) 559c.
- [2] L. Rolandi, Internal Note CERN-ALEPH-84-004.
- [3] C. Brandt, in Proc. of the AIP Conference 1984, 108 94-109.
- [4] F. Sauli et al., Nucl. Instrum. Methods **A386** (1997) 531.
- [5] ALICE Collaboration, Technical Proposal, Addendum 2, CERN/LHCC/99-13.
- [6] S. Afanasiev et al. (NA49 Collaboration), Nucl. Instrum. Methods **A430** (1999) 210.
- [7] A. Marín (CERES/NA45 Collaboration), First Results from the CERES Radial TPC, in Proc. of the Quark Matter'99 Conference, Torino, Italy (to be published in Nucl. Phys. A).
- [8] W. Blum and L. Rolandi, Particle Detection with Drift Chambers, Springer Verlag, Berlin, Heidelberg, New York, 1993, ISBN 3-540-56425-X.
- [9] <http://www.cern.ch/Alice/transparencies/rjd/Welcome.html>.
- [10] E. Mathieson, Nucl. Instrum. Methods **A270** (1988) 602.
- [11] B. Yu et al., IEEE Trans. Nucl. Sci. **NS-38** (1991) 454.
- [12] T. Lohse and W. Witzeling, Internal Note CERN-ALEPH-91-156.
- [13] R.L. Gluckstern, Nucl. Instrum. Methods **24** (1963) 381.
- [14] ALICE Collaboration, Technical Proposal, CERN/LHCC/95-71.

- [15] I. Lehraus, Nucl. Instrum. Methods **217** (1983) 43.
- [16] W.W.M. Allison and J.H. Cobb, Ann. Rev. Nucl. Part. Sci. **30** (1980) 253.
- [17] J.A. Hornbeck, Phys. Rev. **84** (1951) 615.
- [18] E.C. Beaty and P.L. Patterson, Phys. Rev. **170** (1968) 116.
- [19] A. Barr et al., Nucl. Phys. **B61**(1998) 264.
- [20] P. Bonneau and M. Bosteels, CERN/LHCC/99-33.
- [21] CMS Collaboration, CMS TDR 5, CERN/LHCC/98-6.
- [22] J. Bächler et al., Internal Note ALICE INT-99-48.
- [23] D. Decamp et al. , Nucl. Instrum. Methods **A294** (1990) 121.
- [24] P. Némethy et al., Nucl. Instrum. Methods **212** (1983) 273.
- [25] S.R. Amendolia et al., Nucl. Instrum. Methods **234** (1985) 47.
- [26] A. Lebedev, Private Communication;
M. Alyushin et al., IEEE Nuclear Science Symposium 1996, Anaheim, CA, Conference Record, N27-33, p 499–503.
- [27] L.V. Griffith et al., Rev. Sci. Instrum. **61** (1990) 2138.
- [28] F. Bieser et al., Nucl. Instrum. Methods **A385** (1997) 535.
- [29] S. Bauer, Diplomarbeit, Universität Frankfurt, 1997.
- [30] F. Gabler, Diplomarbeit, Universität Frankfurt, 1995.
- [31] B. Lasiuk and C.A.Whitten, Internal Note STAR 360, 1998.

Chapter 5

- [1] J.C. Berset, L. Musa, M. Richter, Internal Note ALICE99-49 (in preparation).
- [2] L. Musa, Internal Note ALICE99-50.
- [3] ALICE Collaboration, Technical Proposal, CERN/LHCC/95-71.
- [4] QSE-SAMTEC, Matched Impedance Connector.
- [5] R. Baur et al., Nucl. Instrum. Methods **A409** (1998) 278 and in Proc. of the 3rd Workshop on Electronics for LHC Experiments, CERN-LHCC-97-60.
- [6] D.A. Landis et al., IEEE Trans. Nucl. Sci. **NS-29**, No. 1, 1982.
- [7] G. Gramegna et al., Nucl. Instrum. Methods **A390** (1997) 241.
- [8] J.C. Berset et al., Internal Note ALICE99-51 (in preparation).
- [9] P. Szymanski, Internal Note ALICE INT-98-13.
- [10] J.C. Berset et al., Internal Note ALICE99-52 (in preparation).
- [11] L. Musa et al., Front-End Electronics for the ALICE TPC-Detector, in Proc. of the 4th Workshop on Electronics for LHC Experiments Rome, September 21-25, 1998.
- [12] F. Anghinolfi et al., IEEE Trans. Nucl. Science **42**, No. 4, 1995, p.772.
- [13] R.A. Boie, A.T. Hrisoho, and P. Rehak, Nucl. Instrum. Methods **A192** (1982) 365.
- [14] High Performance Backplane Design with GTL+, SCEA011 Texas Instruments, June 1999.
- [15] G. Rubin and P. Vande Vyvre, Internal Note ALICE 96-43.
- [16] G. Rubin, Internal Note ALICE 98-21.
- [17] <http://www.cern.ch/TTC/intro.html>.
- [18] STAR collaboration, STAR Conceptual Design Report, Lawrence Berkeley Laboratory, University of California, PUB-5347, June 1992.
- [19] A. Ljubicic, Jr. et al., Design and Implementation of the STAR Experiment's DAQ, in Proc. of the 10th IEEE Real Time Conference, 9/22-26/97, Beaune, France.
- [20] J. Berger et al., IKF-report, IKF-HENPG/1-98, University of Frankfurt.
- [21] ALICE Collaboration, Technical Proposal, Addendum 1, CERN/LHCC/96-32.
- [22] ALICE Collaboration, Technical Proposal, Addendum 2, CERN/LHCC/99-13.
- [23] ALICE Collaboration, ALICE TDR 2, CERN/LHCC/99-4.
- [24] J. Berger, Diploma thesis, University of Frankfurt, 1998.

- [25] M. Nelson and J.L. Gailly, *The Data Compression Book*, M&T Books, New York (1996).
- [26] K. Sulimma, Private Communication.
- [27] STAR Collaboration, DAQ Review, BNL, 1997.
- [28] C.E. Shannon, *Bell System Technical Journal*, **27** (1948) 379-423.
- [29] H. Beker and M. Schindler, Data compression on zero suppressed High Energy Physics Data, Institute of Computer Graphics, Technical University Vienna (1997).
- [30] Gray, R. M., *IEEE ASSP Magazine* April (1984) 4.
- [31] Linde, Y., Buzo, A, and Gray, R. M., *IEEE Transactions on Communications* **28** (1980) 84.
- [32] M. Mattavelli, Private Communication.
- [33] H. Appelshäuser, PhD thesis, University of Frankfurt, 1996.
- [34] J. Günther, PhD thesis, University of Frankfurt, 1998.
- [35] http://sol.star.bnl.gov/STAR/html/daq_l/public/softwarecluster.html.
- [36] C. Adler et al., The proposed Level-3 Trigger System for STAR, subm. to *IEEE Transactions in Nuclear Science* (1999).
- [37] <http://ikf1.star.bnl.gov/l3/l3clstatus.ps>
- [38] P. Yepes, Internal Note STAR 246 (1995).
- [39] P. Yepes, Internal Note STAR 248 (1996); *Nucl. Instrum. Methods* **A380** (1996) 582.
- [40] F. Pühlhofer, D. Röhricht, R. Keidel, *Nucl. Instrum. Methods* **A263** (1988) 360.
- [41] D. Brinkmann et al., *Nucl. Instrum. Methods* **A354** (1995) 419.
- [42] <http://www.pcisig.com>.
- [43] CERN ALICE DAQ group, Internal Note ALICE 99-03.
- [44] CERN ALICE DAQ group, Internal Note ALICE 99-04.
- [45] G. Rubin and J. Sulyan, Internal Note ALICE 97-14.
- [46] Report by Electronic Department of the Departamento de Física Facultad de Ciencias Exactas Universidad Nacional de La Plata.
- [47] The Programmable Logic Data Book 1994, Xilinx Inc. (1995) San Jose, California.

Chapter 7

- [1] ALICE Collaboration, Technical Proposal, CERN/LHCC/95-71.
- [2] M. Kowalski, Internal Note ALICE/96-36.
- [3] <http://AliSoft.cern.ch/offline>
- [4] G.F. Knoll, *Radiation Detection and Measurements*, Wiley, New York, 1979.
- [5] I. Lehrhaus et al., *IEEE Trans. Nucl. Sci.* **NS-30** (1983) 50.
- [6] W. Blum and L. Rolandi, *Particle Detection with Drift Chambers*, Springer Verlag, Berlin, Heidelberg, New York, 1993, ISBN 3-540-56425-X.
- [7] J.E. Moyal, *Phil. Mag.* **46** (1955) 263;
W.W. M. Alisson and J. H. Cobb, *Ann. Rev. Nucl. Part. Sci.*, **30** (1980) 253;
S.K. Kotelnikov et al., *Nucl. Instrum. Methods* **A307** (1991) 273.
- [8] K. Lassila-Perini, L. Urbán, *Nucl. Instrum. Methods* **A362** (1995) 416.
- [9] H.-G. Fischer, Private Communication.
- [10] W. Betts et al., Internal Note STAR SN0263 (1996).
- [11] J.S. Gordon and E. Mathieson, *Nucl. Instrum. Methods* **227** (1984) 267;
E. Mathieson and J.S. Gordon, *Nucl. Instrum. Methods* **227** (1984) 277;
J.R. Thompson et al., *Nucl. Instrum. Methods* **A234** (1985) 505;
E. Mathieson, *Nucl. Instrum. Methods* **A270** (1988) 602.
- [12] P. Billior, *Nucl. Instrum. Methods* **225** (1984) 352;
M. Regler and R. Frühwirth, Reconstruction of Charged Tracks, in Proc. of the Advanced Study Institute on Techniques and Concepts in High Energy Physics, Plenum Publ. Corp., 1989;
R. Frühwirth, Application of Filter Methods to the Reconstruction of Tracks and vertices in Events

- of Experimental High Energy Physics, HEPHY-PUB 516/88, Vienna 1988;
 B. Batyunya et al., Internal Note ALICE INT-97-24.
 [13] ALICE Collaboration, ALICE TDR 4, CERN/LHCC 99-12.

Chapter 8

- [1] ALICE Collaboration, Technical Proposal, CERN/LHCC/95-71 (1995).
- [2] RD-32 Collaboration, R&D Proposal, CERN/DRDC 92-32, DRDC/P-43;
 RD-32 Collaboration, Final Report, CERN LHCC 96-16.
- [3] S. Afanasiev et al., Nucl. Instrum. Methods **A430** (1999) 210.
- [4] P. Szymanski et al., Internal Note ALICE INT-98-48.
- [5] E. Gatti et al., Nucl. Instrum. Methods **163** (1979) 83-92.
- [6] I. Endo et al., Nucl. Instrum. Methods **188** (1981) 51-58.
- [7] J. Bächler et al., Internal Note ALICE INT-97-19.
- [8] F. Sauli et al., Nucl. Instrum. Methods **A386** (1997) 531.
- [9] H.R. Schmidt and H. Stelzer, Internal Note ALICE INT-99-54.
- [10] S. Bachmann et al, Charge Amplification and Transfer Processes in the Gas Electron Multiplier, CERN-EP/99-48 (to be published in Nucl. Instrum. Methods).
- [11] M. Hoch, Doctoral Thesis, TU Vienna (1998).
- [12] A. Mykulyak et al., Internal Note ALICE INT-99-55.
- [13] A. Bressan et al., Nucl. Instrum. Methods **A425** (1999) 262; CERN preprint CERN-EP-98-163 (1998).
- [14] J. Benlloch et al., Nucl. Instrum. Methods **A419** (1998) 410.
- [15] H.R. Schmidt, H. Sann and H. Stelzer, Internal Note ALICE INT-99-56.
- [16] P. Vanlaer et al, Internal Note CMS IN-1999/024.
- [17] M. Hildebrandt, PhD. Thesis, Heidelberg (1999).
- [18] A. Bressan et al., Nucl. Instrum. Methods **A424** (1999) 321.

Chapter 9

- [1] J. Bielski, Internal Note ALICE/97-32 (updated with an annex in July 1999).
- [2] ALICE Collaboration, ALICE TDR 4, CERN/LHCC 99-12.
- [3] O. Villalobos et al., Internal Note ALICE 98-23 (new updated version in preparation).
- [4] ALICE/LHCb Teams, Internal Note ALICE/98-03.
- [5] D. Blanc et al., CERN-EP-071 (EOS) May 1998.
- [6] <http://www.opceurope.org>; <http://www.opcfoundation.org/opc-public-tech.htm>.
- [7] <http://www.microsoft.com/activex/default.asp>.
- [8] CMS Collaboration, CMS TDR 5, CERN/LHCC 98-6.
- [9] Initial Safety Discussion for the ALICE TPC Detector, TIS/GS/WW/1999-054.